



UCGE Reports

Number 20335

Department of Geomatics Engineering

## **Space-Time Equalization Techniques for New GNSS Signals**

(URL: <http://www.geomatics.ucalgary.ca/graduatetheses>)

by

**Pratibha B Anantharamu**

**September 2011**



UNIVERSITY OF CALGARY

Space-Time Equalization Techniques for New GNSS Signals

by

Pratibha B Anantharamu

A THESIS

SUBMITTED TO THE FACULTY OF GRADUATE STUDIES  
IN PARTIAL FULFILMENT OF THE REQUIREMENTS FOR THE  
DEGREE OF DOCTOR OF PHILOSOPHY

DEPARTMENT OF GEOMATICS ENGINEERING

CALGARY, ALBERTA

SEPTEMBER, 2011

© Pratibha B Anantharamu 2011

## **Abstract**

The Galileo satellite program has opened the possibility of tracking signals with a variety of modulation schemes. One of these modulations, the Binary Offset Carrier (BOC) signal, has several advantages over the traditional BPSK modulation such as an increased resilience against multipath and improved tracking performance. However, BOC signals are characterized by autocorrelation functions with multiple peaks that may lead to false tracking lock.

In this dissertation, BOC signal tracking techniques using space-time processing are considered. A new class of temporal equalizers capable of providing unambiguous tracking is first proposed based on the zero-forcing (ZF) and minimum mean square error (MMSE) criteria. The proposed approaches reshape the ambiguous BOC autocorrelation function into a single peaked curve. The performance of the proposed ZF Shaping (ZFS) and MMSE Shaping (MMSES) tracking techniques is thoroughly analyzed using signal simulations. Live data collected from the GIOVE A/B satellites is also used to complement and further verify the analysis. Results indicate that the ambiguity in BOC signal tracking is removed with no significant performance loss.

In the second part of the thesis, antenna arrays are considered to enhance the quality of BOC signals. In this respect, an innovative calibration technique exploiting the properties of GNSS signals is proposed. This methodology exploits the fact that GNSS satellite positions are known to the receiver, thereby allowing antenna array calibration without pilot signal requirement. The proposed methodology is tested and analyzed using live GNSS signals with arrays of up to four antennas. Experiments using live GNSS data

demonstrate the feasibility and effectiveness of the proposed calibration algorithm that enables multi-antenna processing.

Finally, the advantages of space-time processing techniques and their application to GNSS signal processing are studied. A combined space-time technique based on the MMSES and minimum variance criterion is proposed and the advantages of combined temporal and spatial processing are shown. The performance of BOC signal tracking using combined space-time processing is analyzed using live data from the GIOVE-A satellite to demonstrate the effectiveness of the developed technique.

## Acknowledgements

I offer my sincere gratitude to my supervisor, Professor Gérard Lachapelle, who supported me throughout my doctoral studies. I take this opportunity to attribute the level of my research work to his encouragement, profound knowledge and enthusiasm for new research work that constantly motivated me. His constant support, both technically and financially always kept me highly motivated with my doctoral study. I will always be grateful to him for providing me with an opportunity to work under his supervision.

My heartfelt thanks to Dr. Daniele Borio for guiding me throughout my graduate studies. He was a constant motivator who imbued in me the spirit of learning new things. I truly appreciate his support and suggestions which helped me to develop as a better person both technically and professionally. His detailed review and comments during thesis writing improved the quality of my thesis. *Grazie Mille Daniele.*

I would like to take this opportunity to thank my managers at Accord Software & Systems Pvt. Ltd, India, namely Dr. Jayanta K Ray and Mr. Rakesh Nayak, who inspired and guided me to take up higher studies at the University of Calgary.

I would like to acknowledge Dr. Aiden Morrison who was always helpful to collect GNSS data using the four-channel front-end developed by him. I would like to thank Anshu and Kannan who were always available for short coffee breaks and all the fun times we had during our studies. Thank you Haris, Ahmed, Mohamed and Billy for being available for technical and non-technical discussions and being my good friends. I would also like to thank all my other PLAN group colleagues who made my study period enjoyable and interesting.

The presence of Gopi, Poorani, Suren, Saranya, Suresh, Ramani, Chandru and Menaka throughout my stay in Calgary provided me a family environment away from my home in India. Thank you friends!!!

Last but not the least, my special thanks to my husband Shashank for his sustained love and constant support without which my dream of doctoral studies would have remained a dream and to my parents, lovely sis and her family, and my in-laws for their constant encouragement and blessings.

*For their endless love...*

*To my beloved parents*

## Table of Contents

Abstract .....	ii
Acknowledgements .....	iv
Table of Contents .....	vii
List of Tables .....	x
List of Figures and Illustrations .....	xi
List of Abbreviations .....	xvii
List of Symbols .....	xviii
CHAPTER ONE: INTRODUCTION .....	1
1.1 Background work .....	3
1.1.1 New GNSS Signals .....	3
1.1.2 Time Domain Processing .....	5
1.1.3 Space Domain Processing .....	6
1.1.4 Space-Time Processing .....	8
1.2 Limitations and motivations .....	9
1.3 Objectives .....	11
1.3.1 Temporal Processing .....	12
1.3.2 Spatial Processing .....	14
1.3.3 Space-Time Processing .....	14
1.3.4 Test Setup and Data Analysis .....	15
1.4 Dissertation outline .....	16
CHAPTER TWO: BOC SIGNAL STRUCTURE AND TRACKING .....	18
2.1 Signal and System model .....	18
2.2 GNSS Signal Tracking .....	20
2.2.1 Phase/Frequency Lock Loop .....	21
2.2.2 Delay Lock Loop .....	23
2.2.3 Correlation Process .....	24
2.3 BOC Signals .....	25
2.3.1 Signal Structure .....	25
2.3.2 Signal Characteristics .....	26
2.3.3 Galileo Signals .....	27
2.4 BOC signal tracking .....	31
2.4.1 Convolutional Representation .....	31
2.4.2 Multiplicative Representation .....	33
2.4.3 Bump-Jump .....	36
2.4.4 Double Estimator .....	39
2.4.5 Pre-filtering .....	40
2.5 Tracking loop analysis techniques .....	42
2.6 Performance metrics .....	44
2.6.1 Tracking Jitter .....	45
2.6.2 Tracking threshold .....	46
2.6.3 MTLL .....	47
2.6.4 Convergence Analysis .....	49
2.6.5 Multipath Error Envelope .....	50

<b>CHAPTER THREE: TEMPORAL PROCESSING OF BOC SIGNALS .....</b>	<b>53</b>
3.1 Time-domain BOC signal tracking.....	54
3.2 Pre-filters .....	56
3.3 MMSES and ZFS .....	60
3.4 Time domain Implementation.....	64
3.5 Delay and Phase Independent Tracking.....	66
3.6 Analytical characterization .....	67
3.6.1 Theoretical Analysis .....	67
3.6.2 Computational Analysis .....	68
3.7 Performance analysis .....	70
3.7.1 Tracking Jitter.....	71
3.7.2 Tracking threshold.....	76
3.7.3 MTLL .....	78
3.7.4 Convergence analysis .....	80
3.7.5 Multipath error envelope .....	82
3.8 Experimental analysis .....	85
3.8.1 ACF Analysis .....	86
3.8.2 C/N <sub>0</sub> Estimation.....	89
3.9 Summary .....	90
<b>CHAPTER FOUR: SPATIAL PROCESSING OF GNSS SIGNALS .....</b>	<b>92</b>
4.1 Introduction to antennas.....	92
4.2 Antenna Arrays .....	96
4.3 Calibration .....	102
4.4 Signal Model.....	104
4.4.1 Mutual Coupling.....	105
4.4.2 The correlation process.....	107
4.5 Projection based calibration methodology.....	109
4.6 Results and analysis .....	113
4.6.1 Monte Carlo Simulations.....	113
4.6.2 Hardware simulator analysis .....	117
4.6.3 Real data analysis .....	120
4.7 Conclusions.....	129
<b>CHAPTER FIVE: COMBINED SPACE-TIME ADAPTIVE PROCESSING .....</b>	<b>130</b>
5.1 Introduction to space-time processing .....	130
5.2 STAP techniques.....	132
5.2.1 MSE .....	133
5.2.2 Maximum SNR.....	135
5.2.3 ML .....	136
5.2.4 MV .....	137
5.3 STAP for GNSS signals.....	139
5.4 Proposed STAP for BOC signals.....	142
5.5 Results and Analysis .....	146
5.5.1 Simulation analysis.....	146
5.5.2 Real data analysis .....	148
5.6 Summary .....	150

CHAPTER SIX: CONCLUSIONS AND RECOMMENDATIONS .....	151
6.1 Conclusions.....	151
6.1.1 Temporal Processing .....	151
6.1.2 Spatial Processing.....	153
6.1.3 Space-Time Processing .....	154
6.2 Recommendations for future work .....	154
References.....	157
APPENDIX A: CODE DISCRIMINATORS AND TRACKING JITTER.....	165
A.1. Code discriminators .....	165
A.1.1. Discriminator Gain .....	165
A.2. Tracking jitter.....	168
APPENDIX B: SEMI-ANALYTIC TECHNIQUE.....	173
B.1. Semi-analytic models .....	173
B.1.1. Bump-Jump.....	176
B.1.2. Double Estimator .....	177
B.1.3. Pre-filtering .....	178

## List of Tables

Table 2-1 GIOVE spreading code and navigation signal parameters .....	30
Table 2-2 Theoretical tracking jitter for different discriminator types .....	45
Table 3-1 Different pre-filtering techniques defined in Yang et al. 2006 .....	58
Table 3-2 Computational complexity of pre-filtering, BJ and DE. ....	69
Table 3-3 Parameters of the real data used for the computational analysis.....	70
Table 3-4 Simulation parameters considered for semi-analytic analysis of BOC tracking techniques .....	71
Table 4-1 Optimum C/N <sub>0</sub> gain achievable using M-antenna array.....	126
Table 4-2 Correlator inputs to the C/N <sub>0</sub> estimation algorithm for the single antenna, before and after calibration case. ....	127
Table A-1 Description of various code discriminators used in GNSS tracking loops....	165
Table A-2 Discriminator gain for BPSK and BOCs (1, 1) signal.....	168
Table A-3 Tracking jitter for BPSK, BOCs (1, 1) and pre-filtered signals .....	172

## List of Figures and Illustrations

Figure 1-1 Structure of thesis.....	17
Figure 2-1 Standard GNSS tracking loop structure .....	20
Figure 2-2 Block diagram of code and carrier tracking loops .....	22
Figure 2-3 BOC Signal structure and its components .....	26
Figure 2-4 BPSK and BOC Signals autocorrelation function and power spectrum .....	27
Figure 2-5 Galileo and GPS frequency plan as provided in Galileo 2008.....	29
Figure 2-6 ACFs and PSDs of Galileo E1 and E6 Signals .....	31
Figure 2-7 Convolutional representation of the ranging code, $c(t)$ . The useful signal is obtained by filtering the PRS modulated Dirac comb with a sub-carrier filter .....	32
Figure 2-8 Multiplicative representation of the ranging code, $c(t)$ . The useful signal is obtained by multiplying the BPSK modulated PRN code by the periodic repetition of the sub-carrier.....	34
Figure 2-9 S-curves of BPSK and BOC (1, 1) modulated signals for a coherent discriminator type with 0.2 chips early-minus-late spacing .....	36
Figure 2-10 Bump-Jump tracking structure.....	37
Figure 2-11 Placement of VE and VL correlator outputs on BOCs(1,1) ACF for BJ decision logic .....	38
Figure 2-12 Double Estimator tracking structure .....	39
Figure 2-13 BOC (1, 1) ACF as a function of code and sub-carrier delays .....	40
Figure 2-14 Pre-filtering tracking structure .....	41
Figure 2-15 Semi-analytic model of a GNSS code tracking loop .....	44
Figure 2-16 Simulation scheme adopted for evaluation of MTLL from Borio et al 2010.....	48
Figure 2-17 S-curve of line-of-sight (LOS), multipath (MP) and combined signal for the single multipath ray model.....	52
Figure 2-18 Multipath error envelope of BPSK and BOC signals; Narrow correlator with $d_s$ equal to 0.1 chips and a coherent discriminator.....	52

Figure 3-1 Different side-peak compensation techniques based on different signal representations. DE exploits the multiplicative representation while the pre-filtering techniques use the convolutional representation.....	55
Figure 3-2 Block diagram of pre-filtering techniques given in Yang et al. 2006. $U(f)$ and $V(f)$ used to filter the incoming and locally generated signals to provide an unambiguous correlation function .....	57
Figure 3-3 Correlation functions after applying a symmetric phase only matched filter for different $C/N_0$ values. An unambiguous correlation function is observed for high SNR values .....	59
Figure 3-4 ACF with and without applying MMSES for an input BOCs(1, 1) signal simulated with a $C/N_0$ of 40 dB-Hz .....	62
Figure 3-5 ACFs of BOCc(10, 5) and BOCc(15, 2.5) before and after applying MMSES for an input signal with a $C/N_0$ of 40 dB-Hz.....	63
Figure 3-6 Filtering effects on BOC signal and its spectrum .....	65
Figure 3-7 Modified tracking structure for independent code and carrier tracking.....	66
Figure 3-8 $C/N_0$ estimates provided by a PLL operating on filtered and unfiltered correlators. The use of unfiltered correlators allows the tracking of weaker signals .....	67
Figure 3-9 Code tracking jitter of BJ and DE techniques as a function of the $C/N_0$ and for non-coherent discriminator with different $d_s$ .....	73
Figure 3-10 Code tracking jitter of ZFS and MMSES as a function of the $C/N_0$ and for non-coherent discriminator with different $d_s$ .....	74
Figure 3-11 Comparison of code tracking jitter a function of input $C/N_0$ for quasi-coherent discriminator, 4 ms coherent integration time and 0.5 Hz DLL .....	75
Figure 3-12 Comparison of code tracking jitter as a function of $C/N_0$ for coherent discriminator, 4 ms coherent integration time and 0.5 Hz DLL .....	75
Figure 3-13 Comparison of tracking thresholds for different BOC tracking techniques, 4 ms coherent integration time and 0.5 Hz DLL bandwidth.....	76
Figure 3-14 Comparison of tracking thresholds for BJ tracking technique after applying modified decision logic .....	77
Figure 3-15 S-curve plots for DE, BJ and MMSES used for determining the stable points for the MTLL computation .....	79

Figure 3-16 Comparison of MTL for DE, BJ, ZFS and MMSES techniques; 0.2 chips early-minus-late spacing, 0.5 Hz DLL bandwidth and 4 ms integration time.	79
Figure 3-17 Code delay error convergence for the MMSES technique for different initial acquisition errors (represented by different colored lines) .....	80
Figure 3-18 Code delay error for DE, BJ and MMSES tracking techniques for an input signal characterized by a $C/N_0$ of 25 dB-Hz.....	82
Figure 3-19 ACF with varying base widths after applying MMSES on BOCs (1, 1) modulated signal .....	83
Figure 3-20 Multipath error envelopes for DE and MMSES techniques, Coherent discriminator with 0.5 chips early-minus-late spacing. ....	83
Figure 3-21 BOCs(1, 1) ACF after applying ZFS as a function of the width of the desired sub-carrier.....	84
Figure 3-22 Experimental setup: the signal was split between two front-ends. One data stream was used as a reference, whereas the other was progressively attenuated in order to simulate weak signal conditions .....	85
Figure 3-23 Scatter plots for different BOC tracking techniques - PLL driven by filtered (left) and unfiltered (right) samples.....	86
Figure 3-24 ACF estimated from real data for different pre-filtering techniques: 1- Standard Correlation, 2-Phase-only matched, 3-Symmetric Phase-only, 4- Square-root normalized, 5-ZFS technique.....	87
Figure 3-25 Analysis of higher order BOC signals after applying the MMSES technique - Real data ACF analysis for BOCc(10, 5) (left) and BOCc(15, 2.5)(right) signals. ....	88
Figure 3-26 $C/N_0$ estimates obtained using live GIOVE data for the considered BOC tracking techniques - After 30 seconds, the signals were progressively attenuated .	90
Figure 4-1 Antenna radiation pattern with its main parameters .....	93
Figure 4-2 Antenna Classification based on the radiation pattern.....	95
Figure 4-3 Different types of antenna array structures .....	97
Figure 4-4 Schematic representation of an antenna array receiving a single signal from a source at a specific elevation and azimuth .....	98
Figure 4-5 Block diagram representing the basic operations performed during beamforming .....	99

Figure 4-6 Comparison of array patterns for different numbers of antenna array elements, $M$ .....	100
Figure 4-7 Comparison of array pattern for varying antenna spacing for a linear array structure, $M = 8$ .....	101
Figure 4-8 Beam pattern of an antenna array as compared to a single antenna in the presence of interference .....	102
Figure 4-9 Two-element antenna array along with mutual coupling coefficients .....	106
Figure 4-10 GNSS signal tracking structure for multi-antenna processing. The same local carrier and code are used for processing different signals, preserving the amplitude/phase relationship among different signal components .....	109
Figure 4-11 Phase mean square error of the projection based calibration algorithm as a function of the coherent integration time, $T$ .....	115
Figure 4-12 Array patterns before and after calibration for a linear, planar and circular array. $M = 8$ .....	116
Figure 4-13 Data collection setup using a hardware simulator to provide dual channel data .....	118
Figure 4-14 Phase of the useful signal components for a dual antenna array using the hardware simulator.....	119
Figure 4-15 Modified hardware data collection setup used to observe phase variations along time.....	119
Figure 4-16 Phase calibration results for the modified hardware simulator setup .....	120
Figure 4-17 Real data collection setup using four antennas. The antennas were selected in different configurations to obtain planar/triangular arrays .....	121
Figure 4-18 Placement of antennas in different structures on the 5x5 antenna array for real data collection .....	121
Figure 4-19 Real data beamforming results before and after applying the projection based calibration methodology on planar array data .....	122
Figure 4-20 Azimuth errors after performing angle of arrival estimation on the calibrated planar array data .....	123
Figure 4-21 Elevation errors after performing angle of arrival estimation on the calibrated planar array data .....	123
Figure 4-22 Real data beamforming results before and after applying the projection based calibration methodology on triangular array data .....	125

Figure 4-23 C/N <sub>0</sub> estimates obtained after performing calibration and beamforming on the linear array data for several satellites (represented by different colored lines).....	128
Figure 4-24 C/N <sub>0</sub> estimates obtained after performing calibration and beamforming on the triangular array data for several satellites (represented by different colored lines).....	128
Figure 4-25 C/N <sub>0</sub> estimates obtained after performing calibration and beamforming on the planar array data for several satellites (represented by different colored lines).....	129
Figure 5-1 Block diagram of space-time processing .....	131
Figure 5-2 Representation of two different space-time processing techniques. ....	132
Figure 5-3 Plot of array factor as a function of the number of snapshots used in adaptive array processing for interference mitigation using a 6-element linear array. Signal DOA = 15 degrees and Interference DOA = 50 degrees .....	134
Figure 5-4 Adaptive array processing mitigating the presence of two interference signals from different directions using LMS algorithm. Signal DOA = 15 degrees, Interference 1 DOA = 45 degrees and Interference 2 DOA = -30 degrees .....	135
Figure 5-5 Performance of MVDR beamforming with and without interference (9-element array) .....	138
Figure 5-6 Array factor after applying MVDR beamforming in the presence of multiple interference sources at DOA 80, -60 and -40 degrees with the desired DOA at 20 degrees (9-element array) .....	138
Figure 5-7 Pre and post-correlation decoupled STAP as applied to GNSS signals.....	140
Figure 5-8 Space-time adaptive processing structure proposed for BOC signal tracking; the temporal filter provides signal with unambiguous ACF and the spatial filter provides enhanced performance to multipath, interference and noise	143
Figure 5-9 Antenna array pattern for a 4-element planar array computed using a MVDR beamformer in the absence of interference .....	145
Figure 5-10 Antenna array pattern for a 4-element planar array computed using a MVDR beamformer in the presence of single and dual interference sources .....	145
Figure 5-11 Semi-analytic simulation model for multi-antenna system comprising of M-antenna with a spatial beamformer .....	147

Figure 5-12 Phase tracking jitter obtained for single, dual and three antenna linear array as a function of input C/N <sub>0</sub> for a Costas discriminator (20 ms coherent integration and 5 Hz bandwidth).....	148
Figure 5-13 Experimental setup with signals collected using two antennas spaced 8.48 cm apart.....	149
Figure 5-14 C/N <sub>0</sub> estimates obtained using a single antenna, temporal only processing and a dual antenna array system using space-time processing .....	150
Figure A-1 Equivalent model of a digital GNSS tracking loop.....	169
Figure B-1 Generalized semi-analytic model for digital GNSS tracking loops analysis	175
Figure B-2 Semi-analytic model for the Bump-Jump technique .....	176
Figure B-3 Semi-analytic model for the Double Estimator technique .....	178
Figure B-4 Semi-analytic model for pre-filtering technique .....	179

## List of Abbreviations

<b>Abbreviations</b>	<b>Description</b>
ACF	: Auto-Correlation Function
BOC	: Binary-Offset-Carrier
BPSK	: Binary Phase Shift Keying
BJ	: Bump-Jump
CDMA	: Code Division Multiple Access
DLL	: Delay Lock Loop
DE	: Double Estimator
DOA	: Direction of Arrival
FLL	: Frequency Lock Loop
FT	: Fourier Transform
GIOVE	: Galileo In-Orbit Verification Experiment
GNSS	: Global Navigation Satellite System
GPS	: Global Positioning System
IF	: Intermediate Frequency
IFT	: Inverse Fourier Transform
ISI	: Inter Symbol Interference
LNA	: Low Noise Amplifier
LOS	: Line-of-Sight
MDR	: Multipath-to-Direct Ratio
MEE	: Multipath Error Envelope
ML	: Maximum Likelihood
MMF	: Mis-Match Filter
MMSES	: Minimum Mean Square Error Shaping
MP	: MultiPath
MSE	: Mean Square Error
MTLL	: Mean Time to Lose Lock
MV	: Minimum Variance
NCO	: Numerically Controlled Oscillator
NI	: National Instruments
PDF	: Probability Density Function
PLL	: Phase Lock Loop
PRN	: Pseudo Random Noise
PRS	: Pseudo Random Sequence
PSD	: Power Spectral Density
RF	: Radio Frequency
SLL	: Sub-carrier Lock Loop
SNR	: Signal to Noise Ratio
STAP	: Space-Time Adaptive Processing
SV	: Satellite Vehicle
VE	: Very Early
VL	: Very Late
ZFS	: Zero-Force Shaping

## List of Symbols

Symbol	Definition
$I$	In-phase Component
$Q$	Quadrature phase component
$\eta$	Noise Component
$P$	Prompt
$s_b(\cdot)$	Sub-carrier
$c(\cdot)$	Ranging code
$q$	Correlator output
$A$	Satellite Amplitude
$R(\cdot)$	Autocorrelation function
$\mathcal{F}$	Fourier Transform operation
$\varepsilon$	Elevation angle [radians]
$\alpha$	Azimuth angle [radians]
$\mathbf{s}$	Steering vector
$M$	Number of Antennas
$L$	Number of Satellites
$\lambda$	Wavelength of signal [m]
$\mathbf{C}$	Calibration Matrix
$\phi$	Carrier Phase [radians]
$f_D$	Doppler frequency [Hz]
$T_c$	Code chip duration [s]
$T_i$	Coherent integration time [s]
$d_s$	Early-minus-Late chip spacing [chips]
$C / N_0$	Carrier-to-noise-density ratio
$\Re(\cdot)$	Real part of a number
$\text{Im}(\cdot)$	Imaginary part of a number
$[\cdot]^H$	Hermitian operation
$[\cdot]^T$	Transpose operation
$[\cdot]^{-1}$	Inverse operation
$(\cdot)^*$	Conjugate operation

## Chapter One: **Introduction**

New and modernized Global Navigation Satellite Systems (GNSS) such as the Global Positioning System (GPS), the European Galileo, the Russian GLONASS and the Chinese Compass broadcast signals with enhanced correlation properties as compared to the first generation GPS signals. These signals provide more accurate and reliable positioning with respect to current GPS signals with the introduction of new modulation schemes. New GNSS signals provide improved time resolution, resulting in more precise range measurements along with the advantage of being more resilient to multipath and radio frequency (RF) interference. One of these modulations is the Binary-Offset-Carrier (BOC) (Betz 1999) transmitted by Galileo.

Accompanying the benefits of BOC modulation scheme are difficulties involved in tracking them. The autocorrelation function (ACF) of a BOC signal is multi-peaked leading to false peak-lock and ambiguous tracking. Thus, new tracking algorithms need to be developed in order to correctly track the primary signal peak. Several works (Fine & Wilson 1999, Yang et al. 2006, Julien et al. 2007, Hodgart et al. 2008) have produced different BOC tracking schemes in which the authors have tried to mitigate false lock on secondary peaks. However, the full benefits of these new algorithms can be determined only after a number of significant analyses. These should be performed in different signal environments and under different operating conditions. Additionally, new tracking schemes including space-time processing techniques can be introduced to further improve the performance of GNSS receivers.

Space-time equalization (Kohno 1998) techniques utilize both spatial and temporal information of signals received from multiple antennas to compensate for the effects of multipath fading and co-channel interference. In the context of BOC signals, these kinds of techniques can be applied to remove the effects of sub-carrier, which introduces multiple peaks in the autocorrelation function, along with reducing multipath and interference effects. In temporal processing, traditional equalizers (Qureshi 1985) in time-domain are useful to compensate for signal distortions. These distortions can be caused by sub-carrier and multipath components, when considering BOC signals, or multipath alone in the Binary Phase Shift Keying (BPSK) case. Temporal equalization for BPSK signals can be achieved by designing filters to mitigate the distortions caused by multipath components. But equalization becomes more challenging in the case of BOC signals where the effect of both sub-carrier and multipath has to be accounted for. On the other hand, by using spatial processing (Van Veen & Buckley 1988), it should be possible to extract the desired signal from a set of received signals by electronically varying the antenna pattern. The combination of an antenna array (spatial processing) and an equalizer (temporal processing) results in better system performance. This concept of space-time processing has been successfully used in other applications (Lindskog 1999) such as radar, aerospace and mobile technologies where this kind of combined processing proved to be beneficial. Hence the main interest of this work is to apply space-time processing techniques to new GNSS signals in order to enhance the signal quality, avoid ambiguous tracking and improve tracking performance under weak signal environments or in the presence of harsh multipath components.

## 1.1 Background work

GPS modernization and the introduction of new GNSS such as Galileo and GLONASS have stimulated the development of new applications including automotive, aerospace, personal and vehicular navigation, location based services, surveying, precise timing systems and many others. With the practical knowledge stemming from the GPS experience, new GNSS modulations have incorporated several changes to the signal structure to improve signal characteristics such as correlation properties, multipath mitigation and interference rejection, to name a few.

The European GNSS, Galileo, is expected to provide highly accurate and reliable global positioning services for civilian applications. It will be interoperable with GPS and GLONASS to provide better performance for civilian users. Galileo satellites will transmit signals on four frequencies namely the E1, E5a, E5b and E6 bands (Galileo 2008). It will provide Open Service signals on both E1 and E5 making them available anytime for the GNSS user community. Currently, there are two operational test satellites GIOVE-A, launched on 28 December 2005 and GIOVE-B, launched on 27 April 2008, available for the users to analyze the performance of the newly proposed modulations. In this thesis, different equalization techniques will be applied to these new signals to improve tracking performance. In particular, BOC modulated GNSS signals are considered.

### 1.1.1 New GNSS Signals

Current GPS satellite signals use BPSK to modulate the navigation bits, along with the spreading code and the carrier. Galileo signals use a new kind of modulation

scheme, the BOC modulation (Betz 1999). It consists of an additional component named sub-carrier that shapes the ACF and the spectrum of the transmitted signal.

In the case of BOC signals, the slope of the ACF is steeper as compared to the BPSK one providing an increased resilience against multipath and improved code tracking performance. In addition, the presence of a sub-carrier produces a symmetric spectrum with two main lobes shifted from the carrier frequency, allowing for sufficient spectral separation from the BPSK spectrum. This allows one to process BPSK and BOC signals simultaneously with minimal inter-system interference.

However, the BOC ACF has multiple peaks comprising a primary peak and several secondary peaks. This may lead to false acquisition and secondary peak lock during tracking resulting in ambiguous/biased measurements. The use of these biased measurements may lead to unacceptable errors in the position domain and hence false locks need to be detected and corrected to provide good measurements.

The secondary peak ambiguity problem has led to the design of various BOC tracking algorithms such as Bump-Jump (BJ) (Fine & Wilson 1999), Pre-filtering methods (Yang et al. 2006), Autocorrelation Side-Peak Cancellation Technique (ASPeCT) (Julien et al. 2007) and Double Estimator (DE) (Hodgart et al. 2008) that solve the problem of incorrectly locking onto secondary peaks, ensuring the lock on the main peak. In (Fine & Wilson 1999), a technique called Bump-Jump was proposed. It is based on the detection and rejection of secondary peak locks in the signal correlation function. It is assumed that the receiver has locked to one of the correlation peaks. The algorithm determines if the correct peak is tracked. In (Julien et al. 2007), the authors suggested a technique to modify the ambiguous ACF of a specific type of BOC signal to a nearly unambiguous

ACF. This was achieved by developing an enhanced dot-product discriminator that provides unambiguous measurements. Mapping of BOC ambiguous correlation over an unambiguous bi-dimensional function was proposed in (Hodgart et al. 2008). The sub-carrier and the PRN code are tracked independently and an additional tracking loop for the sub-carrier is required. A two dimensional search is performed with respect to the sub-carrier and code delays and the final delay estimate is obtained using the combination of the two delays. This method always ensures a false lock free tracking. Several other techniques have been provided in the literature (Fante 2003, Ward 2003, Yao 2008, Dovis et al. 2005) which are limited in terms of tracking a particular type of BOC signal. In this thesis, a different approach is considered for tracking BOC signals unambiguously, namely temporal and spatial processing. An introduction to these kinds of techniques is provided in the following sections.

### ***1.1.2 Time Domain Processing***

In communication theory, the effect of the communication channel is usually compensated for by the adoption of equalization techniques (Qureshi 1985). These techniques filter the input signal to obtain an output with the desired characteristics. All pre-filtering techniques are based on the fact that the spectrum of a signal can be modified by filtering. In case of BOC signals, the effect of sub-carrier can be interpreted as a selective communication channel that distorts the useful signal. Thus, the input BOC signal can be filtered in order to reproduce a BPSK-like spectrum with unambiguous autocorrelation to mitigate the impact of the sub-carrier.

Filtering can also be applied to improve the performance of code tracking loops for reducing the multipath effects. The base width of the correlation triangle can be controlled by this type of filtering. This results in narrower correlation functions that can be used to mitigate multipath effects.

### ***1.1.3 Space Domain Processing***

GNSS signals are highly attenuated in environments such as urban canyons, indoors and under foliage. In addition to this, the presence of several multipath rays makes challenging the processing of such weak signals. This is also true in the case of new GNSS signals. In such environments, a single element antenna with a fixed radiation pattern becomes unsuitable for the processing of weak signals. Beamforming (Van Veen & Buckley 1988) is an effective and versatile means of spatial filtering that exploits several antennas to enhance the signal quality and lower the impact of multipath. Beamforming is a process where input data from several antennas are combined to produce a single equivalent beam steered towards the angle of arrival of the signal. Signals from multiple antennas can be combined to steer electronically the beam pattern, which is fixed for most of the GNSS antennas. It is always desired to produce amplification in certain directions of arrival where the line of sight signal is available and attenuate signals from other angles. This process produces attenuated multipath (Pany & Eissfeller 2008) and interference signals. The beam pattern of an antenna array can be steered electronically to maintain maximum amplitude response at the desired angle of arrival by combining signals from multiple antennas.

Several attempts have been made to analyze the performance of multi-antenna systems (Kalyanaraman & Braasch 2006, Fu et al. 2003, Lin et al. 2009, Seco-Granados et al. 2005) for the mitigation of multipath and interference on GNSS signals. Phase compensation methods applied to adaptive array processing based on the minimum variance approach using GPS signals were proposed by (Kalyanaraman & Braasch 2006). Different beamforming techniques to suppress multipath and jamming signals applicable to GNSS/Galileo were explained in (Fu et al. 2003). Synthetic array based beamforming algorithms were investigated by (Lin et al. 2009) using GNSS signals. In (Seco-Granados et al. 2005), a maximum likelihood (ML) estimation method for code and carrier phase along with a hybrid beamformer was proposed. These research works showed the effectiveness of spatial processing in enhancing the quality of GNSS signals.

For their potential and their ability of determining the direction of arrival of a RF signal (Broumandan et al. 2007), array processing and beamforming algorithms are considered in this research work with particular emphasis on practical aspects such as array calibration and with the intent of providing a signal with minimal multipath components and increased strength. Array calibration refers to the process of compensating for antenna's imperfections and adjusting the antenna array parameters before beamforming. Calibration (Ng & See 1996, Gupta et al. 2003, Backen et al. 2008) compensates for the combined effect of the unknown antenna phase and gain factors and mutual coupling which would degrade the performance of array processing algorithms if not addressed.

#### ***1.1.4 Space-Time Processing***

Space-Time processing techniques (Kohno 1998) combine the benefits of spatial and temporal processing to enhance the performance of the system. As mentioned earlier, temporal processing can be used to mitigate the effects of the communication channel that causes signal distortion through equalization. In spatial processing, spatial filtering can be used to mitigate the effect of multipath and interference components along with maximization of useful signal strength. Hence in this research work, these two techniques are combined and space-time algorithms capable of providing a signal devoid of sub-carrier/channel distortions, multipath and interference along with an enhanced Signal to Noise Ratio (SNR) are developed.

Space-time processing algorithms have been widely used in mobile communications especially in base stations and have proven to be beneficial in terms of signal quality enhancements and improvements in multipath fading environments (Kohno 1997). These kinds of techniques have been adopted for GNSS signal processing in (O'Brien & Gupta 2008). Here, a Space-Time Adaptive Processing (STAP) filtering algorithm was derived to maximize the SNR while simultaneously calibrating the system to nullify the effects of antenna induced biases. In the context of new GNSS signals, efforts to utilize multi-antenna array for BOC signal processing has been documented (Cuntz et al. 2008, Prades & Rubio 2004, Iubatti et al. 2006). A prototype GNSS array processing system was developed in (Cuntz et al. 2008) for processing Galileo signals to enhance signal reception and mitigate interference. Initial results for beamforming and signal reception improvements were shown using GPS signals. An antenna array method using the ML approach was proposed in (Prades & Rubio 2004) to synchronize the antenna arrays used

for BOC signal processing. Simulation results showed good improvements in terms of multipath mitigation using the ML approach. A joint space-time-frequency technique based on a subspace projection approach to mitigate interference affecting the Galileo system was proposed in (Iubatti et al. 2006). The received signal was projected onto the subspace orthogonal to the interference subspace and hence estimation of interference parameters needed to be accurate. Numerical simulations validated the robustness of the proposed approach for possible errors in estimating the interference frequency and angle of arrival.

These space-time techniques make use of the combination of spatial and temporal processing to produce better signal quality as compared to a single antenna and a temporal processor. The limited research effort involved in space-time processing of new GNSS signals provides the opportunity to further explore the benefits of space-time processing for BOC modulated signal tracking.

## **1.2 Limitations and motivations**

Tracking of new GNSS signals can be biased by the presence of multiple correlation peaks and different algorithms have been developed in the past to mitigate the effect of secondary peaks that can lead to these ambiguities. However these tracking algorithms have been limited to certain types of new GNSS signals. Hence, the need to develop algorithms applicable to a wide variety of BOC modulated signals.

Although several methods for mitigating the problem of secondary peak lock have been introduced (Fante 2003, Fine & Wilson 1999, Yang et al. 2006, Julien et al. 2007, Hodgart et al. 2008), each technique has its own advantages and disadvantages. The

method proposed in (Fine & Wilson 1999) is suitable for signals with high/medium C/N<sub>0</sub> and tends to provide poor performance for low C/N<sub>0</sub>. While the technique proposed in (Hodgart et al. 2008) always ensures primary peak tracking, it is restricted in terms of multipath mitigation. Pre-filtering techniques such as the ones proposed in (Yang et al. 2006) can lead to noise amplification. More specifically, in order to equalize the BOC spectrum it is required to compensate for its zeros which lead to singularities in the filter transfer function. These singularities are the main cause for noise amplification. The pre-filtering techniques proposed in this thesis can be considered an extension of algorithms proposed in the communication context such as the Mis-Match Filter (MMF) (Nuthalapati 2008) and the clean algorithm (Hogbom 1974). The MMF operates on the temporal input data whereas the clean algorithm works in the frequency domain to obtain a desired sequence or spectrum. In these techniques, a different signal structure was considered and the spectrum of the received signal was shaped for inter symbol interference (ISI) cancellation. The problem of secondary autocorrelation peaks was not considered. The noise amplification problem of previous pre-filtering techniques and the limitations of MMF and clean algorithms motivate additional studies and analysis for the development of new pre-filtering techniques. These techniques are considered in Chapter 3 of this thesis.

Although the use of multiple antennas (Balanis & Ioannides 2007) has proven to provide improvements in communication receivers, research work relative to the usage of spatial processing for new GNSS signal tracking is still ongoing. The beamforming techniques for GNSS signals mentioned in Section 1.1.3 were developed either under the assumption of an ideal array, i.e., phase and gain mismatches between different antennas were

neglected along with mutual coupling or the effects due to these mismatches were compensated using reference antennas or additional calibration signals. In order to take complete advantage of the antenna array system, calibration techniques are thus required for compensating the aforementioned phenomena. Previous calibration algorithms require a perfect knowledge of the array manifold or a reference antenna with known gain and phase patterns which are not available in practice. For this reason, the development of a calibration algorithm not requiring any additional reference signal is worth of investigation. This topic is developed in Chapter 4 where a self-contained calibration technique is developed. The application of this technique to GNSS signals along with space processing techniques are also analyzed.

Combined space-time processing has been extensively used in communication systems (Huang & Leib 2000, Khalaj et al. 1995) exploiting the benefits of both spatial and temporal filtering. Combined temporal and spatial processing for GNSS signals has been only marginally analyzed. This is an interesting research opportunity for the combined processing of new GNSS signals. This topic will be developed in Chapter 5.

### **1.3 Objectives**

The main objectives of this thesis are divided into three categories, namely temporal processing, spatial processing and spatio-temporal processing. With respect to temporal processing, the main objective is the development of new pre-filtering techniques able to provide unambiguous tracking reducing the noise amplification problem affecting existing pre-filtering algorithms. In addition to this, the thesis aims at completing the analysis of existing BOC tracking techniques. Additional aspects, not

considered in the previous literature, are analyzed and BJ and DE are characterized through simulations and real data analysis. Semi-analytic techniques (Golshan 2006, Borio et al. 2010) are developed for the characterization of the mentioned techniques. With respect to spatial processing, the development of a self-contained calibration technique is considered of primary importance since it is essential for the proper functioning of any spatial processing. The limitation of previous calibration techniques are analyzed and overcame by exploiting the properties of GNSS signals. Showing the feasibility of GNSS spatial processing using live GPS signal is also one of the main objectives of this thesis.

Finally, the development of joint space-time algorithms for BOC signals is considered of particular importance for fully exploiting the potential of array processing. The objective is to combine the advantages of the techniques developed in the first two parts of the thesis. A new scheme integrating spatial and temporal approaches for the processing of BOC signals is considered.

The following subsections details the different tasks that are carried out to fulfill the objectives highlighted above.

### ***1.3.1 Temporal Processing***

- Zero Forcing (ZF) and Minimum Mean Square Error (MMSE) equalizers are developed and tested for sub-carrier equalization and multipath mitigation. These equalizers shape the BOC ACF to provide an unambiguous ACF and hence are termed as ZF shaping (ZFS) and MMSE shaping (MMSES) (Anantharamu et al. 2011). The proposed MMSES is designed based on the estimated  $C/N_0$  that is

used to obtain the filter parameters as described in Section 3.3. Multipath mitigation is also achieved by varying the width of the correlation function of the filtered signal

- The weak link in any tracking loop is known to be the carrier phase/frequency lock loop. Filtering of local/incoming signals directly affects the performance of the carrier lock loop. Hence it becomes necessary to mitigate the effect of filtering on the carrier loop performance. Thus, a modified tracking loop structure is considered where an unfiltered correlator output is used. The code generation of this unfiltered correlator is driven by the delay estimated by the pre-filtering technique. This technique also ensures the estimation of unbiased  $C/N_0$  values
- The proposed equalizers are derived at first in the frequency domain resulting in a high computational load. Time-domain implementation enabling the usage of temporal filtering techniques in real time applications is later attempted
- The proposed algorithms are thoroughly analyzed and compared against existing BOC tracking techniques using a semi-analytic technique approach (Borio et al. 2010, Borio et al. 2011). This approach is considered to analyze the tracking loop performance in terms of tracking jitter, tracking threshold, Mean Time to Lose Lock (MTLL), convergence analysis and Multipath Error Envelope (MEE). The proposed techniques are compared against the BJ and DE (Hodgart et al. 2008). The DE technique has been used for comparison purposes due to its close approximation to a matched filter receiver.

### ***1.3.2 Spatial Processing***

- A self-contained calibration algorithm is developed. The proposed technique uses the fact that GNSS signals broadcast the position of their source. In this way, a new calibration algorithm, not requiring any additional reference signal, is developed in Chapter 4.
- Beamforming is performed before and after calibration to show the effectiveness of the developed calibration algorithm (Anantharamu et al. 2011)
- The calibration technique is tested under various antenna structures including linear and planar arrays.

### ***1.3.3 Space-Time Processing***

- The advantage of spatial and temporal combining is studied and a space-time combining technique is designed to achieve better performance under attenuated signal conditions in Chapter 5.
- A combined space-time processing technique based on MMSES in time domain and a spatial beamformer based on the minimum variance criteria is proposed. The proposed technique is tested for interference mitigation and tracking performance improvement using simulations. Real BOC data from a dual antenna array system has been used to show the effectiveness of the proposed space-time technique in attenuated signal conditions.

#### ***1.3.4 Test Setup and Data Analysis***

The techniques described above are tested using the methodologies described in the following.

- Semi-analytic techniques/Monte-Carlo simulations are used to analyze the proposed tracking method performance in terms of tracking jitter, tracking threshold, MTLL, tracking error convergence and MEE.
- An Intermediate Frequency (IF) simulator capable of generating BOC signals is developed to simulate multi-antenna systems (different numbers of antennas and different antenna array structures such as linear, circular and rectangular) and analyze the performance of the calibration technique, spatial filtering effects and improvements in tracking due to space-time processing
- A Spirent GSS 7700 GPS hardware simulator capable of simultaneously providing dual antenna array data is used to validate the antenna array calibration techniques in the absence of mutual coupling
- Real data from GIOVE A/B satellites are
  1. progressively attenuated using digital attenuators, to simulate a weak signal environment
  2. collected from three antennas using a National Instruments (NI) vector analyzer equipped with three PXI-5661 front-ends (NI 2006)
  3. collected from four antennas using a 4-channel front end designed in the PLAN Group (Morrison 2010).

#### **1.4 Dissertation outline**

This dissertation is organized into three different parts, each explicitly describing temporal, spatial and spatio-temporal BOC processing techniques. A brief discussion of the BOC signal structure and standard BOC tracking techniques is provided in Chapter 2 along with the signal and system model considered in this research work.

1. Temporal Processing: Chapter 3 consists of a detailed description of the proposed temporal equalizers for BOC signal tracking. Performance analysis is performed with respect to existing BOC tracking techniques using both simulated and real data
2. Spatial Processing: Chapter 4 discusses spatial processing of multi-antenna arrays including the proposed calibration technique and beamforming. Detailed analysis along with simulation and real data results are presented
3. Space-Time Processing: Chapter 5 provides an introduction to space-time processing and its underlying concepts. A detailed discussion on the proposed space-time processing techniques developed for tracking BOC signals is presented. A comprehensive analysis of the proposed space-time processing technique that includes simulations and real data results is also provided.

Finally, Chapter 6 summarizes the contributions and conclusions of the thesis and provides recommendations for future work. A flowchart depicting the chapters and their inter-dependence is shown in Figure 1-1.

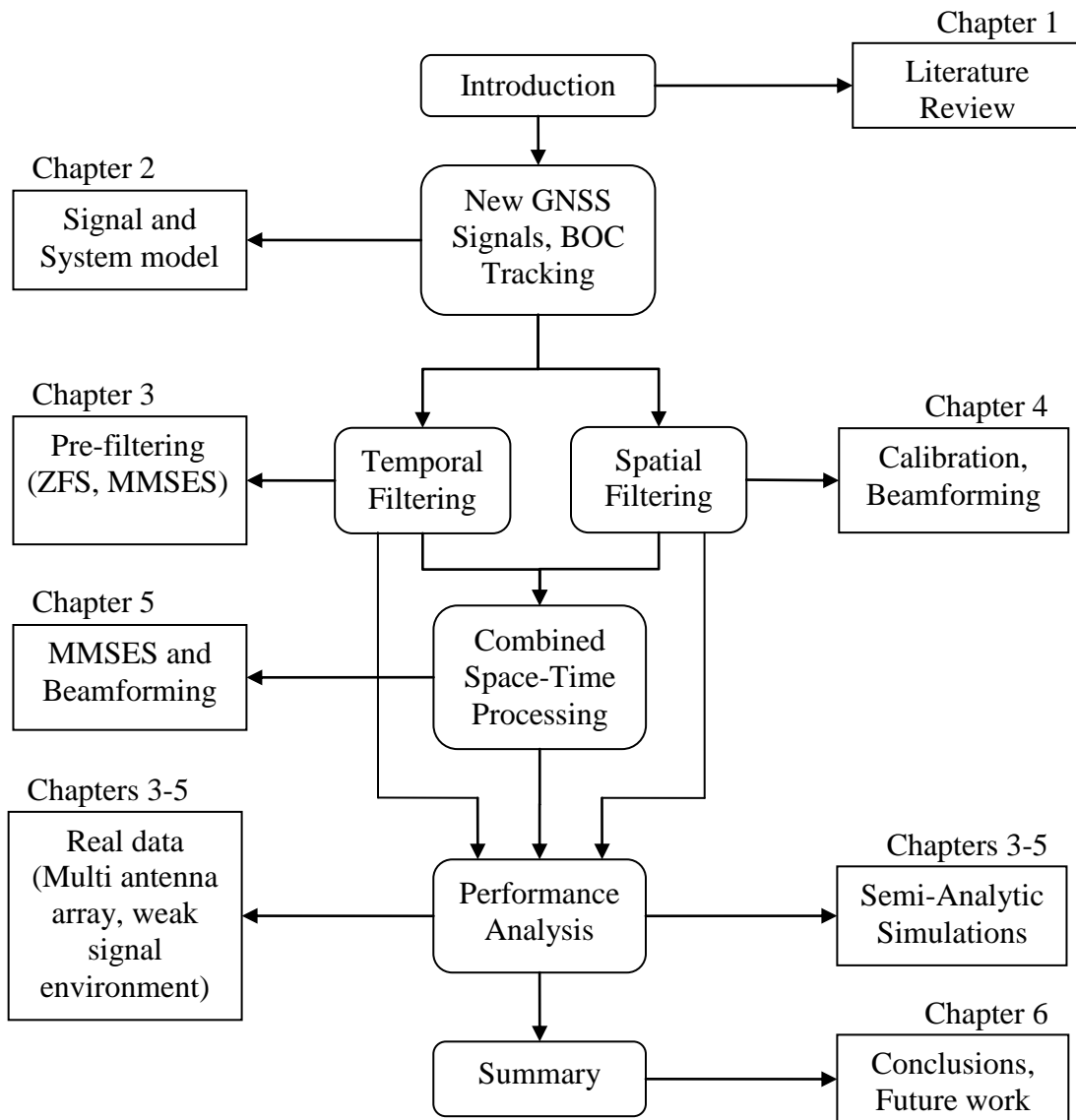


**Figure 1-1 Structure of thesis**

## Chapter Two: **BOC Signal Structure and Tracking**

The Binary Offset Carrier (BOC) is a modulation technique that employs the periodic repetition of a square wave for changing the spectral properties of a GNSS signal. More specifically, each chip of a GNSS PRN sequence is multiplied by a square wave whose repetition rate differs from the code rate. Here, chip refers to the basic interval over which a PRN sequence assumes a constant value in the set  $\{\pm 1\}$ . The periodic repetition of the square wave is usually denoted as sub-carrier and it is one of the main features distinguishing BOC from legacy BPSK signals. BOC square waves can be obtained as the sign of a sinusoidal carrier and have been extensively used in the European Galileo signal design as explained in Section 2.3. In this chapter, the signal and system model considered in this research work along with standard GNSS signal tracking are briefly described. This is followed by a description of BOC signal tracking and about the metrics used for performance analysis.

### 2.1 Signal and System model

The complex baseband sequence at the input of a GNSS tracking loop can be modeled as the sum of a useful signal and a noise term,

$$\begin{aligned} y(t) &= x(t) + \eta(t) \\ &= Ad(t - \tau_0)c(t - \tau_0)\exp\{j\theta_0(t)\} + \eta(t) \end{aligned} \tag{2.1}$$

where

- $A$  is the received signal amplitude;
- $d(\cdot)$  is the navigation message;

- $c(\cdot)$  is the ranging sequence used for spreading the transmitted data;  $c(\cdot)$  is usually made of several components;
- $\tau_0$  models the delay introduced by the communication channel whereas  $\theta_0(t) = 2\pi f_D t + \phi_0(t)$  is a time-varying phase that accounts for the residual frequency,  $f_D$ , and phase,  $\phi_0(t)$ , not recovered by the receiver front-end. Here  $\theta_0(t)$  models the phase variations due to the relative dynamics between receiver and satellite;
- $\eta(t)$  is a Gaussian random process whose spectral characteristics depend on the filtering and down-conversion strategies applied at the front-end level.

In (2.1), the presence of a single useful signal is assumed. Although several signals from different satellites enter the antenna, a GNSS receiver is able to independently process each received signal, thus justifying model (2.1). The ranging code,  $c(t)$ , is made of several components including a primary spreading sequence, a secondary or overlay code and a sub-carrier. In the following, the combination of primary sequence and overlay code will be denoted by  $p(t)$  and referred to as pseudo random sequence (PRS). The ranging code can be expressed as

$$c(t) = \sum_{i=-\infty}^{\infty} p(iT_c) s_b(t - iT_c) \quad (2.2)$$

where  $s_b(\cdot)$  is the sub-carrier of duration  $T_c$ . Eq. (2.2) can be interpreted in different ways leading to the different signal representations discussed in Section 2.4. In the case

of legacy BPSK signals,  $s_b(\cdot)$  is a rectangular pulse with width  $T_c$ . The sub-carrier for BOC signals takes different forms depending on the square wave used for its generation.

## 2.2 GNSS Signal Tracking

Received GNSS signals are buried in noise and hence several procedures need to be followed to extract the signal parameters such as code delay ( $\tau_0$ ), carrier phase ( $\phi_0$ ) and frequency ( $f_D$ ). Acquisition (Tsui 2004) is the first and most demanding step performed by a GNSS receiver to detect the presence of a useful signal and coarsely estimate  $\tau_0$  and  $f_D$ . Tracking (Kaplan & Hegarty 2006) refers to the process of precisely estimating the signal parameters over time and keeping track of the signal variations. A high level structure of a standard GNSS tracking loop is shown in Figure 2-1. The input to the tracking structure is the Intermediate Frequency (IF) signal obtained from the receiver front-end (Kaplan & Hegarty 2006).

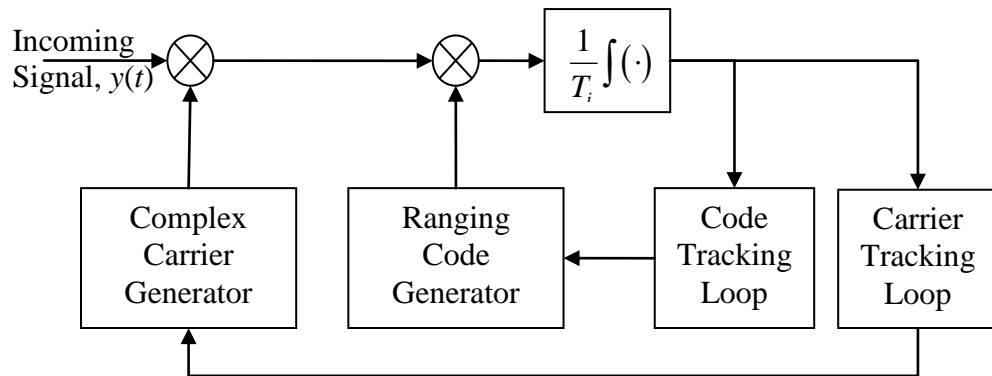


**Figure 2-1 Standard GNSS tracking loop structure**

At first, the IF signal is down-converted to base-band using a complex carrier generator. The spreading code is then wiped off using a local code generator. The signal obtained after carrier and code removal is integrated over  $T_i$  seconds and a single correlator output

is produced. Several correlators for different delays of the local code can also be computed to obtain the error signal used to drive the code and carrier loops to continuously track the incoming signal variations (Kaplan & Hegarty 2006). The complex carrier generator is driven by the carrier phase estimate from the carrier tracking loop whereas the ranging code generator is driven by the code delay estimate from the code tracking loop. A detailed block diagram of the standard tracking structure (Kaplan & Hegarty 2006) consisting of two tracking loops operated synchronously to track the incoming signal code delay and carrier phase is shown in Figure 2-2. Tracking loops are identified by the quantity being tracked; the loop tracking code delay is called Delay Lock Loop (DLL), the loop tracking residual carrier phase is called Phase Lock Loop (PLL) and the loop tracking Doppler frequency is called Frequency Lock Loop (FLL). Both DLL and FLL/PLL operate jointly for the proper functioning of GNSS signal tracking. The following sub-sections briefly describe the operations of DLL and PLL/FLL for tracking GNSS signals.

### ***2.2.1 Phase/Frequency Lock Loop***

Standard carrier tracking involves either FLL or PLL or FLL assisted PLL. FLL/PLL tries to minimize the residual frequency/phase of the signal being tracked. The operations sequentially performed by the FLL/PLL are as follows:

- the carrier Numerically Controlled Oscillator (NCO) generates two versions of the local carrier with a  $90^\circ$  phase shift to produce the in phase (I) and quadrature (Q) components shown in Figure 2-2;

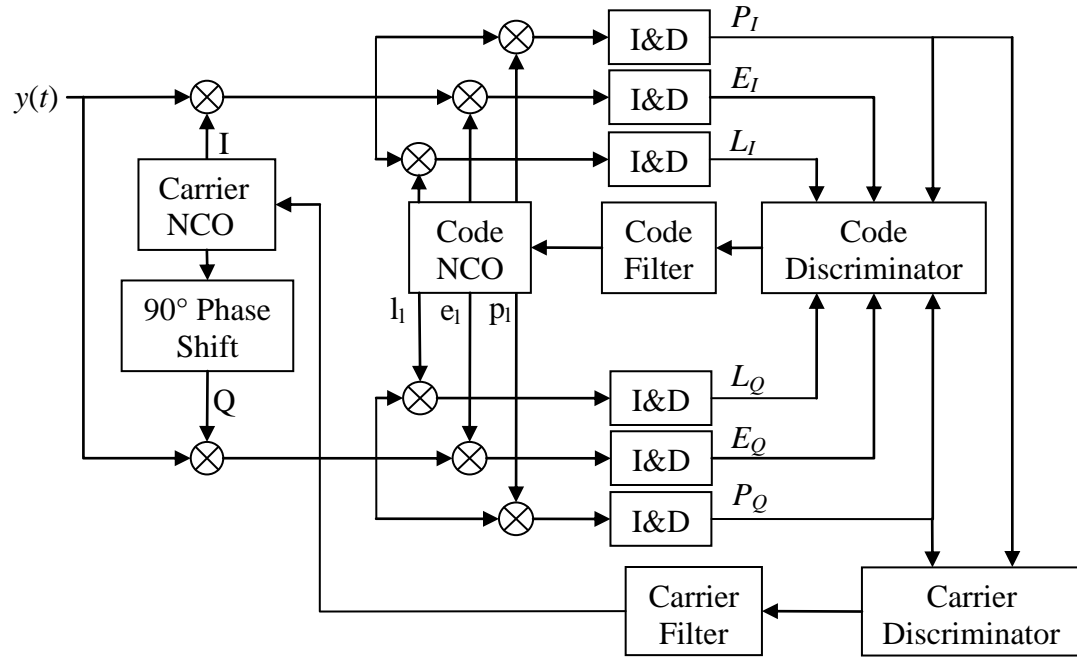


**Figure 2-2 Block diagram of code and carrier tracking loops**

- the incoming signal is multiplied by the Prompt code ( $p_l$ , local version of incoming code) to wipe off the code and is correlated with the I and Q components of the local carrier and integrated over the desired integration time to reduce the effect of noise and improve signal quality. Since a single correlator output is produced, each  $T_i$  seconds, the integrator is often referred to as Integrate & Dump (I&D). The output from the I&D block is the complex correlator value termed as Prompt correlator,  $P = P_I + jP_Q$ ;
- the I&D output is fed to a carrier discriminator that estimates the carrier frequency/phase error using the Prompt correlator output. Different discriminators (Kaplan & Hegarty 2006) are available that provide a mapping from the correlator output to a frequency/phase error;

- the frequency/phase error is passed as input to the loop filter to provide better quality estimates of frequency/phase rate and then fed to the carrier NCO for the generation of local carrier. In the case of a FLL, the NCO includes an additional block to integrate the frequency rate estimates from the filter to provide the phase rate values.

### **2.2.2 Delay Lock Loop**

In the DLL, operations similar to FLL/PLL are performed with fundamental differences in the discriminator. The steps followed in a DLL are as follows:

- The code NCO generates three versions of the local code,
  - early ( $e_l$ ) code is advanced with respect to the current time instant by an amount equal to  $d_s/2$  chips where  $d_s$  is the early-minus-late chip spacing,
  - prompt ( $p_l$ ) code is generated with respect to current time instant and
  - late ( $l_l$ ) code is delayed with respect to current time instant by an amount equal to  $d_s/2$  chips as shown in Figure 2-2,
- the incoming signal is multiplied by the I and Q versions of the local carrier to wipe off the incoming carrier and is correlated with  $e_l$ ,  $p_l$ ,  $l_l$  and integrated over the desired integration time to reduce the effect of noise and improve signal quality. The outputs from I&D are the complex correlator values termed as Early,  $E = E_I + jE_Q$ , Prompt,  $P = P_I + jP_Q$ , and Late,  $L = L_I + jL_Q$ . For advanced tracking techniques (Fine & Wilson 1999, McGraw & Braasch 1999), the number of correlator outputs required can be more than three,

- the I&D outputs are fed to a code discriminator that estimates the code delay error using the E, P and L correlator outputs. Different discriminators (Kaplan & Hegarty 2006) are available that provide a mapping from the correlator output to the code delay error. The discriminators are analyzed in detail in Appendix A,
- The code delay error is passed through a filter to provide better quality estimates of the code rate that are fed to the code NCO for the generation of local codes.

### 2.2.3 Correlation Process

The local signal replica obtained by generating a complex carrier that is used for recovering the effect of the signal phase,  $\theta_0(t)$ , and a local ranging code  $c_l(t) = c(t)$  used for recovering the effect of the code delay,  $\tau$ , is correlated with the incoming signal,  $y(t)$ . The correlator output at the  $k^{th}$  processing epoch,  $q_k$ , for a given code delay,  $\tau$ , and carrier phase,  $\theta$ , can be expressed as

$$\begin{aligned} q_k(\tau, \theta) &= \int_{(k-1)T_i}^{kT_i} y(t)c_l(t-\tau)\exp\{-j\theta(t)\}dt \\ &= A \int_{(k-1)T_i}^{kT_i} d(t-\tau_0)c(t-\tau_0)\exp\{j\theta_0(t)\}c_l(t-\tau)\exp\{-j\theta(t)\}dt + \tilde{\eta} \quad (2.3) \\ &= A \int_{(k-1)T_i}^{kT_i} d(t-\tau_0)c(t-\tau_0)\exp\{j\Delta\theta(t)\}c_l(t-\tau)dt + \tilde{\eta} \end{aligned}$$

where  $\Delta\theta(t) = \theta_0(t) - \theta(t)$ .  $T_i$  is the coherent integration time and  $\tilde{\eta}$  is a noise term obtained by processing the input noise,  $\eta(t)$ . In this work, it is assumed that the receiver is able to perfectly recover the signal phase and  $\Delta\theta(t) = 0$ . Assuming the navigation message,  $d(t)$ , constant during the integration period, Eq. (2.3) simplifies to

$$\begin{aligned}
q_k(\tau) &= A \int_{(k-1)T_i}^{kT_i} c(t - \tau_0) c_l(t - \tau) dt + \tilde{\eta} \\
&= AR(\tau_0 - \tau) + \tilde{\eta} \\
&= AR(\Delta\tau) + \tilde{\eta}
\end{aligned} \tag{2.4}$$

$R(\Delta\tau)$  is the correlation function between the incoming and locally generated signal.

The shape of  $R(\Delta\tau)$  is essentially determined by the sub-carrier. For a BPSK signal,  $R(\Delta\tau)$  is characterized by a single peaked triangular function. But when a BOC is used,  $R(\Delta\tau)$  is characterized by several secondary peaks that can lead to false code locks. In this research work, filtering techniques are developed to modify  $R(\Delta\tau)$  of BOC modulated signals to result in unambiguous tracking. A detailed description of BOC signals and characteristics of sub-carrier are presented in the following sections.

## 2.3 BOC Signals

### 2.3.1 Signal Structure

A BOC signal is obtained by synchronously multiplying the PRS used for spreading the spectrum of a GNSS signal with a sub-carrier (Betz 1999). The phase of the sub-carrier is determined by the phase of the generating sinusoidal carrier that can be either a sine or a cosine. Thus, depending on the sinusoidal carrier, BOC signals are classified as BOCs (sinBOC) and BOCC (cosBOC) signals (Pratt & Owen 2003, Hein et al. 2004). BOC modulations are described by two parameters as BOC( $m, n$ ) where  $m$  defines the sub-carrier frequency,  $f_s = mf_0$ , and  $n$  defines the PRS frequency,  $f_c = nf_0$  (the inverse of  $f_c$  defines the duration of a single chip of the spreading sequence).  $f_0$  is a

reference frequency equal to 1.023 MHz (GIOVEICD 2008). The generation of a square wave sub-carrier,  $s_b(t)$ , can be expressed as

$$s_b(t) = \begin{cases} \text{sign}(\sin(2\pi f_s t)), & \text{BOCs} \\ \text{sign}(\cos(2\pi f_s t)), & \text{BOCc} \end{cases} \quad (2.5)$$

In Figure 2-3, the BOCs and BOCc signal structures are better illustrated. In this case, a BOC (1, 1) signal is considered where  $f_s = f_c$ .

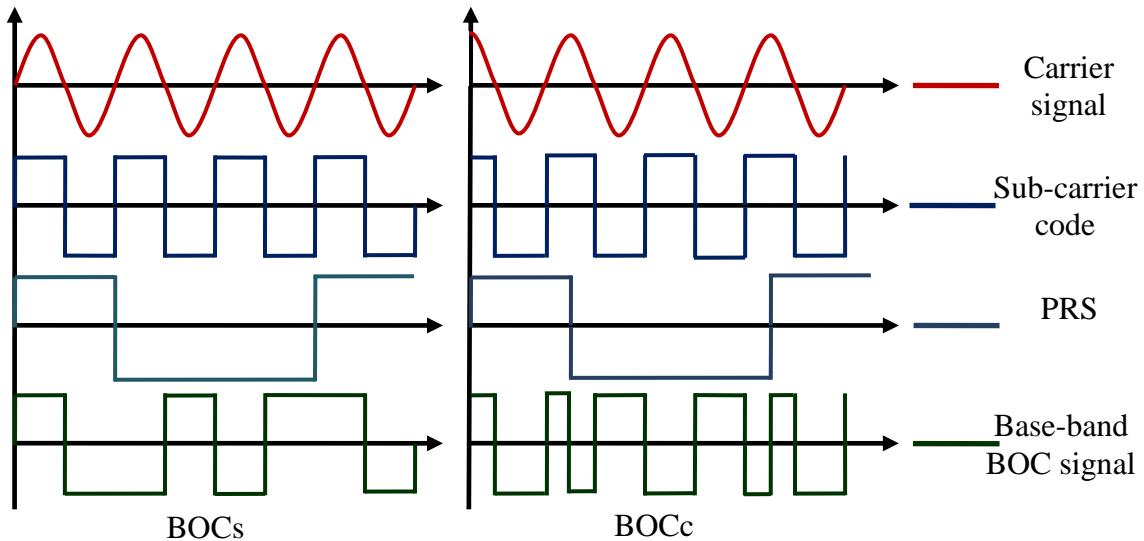


**Figure 2-3 BOC Signal structure and its components**

### 2.3.2 Signal Characteristics

The presence of a sub-carrier provides BOC signals unique characteristics such as a multi-peaked Auto-Correlation Function (ACF) and splits their power on symmetric lobes placed away from the signal centre frequency (Betz 1999). The ACF and Power Spectral Density (PSD) of BPSK and BOCs(1,1) signals are shown in Figure 2-4. In the case of BOC signals, the slope of the ACF is steeper as compared to the BPSK ACF, providing an increased resilience against multipath and improved code tracking

performance. However, the ACF of BOC signals has multiple peaks comprising of one primary peak and several secondary peaks that may lead to ambiguous tracking. The number of secondary peaks,  $N_{sp}$ , in a BOC modulated signal can be obtained as

$$N_{sp} = \begin{cases} 4(m/n) - 2, & \text{BOCs} \\ 4(m/n), & \text{BOCc} \end{cases} \quad (2.6)$$

In addition, the presence of a sub-carrier on the BOC signal produces a symmetric spectrum with two main lobes shifted from the carrier frequency as seen in Figure 2-4, allowing for sufficient spectral separation from the BPSK spectrum (Hein et al. 2004). This allows one to process BPSK and BOC signals simultaneously with minimal inter-system interference.

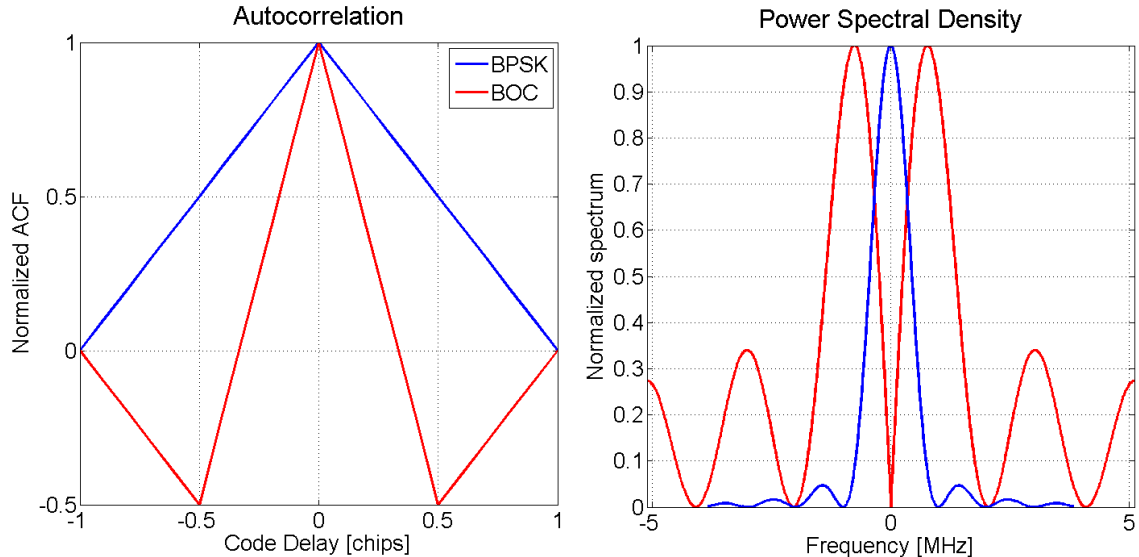


**Figure 2-4 BPSK and BOC Signals autocorrelation function and power spectrum**

### 2.3.3 Galileo Signals

The European GNSS, Galileo, is expected to provide highly accurate and reliable global positioning services for civilian applications. It will be interoperable with GPS and

GLONASS to provide better performance for civilian users. Galileo signals should provide improved performance compared to the existing GPS signals due to the introduction of the BOC modulation. One of the main reasons for adopting BOC modulation is its minimal interference with the GPS signals due to its symmetric split-spectrum and the presence of a narrow ACF primary peak as described in Section 2.3.2. Since in this research work Galileo signals are extensively used for various analyses, a brief introduction to the Galileo signals and their structures is provided below.

### ***Frequency Allocation***

Galileo satellites are designed to provide users with Open Service (OS), Commercial Service (CS), Safety-Of-Life (SOL) along with public regulated services (Galileo 2008). To accomplish these services, Galileo satellites will transmit signals on three frequency bands namely

- E1 at 1575.42 MHz for OS, CS, SOL and public regulated services
- E5 at 1191.975 MHz subdivided as E5a at 1176.45 MHz and E5b at 1207.14 MHz for OS, CS, and SOL
- E6 at 1278.75 MHz for CS and public regulated services

The frequency allocation of Galileo signals along with the GPS signals is shown in Figure 2-5. Currently, there are two operational test satellites; GIOVE-A launched on 28 December 2005 and GIOVE-B launched on 27 April 2008, available for the users to analyze performance of the newly proposed modulations. Both GIOVE-A and GIOVE-B satellites transmit signals on two among of three available frequencies (E1, E5 and E6) in either E1-E5 or E1-E6 combinations (GIOVEICD 2008). The status of signal

transmission on GIOVE-A and GIOVE-B satellites along with the system architecture can be obtained from (GIOVE 2010).

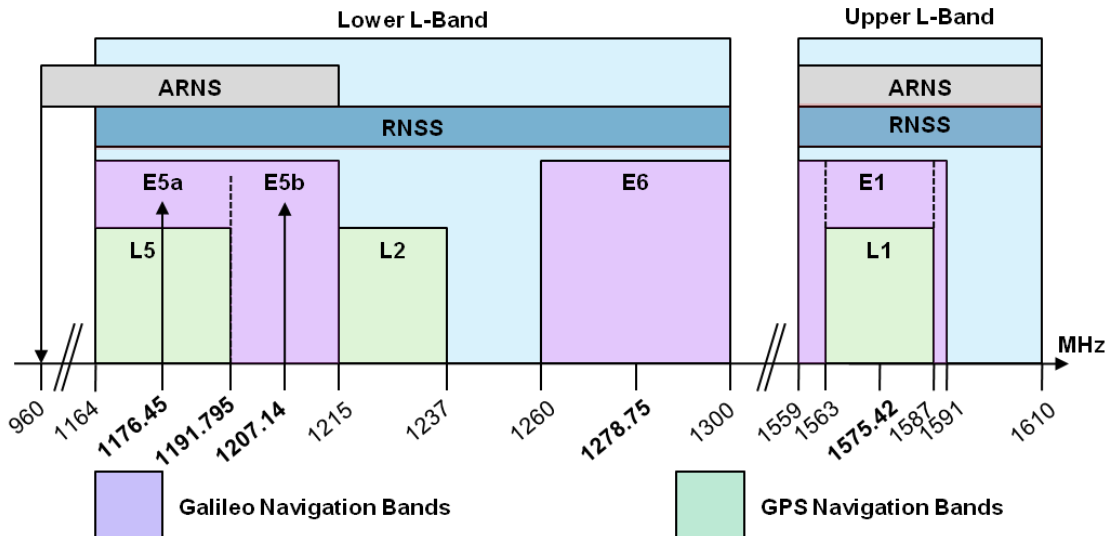


**Figure 2-5 Galileo and GPS frequency plan as provided in Galileo 2008**

### *Galileo Signal Types*

The Galileo signal types considered in this research work include E1 and E6 frequency bands as explained briefly in this section. Galileo signals in the E1 band can be divided into three channels namely A, B and C (Galileo 2008). Channel B and C are used for OS and transmits BOCs(1,1) modulated signals. Channel B is the data channel as it transmits the navigation data bits while Channel C is the pilot channel used to transmit only the PRS to aid data channel. Channel B and C signals are publicly available to be used for navigational purposes. The final proposed signal on Channel B and C is a composite BOC (CBOC(1, 6, 1, 1/10)) which is being transmitted currently by GIOVE-B satellite while GIOVE-A transmits BOCs(1,1) for testing purposes. Channel A on E1 band is used for public regulated services and transmits BOCC(15, 2.5) modulated signals.

with restricted access. Similarly, signals in the E6 band can be divided into three channels. Channel B (data) and Channel C (pilot) transmit BPSK(5) modulated signals that are not considered in this research work. Channel A transmits BOCc(10, 5) modulated signals used for public regulated services. Table 2-1 provides details about the GIOVE-A and GIOVE-B spreading code and navigation signal parameters.

The plots for ACFs and PSDs of E1-A, E1-B and E6-A signals are shown in Figure 2-6. It is clear that, for higher order BOC signals, there are more secondary peaks. The number of secondary peaks for BOCs(1, 1) is 2 while BOCc(10, 5) is 8 and BOCc(15, 2.5) is 24.

**Table 2-1 GIOVE spreading code and navigation signal parameters**

Satellite	Signal	Modulation Type	Symbol rate [Hz]	Code length [ms]	Primary code [chips]	Secondary code [chips]
GIOVE-A	E6-A	BOCc(10, 5)	100	10	51150	1
	E1-A	BOCc(15, 2.5)	100	10	25575	1
	E1-B	BOCs(1, 1)	250	4	4092	1
	E1-C			200	8184	25
GIOVE-B	E6-A	BOCc(10, 5)	100	10	10230	5
	E1-A	BOCc(15, 2.5)	100	10	5115	5
	E1-B	CBOC(1,6,1,1/10)	250	4	4092	1
	E1-C			200	8184	25

Also from the PSD plot, it is evident that the bandwidth required to acquire the entire spectrum gets larger for higher order BOC signals. To acquire the two main lobes of BOCs(1, 1) spectrum, a bandwidth of 4 MHz would be sufficient; but a bandwidth of approximately 32 MHz and 40 MHz is required for BOCc(15, 2.5) and BOCc(10, 5) signals, respectively (GIOVEICD 2008). The following sections explain the main

operations performed in a receiver to track BOC signals along with different BOC tracking techniques available for Galileo signals.

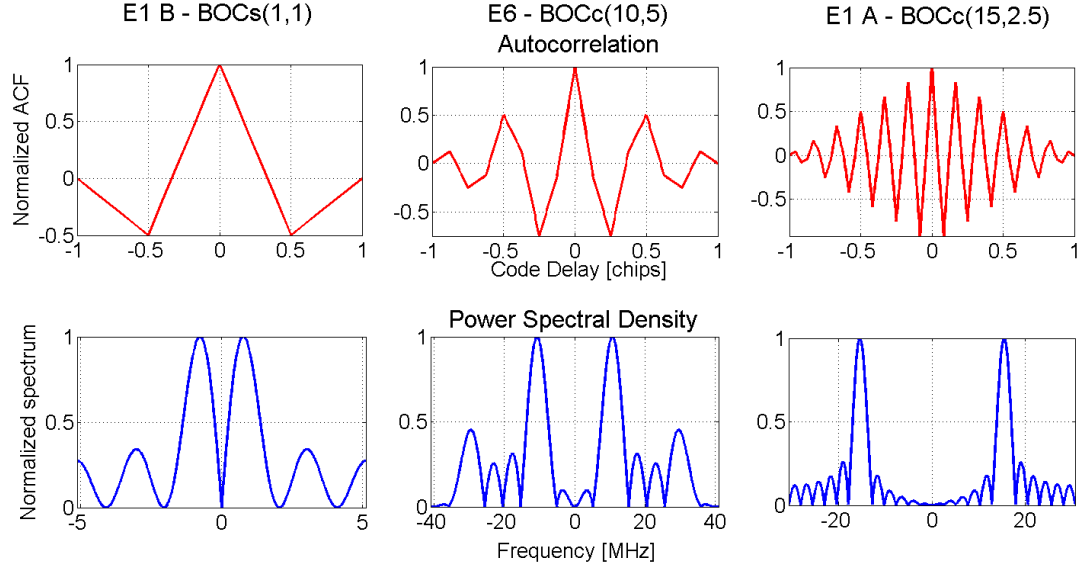


**Figure 2-6 ACFs and PSDs of Galileo E1 and E6 Signals**

## 2.4 BOC signal tracking

To analyze the performance of different BOC tracking techniques, two representations of the ranging code in Eq. (2.2) are considered in this research work. The convolutional and multiplicative representations of the ranging code explained in this section allow one to develop and analyze the performance of different BOC tracking techniques.

### 2.4.1 Convolutional Representation

Eq. (2.2) can be represented as the convolution of the PRS with a sub-carrier sequence:

$$\begin{aligned}
 c(t) &= \sum_{i=-\infty}^{\infty} p(iT_c) s_b(t-iT_c) \\
 &= \sum_{i=-\infty}^{\infty} p(iT_c) \delta(t-iT_c) * s_b(t) \\
 &= \tilde{p}(t) * s_b(t)
 \end{aligned} \tag{2.7}$$

where  $\tilde{p}(t)$  indicates the Dirac comb modulated by the PRS. From (2.7), it is noted that  $s_b(t)$  acts as a filter that shapes the spectrum and autocorrelation function of the useful signal. In Figure 2-7, the convolutional representation of the ranging code,  $c(t)$ , is better illustrated. More specifically, the final ranging code is obtained by filtering the PRS modulated Dirac comb with the sub-carrier. In Figure 2-7, the case of BOCs(1,1) is considered for illustration purpose. Thus the sub-carrier can be expressed as

$$s_b(t) = \begin{cases} 1 & 0 \leq t \leq T_c/2 \\ -1 & T_c/2 < t \leq T_c \\ 0 & \text{otherwise} \end{cases} \quad (2.8)$$

In standard BPSK tracking,  $s_b(t)$  is a rectangular window with duration equal to  $T_c$ .

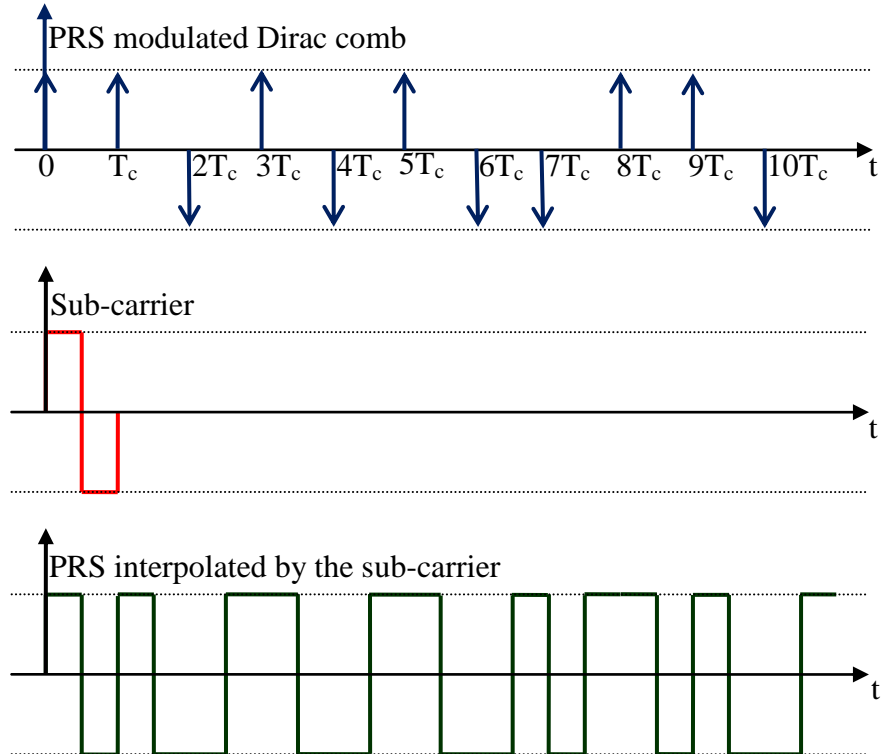


**Figure 2-7 Convolutional representation of the ranging code,  $c(t)$ . The useful signal is obtained by filtering the PRS modulated Dirac comb with a sub-carrier filter**

### 2.4.2 Multiplicative Representation

An alternative representation of the ranging code,  $c(t)$ , can be provided using the multiplicative operation given by

$$\begin{aligned} c(t) &= \sum_{i=-\infty}^{\infty} p(iT_c) s_b(t - iT_c) \\ &= \sum_{i=-\infty}^{\infty} p(iT_c) s_{BPSK}(t - iT_c) \cdot \sum_{k=-\infty}^{\infty} s_b(t - kT_c) \\ &= c_{BPSK}(t) \tilde{s}_b(t) \end{aligned} \quad (2.9)$$

where  $s_{BPSK}(t)$  is the BPSK sub-carrier and is equal to a rectangular window of duration  $T_c$ ,  $\tilde{s}_b(t)$  is the signal obtained by periodically repeating the sub-carrier  $s_b(t)$  and  $c_{BPSK}(t) = \sum_{i=-\infty}^{\infty} p(iT_c) s_{BPSK}(t - iT_c)$ . Representation (2.9) is based on the bipolar nature of all the components of the ranging code,  $c(t)$ , and is better illustrated in Figure 2-8.

Here a BPSK modulated PRS is multiplied by the periodic repetition of the sub-carrier. It is noted that the final signal obtained in Figure 2-7 is equal to the one in Figure 2-8. The multiplicative representation is provided here for better understanding of the DE technique (Hodgart et al. 2008) and the convolutional representation is the basis for the development of proposed pre-filtering algorithms.

The main objective of tracking loops is to drive the error between the incoming and local signals to zero. DLL tries to drive the code delay error to zero while the FLL/PLL tries to drive the frequency/phase error to zero. This is achieved by maintaining the tracking loops such that the estimated parameter values are as close as possible to the incoming signal parameters. Different factors like signal dynamics, user dynamics and receiver clock drift affect signal tracking. For BOC signals, another factor to be taken into account

is the signal ACF. The presence of multiple peaks in BOC ACF leads to tracking ambiguities as explained here.

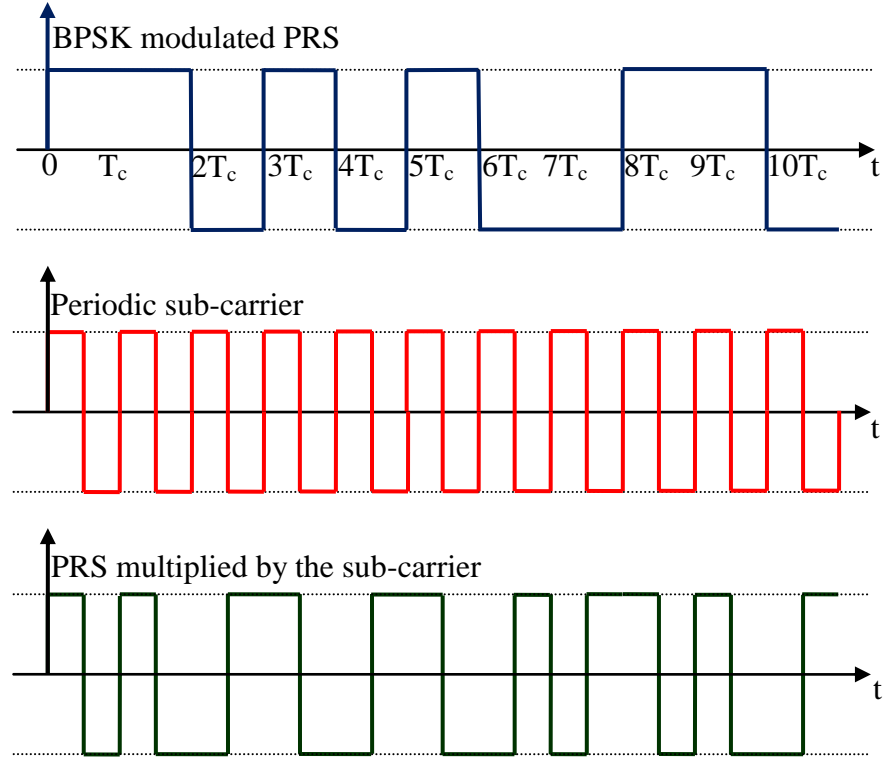


**Figure 2-8 Multiplicative representation of the ranging code,  $c(t)$ . The useful signal is obtained by multiplying the BPSK modulated PRN code by the periodic repetition of the sub-carrier**

In FLL/PLL operation, only the Prompt correlator output is required, which is unaffected by the signal type (Pany et al. 2002). The FLL/PLL structure is unaltered irrespective of the data modulation. Hence the standard FLL/PLL (Kaplan & Hegarty 2006) architecture is used for BOC signal carrier tracking. BOC signals have ACFs that have different characteristics compared to the existing BPSK signals. Hence DLL performance is analyzed in detail in this research work for its effects on BOC signal tracking. In DLL, the discriminator is based on the ACF of the signal considered. The principal operation of a discriminator can be explained using the S-curve (Borio & O'Driscoll 2009). The S-

curve provides a mapping between the input parameter and estimated discriminator output and determines the properties of the loops for stable lock conditions.

A combination of E, P and L correlator values are the inputs to the code discriminator whereas a control signal proportional to the code delay error is its output. In order to operate correctly, a tracking loop is required to maintain the code delay error within the stability region of the S-curve (Borio 2010). In the stability region, the discriminator output is proportional to the input delay error. In addition to this, the delay error has to be within the linearity region around the main stable point of the S-curve. A point of the S-curve is said to be stable if it produces a zero output signal and thus the loop will tend to operate at that point. The main stable point is the one that produces a zero output for a null code delay error. For a tracking loop to maintain continuous lock on the primary peak, a single stable point within  $\pm 1$  chip is desired. The S-curve for BPSK and BOCs(1,1) signal (in the absence of noise) for a coherent discriminator is shown in Figure 2-9.

For BPSK modulated signals, there is only one stable point within  $\pm 1$  chip. But for a BOCs(1,1) modulated signal, there are multiple stable points that can lead to ambiguous tracking. If the loop is tracking a secondary stable point, the code measurements produced by the DLL will be biased. Several BOC tracking techniques (Fante 2003, Fine & Wilson 1999, Hodgart et al. 2008, Julien et al. 2007, Yang et al. 2006) have been introduced to mitigate the secondary peak lock conditions. For the performance analysis and comparison with the techniques proposed in this thesis, Bump-Jump (BJ) (Fine & Wilson 1999) and DE (Hodgart et al. 2008) are considered for their close approximation

to a matched filter (Kay 2008). BJ and DE along with a brief introduction to pre-filtering techniques are described in the following sections.

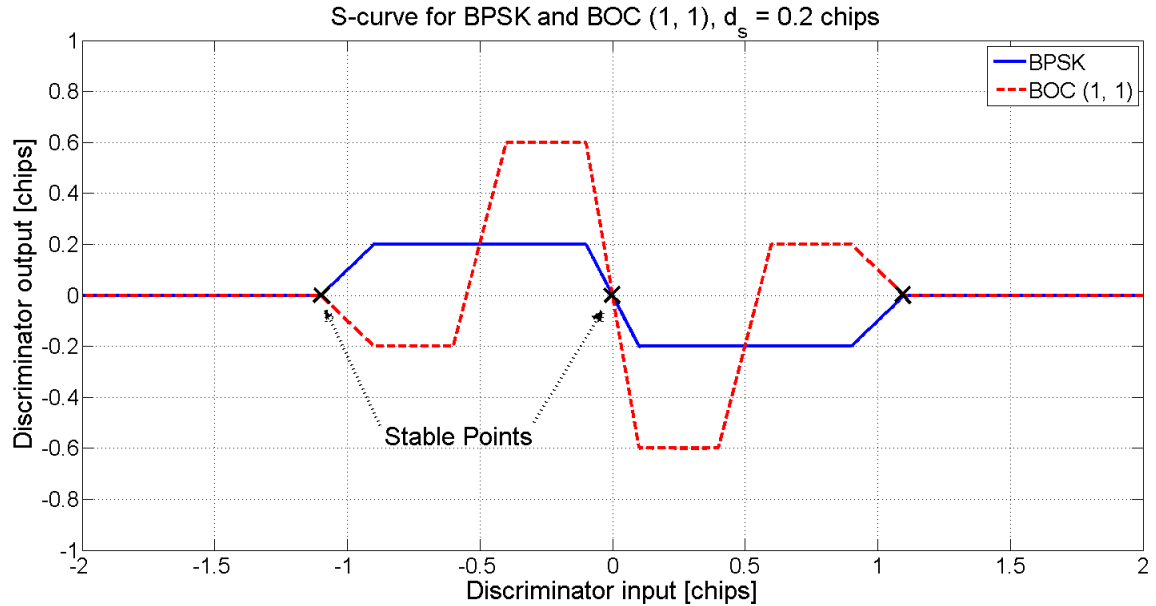


**Figure 2-9 S-curves of BPSK and BOC (1, 1) modulated signals for a coherent discriminator type with 0.2 chips early-minus-late spacing**

#### 2.4.3 Bump-Jump

BJ like techniques (Fine & Wilson 1999) adopt a post-correlation kind of processing to detect if the receiver is tracking the main peak and takes necessary steps to correct the code delay if the receiver is in a false lock condition on the secondary peak. This includes the implementation of additional correlators and decision logic to ensure proper tracking of the main peak. BJ assumes that the receiver has locked to one of the primary or secondary peaks. The decision logic determines if the primary peak is being tracked. This decision is based on two additional correlators, the very early (VE) and very late (VL). If a secondary peak is detected, the decision logic provides corrections to the code delay estimates obtained from the DLL. In this algorithm, the code delay is tracked

using a standard tracking loop as shown in Figure 2-10 and an additional decision logic is used to determine correct lock on the correlation primary peak.

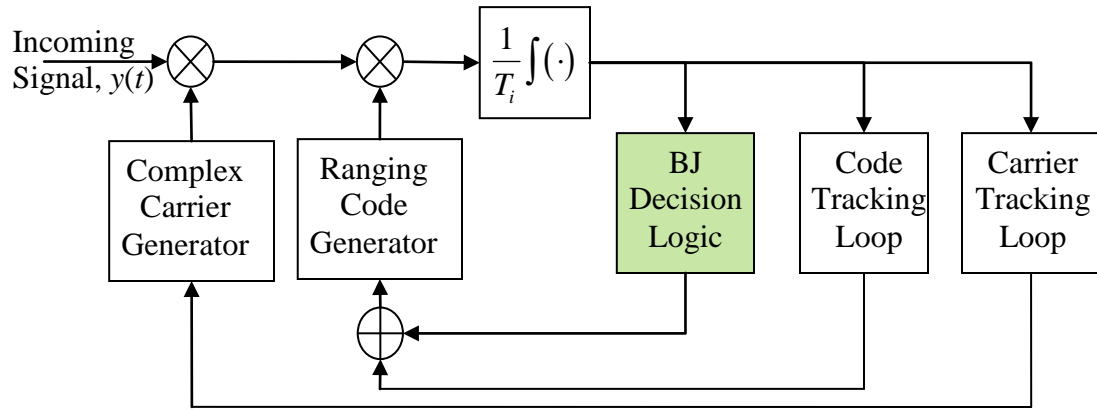


**Figure 2-10 Bump-Jump tracking structure**

The decision logic in the BJ technique comprises of the following steps.

*Step 1:* Initialize two counters, VE and VL counters, to zero.

*Step 2:* For every tracking epoch, compare the values of VE/VL against the P correlator output

*Step 3:* If either of VE or VL exceeds P, increment the respective counter and decrement the other counter otherwise decrement both counters. Care must be taken to reinitialize the counters to zero when negative

*Step 4:* If either the VE or VL counter has reached a pre-defined threshold, provide the corresponding correction parameter for code delay estimate and reset both the counters to zero

*Step 5:* Keep repeating Steps 2-4 for successive tracking epochs.

When the sub-carrier frequency is higher it introduces more secondary peaks on the autocorrelation function degrading the detection performance of the decision logic. As the sub-carrier frequency increases, the number of VE and VL correlators also increases

making the computation even more complex. A sample plot depicting the placement of VE/VL correlators required for BOCs(1, 1) modulated signal is shown in Figure 2-11.

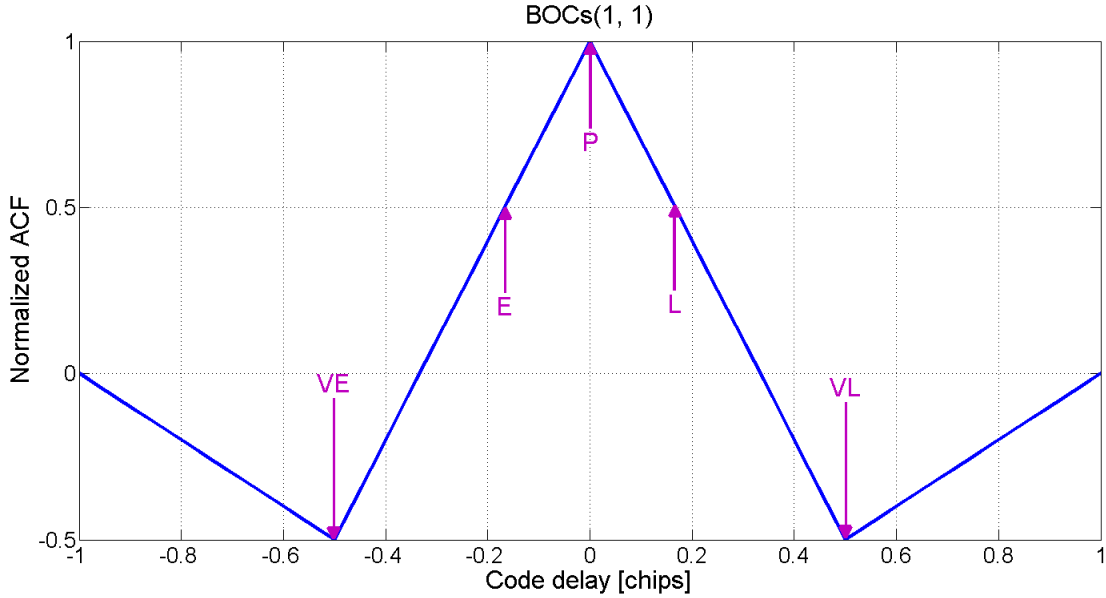


**Figure 2-11 Placement of VE and VL correlator outputs on BOCs(1,1) ACF for BJ decision logic**

It should be noted that for increasing sub-carrier ratios, the secondary peak amplitude approaches the primary peak amplitude. Since the receiver can correct only one sub chip at a given time, there is a tradeoff between the tracking sensitivity and the threshold. If the receiver is locked onto a secondary peak and the threshold is kept high, then the time to recover shall be longer but with a better tracking sensitivity; On the other hand if the threshold is kept low, the recovery time is lower but with a decreased tracking sensitivity. In this algorithm, the performance of the decision logic is efficient for strong signals but if the signal is weak, the algorithm can falsely apply correction and jump to another peak when it is not supposed to. Several papers (Hodgart et al. 2008, Blunt et al. 2007) have demonstrated the ineffectiveness of this algorithm.

#### 2.4.4 Double Estimator

In the DE technique, the sub-carrier and the PRS are tracked independently and an additional tracking loop for the sub-carrier is required (Hodgart et al. 2008, Blunt et al. 2007). This includes the implementation of a third tracking loop for the sub-carrier called the Sub-carrier Lock Loop (SLL) along with DLL and FLL/PLL as shown in Figure 2-12. Here the sub-carrier and the code of incoming signal are tracked independently by the SLL and DLL, respectively.

The DE technique maps the BOC ambiguous correlation over an unambiguous bi-dimensional function as illustrated in Figure 2-13. It is observed from Figure 2-13 that a periodic ACF is obtained in the sub-carrier delay domain. This is due to the fact that the sub-carrier delay can be estimated modulo by the sub-carrier period. An unambiguous ACF is instead obtained in the code domain.

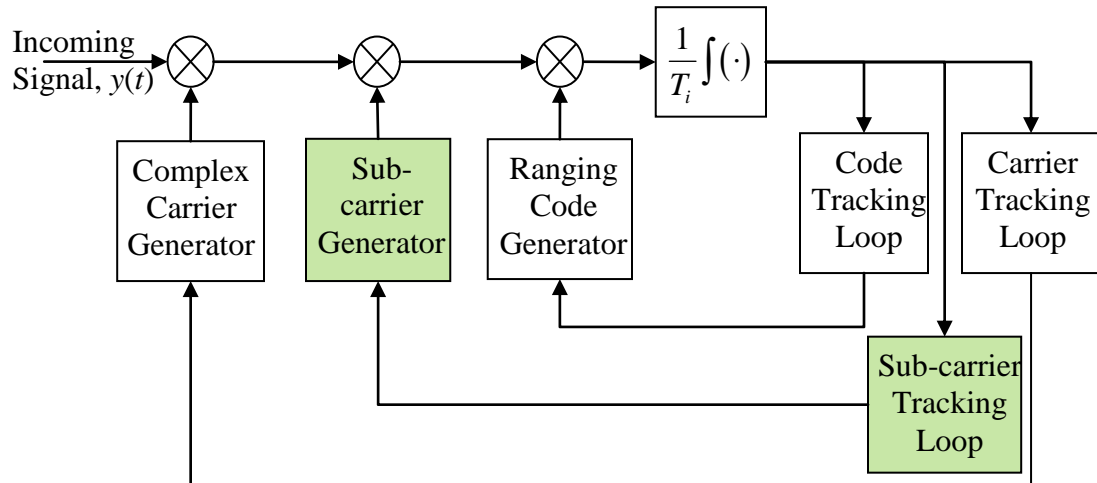


**Figure 2-12 Double Estimator tracking structure**

Thus, the DE technique performs a two dimensional tracking on sub-carrier and code delays independently. The DLL operates on the unambiguous ACF while the SLL operates on the periodic ACF.

The final code delay estimate,  $\hat{\tau}[k]$ , is obtained using the combination of the code delay,  $\hat{\tau}_c[k]$ , and sub-carrier delay,  $\hat{\tau}_s[k]$ , as (Hodgart et al. 2008)

$$\hat{\tau}[k] = \hat{\tau}_s[k] + T_{sl} \cdot \text{round} \left[ \frac{\hat{\tau}_c[k] - \hat{\tau}_s[k]}{T_{sl}} \right] \quad (2.10)$$

where  $T_{sl}$  is the duration of a sub-carrier slot. The composite ACF is a function of both sub-carrier and code delays and provides a maximum correlation only when both code and sub-carrier are locked onto their respective primary peaks. Thus the DE method always ensures a false lock free detection of the main correlation peak.

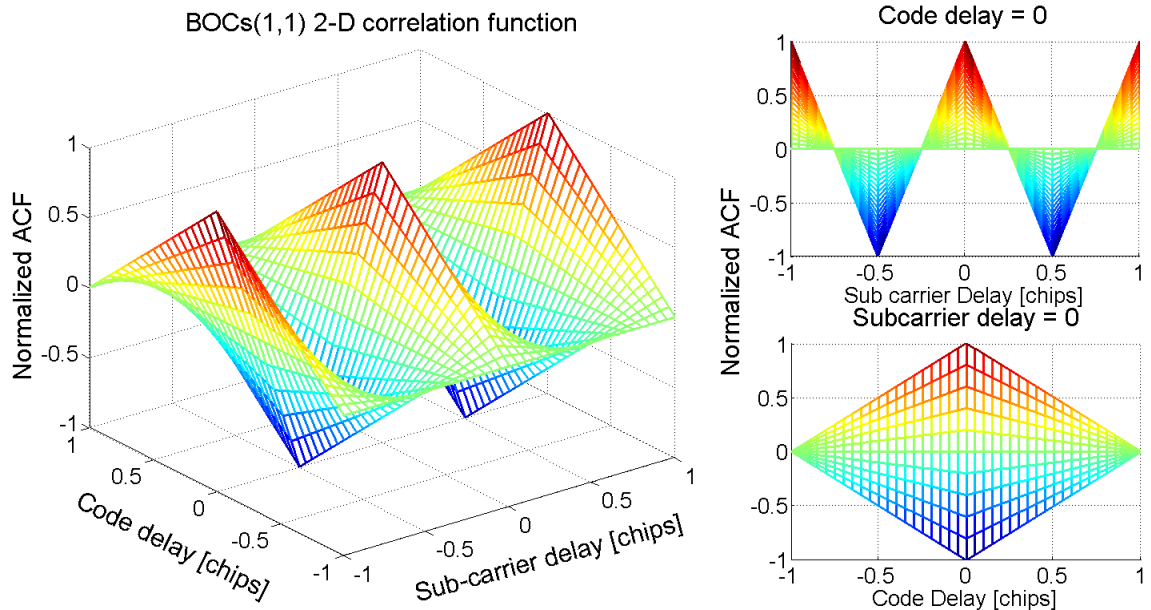


**Figure 2-13 BOC (1, 1) ACF as a function of code and sub-carrier delays**

#### 2.4.5 Pre-filtering

All pre-filtering techniques are based on the fact that the spectrum of a signal can be modified by filtering. In this research work, the input BOC signals are filtered in order to reproduce a BPSK-like spectrum and autocorrelation at the output of the I&D block as shown in Figure 2-14.

The filter  $h(t)$  is applied to the input signal  $y(t)$  prior to entering the tracking loops. The filtered signal is then tracked using a standard GNSS tracking structure. The design of  $h(t)$  is usually carried out in the frequency domain for ease of implementation.

Using the well-known properties of the Fourier Transform, the correlator output after filtering can be expressed as

$$q(\tau) = \mathcal{F}^{-1} \left\{ \mathcal{F}\{y(t)\} \cdot H(f) \cdot \mathcal{F}\{c_l(t)\}^* \right\}_{t=\tau} \quad (2.11)$$

where  $H(f) = \mathcal{F}\{h(t)\}$ ,  $\mathcal{F}$  is the Fourier Transform (FT) operation and  $(\cdot)^*$  denotes the complex conjugate operation. The filtered input spectrum and the complex conjugate of the local code spectrum are multiplied to produce an output spectrum whose Inverse Fourier Transform (IFT) produces the desired signal.

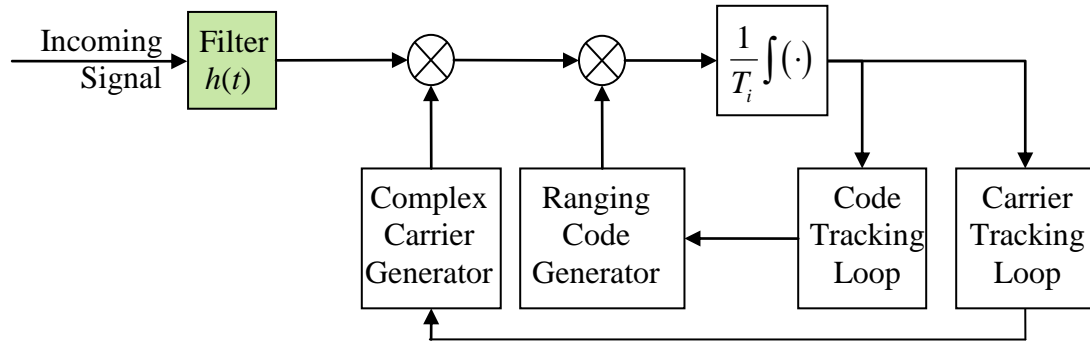


**Figure 2-14 Pre-filtering tracking structure**

In these kinds of techniques, the signal correlation function is modified through filtering. Pre-filtering techniques such as the ones proposed in (Yang et al. 2006) can lead to noise amplification. More specifically, in order to equalize the BOC spectrum it is required to compensate for its zeros which lead to singularities in the filter transfer function. These singularities are the main cause for noise amplification. In this research work, pre-

filtering techniques are developed to reduce the noise amplification and shape the BOC ACF for unambiguous tracking. The following section describes different analysis techniques that can be used to analyze the performance of BOC tracking techniques.

## 2.5 Tracking loop analysis techniques

The core of GNSS tracking loops consists of both linear and non-linear blocks. To analyze the performance of these kinds of system, analytical models and Monte Carlo simulations (Tranter et al. 2004) are a possible solution. Analytical models are best suited for linear systems where the mathematical derivations are simple and possibly allow a closed form solution. In the case of GNSS tracking loops, the existence of non-linear blocks makes the derivation of an accurate analytical model unfeasible, resulting in the limited applicability of analytical techniques. On the other hand, Monte Carlo simulations are extremely versatile and can be applied to a wide range of scenarios. But the presence of the I&D blocks that are used for despreading the incoming GNSS signals are computationally demanding resulting in a higher computational load and long simulation time when Monte Carlo techniques are used. The I&D blocks rely on simple operations that can be analytically modeled while the non-linear blocks can be analyzed using Monte Carlo simulations. For these reasons, semi-analytic models (Golshan 2006) exploiting the knowledge of the I&D blocks and simulating only the non-linear parts of the system are used in this research work. This results in an efficient analysis tool requiring reduced processing time with the application of Monte Carlo simulations.

Tracking loops described in Figure 2-2 are complex in their structure including linear (carrier/code wipe off, I&D, filter, NCO) and non-linear (discriminator) blocks. The IF

signals entering the tracking loops arrive at a signal rate in the order of MHz and requires long simulation times and are limited with their approximations for higher order, non-linear block. The intermediate representation of the semi-analytic model progressively moves the focus from the input signal to the quantity to be tracked (code delay). Noise and signal components are propagated independently through the linear part of the loop and equivalent representations of both components are provided. The noise is propagated at the correlator outputs and the useful signal component is obtained as a function of the quantity tracked by the loop. Hence semi-analytic techniques (Borio et al. 2010) have been used for the simulation of the considered BOC tracking techniques. A semi-analytic model for the standard GNSS DLL described in Section 2.2 is shown in Figure 2-15.

In this case, perfect phase and frequency recovery has been assumed. In Figure 2-15, the delay of the incoming signal,  $\tau[k]$ , and the delay estimate provided by the loop,  $\hat{\tau}[k]$ , are used for computing the delay error,  $\Delta\tau[k]$ . The correlation function  $R(\cdot)$  is then used to convert the delay error into the signal components of the three correlators. The noise components,  $E_n$ ,  $P_n$  and  $L_n$ , are added to the signal terms in order to obtain  $E$ ,  $P$  and  $L$  correlator outputs.

At this point, the non-linear part of the loop is completely simulated and a new discriminator output is obtained from the three correlators. The discriminator output is processed by the loop filter and a new delay estimate,  $\hat{\tau}[k+1]$  is obtained using an NCO model. It is noted that the values of  $\tau[k]$  are known simulation parameters that can be used for generating different dynamic conditions. The process is then iterated and the model is used for characterizing different loop parameters. In (Borio et al. 2010) a

generalized model for the semi-analytic approach allowing for the simulation of the tracking loops independently from the number of correlators and modulation type has been proposed. Using the generalized approach, semi-analytic models of the different BOC tracking techniques has been developed. Detailed descriptions of the semi-analytic models for BJ, DE and pre-filtering techniques are provided in Appendix B. In this research work, semi-analytic techniques are used as a main tool for the quantification of the different performance metrics that are detailed in the following section.

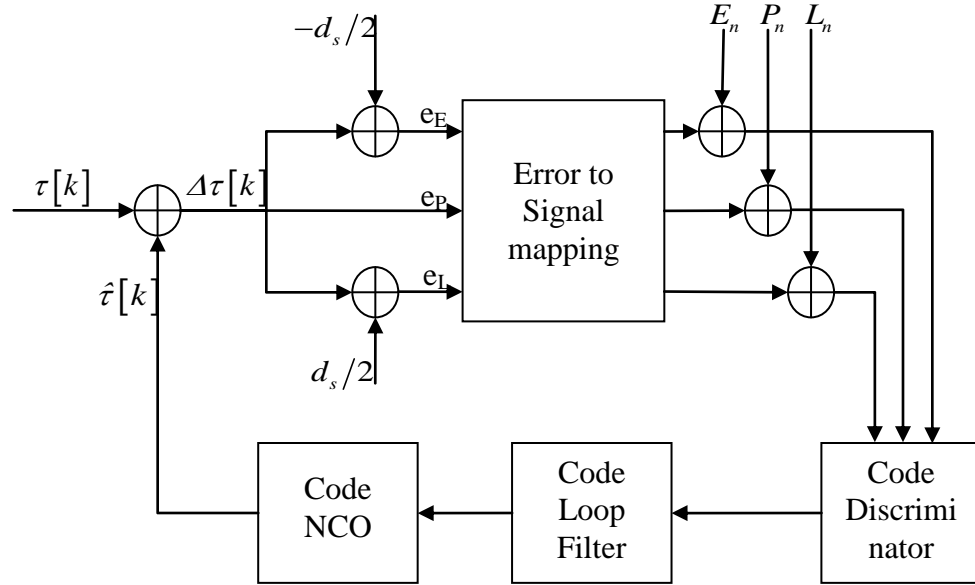


**Figure 2-15 Semi-analytic model of a GNSS code tracking loop**

## 2.6 Performance metrics

In this section, the different metrics used for analyzing the performance of BOC tracking techniques are presented. These include tracking jitter, tracking threshold, Mean Time to Lose Lock (MTLL), tracking error convergence analysis and multipath error envelopes (MEE). In this thesis, code tracking loops are analyzed in detail for different BOC tracking techniques.

### 2.6.1 Tracking Jitter

The tracking jitter quantifies the amount of noise transferred by the tracking loop to the final parameter estimate (Dierendonck et al. 1992). The tracking jitter is the standard deviation of the final parameter estimate normalized by the discriminator gain,  $g_d$  (Appendix A). For a DLL, the tracking jitter refers to the standard deviation of the code delay error,  $\Delta\tau[k]$  (Borio & O'Driscoll 2009). Table 2-2 provides general approximate expressions derived for the code tracking jitter when considering different discriminators.

**Table 2-2 Theoretical tracking jitter for different discriminator types**

Discriminator ( $D$ )	Tracking Jitter ( $\sigma_j$ )
Coherent $\text{Re}\{E - L\}$	$\sqrt{\frac{B_{eq}T_i\sigma_i^2(1 - R_n(d_s))}{2\dot{R}(d_s/2)^2}}$
Quasi-coherent Dot product $\text{Re}\{(E - L)P^*\}$	$\sqrt{\frac{B_{eq}T_i\sigma_i^2(1 - R_n(d_s))}{2\dot{R}(d_s/2)^2}(1 + \sigma_i^2)}$
Non-coherent Early minus Late Power $ E ^2 -  L ^2$	$\sqrt{\frac{B_{eq}T_i\sigma_i^2(1 - R_n(d_s))}{2\dot{R}(d_s/2)^2} \left[ 1 + \sigma_i^2 \frac{(1 + R_n(d_s))}{2R_n^2(d_s/2)} \right]}$

In Table 2-2, the parameters have the following roles:

- $R_n(\cdot)$  is the autocorrelation of the locally generated signals;
- $\dot{R}(\cdot)$  is the first derivative of  $R(\cdot)$  (cross-correlation between incoming and locally generated signals) with respect to  $\tau$  ;
- $B_{eq}$  is the equivalent loop bandwidth;
- $\sigma_i^2$  is the variance of  $\eta$ , the noise present at the correlator outputs.

The noise variance is equal to  $\sigma_i^2 = \gamma \frac{B_{IF}}{C/N_0 N}$ , where  $B_{IF}$  is the front-end filter bandwidth. For BJ and DE techniques,  $\gamma = 1$  whereas for pre-filtering,  $\gamma$  captures the effects of pre-filtering on the noise variance (Appendix B). It is noted that the expressions in Table 2-2 are valid only when the loop is working in its linearity region. Simulations can be performed to determine the performance for low  $C/N_0$ , when the loop operates outside its linear region.

### **2.6.2 Tracking threshold**

The tracking threshold defines the minimum  $C/N_0$  required by the loop to maintain a stable lock with a tracking error variance lower than a predefined threshold (Kaplan & Hegarty 2006). More specifically, this threshold depends on the linearity region of the code discriminator. In (Kaplan & Hegarty 2006), the tracking threshold is set using the rule of thumb

$$3\sigma_{j_{DLL}} = 3\sigma_{n_{DLL}} + R_e \leq d_s / 2 \quad (2.12)$$

where  $R_e$  is the dynamic stress error (in chips) experienced in the DLL.

In this research work, the derived theoretical jitter values are used as a comparison term for the estimated jitter. The theoretical tracking jitter is used as a reference to declare the tracking threshold which defines the minimum required for the tracking loop to be stable (Kaplan & Hegarty 2006). The tracking threshold can be declared as the value of  $C/N_0$  where the estimated tracking jitter exceeds the theoretical jitter by a known factor or exceeds a pre-defined threshold. Tracking techniques provide improved performance when moving from a non-coherent to a coherent code delay discriminator. In this

research work, the tracking threshold has been computed for different BOC tracking techniques considering non-coherent, quasi-coherent and coherent code discriminators.

### 2.6.3 MTLL

The S-curve mentioned in Section 2.4 is characterized by stable points that are those values of  $\Delta\tau[k]$  that provide an output signal equal to zero. Only one stable point is in the lock region and corresponds to the zero error. When a stable point different from  $(0, 0)$  is reached, the loop is no longer able to track the signal and loss of lock occurs. The time required by the code delay error to reach any stable point different from  $(0, 0)$ , starting from the S-curve origin, defines the time to lose lock (TLL) that is in general a random variable (Borio & O'Driscoll 2009). The mean value of TLL is the mean time to lose lock (MTLL) (Golshan et al. 2005).

A tracking loop design should guarantee a MTLL greater than the period of visibility of the satellite, under some minimal working conditions (Borio & O'Driscoll 2009). The definition of MTLL leads to a simple simulation scheme for its determination, as already suggested by (Golshan et al. 2005). More specifically, the simulation scheme adopted for the evaluation of the MTLL is shown in Figure 2-16. The semi-analytic model described in Section 2.6 is used for generating the delay error,  $\Delta\tau[k]$ , as a function of the time index  $k$ . When  $|\Delta\tau[k]|$  passes a pre-defined threshold,  $\Delta\tau_T$ , corresponding to the first stable point different from the origin, a new realization of the TLL is obtained. When  $N_{TOT}$  realizations of the TLL are evaluated, the MTLL is determined as

$$\hat{MTLL} = \frac{1}{N_{TOT}} \sum_{i=0}^{N_{TOT}-1} TLL_i \quad (2.13)$$

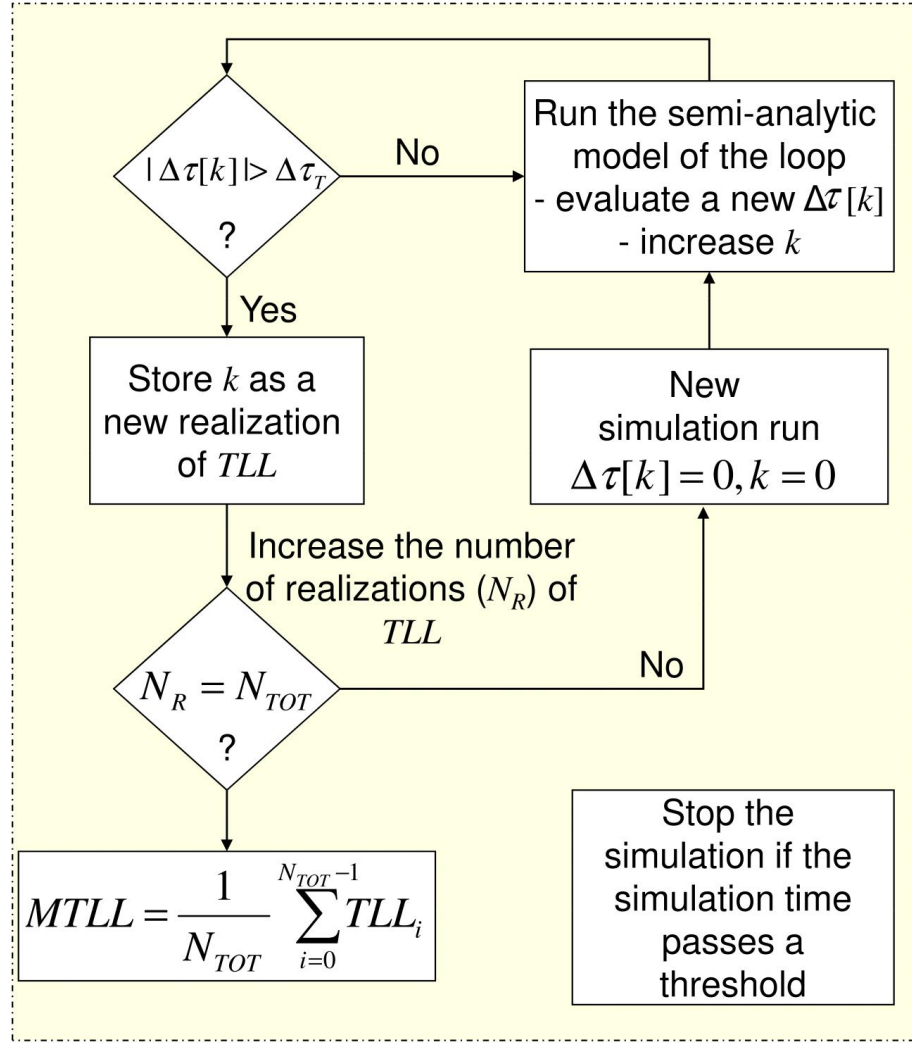


**Figure 2-16 Simulation scheme adopted for evaluation of MTLL from Borio et al 2010**

This type of approach can result in quite long simulation times even using the semi-analytic approach and an additional exit condition is included to terminate the simulation. The time required for the evaluation of the MTLL can be further reduced when considering first order loops (Golshan 2005). In this case, the DLL can be modeled as a first order Markov Chain and its properties used for evaluating the MTLL (Golshan 2005). The approach originally proposed by (Golshan 2005) can be directly applied to PF techniques when opportunely accounting for the filtering effects. The decision logic

present in the BJ does not lead to a simple extension of the Markov Chain approach to this tracking technique and hence the approach provided in Figure 2-16 has been used. However a generalization for the DE is proposed in the following. In the DE technique, loss of lock is essentially due to the DLL. This is due to the periodic nature of the sub-carrier signal that always leads to a sub-carrier delay error distributed within twice the sub-carrier duration. Moreover the probability density function (PDF) of the sub-carrier delay error can be easily estimated using the semi-analytic model considered in Appendix B. Hence, it is possible to determine the DE MTLL by first determining the conditional MTLLs,  $E(TLL_{DLL}|\Delta\tau_s)$ , that are the DLL MTLLs ( $TLL_{DLL}$ ) given a fixed SLL error ( $\Delta\tau_s$ ). When the SLL error is fixed, the Markov Chain approach can be directly applied to the DLL leading to reduced simulation times. The MTLL of the DE is finally determined as

$$\tau_{MTLL} = \int_{-T_{sl}}^{T_{sl}} E(TLL_{DLL}|\Delta\tau_s) p(\Delta\tau_s) d\Delta\tau_s \quad (2.14)$$

where  $p(\Delta\tau_s)$  is the PDF of the SLL delay error. This technique has been used for determining the DE MTLL and the results were compared against those obtained using the simulation scheme reported in Figure 2-16. The good agreement of the two methodologies supports the validity of (2.14).

#### **2.6.4 Convergence Analysis**

The tracking error convergence analysis provides the steady state behavior of the different tracking techniques given an initial delay error. Convergence is declared when the code delay error settles around a constant value (zeros if there are no biases). To

obtain an estimate of the convergence percentage of different BOC tracking techniques, the semi-analytic model described in Section 2.6 has been used to obtain tracking error estimates over time. The tracking error estimates are averaged over several simulation runs to determine the average behavior of the delay error. This kind of analysis provides a tool able to characterize the secondary peak lock conditions for BOC signal types. The expression for the average tracking error for a given initial delay error is given by

$$\tilde{\tau}_e[k] = \frac{1}{M} \sum_{i=1}^M \tau_e^i[k] \mid \tau_e^i[0] = \tau_{acq} \quad (2.15)$$

where  $\tau_{acq}$  is the code delay error from acquisition process and  $M$  is the number of simulation runs used for averaging the tracking error,  $\tau_e^i[k]$ . Here  $i$  denotes the simulation run index and  $k$  denotes the time index.  $\tau_{acq}$  can be varied over a wide range of code delays that includes secondary stable points. This analysis allows one to determine the efficiency of a BOC tracking algorithm to lock onto the primary peak when initialized with a secondary peak track point.

### **2.6.5 Multipath Error Envelope**

A common way of determining the system performance in the presence of multipath signals is given by the MEE (Braasch 1996). Using MEE, the maximum and minimum code tracking error for single path multipath can be obtained (Kaplan & Hegarty 2006). In this research work, a single multipath ray model is considered. For a single multipath ray model, there exists only one reflected signal along with the line-of-sight signal. The expression for the signal model including the multipath signal is given by  $s(t) = y(t) + m(t)$ . Here  $m(t)$  is the multipath signal expressed as

$$m(t) = \alpha_1 d(t - \tau_1) c(t - \tau_1) \exp\{j\theta_1(t)\} \quad (2.16)$$

where  $\alpha_1$ ,  $\tau_1$ ,  $\theta_1$  are the multipath amplitude, code delay and carrier phase, respectively.

Substituting the expression of  $y(t)$  from (2.1), the signal model in the presence of multipath is given by

$$s(t) = \alpha_0 \exp\{j\theta_0(t)\} [d(t - \tau_0) c(t - \tau_0) + \tilde{\alpha}_1 d(t - \tilde{\tau}_1) c(t - \tilde{\tau}_1) \exp\{j\tilde{\theta}_1(t)\}] + \eta(t) \quad (2.17)$$

where  $\tilde{\alpha}_1 = \frac{\alpha_1}{\alpha_0}$  is defined as the multipath-to-direct ratio (MDR),  $\tilde{\tau}_1 = \tau_1 - \tau_0$ ,  $\tilde{\theta}_1 = \theta_1 - \theta_0$

and  $\alpha_0 = A$ . The S-curve for a standard BOC signal (excluding thermal noise) considering the above multipath model with a coherent discriminator, MDR = 0.5,  $\tau_1 = 0.05$  and  $\theta_1 = 0$  is plotted in Figure 2-17. It can be observed that the stable point of the combined signal has shifted from (0, 0), the original stable point in the presence of LOS only. This shift varies according to the multipath signal parameters.

MEE provides a mapping between the multipath delay and the code delay error. Sample MEE plots for BPSK and BOC modulated signals for a narrow correlator (Dierendonck et al. 1992) comprising of a coherent discriminator (front-end filtering effects are not considered) are shown in Figure 2-18.

From Figure 2-18, it can be noted that BPSK and BOCs(1,1) signals behave similarly for short delay and medium delay multipath signals. But for higher delay multipath signals, BOCs(1,1) signals outperform BPSK. Performance in terms of code delay error improves for higher order BOC modulated signals for short delay multipath signals as well. The proposed BOC tracking techniques are compared against the standard MEE of BOC signals for their effectiveness to mitigate multipath.

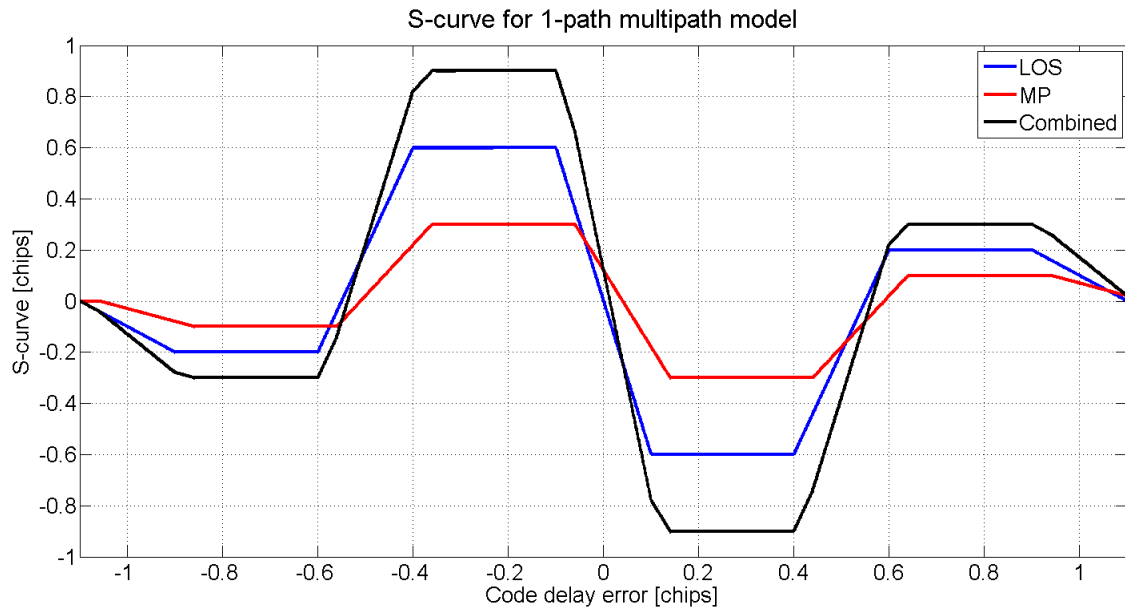


**Figure 2-17 S-curve of line-of-sight (LOS), multipath (MP) and combined signal for the single multipath ray model**

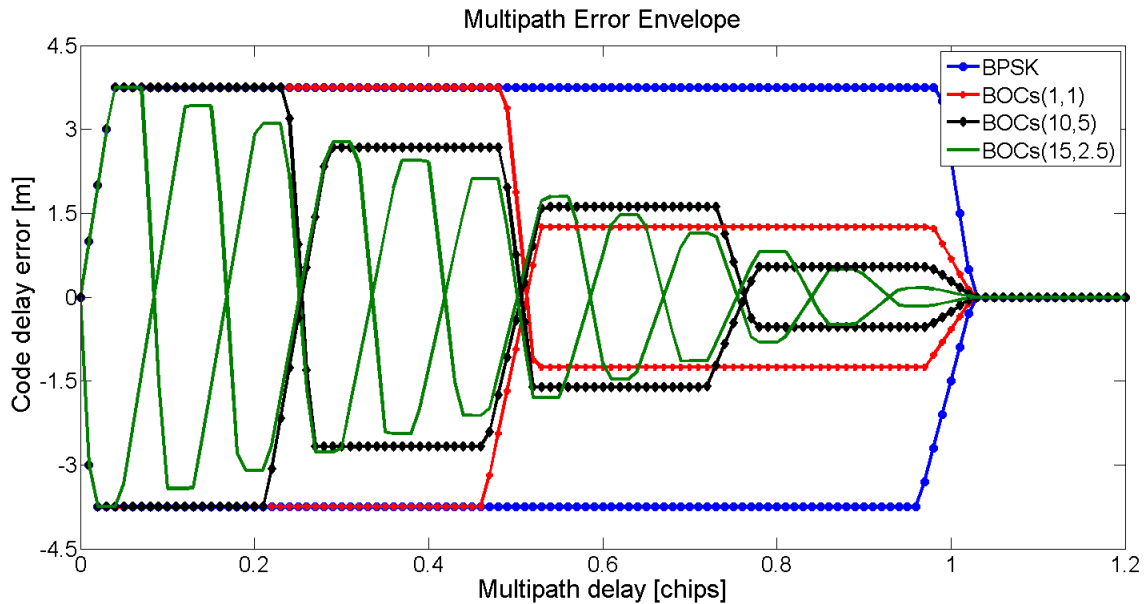


**Figure 2-18 Multipath error envelope of BPSK and BOC signals; Narrow correlator with  $d_s$  equal to 0.1 chips and a coherent discriminator**

### Chapter Three: Temporal Processing of BOC Signals

In communications, the effect of a frequency selective transmission channel is usually compensated by the adoption of equalization techniques (Hogbom 1974, Nuthalapati 2008, Qureshi 1985, Yang et al. 2006). In this chapter, the effect of a sub-carrier is interpreted as a selective communication channel that distorts the useful signal. Thus, an equalization approach can be adopted for mitigating the impact of the sub-carrier. Using this approach, filters analogous to the ZF and MMSE equalizers (Qureshi 1985) are derived in this chapter. Performance analyses for existing and proposed BOC tracking techniques are presented in detail along with an analysis using real data collected from live Galileo test satellites.

All pre-filtering techniques are based on the fact that the spectrum of a signal can be modified by filtering. These techniques can be considered an extension of algorithms proposed in the communication context such as the MMF (Nuthalapati 2008) and the “clean” algorithm (Hogbom 1974). The MMF operates on the temporal input data to obtain a desired sequence whereas the “clean” algorithm works in the frequency domain to obtain a desired spectrum. In these techniques, a different signal structure was considered and the spectrum of the received signal was shaped for ISI cancellation. The problem of secondary autocorrelation peaks was not considered. In this research work, the input BOC signals containing several secondary autocorrelation peaks are filtered in order to reproduce BPSK-like spectra and autocorrelations. Pre-filtering techniques such as the ones proposed in (Yang et al. 2006) can lead to noise amplification. More specifically, in order to equalize the BOC spectrum, it is required to compensate for its

zeros which lead to singularities in the filter transfer function. These singularities are the main causes for noise amplification. The limitations of previous approaches, such as the ones presented by (Yang et al. 2006), are highlighted and a new class of pre-filtering technique is derived from the convolutional representation of the transmitted signal described in Section 2.4.1.

### 3.1 Time-domain BOC signal tracking

Several BOC tracking techniques have been developed on the basis of the multiplicative and convolutional representations described in Section 2.4 to compensate for the side peaks present in its ACF. Side-peak compensation techniques can be divided into the following three classes, depending on the type of processing adopted:

- Convolutional techniques that compensate for the BOC sub-carrier exploiting the signal representation given by (2.7). Pre-filtering techniques proposed by (Yang et al. 2006) belong to this category;
- Multiplicative techniques that try to remove the sub-carrier effect by multiplying the input signal by an appropriate sequence according to (2.9). The DE (Hodgart et al. 2008) adopts this type of processing;
- Post-correlation techniques that operate on the correlation function, adopting different approaches for preventing false secondary locks. BJ (Fine & Wilson 1999) is one of the approaches following this technique.

The principle of multiplicative and convolutional techniques is shown in Figure 3-1 where both DE and pre-filtering are considered.

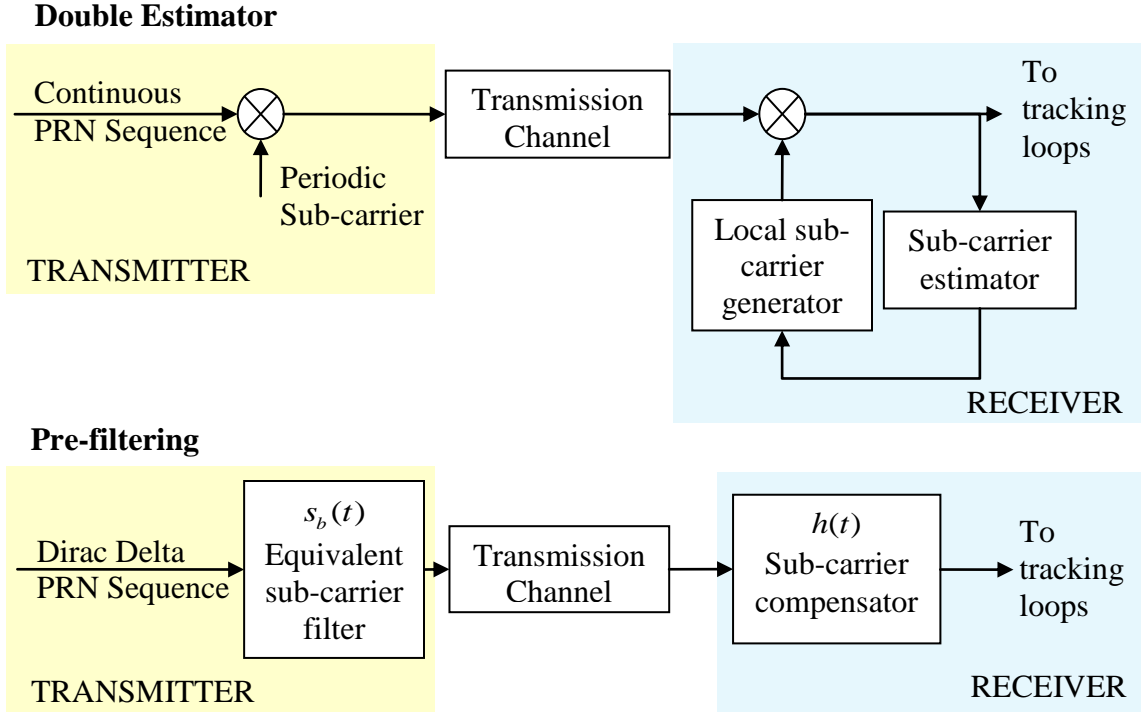


**Figure 3-1 Different side-peak compensation techniques based on different signal representations. DE exploits the multiplicative representation while the pre-filtering techniques use the convolutional representation**

In the pre-filtering case, it is assumed that the transmitted signal is generated using the convolutional representation as described in Section 2.4.1. The sub-carrier effect is alleviated using a filter denoted sub-carrier compensator,  $h(t)$ . These techniques exploit the fact that the sub-carrier effect can be removed by filtering the ranging code

$$\begin{aligned} c(t) * h(t) &= \tilde{p}(t) * s_b(t) * h(t) \\ &= \tilde{p}(t) * s_h(t) \end{aligned} \quad (3.1)$$

with the objective to make the filtered sub-carrier,  $s_h(t) = s_b(t) * h(t)$ , have a correlation function without side-peaks. More details on the design of  $h(t)$  are given in Section 3.3. In the DE technique, it is assumed that the signal transmitted from the satellite is generated using the multiplicative technique detailed in Section 2.4.2. The received signal

after passing through the transmission channel is correlated with a periodic version of the sub-carrier in the receiver. This is achieved by generating a local sub-carrier,  $\tilde{s}_b(t)$ , and estimating the sub-carrier delay to compensate the effects of the transmitted periodic sub-carrier. When the locally generated sub-carrier matches the sub-carrier of the incoming signal, the sub-carrier effect is completely removed from the ranging code and a BPSK-like signal is obtained. Post-correlation techniques, such as the BJ (Fine & Wilson 1999), do not directly operate on the signal but on the correlation function. More specifically, they require additional correlators that are used for monitoring the lock conditions.

In this research work, the convolutional representation of BOC signals is used as basis to derive new pre-filtering techniques. Using this model, filters based on ZF and MMSE equalizers are developed for BOC signal tracking. The DE and BJ tracking techniques are used for performance comparison. The following sections provide details of the existing pre-filtering techniques along with their drawbacks. The proposed pre-filtering techniques are then introduced.

### **3.2 Pre-filters**

The block diagram of the pre-filtering techniques considered in (Yang et al. 2006) is shown in Figure 3-2. The filter  $U(f)$  is applied to the spectrum obtained by performing a Fourier Transform (FT) operation on the incoming signal. Likewise, the filter  $V(f)$  is applied to the spectrum obtained by performing a FT operation on the locally generated signal. These filtered spectra are multiplied resulting in a spectrum whose Inverse FT (IFT) produces the desired signal that will be used to extract the code delay and Doppler.

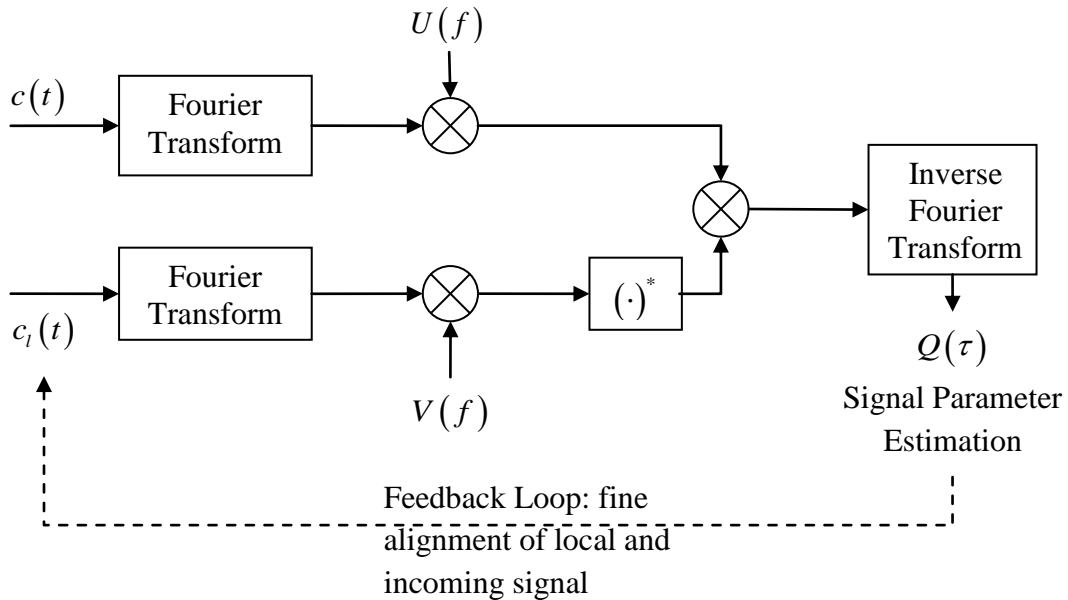


**Figure 3-2 Block diagram of pre-filtering techniques given in Yang et al. 2006.  $U(f)$  and  $V(f)$  used to filter the incoming and locally generated signals to provide an unambiguous correlation function**

The different pre-filtering techniques specified in (Yang et al. 2006) are shown in Table 3-1 along with the expressions for the filters,  $U(f)$  and  $V(f)$ . The “Standard Correlation” technique is based on a conventional frequency-domain correlation where the transfer functions of the two filters,  $U(f)$  and  $V(f)$ , are equal to 1. In the “Impulse Response” filter, only the phase information from the locally generated signal is extracted. The phase-only matched filter correlates the incoming signal with a phase-only replica of the locally generated signal. In certain situations, the phase of the Fourier transformed data contains most of the vital information (Oppenheim 1981). This is the basic assumption in forming a symmetric phase-only matched filter. Here, the filter tries to correlate the phase only versions of both the incoming and the locally generated

signals. Finally, the “Square-root normalized” filter is obtained by normalizing the incoming and the local signal by the square-root of the magnitude of their spectrum.

**Table 3-1 Different pre-filtering techniques defined in Yang et al. 2006**

Pre-filtering Technique	$U(f)$	$V(f)$
Standard Correlation	1	1
Impulse Response	$\frac{1}{ C(f) }$	$\frac{1}{ C(f) }$
Phase-only matched	1	$\frac{1}{ C(f) }$
Symmetric phase-only	$\frac{1}{ R(f) }$	$\frac{1}{ C(f) }$
Square-root normalized	$\frac{1}{\sqrt{ R(f) }}$	$\frac{1}{\sqrt{ C(f) }}$

It is noted that the pre-filtering techniques summarized above were originally proposed for communication applications where the signal strength is not usually a problem (Hassab & Boucher 1979). The amplitude information was removed in order to sharpen the correlation function for improved delay estimation. Moreover, all  $U(f)$  and  $V(f)$  in Table 3-1 are obtained from the FTs of the whole local ranging code and incoming signal. This is one of the main causes of noise amplification. For instance, when using the symmetric phase-only matched filter, the noise present in the input signal heavily impacts the evaluation of  $1/|R(f)|$ . The noise on the incoming signal is then amplified by filtering with  $U(f)$ . The effect of the symmetric phase-only matched filter on the signal correlation function is analyzed in Figure 3-3 for different  $C/N_0$  values. It can be observed that a single peak BPSK-like ACF is obtained only for a very high  $C/N_0$ . As the

$C/N_0$  decreases, noise components tend to prevail on the useful signal and  $|R(f)|$  tend to reflect the amplitude of the noise spectrum, masking the signal component.

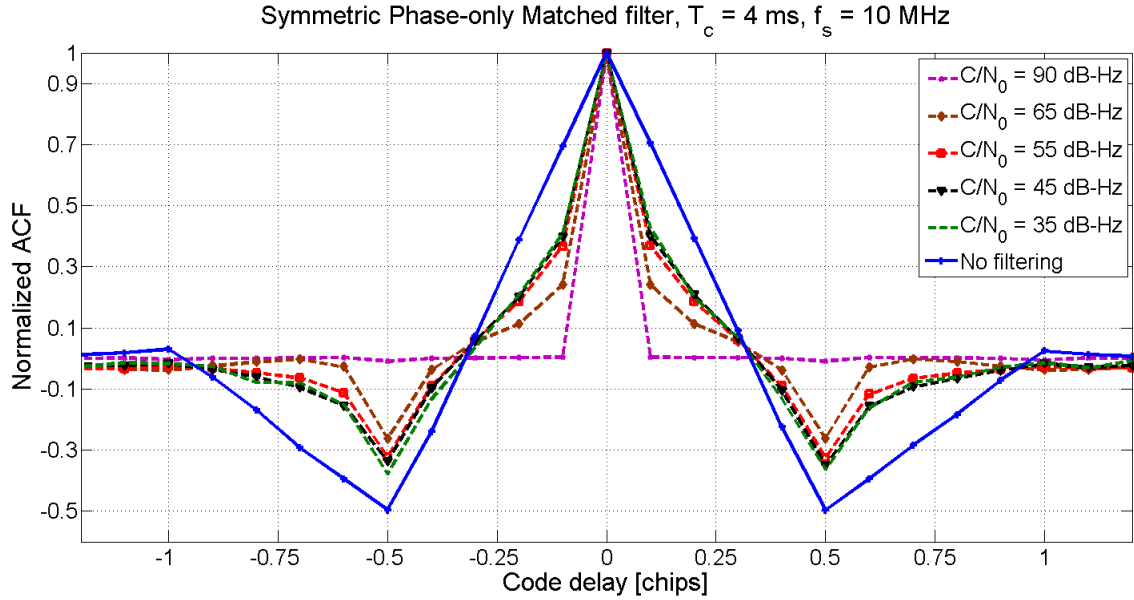


**Figure 3-3 Correlation functions after applying a symmetric phase only matched filter for different  $C/N_0$  values. An unambiguous correlation function is observed for high SNR values**

For this reason, secondary peaks tend to emerge. Similar effects can be observed when using the other pre-filtering techniques: the secondary peaks are removed only for very high  $C/N_0$  values, making their use quite limited. Those techniques can be improved by averaging  $U(f)$  and  $V(f)$  over several epochs. However this would lead to an increased computational load. This problem is solved here by including the effects of  $U(f)$  and  $V(f)$  in a single filter,  $H(f)$  derived from local copies of the sub-carrier,  $s_b(t)$ . Those local sub-carriers are noise-free and their use limits the noise amplification problem without increasing the computational load. The following sub-sections explain the design of  $H(f)$  based on ZF and MMSE equalization. Since the proposed pre-

filtering techniques shape the BOC ACF for unambiguous tracking, they are herein called ZF Shaping (ZFS) and MMSE Shaping (MMSES).

### 3.3 MMSES and ZFS

The block diagram shown in Figure 2-14 is used for the development of the proposed MMSES and ZFS algorithms. Here the filters  $U(f)$  and  $V(f)$  are replaced by the filter  $H(f)$ .  $H(f)$  captures the combined effects of  $U(f)$  and  $V(f)$  as

$$H(f) = U(f)V^*(f) \quad (3.2)$$

and operates on the incoming signal to produce an unambiguous ACF at the correlator output.

The main goal of MMSES is to produce an output signal with unambiguous ACF. A BPSK-like spectrum is thus the desired signal spectrum and the transfer function of the MMSES,  $H(f) = \mathcal{F}\{h(t)\}$ , needs to be designed accordingly. Here,  $\mathcal{F}$  denotes the FT operation. The solution leading to  $H(f)$  is given by the MMSE approach that minimizes the following cost function (Qureshi 1985):

$$\mathcal{E}_{MMSES} = \int_{-B_{IF}}^{B_{IF}} \left[ |G_D(f) - G_x(f)H(f)|^2 + \frac{\lambda N_0}{C} G_L(f) |H(f)|^2 \right] df \quad (3.3)$$

where

- $G_D(f)$  is the desired signal spectrum. Its inverse Fourier transform is the desired correlation function;
- $G_x(f)$  is the Fourier transform of the correlation between incoming and local signals.  $G_x(f)$  and  $G_D(f)$  have been normalized in order to have unit integral;
- $G_L(f)$  is the spectrum of the local code;

- $N_0$  is the PSD of  $\eta(t)$ , the input noise assumed to be white within the receiver bandwidth;
- $\lambda$  is a constant factor used to weight the noise impact;
- $B_{IF}$  is the receiver front-end bandwidth;

It is noted that  $\varepsilon_{MMSES}$  incorporates two terms. The first is the mismatch between desired and actual correlation functions, whereas the second is the noise variance after correlation and filtering. This second term is multiplied by the inverse of the C/N<sub>0</sub> in order to account for the relative impact of signal and noise components. The division by  $C$  in the second term of (3.3) is due to the normalization adopted for  $G_x(f)$  and  $G_D(f)$ . The factor  $\lambda$  allows one to weight the relative contribution of the two terms. Under the assumption that the local code is matched to the incoming signal,  $G_L(f)=G_x(f)$ , (3.3) reduces to

$$\varepsilon_{MMSES} = \int_{-B_{IF}}^{B_{IF}} \left[ |G_D(f) - G_x(f)H(f)|^2 + \frac{\lambda N_0}{C} G_x(f) |H(f)|^2 \right] df \quad (3.4)$$

and the error in (3.4) is minimized by

$$H(f) = \frac{G_D(f)}{G_x(f) + \frac{\lambda N_0}{C}}. \quad (3.5)$$

ZFS is a special case of MMSES in which the noise effect is ignored. Setting  $\lambda=0$  in (3.5) results in the ZFS algorithm

$$H(f) = \frac{G_D(f)}{G_x(f)}. \quad (3.6)$$

In (3.6),  $G_x(f)$  can contain zeros that would make  $H(f)$  diverge to infinity. This is avoided by clipping the amplitude of  $H(f)$  to certain limits thus removing the singularities in  $G_x(f)$ .

Figure 3-4 shows the ACF obtained after applying MMSES on Intermediate Frequency (IF) simulated data. The input  $C/N_0$  is set to 40 dB-Hz and the ACF was averaged over 1 s of data. From Figure 3-4, it can be observed that the multi-peaked BOC ACF (curve indicated as ‘Standard’) was successfully modified by MMSES to produce a BPSK-like ACF without secondary peaks. BOCc(10, 5) and BOCc(15, 2.5) modulated signals were used for the analysis of the proposed technique and the ACF after applying MMSES on simulated data are shown in Figure 3-5.

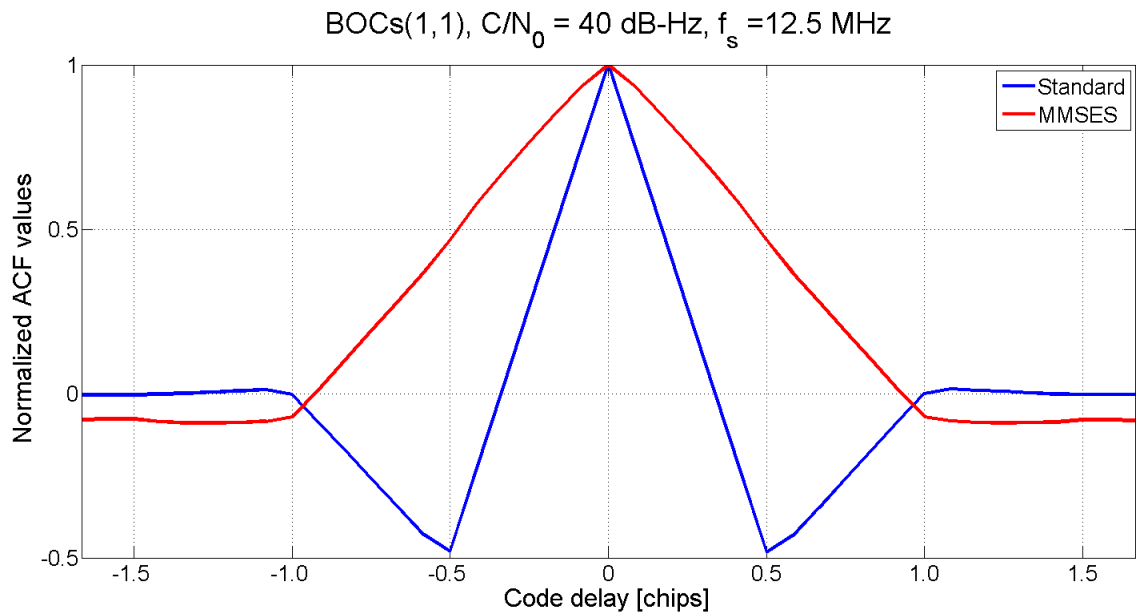


**Figure 3-4 ACF with and without applying MMSES for an input BOCs(1, 1) signal simulated with a  $C/N_0$  of 40 dB-Hz**

Results here show the flexibility of MMSES to provide unambiguous ACF for higher sub-carrier rate ratios of the BOC family. The sub-carrier rate ratio for BOCc(10, 5) is 2

while that of BOCc(15, 2.5) is 6. Although the theory provided above has been developed in the continuous time domain, the algorithms have been practically implemented using digital versions of the incoming and local signals. For this reason, the correlation functions in Figure 3-4 and Figure 3-5 are sampled with a sampling frequency  $f_s$ .

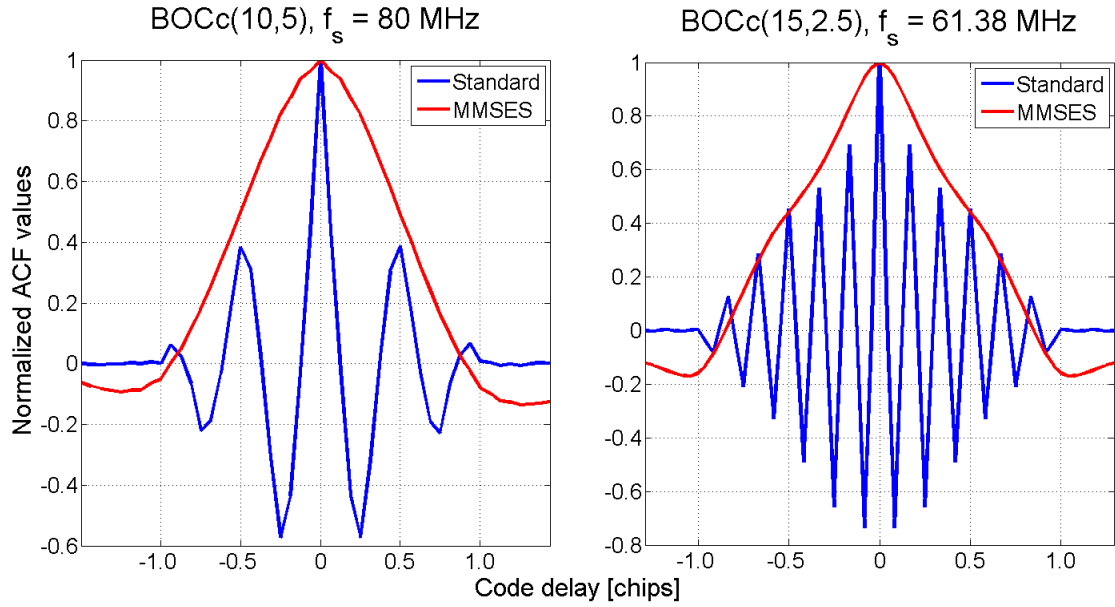


**Figure 3-5 ACFs of BOCc(10, 5) and BOCc(15, 2.5) before and after applying MMSES for an input signal with a C/N<sub>0</sub> of 40 dB-Hz.**

In the proposed approach, it is assumed that the spectrum of the different signal components is essentially determined by the FT of the local and desired sub-carriers. More specifically, the following assumptions are made:

$$G_D(f) = |S_D(f)|^2, G_x(f) = G_L(f) = |S_b(f)|^2 \quad (3.7)$$

where  $S_D(f)$  and  $S_b(f)$  are the FTs of the desired and local sub-carriers,  $s_D(t)$  and  $s_b(t)$ , respectively. Condition (3.7) implies that the spectrum of the PRS modulated Dirac comb can be effectively approximated as a Dirac delta. This approach allows the design of shaping filters independent from the PRS. This approach has proven to be more

effective than other pre-filtering techniques in mitigating the noise amplification problem.

Sampled representation of  $s_D(t)$  and  $s_b(t)$  for a BOCs (1, 1) modulated signal in the discrete-time domain with a sampling frequency,  $f_s = 12$  MHz, is

$$\begin{aligned} s_b[n] &= [1 \ 1 \ 1 \ 1 \ 1 \ 1 \ -1 \ -1 \ -1 \ -1 \ -1] \\ s_D[n] &= [1 \ 1 \ 1 \ 1 \ 1 \ 1 \ 1 \ 1 \ 1 \ 1]. \end{aligned} \quad (3.8)$$

Here,  $s_D[n]$  and  $s_b[n]$  are represented according to the number of samples available for one code chip. The samples in  $s_D[n]$  can be modified to achieve a desired ACF. Using the discrete-time versions of the proposed algorithms, semi-analytic simulations have been performed for the analysis of the pre-filtering techniques and the results are provided in the following sections.

### 3.4 Time domain Implementation

The development of both ZFS and MMSES has been performed at first in the frequency domain as discussed in Section 3.3. The processing load required to track signals in the frequency domain is significant since it involves FT operations. Hence, a more efficient time domain implementation requiring the evaluation of only three correlators has been developed. The final correlator output after frequency domain processing can be expressed as

$$q(\tau) = \mathcal{F}^{-1} \left\{ \mathcal{F}\{y(t)\} \cdot H(f) \cdot \mathcal{F}\{c_l(t)\}^* \right\} \Big|_{t=\tau} \quad (3.9)$$

where  $\mathcal{F}^{-1}\{\cdot\}$  denotes the IFT. Rearranging the terms in (3.9), the filtering operation can be performed solely on the local signal as

$$q(\tau) = \mathcal{F}^{-1} \left\{ \mathcal{F}\{y(t)\} \cdot \mathcal{F}\{\tilde{c}_l(t)\}^* \right\}_{t=\tau} \quad (3.10)$$

where  $\tilde{c}_l(t) = \mathcal{F}^{-1} \left\{ H^*(f) \mathcal{F}\{c_l(t)\} \right\}$  is an equivalent code accounting for the filtering performed by  $H(f)$ . In this way, pre-filtering can be implemented as the time domain correlation with a modified local code,  $\tilde{c}_l(t)$ . More specifically,  $\tilde{c}_l(t)$  is no longer a binary sequence. The modified local code along with its PSD before and after pre-filtering is shown in Figure 3-6.

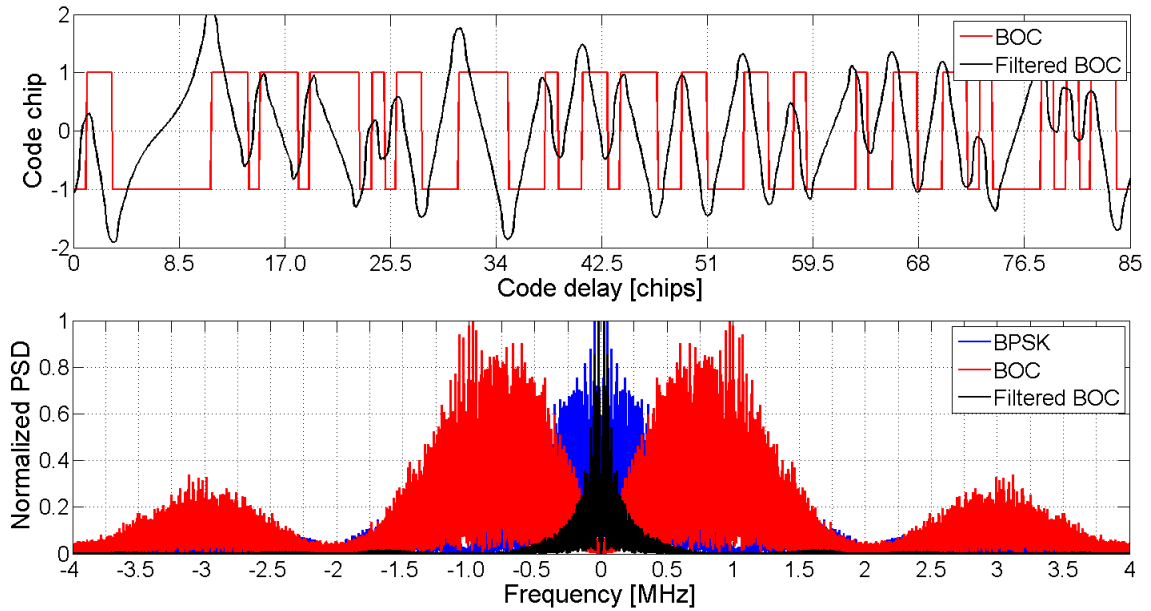


**Figure 3-6 Filtering effects on BOC signal and its spectrum**

The PSD plot shows that the dual lobed BOC spectrum is replaced by a single lobe narrow spectrum after filtering. The main advantage of using  $\tilde{c}_l(t)$  to perform time domain filtering is the reduced computational complexity. The Fourier transform and the operations in the frequency domain are replaced by three correlators, Early, Prompt and Late codes, directly computed in the time domain.

### 3.5 Delay and Phase Independent Tracking

The PLL is always the weakest link in a GNSS receiver (Kaplan & Hegarty 2006) and filtering further amplifies the input noise degrading the PLL performance and resulting in a poor tracking sensitivity. For weak signal environments, it would be beneficial if the PLL and filtering process were independent. For this reason a new architecture, using independent correlators for PLL and DLL has been developed. The proposed architecture is shown in Figure 3-7.

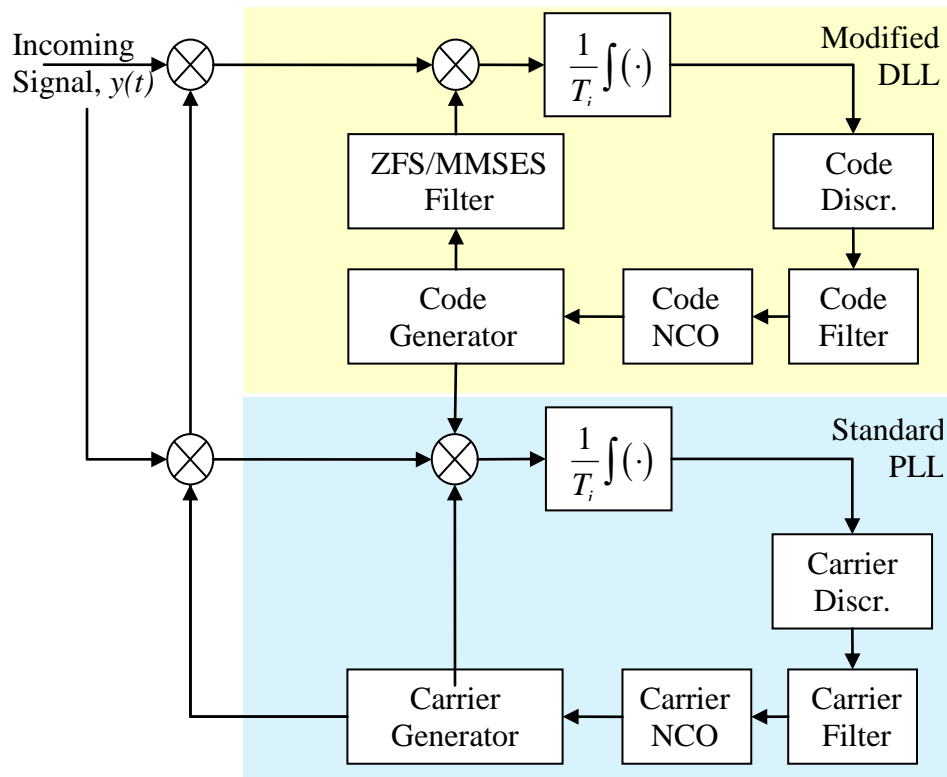


**Figure 3-7 Modified tracking structure for independent code and carrier tracking**

Here, the DLL is driven by the filtered correlators ensuring unambiguous code tracking. On the other hand, the PLL is driven by an additional unfiltered correlator. In this way, the PLL is unaffected by the noise amplification caused by pre-filtering. To verify the effect of the modified tracking structure, attenuated live signals from the GIOVE-B

satellite were used. Figure 3-8 shows the  $C/N_0$  estimates obtained by using the standard and modified tracking loop for the ZFS equalizer. The  $C/N_0$  estimates are used here as a lock indicator (Dierendonck 1996). In the standard case, the PLL is driven by the filtered version of the code and is unable to maintain lock for  $C/N_0$  values lower than 35 dB-Hz. When the PLL is driven by the unfiltered correlator, it is capable of operating for  $C/N_0$  values lower than 30 dB-Hz.

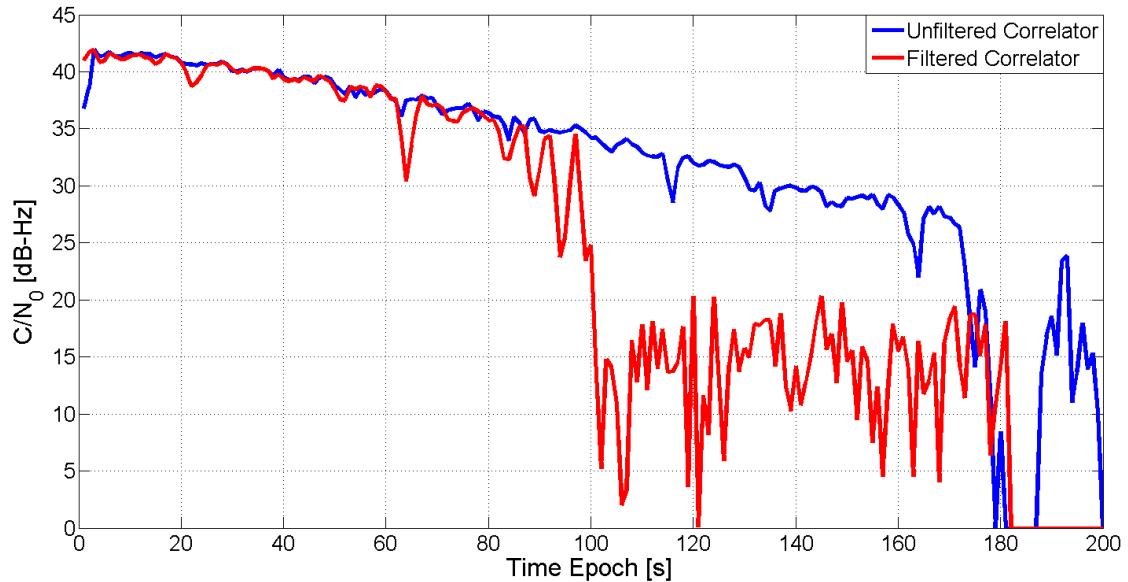


**Figure 3-8**  $C/N_0$  estimates provided by a PLL operating on filtered and unfiltered correlators. The use of unfiltered correlators allows the tracking of weaker signals

### 3.6 Analytical characterization

#### 3.6.1 Theoretical Analysis

The filter used to shape the signal autocorrelation modifies the signal and noise properties. More specifically, a loss in the Signal-to-Noise Ratio (SNR) at the correlator output is introduced. This effect is the already mentioned noise amplification problem and its impact can be determined using an approach similar to the one adopted by (Borio 2008, Betz & Kolodziejki 2009a, Betz & Kolodziejki 2009b).

$H(f)$  generates a colored noise and the post-correlation SNR becomes (Borio 2008, Betz & Kolodziejjski 2009a)

$$SNR = \frac{C}{N_0} T_i \gamma \quad (3.11)$$

where  $\gamma$  is the filtering loss equal to

$$\gamma = \frac{\left| \int_{-B}^B G_x(f) H(f) df \right|^2}{\int_{-B}^B G_x(f) |H(f)|^2 df}. \quad (3.12)$$

It is noted that the numerator and denominator in (3.12) are the signal and noise terms of the cost function (3.4). The MMSES tries to find a compromise between making  $G_x(f) H(f)$  as close as possible to the desired spectrum,  $G_D(f)$ , and reducing the noise term at the denominator of (3.12).

If the amplitude of the Prompt correlator output is assumed to be normalized to unity, the inverse of (3.11) determines the variance of the post-correlation noise components:

$$\sigma_n^2 = \frac{1}{C/N_0 T_i \gamma}. \quad (3.13)$$

This has been used in the computation of tracking jitter for all the three BOC tracking techniques, BJ, DE and pre-filtering, given in Appendix A.

### 3.6.2 Computational Analysis

The computational complexity of the considered algorithms along with the average processing time required for the execution of considered algorithms is detailed in the following. Table 3-2 summarizes the computational complexity of pre-filtering, BJ and DE. The computation of the correlator outputs is the most demanding task of a GNSS

receiver. Thus, the computational complexity is determined as a function of the number of required correlations. The final execution speed of each algorithm depends on the hardware specifications of the platform where the techniques are implemented. For example, modern general purpose processors and DSPs are able to perform real multiplications in a single clock cycle making pre-filtering an attractive solution in terms of computational complexity. The different algorithms have been implemented in MATLAB and tested using live GIOVE-B data. An indication of the effective computational time required by each technique is provided in Table 3-2 where the average times required to process a second of data by the different techniques is reported.

**Table 3-2 Computational complexity of pre-filtering, BJ and DE.**

Algorithm	Number of Complex Correlators	Average Processing Time	Notes
BJ	5-bipolar/binary	6.8 s	The local code is a bipolar sequence and code multiplication can be effectively implemented using sign changes
DE	5-bipolar/binary	7.6 s	Additional logic/circuitry is required for the generation of the local sub-carrier replica. The number of multiplications is doubled since local code and sub-carrier are wiped-off separately
MMSES (independent phase tracking)	3-real 1-bipolar/binary (time domain implementation)	Frequency Domain: 10.8 s Time Domain: 7.3 s	The filtered local code is stored in memory and multi-bit multiplications are required for the code wipe-off.

It is noted that, although code implementing the different algorithms was not designed for real-time operations, the results in Table 3-2 provide an indication of the relative complexity of the three techniques. The values in Table 3-2 have been obtained using

MATLAB directives for measuring the execution time of a single loop update including the computation of the different correlator outputs. A 5-minute long data set was used to average the processing times reported in Table 3-2.

The characteristics of the input signal are summarized in Table 3-3. From Table 3-2, it emerges that the time domain implementation of the MMSES is less computationally demanding than the DE. In addition to this, the MMSES allows one to implement multipath mitigation capabilities without increasing the computation load. This is achieved by changing the filter used for code shaping as detailed in Section 3.7.5.

**Table 3-3 Parameters of the real data used for the computational analysis**

Parameters	Values
Sampling frequency	12.5 MHz
Intermediate frequency	3.42 MHz
Data Duration	5 min
Sampling	8 bit real samples

### 3.7 Performance analysis

In this section, ZFS and MMSES are analyzed and compared against the DE and BJ techniques in terms of tracking jitter, tracking threshold, MTLL, tracking error convergence analysis and MEE for different early-minus-late chip spacing and discriminator types. The analysis is based on the simulation schemes described in Appendix B (Section B.1). The signal parameters used for the semi-analytic analysis are provided in Table 3-4.

### 3.7.1 Tracking Jitter

The tracking jitter is one of the most used metrics for determining the quality of estimates produced by tracking loops. A large tracking jitter indicates poor quality measurements and a large uncertainty in the estimated parameters. In this section, tracking jitter plots comparing the performance of BJ, DE, ZFS and MMSES for non-coherent, quasi-coherent and coherent discriminators as a function of the input C/N<sub>0</sub> are provided.

**Table 3-4 Simulation parameters considered for semi-analytic analysis of BOC tracking techniques**

Parameters	Values
Coherent Integration Time	4 ms
Front-end Bandwidth	4 MHz
Code Bandwidth	0.5 Hz
Code Filter Order	1
Simulation Runs	10000
Signal Type	BOCs(1,1)

The tracking jitter plots provided in this section comprise three different curves. The first one, indicated by *Theory*, is a theoretical approximation obtained using the model in Figure A.5. The second one, named *True*, is obtained by estimating the standard deviation of the actual tracking error,  $\Delta\tau[k]$ . The last curve marked as *Measured*, is obtained by propagating the variance of the discriminator output. The *Measured* curve is not provided in the DE case since the propagation process depends on both SLL and DLL discriminators, thus making its evaluation complex. The agreement between these three curves supports the correctness of the proposed simulation scheme. It can be observed

that the tracking jitter on the coherent discriminator is improved in comparison to the other two discriminator types. It is also noted that, for low  $C/N_0$  values, the three curves diverge. This is due to the fact that the loop is losing lock and the loop discriminator is working in its non-linear region. In contrast, both theoretical and measured curves rely on the linear model of the loop thus leading to a better agreement between the two curves.

In this section, chip spacing,  $d_s = 0.2, 0.3$  and  $0.4$  chips, have been considered along with non-coherent, quasi-coherent and coherent discriminators (Kaplan & Hegarty 2006). The coherent integration time for all the techniques was set to 4 ms with the DLL bandwidth to 0.5 Hz. This bandwidth is typical for Doppler aided code lock loops. The results obtained for the DE and BJ techniques with a non-coherent discriminator are shown in Figure 3-9.

In this case, the code lock loop is able to maintain lock for quite low  $C/N_0$  values and no noise amplification is observed. For the DE technique, since the tracking loops consists of two loops, SLL and DLL, operating in parallel, a theoretical lower bound for the tracking jitter can be obtained as

$$\begin{aligned} \text{Var}\{\hat{\tau}[k]\} &= \text{Var}\{\hat{\tau}_{sc}[k]\} + T_{sl}^2 \text{Var}\left\{\text{round}\left[\frac{\hat{\tau}_c[k] - \hat{\tau}_{sc}[k]}{T_{sl}}\right]\right\} \\ &\quad + 2T_{sl} \text{Cov}\left(\hat{\tau}_{sc}[k], \text{round}\left[\frac{\hat{\tau}_c[k] - \hat{\tau}_{sc}[k]}{T_{sl}}\right]\right). \end{aligned} \quad (3.14)$$

For moderate to high  $C/N_0$  values, the second term in (3.14) tends to be constant, depending on the DLL estimate. Thus, the variance of the final delay estimate and tracking error is dominated by the variance of the SLL delay estimate:

$$\text{Var}\{\hat{\tau}[k]\} = \text{Var}\{\hat{\tau}_{sc}[k]\}. \quad (3.15)$$

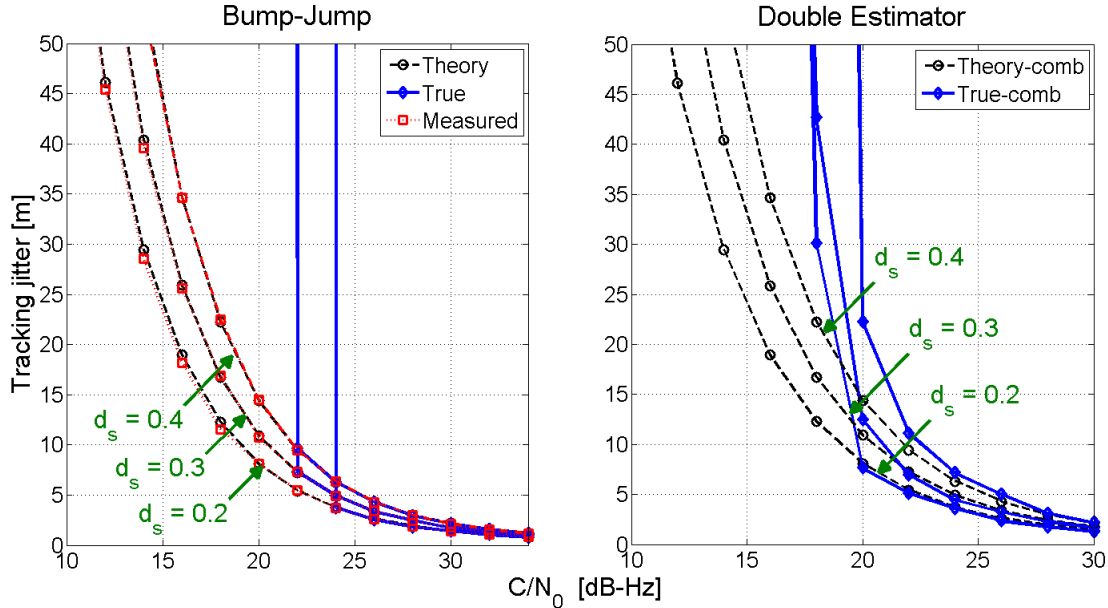


**Figure 3-9 Code tracking jitter of BJ and DE techniques as a function of the  $C/N_0$  and for non-coherent discriminator with different  $d_s$**

The approximation given in (3.15) is used for evaluating the theoretical curve in Figure 3-9 where the performance of the DE with non-coherent discriminator is analyzed. In this case, SLL and DLL have the same bandwidth (0.5 Hz) and the DE has performance similar to that obtained by the BJ. The advantage of the DE is that it is able to maintain lock for lower  $C/N_0$  values. The performance of ZFS and MMSES with a non-coherent discriminator is shown in Figure 3-10 as a function of the input  $C/N_0$  and for different chip spacing.

As already pointed out, pre-filtering techniques enhance the noise present on the correlator outputs and this fact is reflected on the tracking jitter. It is noted that in the ZFS case, agreement between the three mentioned curves is observed only for high  $C/N_0$  values. This is due to the noise amplification problem that makes the loop working in its non-linear region. The theoretical formulae for the tracking jitter are based on the linear

approximation of the loop and thus are the most diverging from the simulation results. ZFS performs poorly for medium to low  $C/N_0$  values and the tracking jitter is always higher than the one obtained for the other BOC tracking techniques. The code tracing jitter due to MMSES is lower as compared to ZFS. This is an indication of the ability of MMSES to mitigate the noise impact. MMSES performs poorly for low  $C/N_0$  values but the tracking jitter is always lower than ZFS.

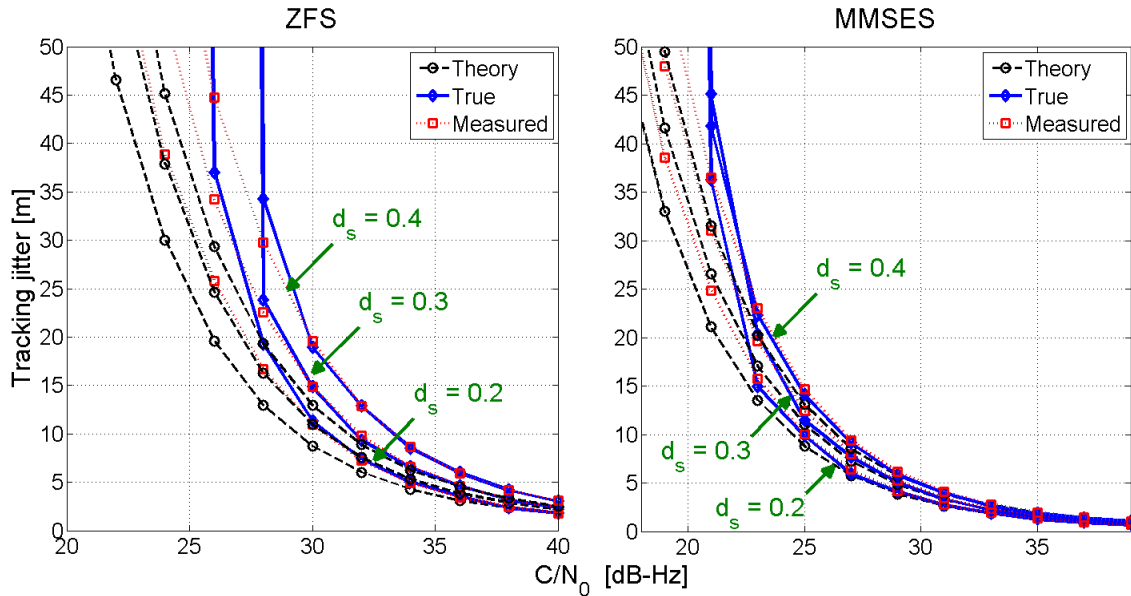


**Figure 3-10 Code tracking jitter of ZFS and MMSES as a function of the  $C/N_0$  and for non-coherent discriminator with different  $d_s$**

The three BOC tracking algorithms are further compared in Figure 3-11 and Figure 3-12, where quasi-coherent and coherent discriminators are used. In all considered cases, the DE outperforms the other techniques in terms of the generated tracking jitter. It shall be noted that MMSES performs similarly to the DE for coherent discriminators while ZFS and BJ lose lock earlier. Although the MMSES is outperformed by the DE in terms of tracking jitter, its adoption is justified by its increased flexibility in for example mitigating multipath as shown in Section 3.7.5.

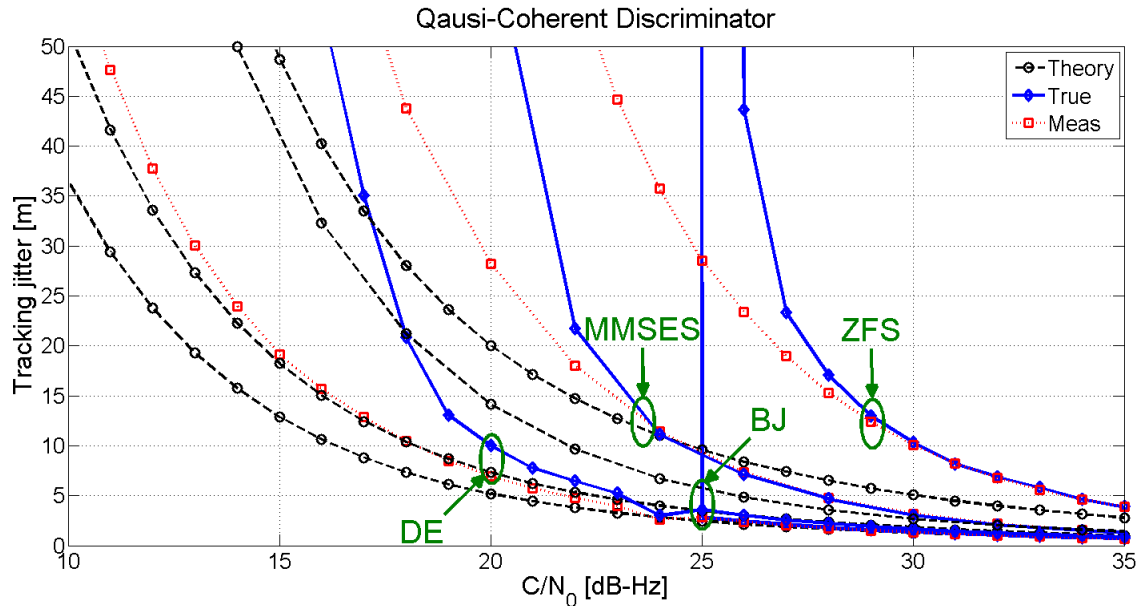


**Figure 3-11 Comparison of code tracking jitter a function of input  $C/N_0$  for quasi-coherent discriminator, 4 ms coherent integration time and 0.5 Hz DLL**

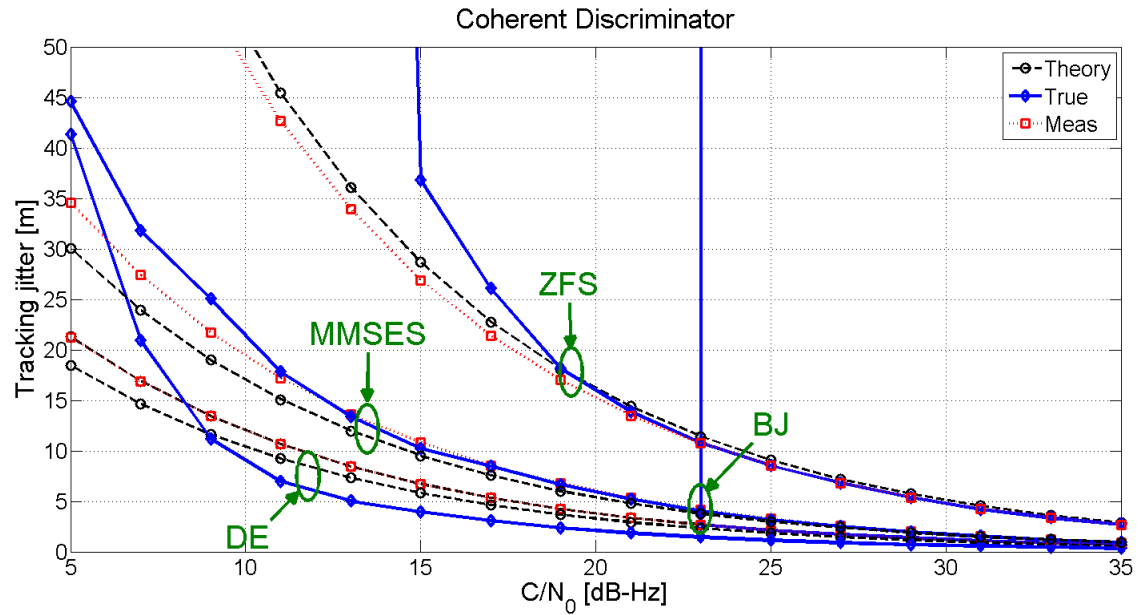


**Figure 3-12 Comparison of code tracking jitter as a function of  $C/N_0$  for coherent discriminator, 4 ms coherent integration time and 0.5 Hz DLL**

### 3.7.2 Tracking threshold

The tracking threshold is the minimum C/N<sub>0</sub> value at which a tracking loop is able to maintain a stable lock (Kaplan & Hegarty 2006). The tracking thresholds of the DE, BJ and the proposed ZFS and MMSES tracking techniques are compared in Figure 3-13 for different types of loop discriminators.

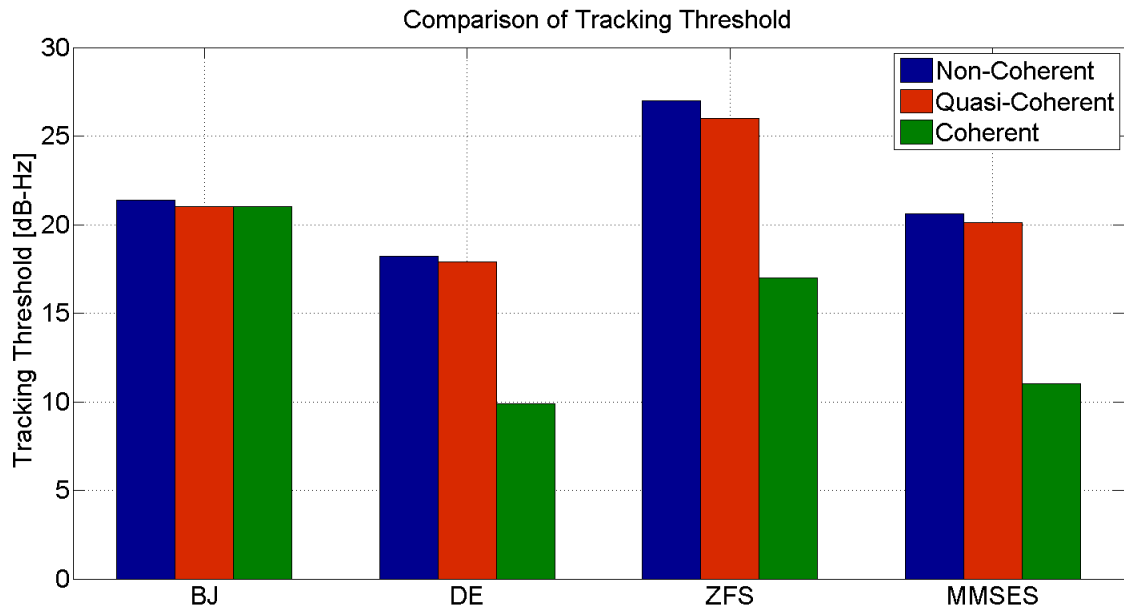


**Figure 3-13 Comparison of tracking thresholds for different BOC tracking techniques, 4 ms coherent integration time and 0.5 Hz DLL bandwidth**

As expected, improvements on all the three techniques (DE, ZFS and MMSES) are observed when moving from a non-coherent to a coherent discriminator. It is noted that the tracking threshold for the BJ seems to be unaffected by the type of discriminator. This can be an indication that, in the BJ case, loss of lock is determined by the control logic for detecting secondary peak lock. The same decision logic has been implemented for the three discriminators and this could be the cause of a tracking threshold insensitive to the type of discriminator. To determine the true threshold for the BJ technique, the decision

logic for detecting the secondary peak can be modified according to the discriminator type as

$$\begin{aligned} \text{NC: } & |VE/VL| > |P| \\ \text{QC: } & \Re\{(VE/VL)P^*\} > |P|^2 \\ \text{C: } & \Re\{VE/VL\} > \Re\{P\} \end{aligned} \quad (3.16)$$

where the notation VE/VL is used to indicate “either VE or VL”. In this way the decision logic is modified according to the same criterion adopted for the discriminator design. Figure 3-14 shows the tracking threshold results after applying the correct decision logic given in (3.16) for BJ tracking technique.

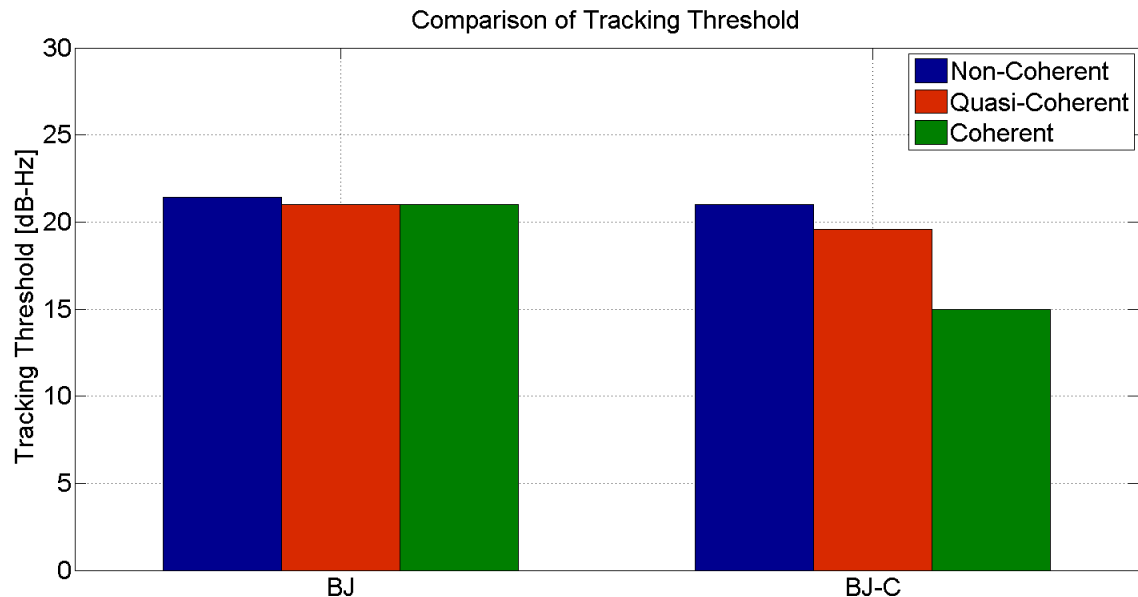


**Figure 3-14 Comparison of tracking thresholds for BJ tracking technique after applying modified decision logic**

It is noted that the BJ has higher tracking thresholds than the other two algorithms. This is due to the way the threshold on the delay error variance is defined. More specifically, this threshold depends on the linearity region of the code discriminator. This linearity region is larger in ZFS/MMSES since the correlation function assumes a triangular shape

with base width larger than the BJ case. MMSES efficiently mitigates the noise amplification problem, leading to a tracking threshold comparable to that achieved by the DE.

The results reported in Figure 3-13 have been empirically validated using live GIOVE data presented in Section 3.8.2, further supporting the validity of the developed model. It can be observed that the DE technique outperforms the other two techniques in all the discriminator types. The tracking threshold on the ZFS and MMSES technique has a similar trend in the tracking threshold values when moving from non-coherent to coherent discriminators. This loss in the tracking threshold is the effect of filtering the code to obtain an unambiguous correlation function. It is noted that the curves shown above were obtained assuming ideal phase synchronization. In a real receiver, loss of lock will be determined by the PLL in which case the  $C/N_0$  limits achieved by the tracking techniques will not be attained in practice.

### **3.7.3 MTL**

The MTL for different tracking techniques have been evaluated using the methodologies described in Section 2.6.3. Figure 3-15 shows the S-curve derived for the non-coherent discriminators for all the three tracking techniques. The stable points are extracted from the S-curve and fed to the MTL computation algorithm described in Figure 2-16. When the delay estimate jumps from one stable point to another, a new instance of the time to lose lock is measured and averaged over several simulation runs to obtain the MTL (Golshan 2005). It can be observed from the S-curves that DE and MMSES have only one stable point in the tracking region of  $\pm 1$  chip while BJ has

multiple stable points. This indicates that the signal obtained after applying MMSES has an unambiguous ACF. Figure 3-16 shows the MTLL for all the tracking techniques as a function of different  $C/N_0$  values.

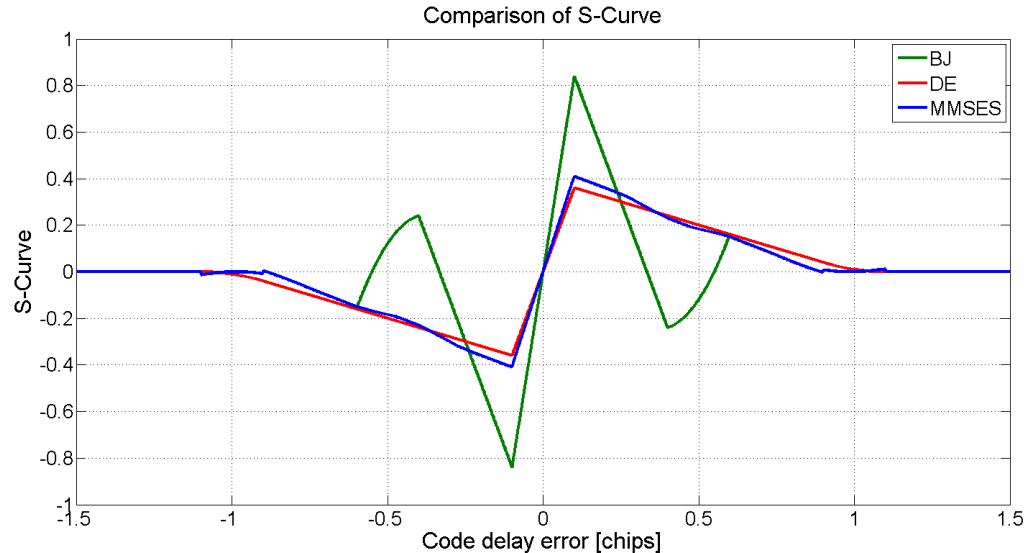


**Figure 3-15 S-curve plots for DE, BJ and MMSES used for determining the stable points for the MTLL computation**

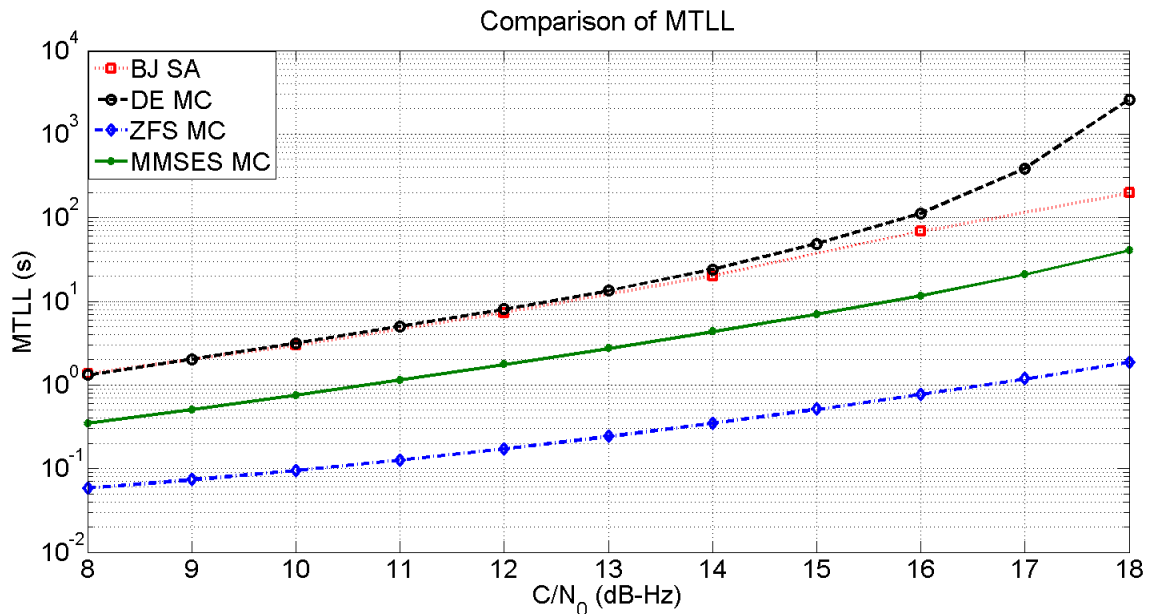


**Figure 3-16 Comparison of MTLL for DE, BJ, ZFS and MMSES techniques; 0.2 chips early-minus-late spacing, 0.5 Hz DLL bandwidth and 4 ms integration time**

The MTLI of the ZFS is relatively poor as compared to that of the other techniques. This is expected from the tracking jitter results. It can be observed that the MTLI of MMSES is better than the MTLI of ZFS with performance close to the DE and BJ techniques.

### 3.7.4 Convergence analysis

The tracking error convergence analysis provides the steady state behavior of the different tracking techniques given an initial delay error. It provides a measure of the ability of a tracking technique to reach primary peak lock.

Figure 3-17 provides the code tracking error for the MMSES technique over duration of 4 s for a non-coherent code discriminator. The simulated signal was characterized by a C/N<sub>0</sub> of 25 dB-Hz.

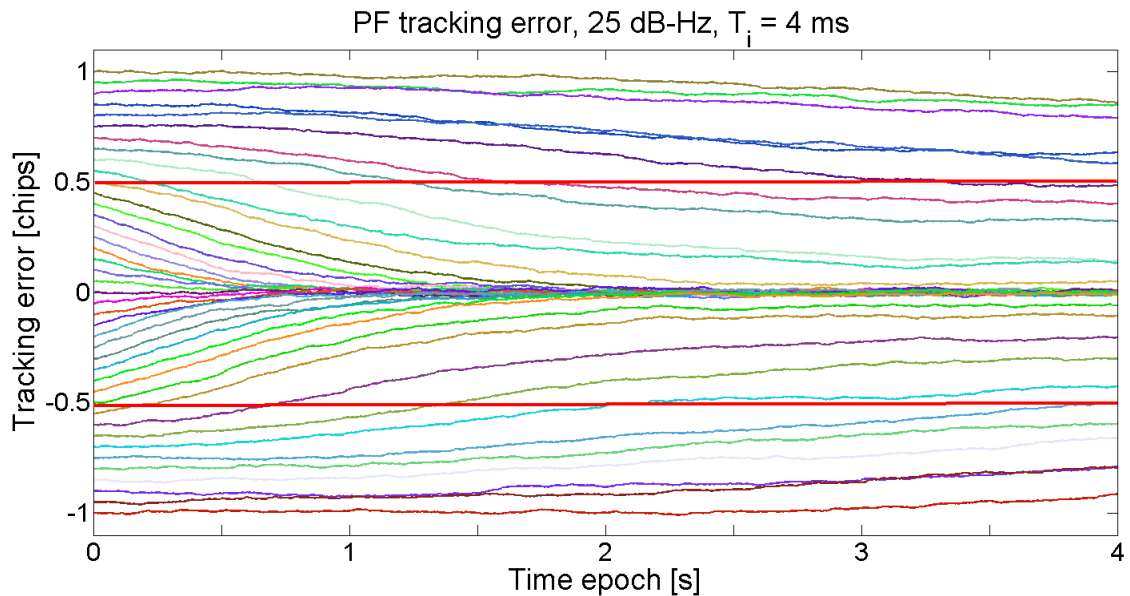


**Figure 3-17 Code delay error convergence for the MMSES technique for different initial acquisition errors (represented by different colored lines)**

In Figure 3-17, the initial values of the code tracking errors for different curves represent the initial error from the acquisition block. It can be observed that there is no

discontinuity in the trajectory of the tracking error. This indicates that neither the loop is losing lock nor is it tracking a secondary peak. Also symmetry in the tracking errors can be observed for symmetric acquisition errors around zero. Hence the analysis is carried out for positive acquisition code delay errors only.

Figure 3-18 provides the code tracking error for the three tracking techniques BJ, DE and MMSES. The curves in Figure 3-18a show the average tracking errors for different simulations runs. In Figure 3-18a, an initial acquisition error of 0.5 chips is considered to evaluate the tracking error convergence. When the DLL is initialized on a secondary peak, both MMSES and DE converge to a zero delay error whereas BJ is characterized by a steady state error of about -0.15 chips. This phenomenon is better investigated in Figure 3-18b and Figure 3-18c where different error trajectories are shown for MMSES and BJ. These trajectories show the evolution of the delay error as a function of time for different simulation runs.

In the MMSES case, all the trajectories reach a zero steady state error whereas the BJ code error is characterized by two different behaviors. In some cases, the BJ decision logic correctly detects the false peak lock and the code delay error is corrected accordingly. In other cases, however, tracking is too noisy and the algorithm is unable to recover the false peak lock. The curves in Figure 3-18a summarize the average behavior of the three algorithms considered, determining the average tracking error defined in (2.14). Only MMSES and DE are able to provide a completely unambiguous BOC tracking. While all the three techniques behave similarly for high  $C/N_0$  ratios, BJ has a higher probability to lose lock and track secondary peaks for low  $C/N_0$  values.

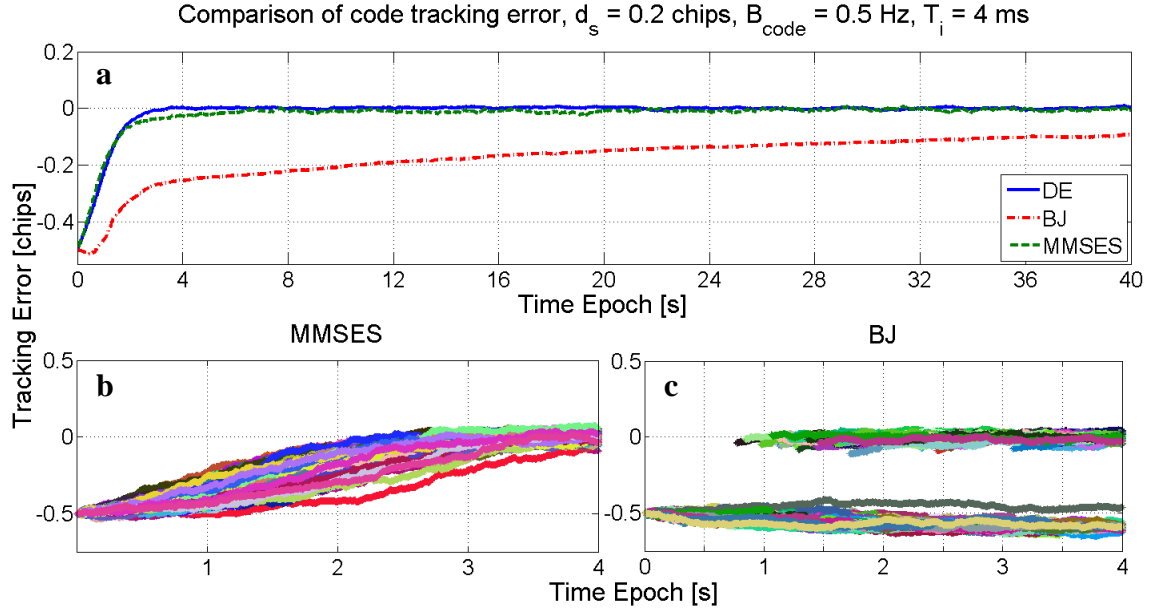


**Figure 3-18 Code delay error for DE, BJ and MMSES tracking techniques for an input signal characterized by a  $C/N_0$  of 25 dB-Hz**

### 3.7.5 Multipath error envelope

One of the advantages of using MMSES and ZFS is the flexibility to generate signals with varying ACF base-width as shown in Figure 3-19. It can be noted that the desired autocorrelation is obtained by changing the duration of the desired sequence,  $s_D(t)$ , and correspondingly modifying the locally generated signal.

The multipath error envelope for the standard BPSK, DE and MMSES tracking techniques using the ACFs obtained above are shown in Figure 3-20. The case of MDR equal to 0.5 is considered with 0.5 chip early-minus-late spacing. The results shown in Figure 3-20 are obtained assuming an infinite front-end bandwidth. From Figure 3-20, it can be observed that in the MMSES case, when the desired sub-carrier width,  $T_d$ , is equal to the chip duration,  $T_c$ , the resulting multipath error envelope is similar to that of a standard BPSK tracking technique.

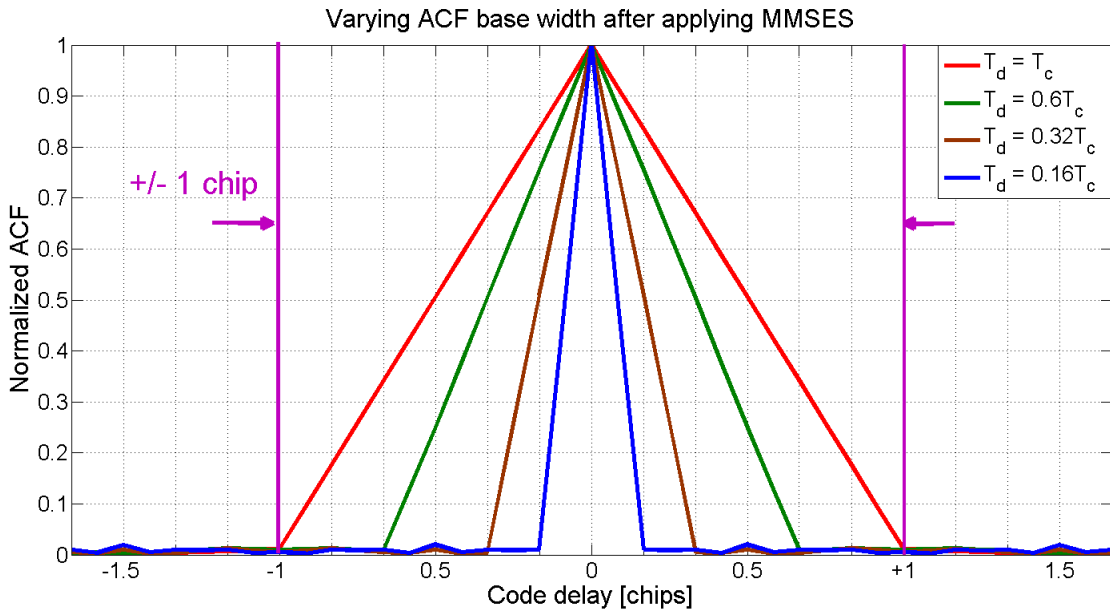


**Figure 3-19 ACF with varying base widths after applying MMSES on BOCs (1, 1) modulated signal**

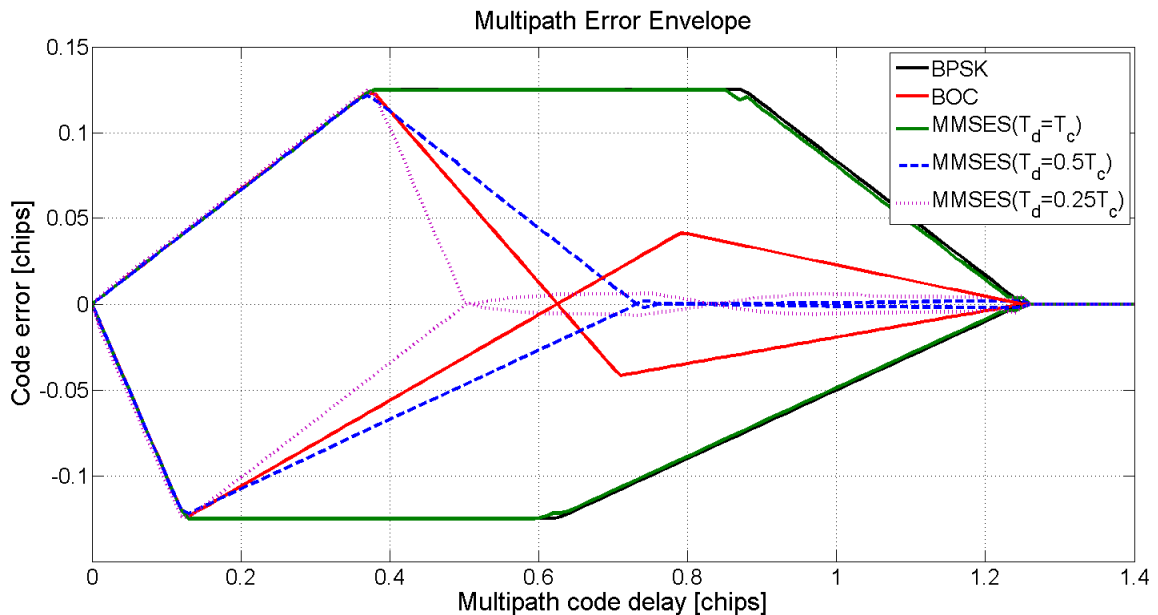


**Figure 3-20 Multipath error envelopes for DE and MMSES techniques, Coherent discriminator with 0.5 chips early-minus-late spacing.**

Considering the flexibility of MMSES, when  $T_d = 0.5T_c$ , the error envelope is similar to the DE tracking technique. Further reducing the desired sub-carrier width,  $T_d = 0.25T_c$ , leads to improved performance that cannot be achieved by the DE. Also, the effect of secondary peaks observed in the DE envelope (the presence of a second lobe in the curve) is not present in the MMSES technique. The ability of ZFS and MMSES to reshape the BOC ACF can be observed in Figure 3-21 where live BOCs(1, 1) signals from the GIOVE-B satellite have been used.

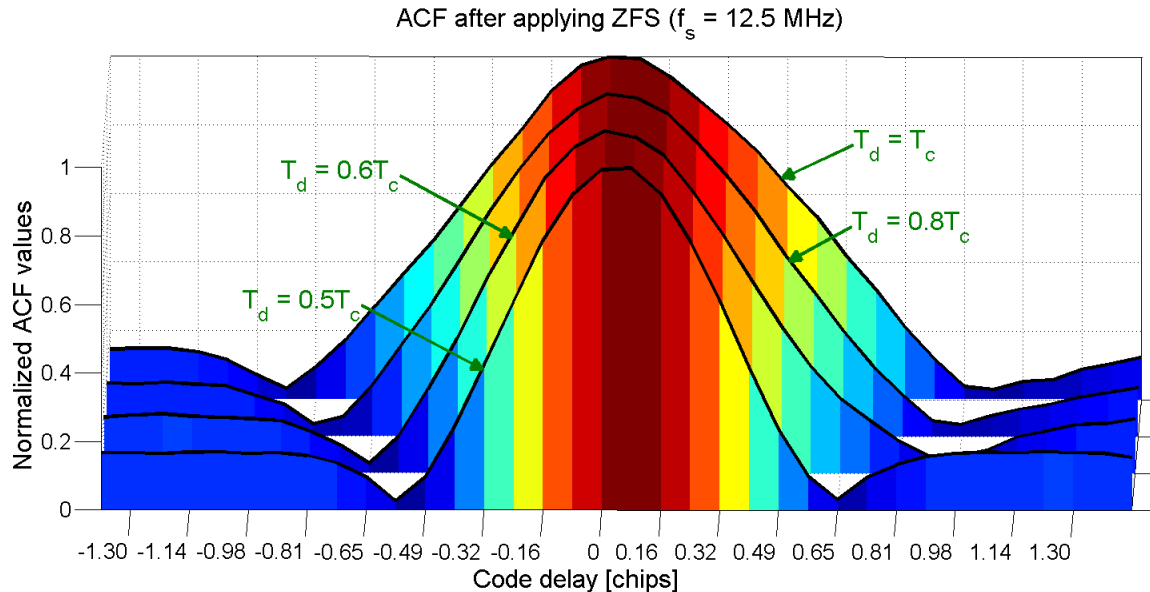


**Figure 3-21 BOCs(1, 1) ACF after applying ZFS as a function of the width of the desired sub-carrier.**

The desired autocorrelation functions for the ZFS are obtained by changing the spectrum of the desired signal. This was achieved by varying the number of samples considered in  $s_D[n]$ , the desired sequence. From Figure 3-21, it can be noted that the base width of the autocorrelation function is reduced by decreasing the number of samples in  $s_D[n]$  (inherently decreasing the duration,  $T_d$  of the desired sub-carrier,  $s_D(t)$ ). This shows the

advantage of using the ZFS and MMSES over the DE technique. In the DE technique, the ACF is fixed whereas in ZFS and MMSES, it can be selected according to different applications.

### 3.8 Experimental analysis

In order to further test the tracking techniques described above, live data from the experimental GIOVE-B satellite have been used. Data were progressively attenuated in order to simulate weak signal conditions. The experimental setup adopted for the experiment is shown in Figure 3-22. The GIOVE-B signal was split between two different front-ends. One of the signal streams was used as reference whereas the second was progressively attenuated. The signal was maintained at its nominal strength for 30 seconds, the attenuation was then progressively increased by 1 dB every 10 seconds. Data were collected using a National Instruments (NI) vector analyzer equipped with three PXI-5661 front-ends (NI 2006).

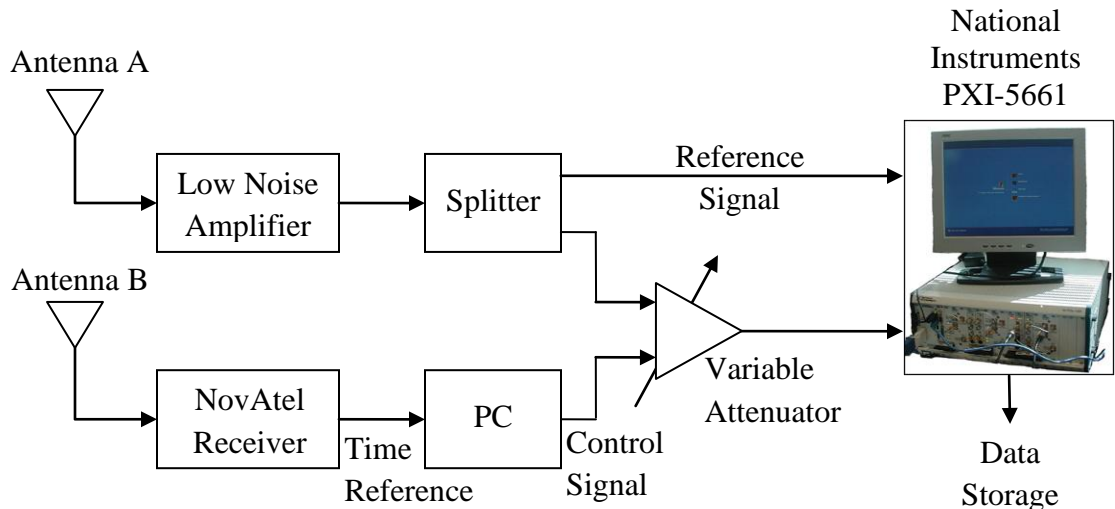


**Figure 3-22 Experimental setup: the signal was split between two front-ends. One data stream was used as a reference, whereas the other was progressively attenuated in order to simulate weak signal conditions**

All the considered techniques were able to successfully track the signal at the nominal signal strength (41 dB-Hz) as reported in Figure 3-23, where the scatter plot of the demodulated in-phase (I) and quadrature (Q) components is shown. It can be observed that BJ and DE behave similarly, showing a similar I and Q spread. As expected, the ZFS and MMSES technique produces noisier correlator outputs when the filtered prompt is used, Figure 3-23 (left). MMSES and ZFS produce correlator outputs comparable to the ones provided by BJ and DE when independent PLL tracking described in Section 3.5 is considered as shown in Figure 3-23 (right). For this reason, independent PLL tracking should be always preferred.

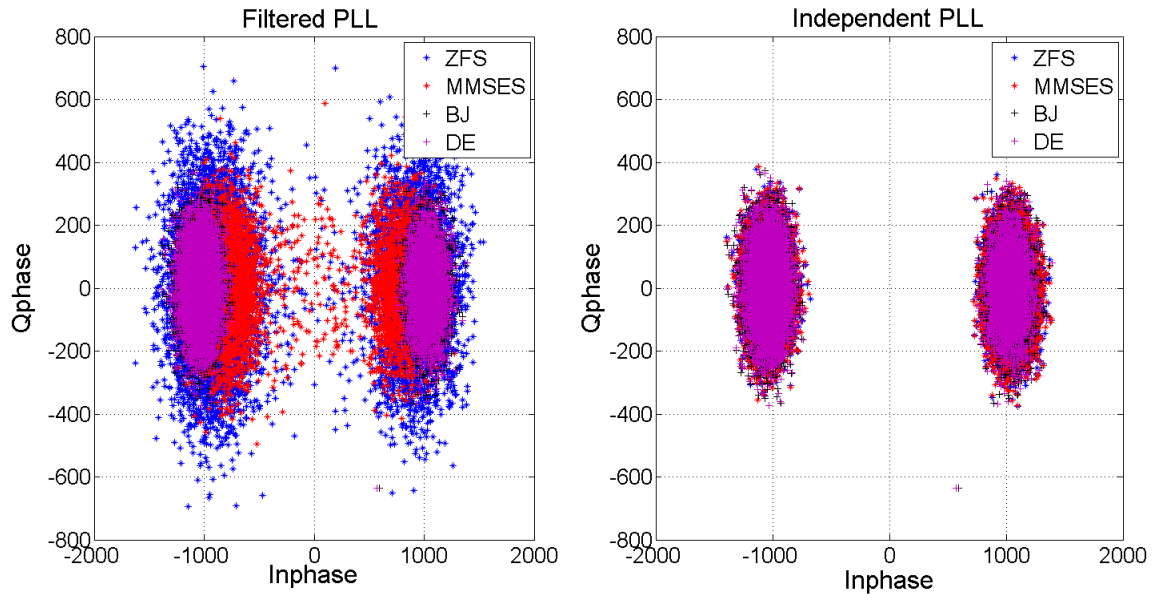


**Figure 3-23 Scatter plots for different BOC tracking techniques - PLL driven by filtered (left) and unfiltered (right) samples.**

### 3.8.1 ACF Analysis

The proposed ZFS method has been implemented by using  $s_D[n] = s_{BPSK}[n]$ .

Some sample results obtained using this technique are shown in Figure 3-24 that shows

the correlation functions obtained for the different pre-filtering techniques. More specifically, the ZFS approach is compared with the techniques proposed by (Yang et al. 2006). These correlations have been obtained from live data broadcast by the GIOVE-B satellite on L1 band (BOCs (1, 1) modulation). The correlation values were non-coherently averaged over 1 s total duration with a coherent integration time equal to 4 ms. The input signal was characterized by an estimated  $C/N_0$  equal to 41 dB-Hz. The proposed technique results in a BPSK-like correlation function while the previous approaches (Yang et al. 2006) are not effective in canceling the secondary peaks of the BOC modulation.

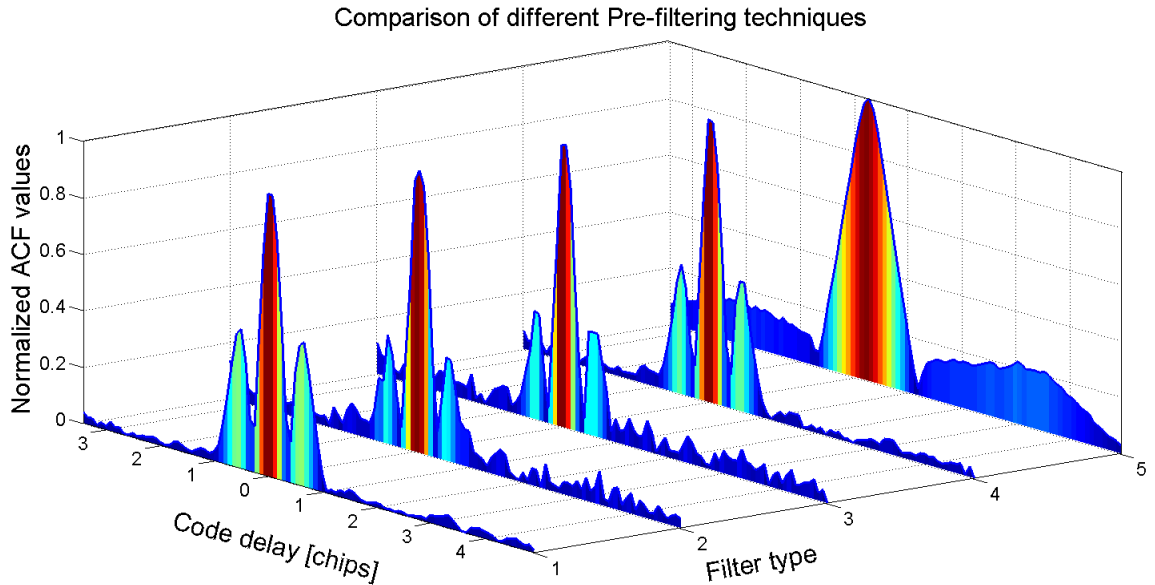


**Figure 3-24 ACF estimated from real data for different pre-filtering techniques: 1-Standard Correlation, 2-Phase-only matched, 3-Symmetric Phase-only, 4-Square-root normalized, 5-ZFS technique.**

To further analyze the effectiveness of the proposed ZFS and MMSES technique, BOCc(10, 5) and BOCc(15, 2.5) modulated signals from live Galileo satellites were collected. BOCc(10, 5) modulated E6 signal was collected using a wide band RF front-

end, with 40 MHz bandwidth, designed in the PLAN Group (Morrison 2010). The front-end is made of two independent channels that are capable of simultaneously collecting E1 and E6 signals. BOCc(15, 2.5) modulated E1 signals were obtained using the wide band signal recovery strategy developed in (Borio et al. 2009). The upper and lower bands of BOCc(15, 2.5) were independently collected using the two channels of the NI RF front-end and later reconstructed with a sampling frequency equal to 100 MHz. The ACF results, after applying MMSES on the BOCc(10, 5) and BOCc(15, 2.5) modulated signals, are shown in Figure 3-25.

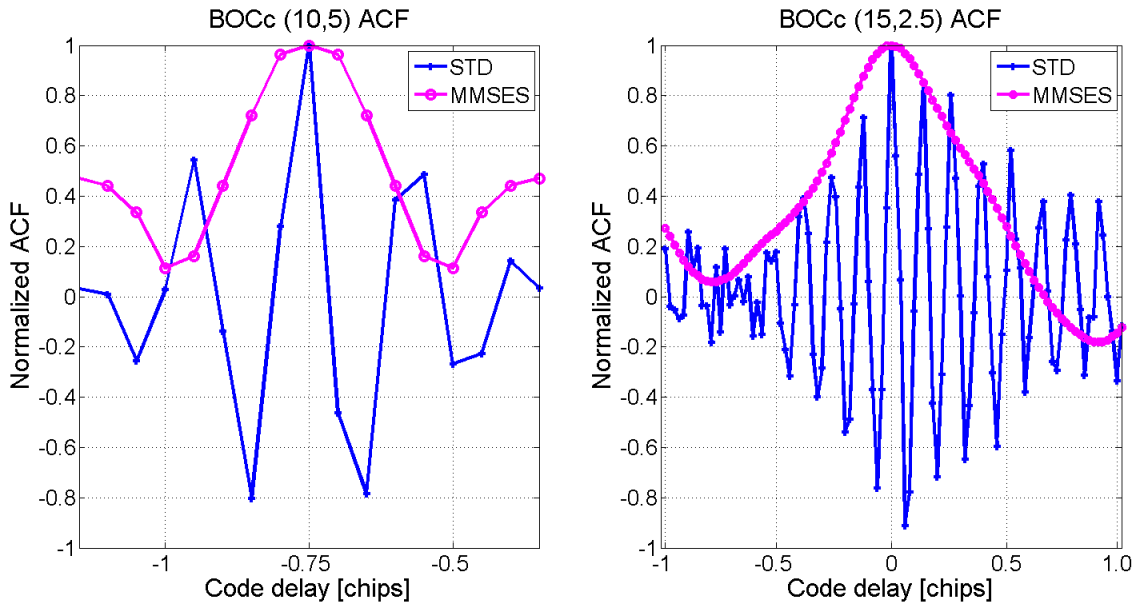


**Figure 3-25 Analysis of higher order BOC signals after applying the MMSES technique - Real data ACF analysis for BOCc(10, 5) (left) and BOCc(15, 2.5)(right) signals.**

It can be clearly observed that the multi-peaked ACF of both the higher order BOC signals have been modified to a BPSK-like ACF, showing the effectiveness of the proposed approach to mitigate side-peaks.

### 3.8.2 $C/N_0$ Estimation

The results obtained using the progressively attenuated signals are summarized in Figure 3-26 where the estimated  $C/N_0$  is shown for the different techniques. The  $C/N_0$  estimator is used here as code lock indicator providing an indication about the level of attenuation that the different tracking techniques can sustain. As explained by (Dierendonck 1996), the  $C/N_0$  estimator is often used as a delay lock indicator. More specifically, the  $C/N_0$  is estimated from the average post-correlation power, i.e. the  $C/N_0$  is directly proportional to the correlation value that is in turn an indicator of the delay error.

If a large delay error is committed then the correlation value and the  $C/N_0$  are significantly reduced. Loss of lock on the delay is thus reflected in randomly varying  $C/N_0$  estimates. In Figure 3-26, loss of lock is declared on the basis of the true signal parameters. More specifically, the experiment has been conducted using two front-ends collecting synchronized signals. From the first un-attenuated signal, reference parameters, i.e. Doppler frequency and code delay, were determined. When the parameters estimated from the second front-end started differing from the reference ones, loss of lock was declared. In the pre-filtering case, the additional unfiltered correlator used by the PLL was also employed to evaluate the  $C/N_0$  estimates. The code generation for the unfiltered correlator was driven by the delay estimated by the pre-filtering technique.

As expected the DE outperforms the other tracking techniques, being able to maintain lock for lower  $C/N_0$  values. Because of the noise amplification the ZFS loses lock for a  $C/N_0$  of approximately 25 dB-Hz. These findings are in agreement with the simulation results obtained in Figure 3-13, where a 25 dB-Hz tracking threshold was determined for the non-coherent discriminator case. But MMSES loses lock for a  $C/N_0$  of approximately

2 dB-Hz lower, as compared to BJ and a performance similar to the DE. Here, the loss of lock is determined at the time epoch when the estimated carrier Doppler starts deviating from the actual Doppler. These findings are in agreement with the simulation results obtained in Section 3.7.2. It shall be noted that MMSES achieves performance similar to the DE.

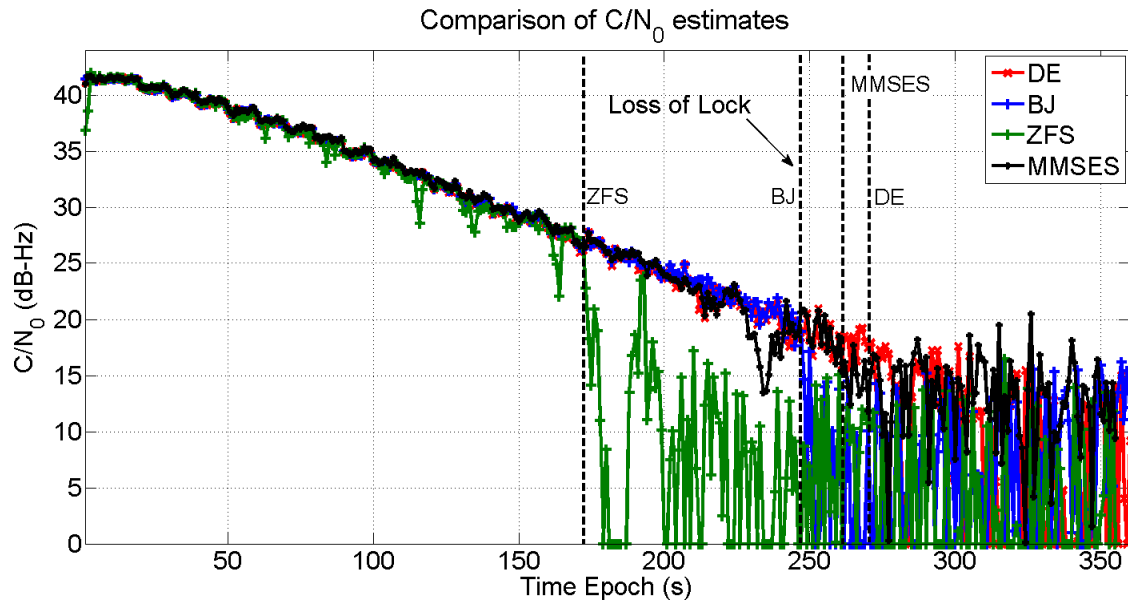


**Figure 3-26**  $C/N_0$  estimates obtained using live GIOVE data for the considered BOC tracking techniques - After 30 seconds, the signals were progressively attenuated

### 3.9 Summary

In this chapter, the MMSES and ZFS techniques were provided for unambiguous BOC signal tracking. Existing pre-filtering techniques were analyzed and used as comparison terms showing the advantages of the proposed techniques. BJ and DE were also considered for the analysis. A semi-analytic approach has been used for the analysis of the proposed techniques and different performance metrics including tracking jitter, tracking threshold, MTLL, tracking error convergence and multipath error envelopes were provided for all the considered BOC tracking techniques namely BJ, DE and the

proposed ZFS and MMSES. A good improvement was observed when moving from the ZFS to the MMSES technique in terms of tracking performance with MMSES providing unambiguous tracking and performance comparable to DE. A time domain implementation that uses only three correlators for the pre-filtering techniques was provided along with a modified tracking structure adopted for DLL and PLL. Real data results have been provided for attenuated data sets for BOCs (1, 1) signals collected from Galileo test satellites, GIOVE-A/B. It was observed that ZFS lose lock at  $C/N_0$  around 25 dB-Hz while MMSES loses lock for a  $C/N_0$  of approximately 2 dB-Hz lower as compared to BJ and performance similar to DE. It was also shown that the MMSES tracking technique is flexible in terms of varying the ACF base-width, thus enhancing the multipath mitigation capabilities of the algorithm.

## Chapter Four: Spatial Processing of GNSS Signals

The continuously evolving GNSS technology is moving towards the development of receivers equipped with several antennas. The use of antenna arrays (Balanis & Ioannides 2007) provides enhanced performance such as improved signal quality and detectability, anti-jamming, interference rejection and improved multipath mitigation compared to single antenna techniques. Antenna arrays are capable of steering their beam pattern towards desired directions to maximize the signal-to-interference-plus-noise ratio and cancel co-channel interference from particular directions.

In this chapter, the basic principles of antenna array processing are first briefly summarized. The antenna array model considered in this research work for processing GNSS signals is then provided. An antenna array calibration algorithm based on the availability of GNSS signals is finally proposed with the main objective to obtain a calibration technique not requiring any additional equipment than the already available GNSS signals. A least squares solution based on a projection methodology is proposed to determine the calibration parameters. Calibration results obtained using simulations and real GPS data are also provided.

### 4.1 Introduction to antennas

An antenna is a communication device that is capable of radiating (receiving) electromagnetic energy to (from) space (Balanis 1992). The response of an antenna to an incoming signal can be defined by its radiation properties. The antenna radiation pattern (or beam pattern) defines the variation of the power radiated/received by an antenna as a function of the direction away from the antenna. Radiation patterns are usually expressed

in polar or rectilinear form that defines the power variation of an impinging signal observed in the far field (Van Trees 2002) as a function of the signal angle of arrival. These patterns are observed at a particular frequency and a defined polarization and are useful for visualizing the directions in which the antenna radiates/receives energy. Radiation patterns vary with frequency although, in general, their shape changes smoothly as a function of this parameter. A sample radiation pattern in the elevation domain along with its main parameters is provided in Figure 4-1.

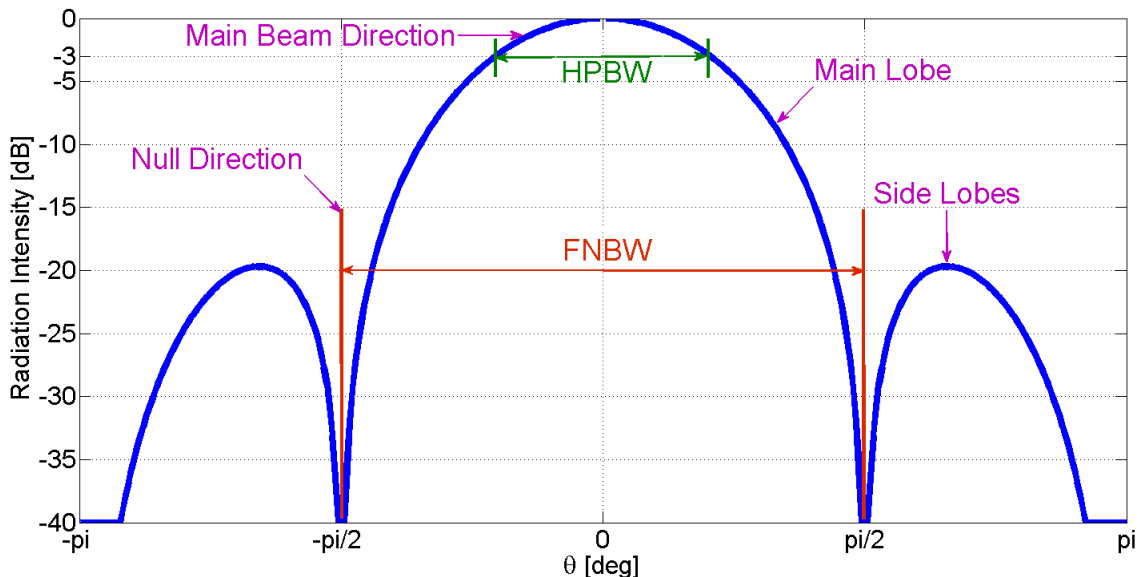


**Figure 4-1 Antenna radiation pattern with its main parameters**

A radiation pattern is usually characterized by:

- The **main lobe** is the region around the direction of maximum radiation. In Figure 4-1, the major lobe is centered on a 0 degrees elevation.
- **Sidelobes** are the undesired smaller beams away from the main beam and which can never be completely eliminated. In Figure 4-1, sidelobes are present at 40 and 135 degrees.

- The **Half Power Beam Width** (HPBW) is the angular separation in which the magnitude of the radiation pattern decrease by 50% (or equivalently 3 dB) compared to the maximum value of the major lobe.
- The **First Null Beam Width** (FNBW) is the angular separation between the first nulls around the major lobe.
- **Sidelobe level** (SL) is another important parameter that defines the maximum value of the sidelobes.

In Figure 4-1, HPBW is equal to 80 degrees, FNBW is equal to 180 degrees and the SL is -20 dB with respect to the maximum of main lobe.

Based on the radiation pattern, antennas are classified as isotropic, omnidirectional and directional antennas (Johnson 1993). Examples of these classes of antennas are shown in Figure 4-2. Isotropic antennas provide the same radiation pattern (gain) in all directions whereas omnidirectional antennas provide the same gain only in a single plane. Directional antennas are configurable to provide high antenna gains in a particular direction of interest. Depending on the application, antennas can be selected accordingly from the three classes mentioned above. Omnidirectional antennas above the horizon are generally used in GNSS applications. GNSS antennas receive incoming signals uniformly by providing a constant radiation pattern along the azimuth plane while the radiated/received signal experiences a decrease in the signal power for decreasing elevation angles above the antenna plane. The major lobe of GNSS antennas is centered at 90 degrees above the antenna plane and SL are designed to be typically below -25 dB.

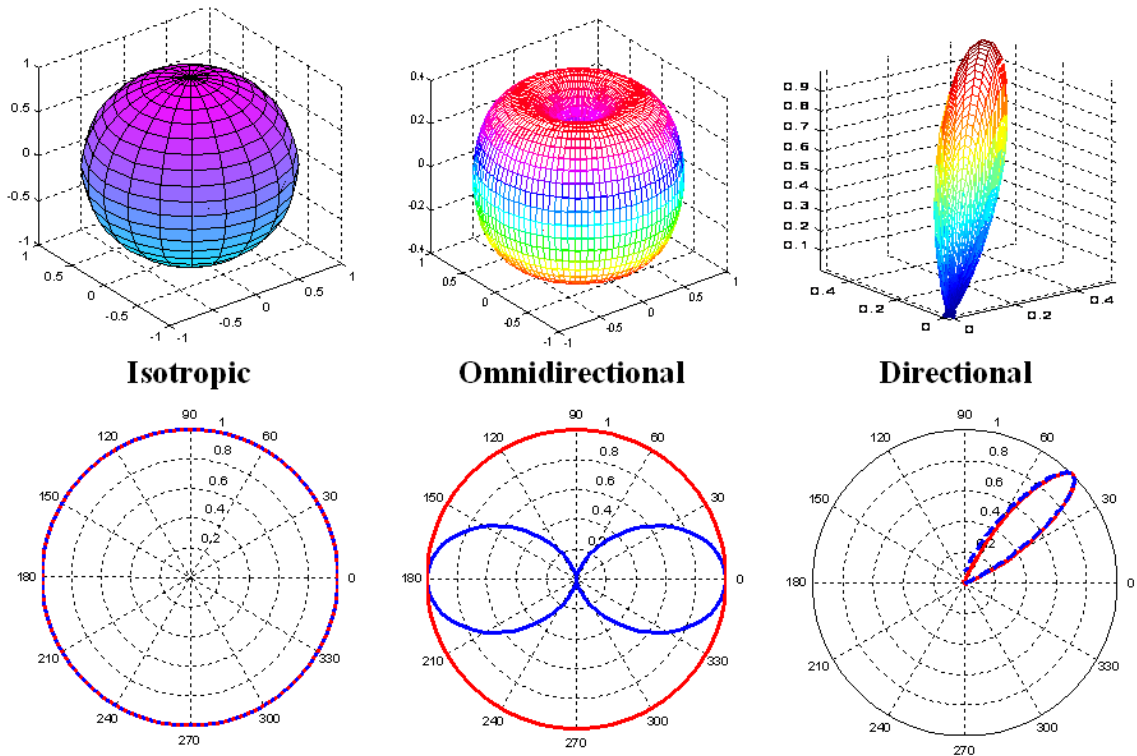


**Figure 4-2 Antenna Classification based on the radiation pattern**

In applications like long distance communications, for interference/multipath mitigation and to improve the signal-to-noise ratio of the incoming signal, antennas with distinctive characteristics are required. For example, the presence of an interfering signal can be mitigated by adopting a radiation pattern with nulls in the direction of the disturbing signal.

In general, it is difficult for a single-element antenna to achieve narrow beams, low SL, high main lobe gains, and selective null placement. In addition to this, the real time modification of the antenna radiation characteristics cannot be achieved with a single antenna unless using mechanical steering. An alternative method that can be effectively adopted without altering the physical or electrical configurations of a single antenna is the usage of collection of antennas in different geometrical configurations. Such an

assembly of multiple antennas is termed as antenna arrays. The following section provides a detailed description of antenna arrays and their advantages over a single antenna.

## 4.2 Antenna Arrays

An antenna array is a combination of antennas arranged in one, two or three dimensional planes that can provide the following advantages (Alexiou & Haardt 2004) over a single antenna:

- increase the overall gain of the system;
- determine the direction of arrival of desired and interfering signals;
- cancel interference from particular directions by combining antenna array data;
- steer array in a particular direction by electronically varying the antenna array radiation pattern (or simply array pattern);
- maximize signal-to-interference-plus-noise ratio by performing advanced signal processing on the antenna array data.

Antenna arrays can be structured as linear, planar or circular arrays as shown in Figure 4-3 to provide the above advantages. Linear arrays form a one dimensional pattern providing a single degree of freedom thus their pattern can be modified in either the elevation or azimuth plane. On the other hand, planar arrays provide array pattern control in both elevation and azimuth plane. Planar arrays are a combination of linear arrays in a two dimensional plane. Circular arrays are a special form of planar array.

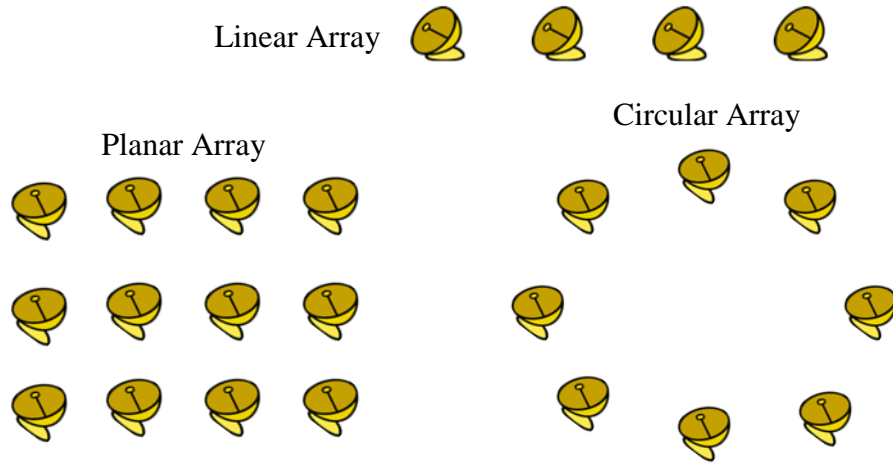


**Figure 4-3 Different types of antenna array structures**

An array of  $M$  elements on a plane with a single signal source (GNSS satellite) is shown in Figure 4-4. Under ideal conditions, the relative phase between signals received from different antennas can be expressed as a function of the vector wave number (Van Trees 2002) as

$$\mathbf{k} = \frac{2\pi}{\lambda} [\cos \varepsilon \sin \alpha \quad \cos \varepsilon \cos \alpha \quad \sin \varepsilon]^T \quad (4.1)$$

where  $\varepsilon$  and  $\alpha$  are the elevation and azimuth angle of the signal source defined with respect to a triplet of orthogonal axes as shown in Figure 4-4.  $\lambda$  denotes the wave-length of the signal carrier. In the case of narrow band signals, the time delay corresponding to the time of arrival of the incoming signals at each antenna element can be approximated by a phase delay (Van Trees 2002). Thus each antenna element receives a copy of the useful signal with a different phase defined by the complex steering vector that can be expressed as

$$\begin{aligned} \mathbf{s}(\varepsilon, \alpha) &= [s_0 \quad s_1 \quad s_2 \quad \cdots \quad s_{M-1}]^T \\ &= [1 \quad \exp\{-j\mathbf{k}^T \mathbf{r}_1\} \quad \exp\{-j\mathbf{k}^T \mathbf{r}_2\} \quad \cdots \quad \exp\{-j\mathbf{k}^T \mathbf{r}_{M-1}\}]^T \end{aligned} \quad (4.2)$$

where  $\mathbf{r}_m = [e_m \ n_m \ u_m]$  is the vector defining the position of the  $m^{\text{th}}$  antenna. The first element of the antenna is placed in the centre of the coordinate system justifying the fact that  $s_0 = 1$ .

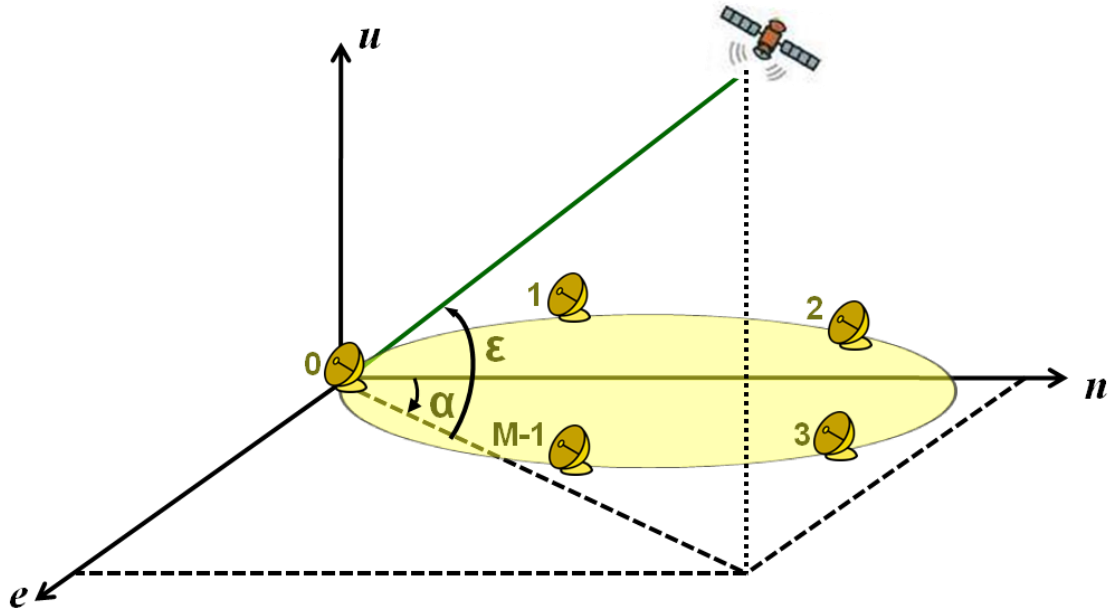


**Figure 4-4 Schematic representation of an antenna array receiving a single signal from a source at a specific elevation and azimuth**

The process of combining signals from antenna array is called beamforming (Van Veen & Buckley 1988). The antenna array output is obtained by combining data from individual antennas according to Figure 4-5 and is expressed as

$$z(t) = \sum_{m=0}^{M-1} w_m^H (s_m y(t)) = \mathbf{w}^H \bar{\mathbf{y}}(t) \quad (4.3)$$

where  $\mathbf{w} = [w_0 \ w_1 \ \dots \ w_{M-1}]^T$  represents the complex weight vector, and  $\bar{\mathbf{y}}(t) = [s_0 \ s_1 \ \dots \ s_{M-1}]^T y(t)$  with Eq. (2.1) defining  $y(t)$ .

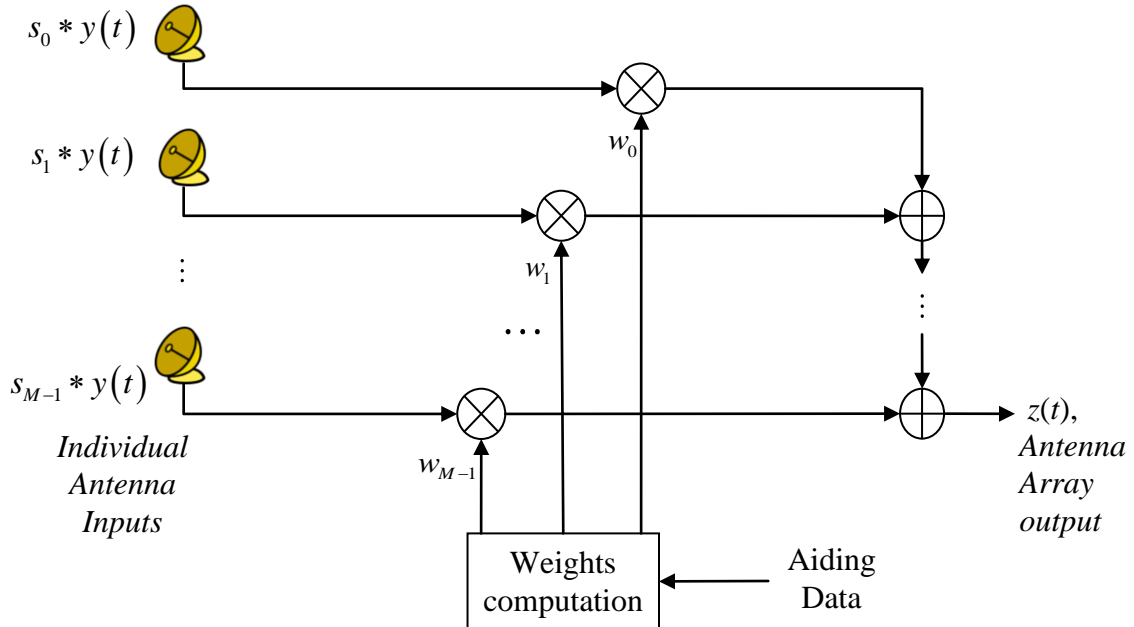


**Figure 4-5 Block diagram representing the basic operations performed during beamforming**

The weights are computed in a way to add the individual antenna signals constructively and can be updated to maximize the antenna gain along the direction of arrival of the desired signal. Several techniques like the conventional beamformer, Minimum Variance Distortionless Response (MVDR) beamformer and MMSE beamformer (Balanis & Ioannides 2007) can be used to compute the weights to form the array beam in a desired direction along with minimizing the impact of noise and interference. In a conventional beamformer, the weights are set to be equal to the steering vector of the desired signal as

$$\mathbf{w}^H = \frac{1}{M} \mathbf{s}^H. \quad (4.4)$$

Thus, the antenna array output,  $z(t)$ , obtained using the above weight vector can provide maximum gain in the desired direction. There are several independent factors that can be

controlled in (4.2) and (4.3) to modify the array pattern effectively that include (Balanis & Ioannides 2007):

- i. Type of array structure (linear or planar)
- ii. Number of antennas ( $m = 1, 2, \dots, M$ )
- iii. Antenna array spacing (relative positioning between  $\mathbf{r}_m$ )
- iv. Individual antenna radiation pattern (isotropic or directional)

Sample radiation patterns for a linear array are shown in Figure 4-6 and Figure 4-7. The array patterns are obtained by varying the number of antennas and antenna array spacing in (4.2). It can be observed in Figure 4-6 that the SL of the system array pattern can be improved by increasing the number of antennas. Also the level of SL can be modified by the adaptation of different array structures (Van Trees 2002).

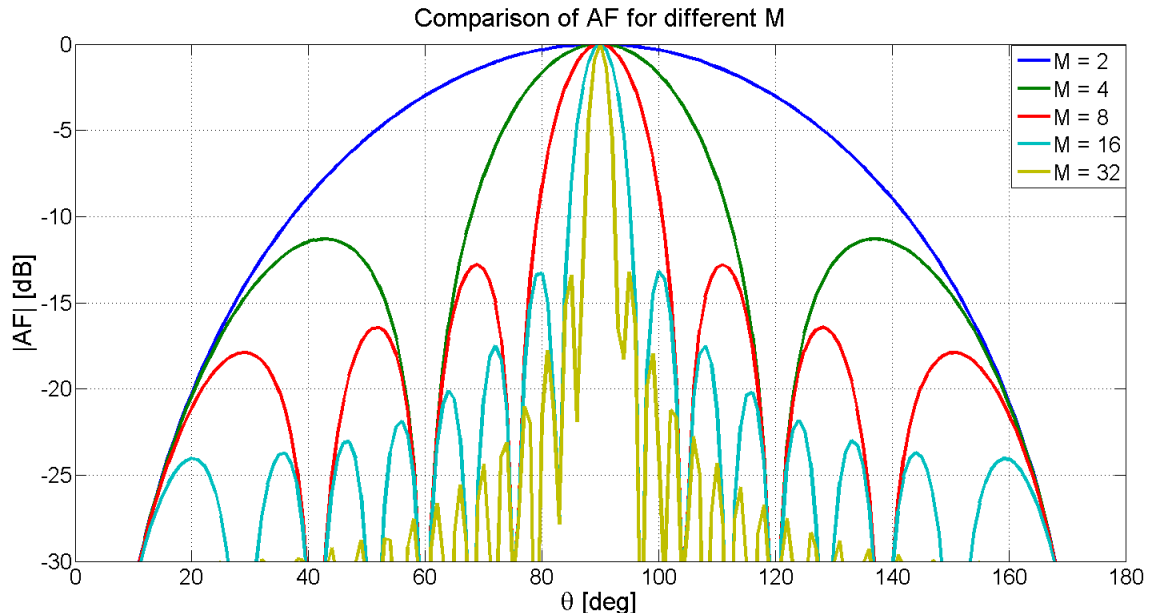


**Figure 4-6 Comparison of array patterns for different numbers of antenna array elements,  $M$**

In Figure 4-7, it is shown that the HPBW of the array pattern can be varied by adjusting the inter-antenna spacing. It should also be noted that when the spacing is increased to more than  $\lambda$ , grating lobes (undesired lobes which have performance similar to major lobes) start to show up in the array pattern.

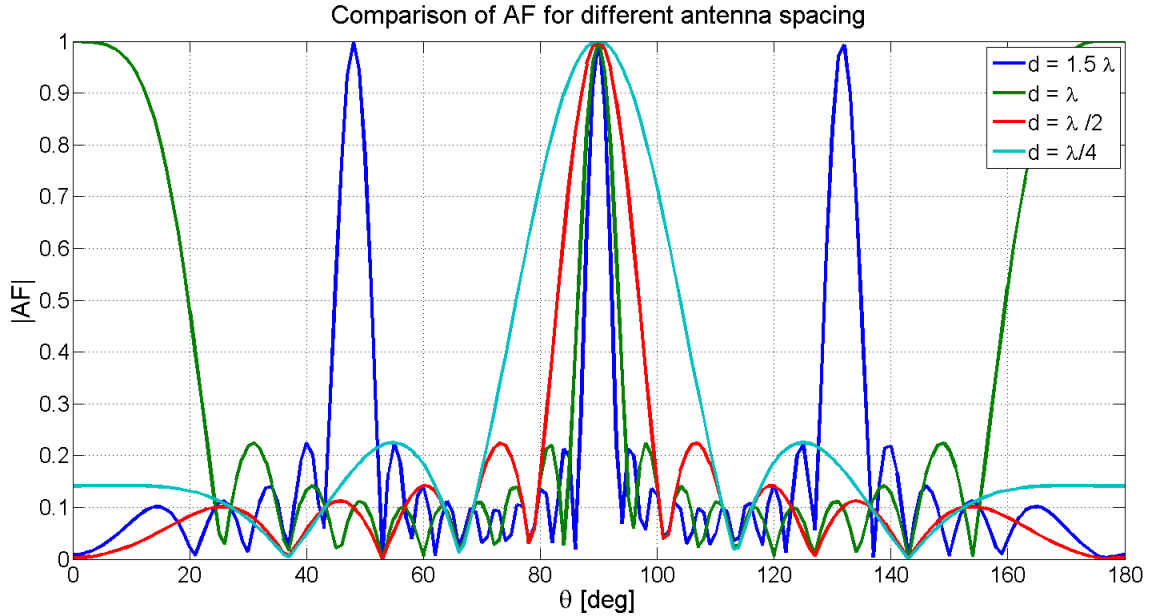


**Figure 4-7 Comparison of array pattern for varying antenna spacing for a linear array structure,  $M = 8$**

The advantage of using an antenna array for interference mitigation over single antenna (Novatel 2006) is further shown in Figure 4-8. It should be noted that using an antenna array, nulls can be placed in the direction of the interference signal while maintaining maximum gain along the direction of the desired signal which is not possible with a single antenna. As it is evident from Figure 4-8, the antenna array is able to provide a null at the direction of arrival of the interfering signal (i.e., 30 degrees) while maintaining a maximum beam along the signal direction (i.e., 60 degrees) which is otherwise not possible with a single antenna.

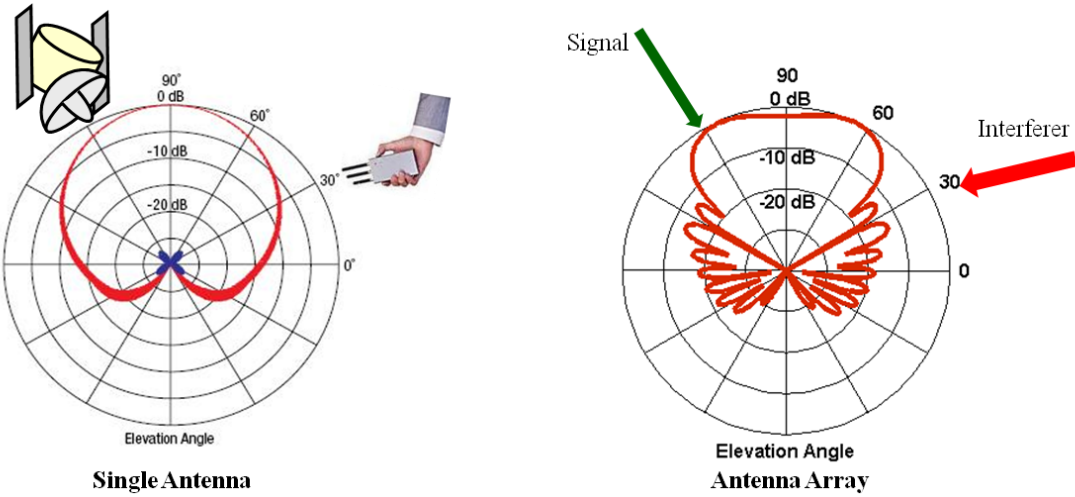


**Figure 4-8 Beam pattern of an antenna array as compared to a single antenna in the presence of interference**

### 4.3 Calibration

One of the main challenges faced while using antenna arrays is their calibration (Gupta et al. 2003). Signal received from different sensors in the array suffer from additional phase offsets due to antenna mutual coupling, antenna gain/phase mismatches, antenna phase center variations and distortions introduced by different RF front-ends along with phase offsets due to the antenna array structure. In addition, environmental parameters such as temperature and multipath influence the overall gain and phase response of an antenna array. A perfect knowledge of the array manifold for these kinds of variations is not available in practice. Calibration compensates the combined effect of different delays which would degrade the performance of array processing algorithms if not addressed. The main factors affecting the phase of the incoming signals from antenna arrays can be modeled as

- Geometric delay: the delay introduced due to the presence of different array configurations

- Electronic delay: the delay caused by the presence of different hardware paths from the antenna outputs to the receiver inputs
- Antenna delay: the delay caused mainly by non-identical array designs, mutual coupling, antenna orientation and phase center variations.

For effective array processing, calibration becomes one of the vital processes to be performed before combining the signals from the array. Thus, the design of robust calibration algorithms that corrects for the phase mismatch among array data becomes a necessity. Several approaches (Gupta et al. 2003, Ng & See 1996) have been proposed based on the maximum likelihood and least squares approaches. These techniques assume that there is a one-to-one correspondence between the covariance matrix of the received signals and the array vector, which seldom holds true when GNSS signals are involved.

Antenna array calibration algorithms require reference signal sources in known locations. GNSS receivers are capable of providing the satellite locations within metre level accuracy, which is sufficiently good for calibration algorithms. Calibration of antenna arrays using GNSS signals have been proposed in (Backen et al. 2008, Church & Gupta 2009). A seven element custom array was calibrated for antenna gain/phase mismatches using a least squares formulation on the GPS correlator outputs in (Backen et al. 2008). In (Church & Gupta 2009), a procedure to obtain the array manifolds of GNSS antennas using space-time adaptive processing (STAP) was proposed. In this procedure, the STAP weights were updated in order to maximize the cross-correlator outputs; in a second step, the array manifold was determined in the least squares sense. In these approaches, it is however assumed that the properties of a reference antenna, in terms of gain pattern and

phase response, are perfectly known. All the processing is performed relative to this reference antenna that is strictly required for the algorithm implementation.

In the following, a new calibration methodology is proposed.

#### 4.4 Signal Model

The complex baseband signal (2.1) received by a single antenna GNSS receiver can be extended to include the presence of  $L$  different satellites as

$$\begin{aligned} y(t) &= \sum_{i=0}^{L-1} x_i(t) + \eta(t) \\ &= \sum_{i=0}^{L-1} A_i d_i(t - \tau_{0,i}) c_i(t - \tau_{0,i}) \exp\{j\theta_{0,i}\} + \eta(t) \end{aligned} \quad (4.5)$$

which is the sum of  $L$  useful components and a noise term,  $\eta(t)$ .  $A_i$  is the amplitude of the  $i^{\text{th}}$  signal component and  $\theta_{0,i} = 2\pi f_{0,i} t + \phi_{0,i}$  is the phase of the useful signal with  $f_{0,i}$  and  $\phi_{0,i}$  its Doppler frequency and carrier phase.  $c_i(\cdot)$  is the ranging code used to spread the navigation data,  $d_i(\cdot)$ , and  $\tau_{0,i}$  denotes the code delay introduced by the communication channel on the  $i^{\text{th}}$  useful component.

In Eq. (4.5),  $L$  GNSS signals are received from  $L$  different directions and a different steering vector is associated to each useful component. Thus, under ideal conditions, the vector of the signals received by the antenna array can be modeled as

$$\mathbf{y}(t) = \begin{bmatrix} y_0(t) \\ y_1(t) \\ \vdots \\ y_{M-1}(t) \end{bmatrix} = \sum_{i=0}^{L-1} \mathbf{s}_i x_i(t) + \mathbf{n}(t) \quad (4.6)$$

where  $\mathbf{s}_i = [s_{i,0} \ s_{i,1} \ \cdots s_{i,M-1}]^T$  denotes the steering vector associated to the  $i^{th}$  GNSS signal defined by (4.2).  $\mathbf{n}(t) = [\eta_0(t) \ \eta_1(t) \ \cdots \ \eta_{M-1}(t)]^T$  is the vector of the noise components observed by the  $M$  antennas. Each antenna receives an independent noise component and an index has been added to indicate signals from a specific antenna. Equation (4.6) represents the model of the signals received by an ideal antenna array where the different location of the sensor only introduces a fixed additional phase captured by the steering vector. This model is simplistic and neglects the effects of mutual coupling (Gupta & Ksieinski 1983) and gain/phase mismatches among different array elements.

#### 4.4.1 Mutual Coupling

Mutual coupling in antenna arrays exist due to the fact that antennas reradiate part of their received signals that are recovered by the other elements of the array (Balanis 2005). Gain and phase mismatches make different antennas observe different signal amplitudes and phases as shown in Figure 4-9 for a two-element antenna array. The coefficients,  $\nu_{00}$  and  $\nu_{11}$ , captures individual antenna gain and phase responses while  $\nu_{01}$  and  $\nu_{10}$  capture the effect of mutual coupling due to the presence of another antenna in the vicinity. Thus, the signal received by the  $m^{th}$  antenna can be modeled as a linear combination of the signals received by all the array elements as

$$\tilde{y}_m(t) = \sum_{k=0}^{M-1} \sum_{i=0}^{L-1} \nu_{m,k} s_{i,k} x_i(t) + \eta_m(t) \quad (4.7)$$

where the symbol  $\sim$  is used to denote quantities affected by the presence of mutual coupling and amplitude/phase mismatches.

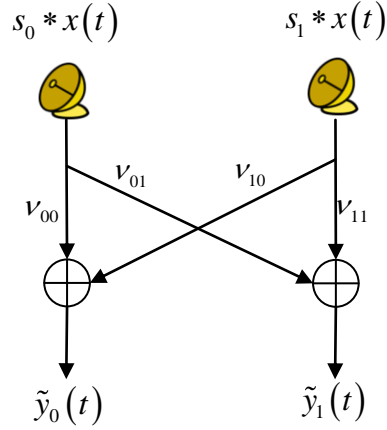


**Figure 4-9 Two-element antenna array along with mutual coupling coefficients**

$\nu_{m,k}$  is a complex weight determining the impact of the signal from the  $k^{\text{th}}$  antenna on the  $m^{\text{th}}$  array element. In the following, it is assumed that  $\nu_{m,k}$  does not depend on the direction of arrival of the  $i^{\text{th}}$  signal. Equation (4.7) can be written in matrix form as

$$\tilde{\mathbf{y}}(t) = \begin{bmatrix} \tilde{y}_0(t) \\ \tilde{y}_1(t) \\ \vdots \\ \tilde{y}_{M-1}(t) \end{bmatrix} = \sum_{i=0}^{L-1} \mathbf{C} \mathbf{s}_i x_i(t) + \mathbf{n}(t) \quad (4.8)$$

where

$$\mathbf{C} = \begin{bmatrix} \nu_{0,0} & \nu_{0,1} & \cdots & \nu_{0,M-1} \\ \nu_{1,0} & \nu_{1,1} & \cdots & \nu_{1,M-1} \\ \cdots & \cdots & \cdots & \cdots \\ \nu_{M-1,0} & \nu_{M-1,1} & \cdots & \nu_{M-1,M-1} \end{bmatrix} \quad (4.9)$$

is a  $M \times M$  matrix containing the coefficients  $\nu_{m,k}$ .  $\mathbf{C}$  is assumed full-rank and calibration is defined as the process of estimating the coefficients of  $\mathbf{C}$  and inverting the effects of mutual coupling and amplitude/phase mismatches.

#### 4.4.2 The correlation process

As described in Section 2.2.3, the incoming signal needs to be correlated with a local version of the code and carrier to extract signal parameters. Thus Eq. (2.3) can be modified to include the effects of multiple antennas by replacing  $y(t)$  with  $\tilde{y}(t)$  to provide correlator outputs as

$$\begin{aligned}
q_{m,h}(\tau, \theta) &= \frac{1}{T} \int_0^T \tilde{y}_m(t) c_h(t - \tau_h) \exp\{-j\theta_h\} dt \\
&= \frac{1}{T} \int_0^T \sum_{k=0}^{M-1} \sum_{i=0}^{L-1} v_{m,k} s_{i,k} x_i(t) c_h(t - \tau_h) \exp\{-j\theta_h\} dt + \bar{\eta}_{m,h} \\
&= \sum_{k=0}^{M-1} \sum_{i=0}^{L-1} v_{m,k} s_{i,k} \frac{1}{T} \int_0^T x_i(t) c_h(t - \tau_h) \exp\{-j\theta_h\} dt + \bar{\eta}_{m,h} \\
&\approx \sum_{k=0}^{M-1} v_{m,k} s_{h,k} \frac{1}{T} \int_0^T x_h(t) c_h(t - \tau_h) \exp\{-j\theta_h\} dt + \bar{\eta}_{m,h} \\
&= \sum_{k=0}^{M-1} v_{m,k} s_{h,k} A_h R(\Delta\tau_h) \frac{\sin(\pi\Delta f_{D,h} T)}{\pi\Delta f_{D,h} T} \exp\{j\pi\Delta f_{D,h} T + j\Delta\phi_h\} + \bar{\eta}_{m,h}
\end{aligned} \tag{4.10}$$

where

- $q_{m,h}$  represents the correlator output obtained considering the signal from the  $m^{th}$  antenna and with the  $h^{th}$  local code;
- $\tau_h$  is the delay estimate provided by the receiver for the  $h^{th}$  signal component and  $\Delta\tau_h = \tau_{0,h} - \tau_h$  is the code delay error;
- $\Delta f_{D,h} = f_{0,h} - f_{D,h}$  is the Doppler frequency error with  $f_{D,h}$  being the Doppler frequency estimated by the receiver for the  $h^{th}$  signal component and;
- $\Delta\phi_h = \phi_{0,h} - \phi_h$  is the residual phase error with  $\phi_h$  the estimated carrier phase;
- $R(\cdot)$  denotes the correlation function of the ranging code;
- $\bar{\eta}_{m,h}$  is a Gaussian random variable obtained by processing  $\eta_m(t)$  using the  $h^{th}$  local signal. In the following,  $\bar{\eta}_{m,h}$ , for  $m=0, \dots, M-1$  and  $h=0, \dots, L-1$  are assumed to be zero mean independent identically distributed (i.i.d) complex random variables. The real and imaginary parts of  $\bar{\eta}_{m,h}$  are independent with variance  $\sigma_\eta^2$ .

In Eq. (4.10), the impact of the navigation message, that is assumed constant during the integration interval,  $T$ , is neglected. In the following, it is assumed that  $\Delta\tau_h \approx 0$  and  $\Delta f_{D,h} \approx 0$ , implying

$$q_{m,h} = \sum_{k=0}^{M-1} v_{m,k} s_{h,k} A_h \exp\{j\Delta\phi_h\} + \bar{\eta}_{m,h}. \quad (4.11)$$

The delay, frequency and phase estimates can be obtained using the processing described in Section 2.2 and the tracking structure is shown in Figure 4-10. The signal from the first antenna is used as a reference and tracked using standard PLL and DLL (Kaplan & Hegarty 2006).

Signals from the other array elements are tracked using the Doppler frequency, carrier phase and code delay provided by the DLL and PLL locked on the reference signal. This type of processing preserves the amplitude/phase relationship among signals from different antennas. Using the same local signal replica for the de-spreading of the signals from different antennas, it is possible to write the vector of the correlator outputs for the  $h^{\text{th}}$  spreading code as

$$\mathbf{q}_h = \begin{bmatrix} q_{0,h} \\ q_{1,h} \\ \vdots \\ q_{M-1,h} \end{bmatrix} = \mathbf{Cs}_h A_h \exp\{j\Delta\phi_h\} + \begin{bmatrix} \bar{\eta}_{0,h} \\ \bar{\eta}_{1,h} \\ \vdots \\ \bar{\eta}_{M-1,h} \end{bmatrix}. \quad (4.12)$$

Eq. (4.12) is the basic equation that will be used in the next section to derive a calibration methodology based on the availability of GNSS signals. It is noted that GNSS signals continuously broadcast the position of their sources. Thus, the steering vector  $\mathbf{s}_h$  is

assumed known. In the next section, a calibration methodology based on the availability of GNSS signals is proposed.

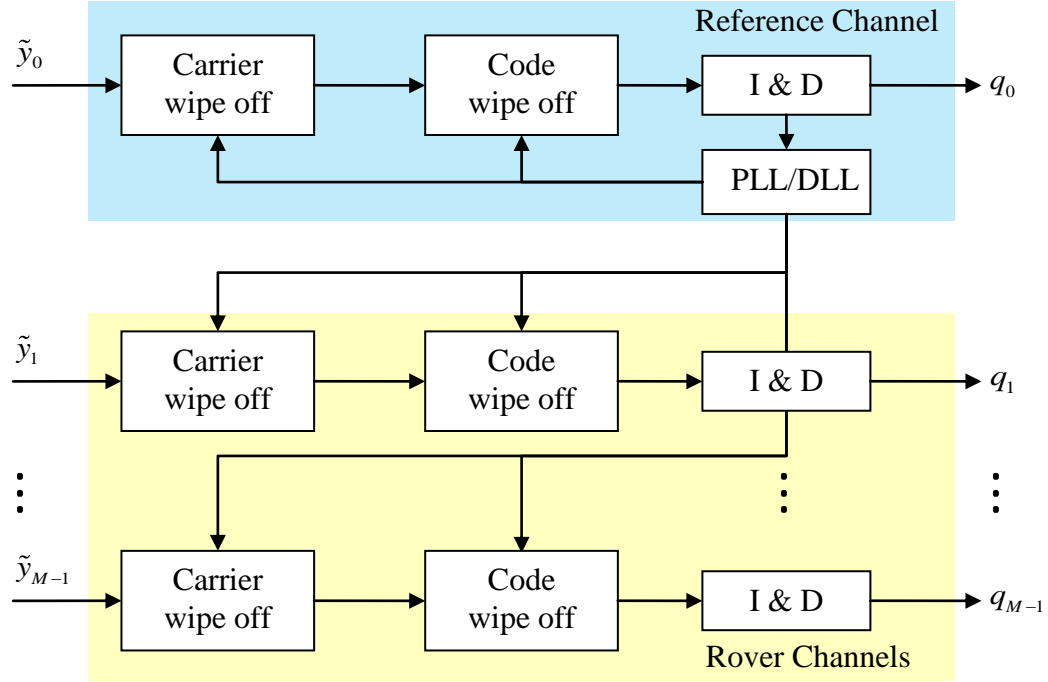


**Figure 4-10 GNSS signal tracking structure for multi-antenna processing. The same local carrier and code are used for processing different signals, preserving the amplitude/phase relationship among different signal components**

#### 4.5 Projection based calibration methodology

The main idea behind the proposed technique is to obtain a linear relationship between the calibration parameters and the observed correlator outputs. This relationship has to be independent from relative satellite signal amplitude and phase differences. This is achieved by projecting the correlator outputs from the array data onto the steering vector null space. In a second stage, the calibration parameters are estimated by solving the obtained linear system in the least squares sense.

The proposed calibration technique exploits the orthogonal projection principle already adopted by algorithms such as the multiple signal classification (MUSIC) (Schmidt 1986)

and subspace optimization technique (Park & Bang 2003). The MUSIC algorithm estimates the direction of arrival of incident signals by exploiting the orthogonality between signal and noise subspaces. The noise subspace is identified using the Eigen-decomposition of the received signal covariance matrix which is used in the determination of desired signals. In the subspace optimization technique (Park & Bang 2003), a calibration algorithm based on the minimization of a cost function is proposed. The cost function is determined on the basis of minimizing the product of the actual array response and its orthogonal counterpart. Orthogonal vectors are obtained as the eigenvectors of the noise correlation matrix. Thus, in these techniques, the covariance matrix of the incoming signals is assumed to be known. This stringent requirement is no longer necessary in the proposed technique that allows array calibration without any additional knowledge on the received GNSS signals. This methodology essentially differs from the above mentioned techniques since it does not rely on the knowledge of the signal/noise correlation matrices. The following section details the proposed methodology allowing one to estimate the calibration parameters independently from the relative satellite signal amplitude and phase values.

In (4.12), the effect of relative amplitude and phase variations among different satellite signals,  $A_h$  and  $\Delta\phi_h$ , are unknown and can be considered as nuisance parameters during the estimation of the coefficients of the calibration matrix.

For each satellite steering vector,  $\mathbf{s}_h$ , it is possible to determine  $M - 1$  orthogonal vectors using for example the Gram–Schmidt process (Trefethen & Bau 1997). These vectors, denoted by  $\mathbf{h}_{k,h}$ , satisfy the following property:

$$\mathbf{h}_{k,h}^H \mathbf{s}_h = 0, \quad \text{for } k = 0, \dots, M-2 \quad (4.13)$$

where  $(\cdot)^H$  denotes Hermitian transpose. Property (4.13) is preserved through multiplication by a complex constant:

$$\mathbf{h}_{k,h}^H \mathbf{s}_h A_h \exp\{j\Delta\phi_h\} = 0, \quad \text{for } k = 0, \dots, M-2. \quad (4.14)$$

Collecting the  $M-1$  orthogonal vectors in a single matrix,  $\mathbf{H}_h$ , leads to the following condition:

$$\mathbf{H}_h^H \mathbf{s}_h A_h \exp\{j2\pi\Delta\phi_h\} = \mathbf{0} \quad (4.15)$$

where

$$\mathbf{H}_h = [\mathbf{h}_{0,h} \quad \mathbf{h}_{1,h} \quad \cdots \quad \mathbf{h}_{M-2,h}]. \quad (4.16)$$

The columns of the matrix  $\mathbf{H}_h$  define the null space of the steering vector  $\mathbf{s}_h$ . It is noted that the projection (4.16) is independent from the amplitude/phase of the complex correlators,  $A_h \exp\{j\Delta\phi_h\}$ , and thus can be used for obtaining linear equations for determining  $\mathbf{C}$ , the calibration matrix. More specifically, by neglecting the impact of noise, the following conditions can be imposed:

$$\mathbf{H}_h^H \mathbf{C}^{-1} \mathbf{q}_h = \mathbf{0} \quad \text{for } h = 0, 1, \dots, L-1. \quad (4.17)$$

The inverse of the calibration matrix,  $\mathbf{C}^{-1}$ , will be denoted as

$$\mathbf{C}^{-1} = \mathbf{A} = \begin{bmatrix} a_{0,0} & a_{0,1} & \cdots & a_{0,M-1} \\ a_{1,0} & a_{1,1} & \cdots & a_{1,M-1} \\ \cdots & \cdots & \cdots & \cdots \\ a_{M-1,0} & a_{M-1,1} & \cdots & a_{M-1,M-1} \end{bmatrix} \quad (4.18)$$

and condition (4.17) will be used to determine its coefficients,  $a_{i,j}$ .

As already pointed out, (4.17) is preserved through scaling. Thus,  $\mathbf{A}$  can be univocally determined only by imposing a normalization condition on its coefficients. The convention

$$a_{0,0} = 1 \quad (4.19)$$

is adopted here and used to transform (4.17) into linear equations. More specifically, a single condition from (4.17) can be written as

$$\begin{aligned} \mathbf{h}_{k,h}^H \mathbf{C}^{-1} \mathbf{q}_h &= \mathbf{h}_{k,h}^H \mathbf{A} \mathbf{q}_h \\ &= \sum_{i=0}^{M-1} \sum_{j=0}^{M-1} h_{k,h,i}^* a_{i,j} q_{j,h} = h_{k,h,0}^* q_{0,h} + \sum_{i \neq 0, j \neq 0} a_{i,j} h_{k,h,i}^* q_{j,h} \\ &= b_{k,h} + \sum_{i \neq 0, j \neq 0} a_{i,j} b_{k,h}^{i,j} = 0 \end{aligned} \quad (4.20)$$

where  $b_{k,h} = h_{k,h,0}^* q_{0,h}$  and  $b_{k,h}^{i,j} = h_{k,h,i}^* q_{j,h}$ .

Eq. (4.20) defines a linear equation in  $M^2 - 1$  unknowns. When  $L$  satellites are in view  $L(M-1)$  equations can be found and the matrix  $\mathbf{A}$  can be determined when  $L \geq M+1$ . If  $L > M+1$ , the system of equations defined by (4.20) can be solved in the least squares sense (Mikhail 1976). The calibration procedure based on the projection methodology described above is summarized in Algorithm 1. The matrix  $\mathbf{A}$  can be used to compensate the effects of mutual coupling and apply beamforming and angle-of-arrival estimation algorithms. Data obtained using simulations and live GPS signals have been used to validate the proposed calibration methodology. A standard beamforming (Van Veen & Buckley 1988) algorithm has been implemented to test the effectiveness of the proposed calibration technique.

<b>Data</b>	: The signal vector $\tilde{\mathbf{y}}(t)$
<b>Result</b>	: Estimate of the inverse of the calibration matrix, $\mathbf{A} = \mathbf{C}^{-1}$
<b>begin</b>	
1) Compute the correlator outputs, $\mathbf{q}_h$ using a common signal replica	
2) Determine the steering vectors, $\mathbf{s}_h$ from the navigation messages	
3) <b>for</b> each steering vector, $\mathbf{s}_h$ , $h = 0, 1, \dots, L-1$ <b>do</b>	
Use the Gram–Schmidt process to determine the orthogonal vectors, $\mathbf{h}_{k,h}$	
Use (4.20) to determine linear equations in the coefficients of $\mathbf{A}$	
<b>end</b>	
4) Solve the linear system and determine $\mathbf{A}$ .	
<b>end</b>	

### Algorithm 1 Procedure for the estimation of the inverse of the calibration matrix, A

#### 4.6 Results and analysis

In this section, the proposed projection methodology for antenna array calibration is analyzed for different array structures, number of antenna elements and satellite constellation.

##### 4.6.1 Monte Carlo Simulations

A Monte Carlo approach (Tranter et al. 2004) has been used for the analysis of the proposed methodology where model (4.12) was directly simulated for different satellites and antenna array configurations. A constellation of ten satellites with elevation angles ranging from 10 to 90 degrees was simulated and correlator outputs were generated in order to match input  $C/N_0$  values varying in the 30-50 dB-Hz range (Kunysz 2000). Calibration matrices with coefficients selected in a random way, using a complex Normal distribution, was used to simulate mutual coupling and amplitude/phase mismatches. The correlator outputs were then fed to the calibration algorithm for estimating the array

parameters. Finally, the estimated calibration matrix was compared against the one used for the simulation.

Sample results of this analysis are shown in the following. The performance of the calibration algorithm has been analyzed as a function of the integration time,  $T$ , required to obtain the correlator outputs for a five element linear array with inter-antenna spacing equal to  $\lambda/2$ . The mean square error (MSE) for different  $T$  using the projection based calibration methodology is shown in Figure 4-11. For the calibration methodology to be effective during array processing, the phase of the estimated calibrated signal should be accurate. Hence MSE in terms of phase error is analyzed in this research work. The MSE values are computed as

$$\text{MSE} = \frac{1}{K} \sum_{i=1}^K \|\angle \hat{C}_i - \angle C\|^2 \quad (4.21)$$

where  $\angle \hat{C}_i$  and  $\angle C$  are the phase values of the estimated and simulated calibration matrix, respectively, and  $K$  is the number of simulation runs.

From Figure 4-11, it can be observed that the proposed methodology is significantly sensitive to the input noise when  $T < 100\text{ms}$ . But the MSE of the estimated calibration parameters improves for longer coherent integration times. For further analysis,  $T = 1\text{s}$  is considered. It is noted that in real scenarios, the data bits can be wiped-off using bit estimation algorithms applied on the signals from the first antenna.

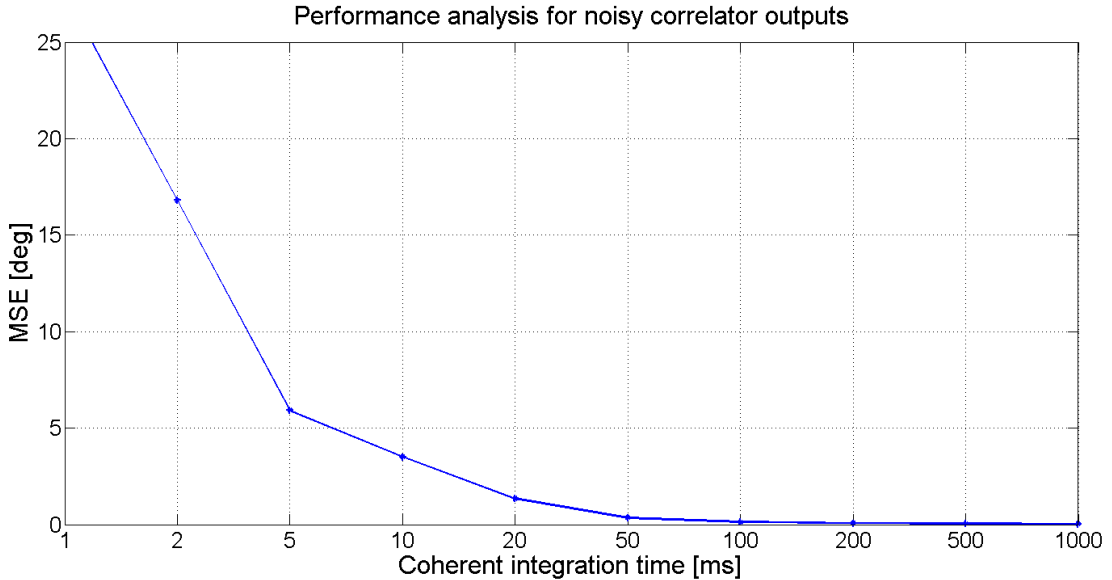


**Figure 4-11 Phase mean square error of the projection based calibration algorithm as a function of the coherent integration time,  $T$**

Calibration results in terms of the post-beamforming array pattern are shown in Figure 4-12 for 8-element linear, planar and circular arrays. The plots show the array pattern obtained using conventional beamformer (Balanis & Ioannides 2007) before and after calibration. The polar plot depicts the response of the array as a function of both azimuth and elevation angle. The intensity of the plot shows the array gain (expressed in dB) obtained by normalizing the array pattern with respect to its maximum. It can be observed that before calibration the array pattern is displaced from the true direction of arrival but after calibration the array pattern shows a maximum along the true direction of arrival indicated with an ‘x’ mark on the polar plots.

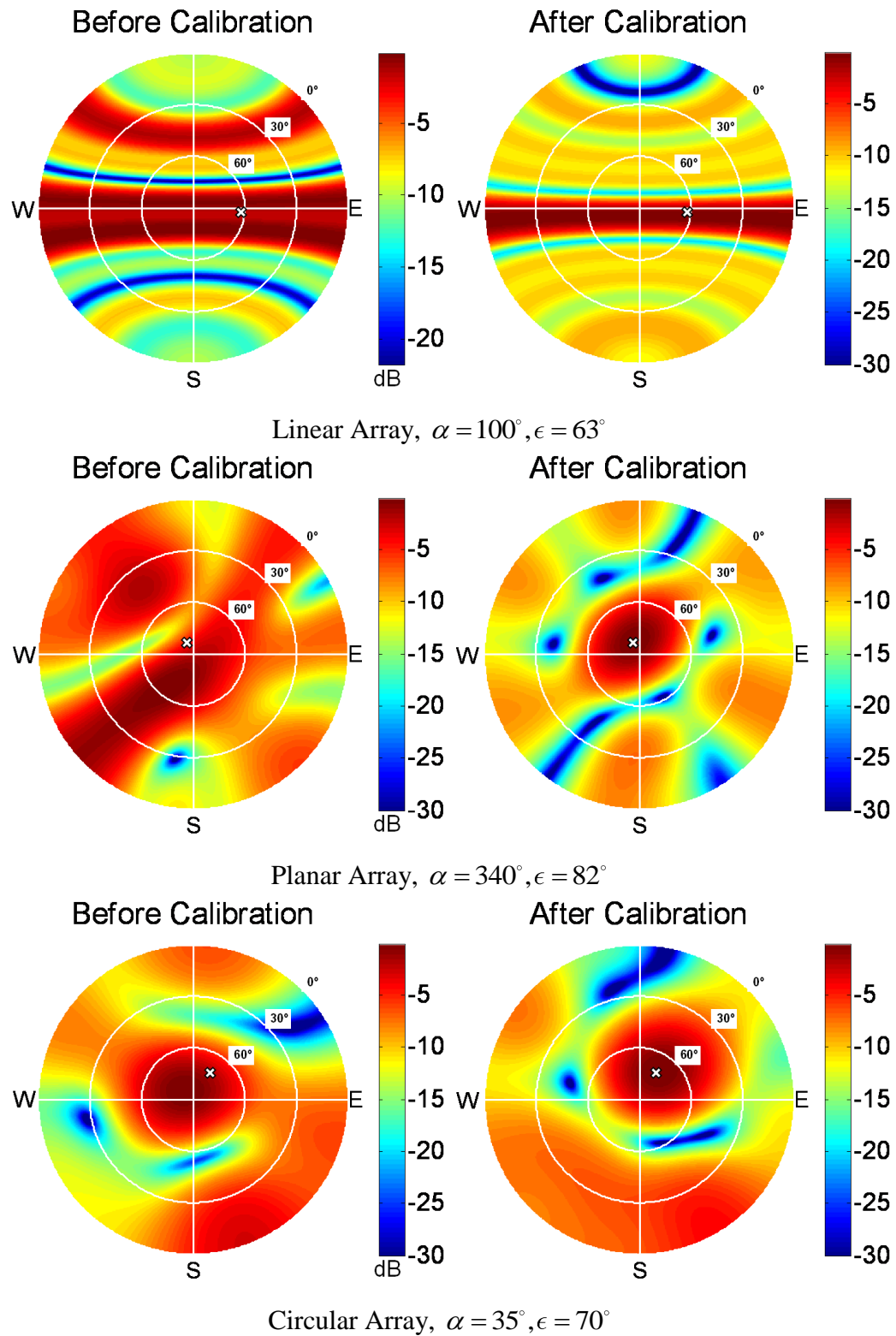


**Figure 4-12** Array patterns before and after calibration for a linear, planar and circular array.  $M = 8$

#### 4.6.2 Hardware simulator analysis

GPS signals were simulated using a Spirent GSS 7700 GPS hardware simulator capable of producing data from two separate antennas. The hardware simulator was used as an initial step before using real data. In this way, it was possible to test the proposed algorithm in a controlled environment where the impact of different factors such as antenna gain/phase mismatch and different hardware signal paths could be studied separately. The NI front-end used in Section 3.8 was employed for the data collection process. The test setup is shown in Figure 4-13 where Channel 1 and Channel 2 correspond to Antenna 1 and Antenna 2, respectively.

The setup introduces a phase mismatch between channels due to the presence of different signal hardware paths. This kind of setup allows the analysis of the calibration algorithm in the absence of mutual coupling. The processing of multi-antenna data was performed using a modified version of the University of Calgary software receiver GSNRx<sup>TM</sup> (Petovello et al. 2009), able to provide synchronous correlator outputs. The modified software, GSNRX<sup>TM</sup>-rr, (Satyanarayana et al. 2010) is capable of tracking a reference channel and aiding several rover channels as shown in Figure 4-10 to produce correlator outputs according to (4.12). Here  $\tilde{y}_0(t)$  is used as reference signal and  $\tilde{y}_1(t), \tilde{y}_2(t), \dots, \tilde{y}_{M-1}(t)$  are fed to the rover processing channels.

In order to reduce the noise impact, a coherent integration time  $T = 1$  s was adopted. Long coherent integration was achieved by estimating and removing the data bits using the reference signal from the first antenna. The front-ends used for the data collection were driven by the same clock; however two different PLLs were used for the signal down-conversion to IF. For this reason, it was not possible to guarantee phase coherence

among the channels. Thus, even after calibration, a relative phase drift was observed between the signal components of the two channels. The phase of the signal components after applying the proposed calibration methodology is shown in Figure 4-14. The phase of all the signals in Channel 2 drifts coherently over time.

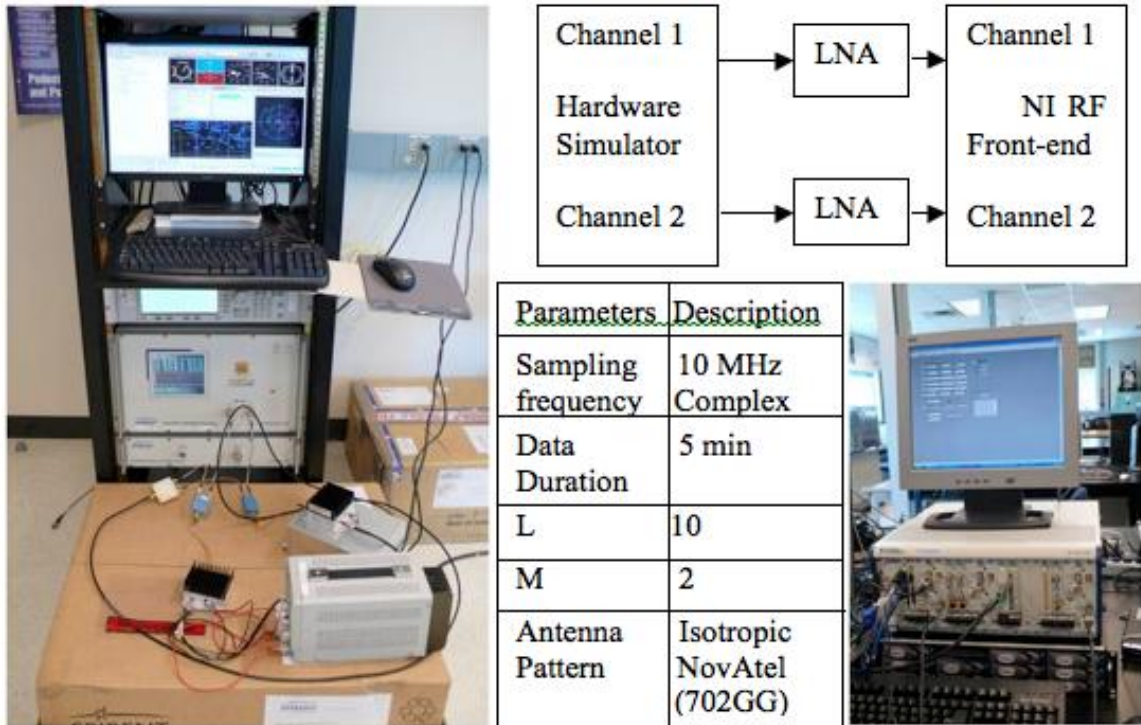


**Figure 4-13 Data collection setup using a hardware simulator to provide dual channel data**

In order to compensate for relative phase variations along time among different front-ends, a reference sine wave was combined with the simulator data as shown in Figure 4-15. The reference sine wave was generated at an offset of 2 MHz (on the second null of the GPS signals power spectral density) to reduce interference issues. The reference tone was used to estimate and compensate for phase variations due to the different front-ends. The results of the phase compensation are shown in Figure 4-16 where two different data sets are considered. After phase compensation, constant phase differences are obtained.

These results show the ability of the proposed calibration technique to estimate the array parameters in a controlled simulation environment.

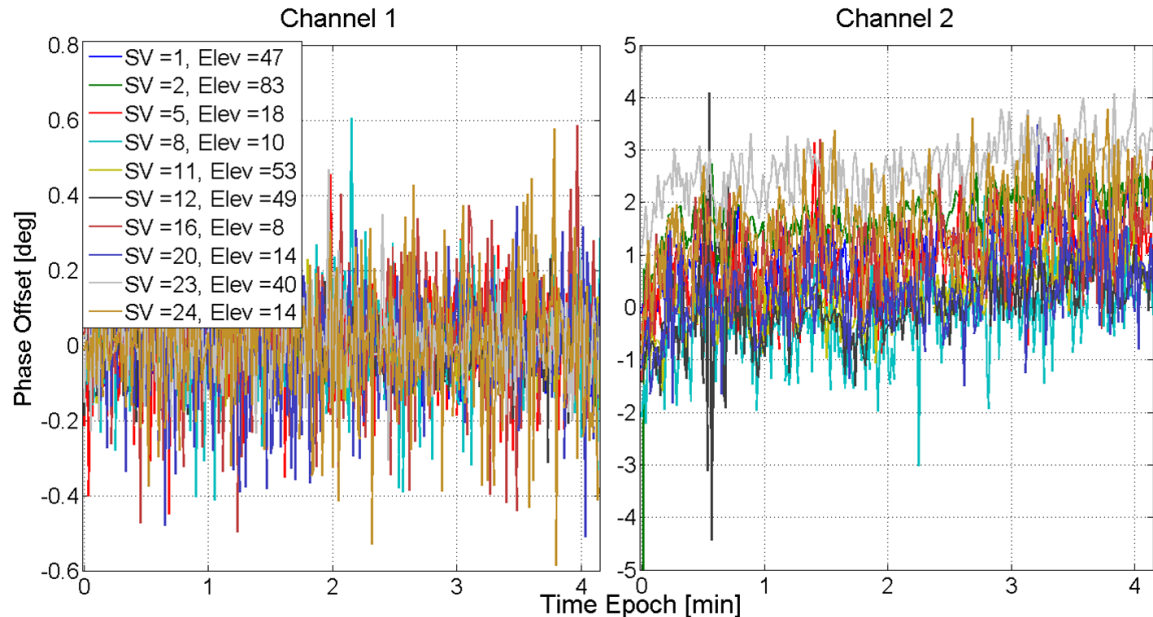


**Figure 4-14 Phase of the useful signal components for a dual antenna array using the hardware simulator**

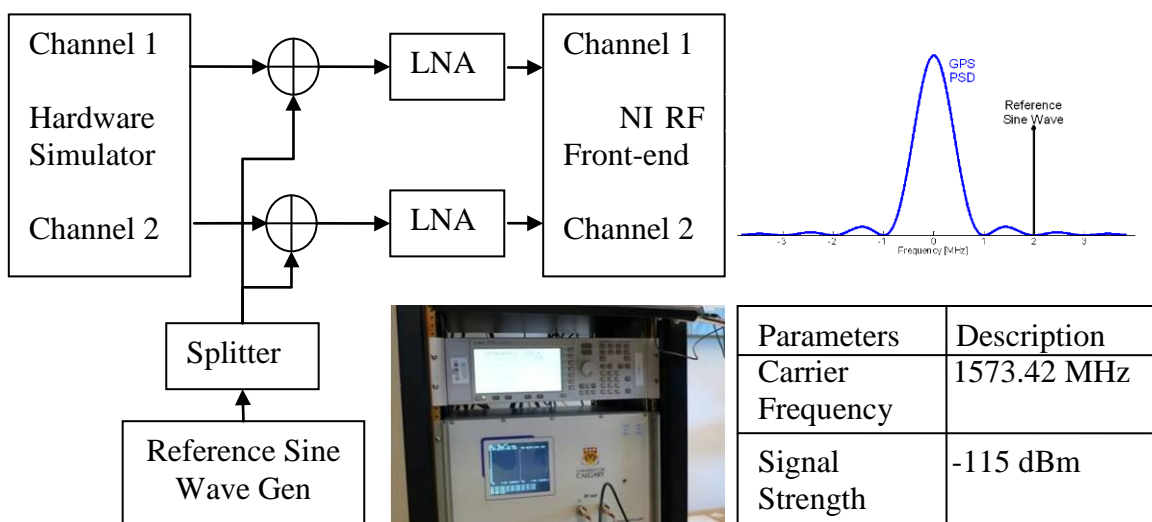


**Figure 4-15 Modified hardware data collection setup used to observe phase variations along time**

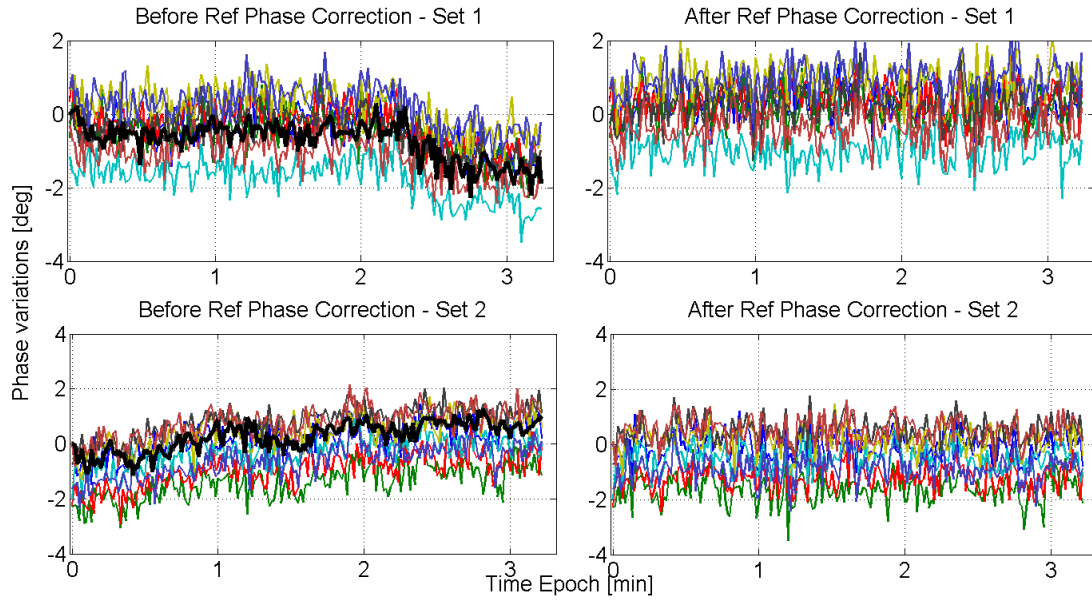


**Figure 4-16 Phase calibration results for the modified hardware simulator setup**

#### 4.6.3 Real data analysis

In order to further test the proposed calibration technique, live data from GPS satellites were used. The test setup adopted for the experiment is shown in Figure 4-17. GPS signals were collected from different antennas using an approach similar to that adopted for the hardware simulated data described in Section 4.6.2. Four antennas were spaced 6 cm apart in a planar structure as shown in Figure 4-18 and data were synchronously collected using a 4-channel front-end. The 4-channel front-end is an extension of the single channel front-end (Morrison 2010) designed for synchronous data collection. The front-end has an option for external clock input that enables the usage of precise clocks. In this research work, the front-end was driven by an external OCXO (Morion 2010). Similarly, data were collected using a triangular array structure to analyze the performance of the calibration algorithm for varying array configurations as shown in

Figure 4-18. Here A0-A4 represents locations of different antennas used to form the planar/triangular structure.

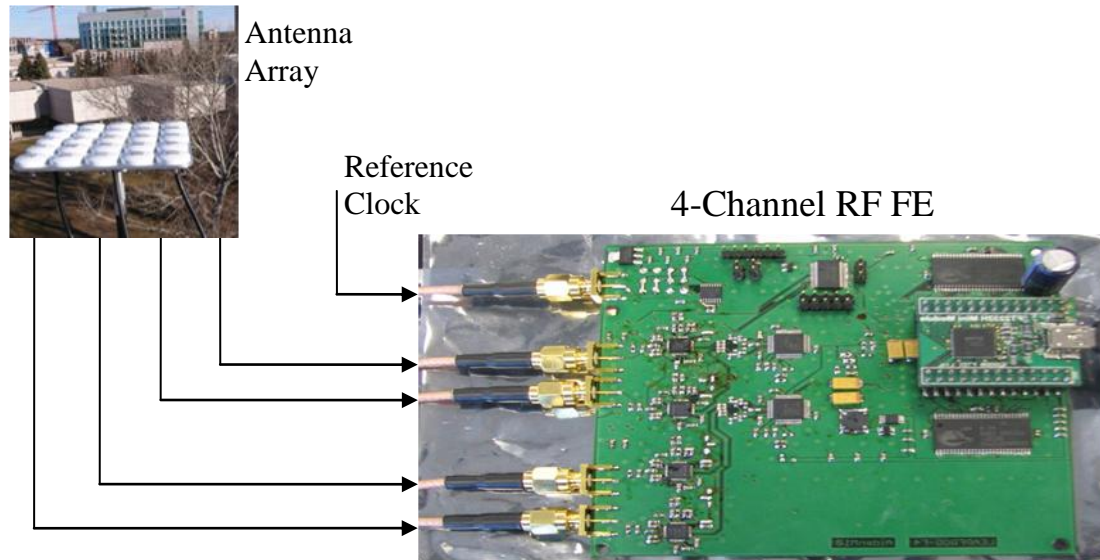


**Figure 4-17 Real data collection setup using four antennas. The antennas were selected in different configurations to obtain planar/triangular arrays**

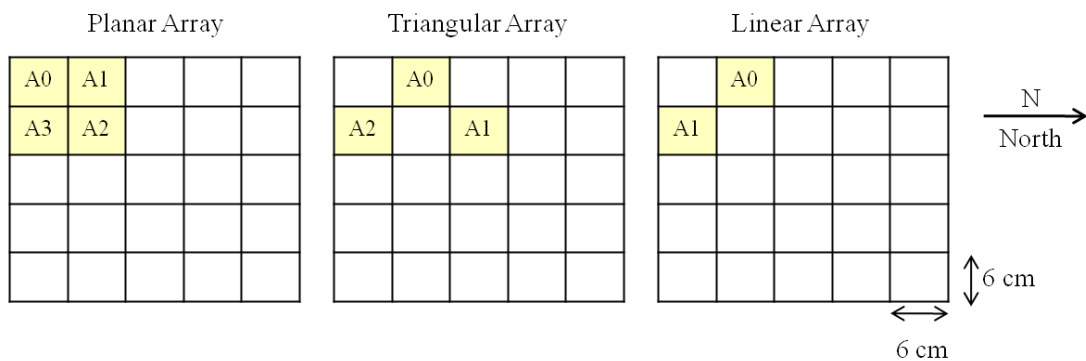


**Figure 4-18 Placement of antennas in different structures on the 5x5 antenna array for real data collection**

Figure 4-19 shows sample beamforming results for two different satellites, SV-ID 3 and SV-ID 22 with elevation angles of  $21^\circ$  and  $80^\circ$ , respectively. It can be observed that before calibration, the array pattern maximum is away from the true direction of arrival (denoted by 'x'). After applying the proposed projection based calibration methodology,

the array pattern has a maximum around the true direction of arrival for both satellites. Similar results have been observed for the other satellites in view.

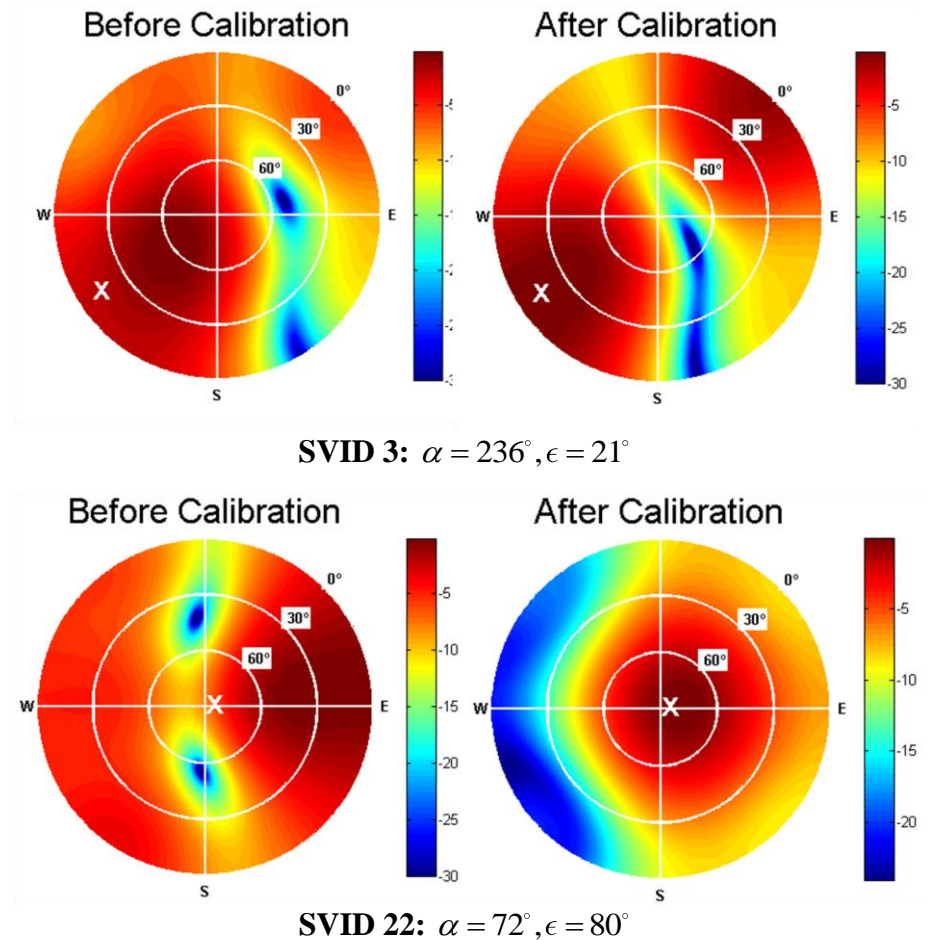


**Figure 4-19 Real data beamforming results before and after applying the projection based calibration methodology on planar array data**

To further analyze the effect of calibration errors on real data, phase errors on the estimated elevation and azimuth angles has been evaluated. The results for the phase errors in azimuth and elevation for the different satellites in view are provided in Figure 4-20 and Figure 4-21, respectively. The plots in Figure 4-20 and Figure 4-21 provide phase errors obtained after applying beamforming on calibrated array outputs for different GPS satellites.

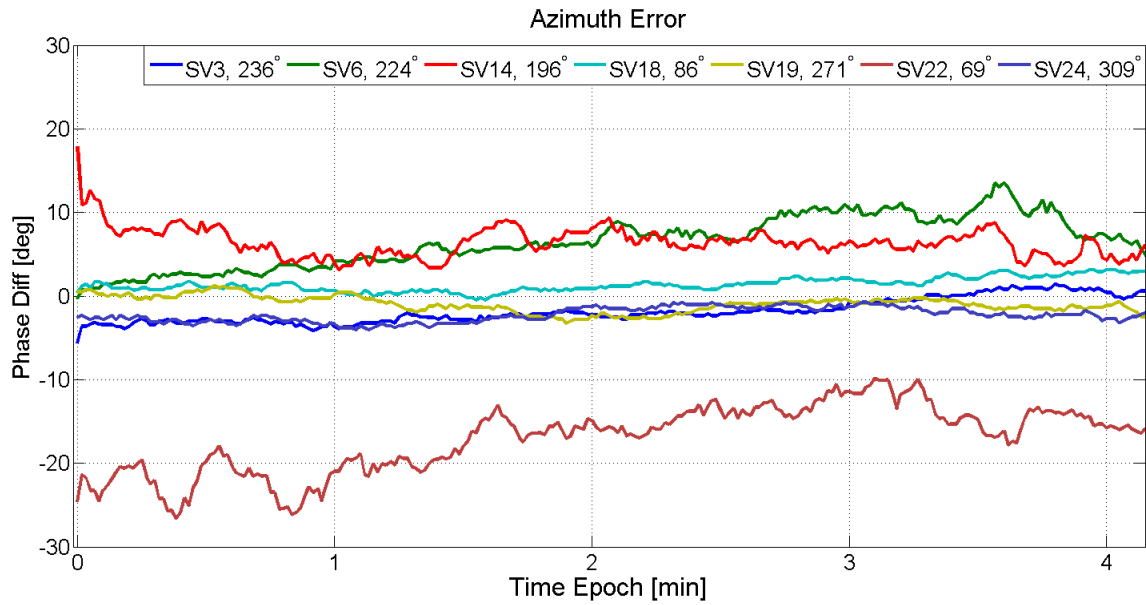


**Figure 4-20 Azimuth errors after performing angle of arrival estimation on the calibrated planar array data**

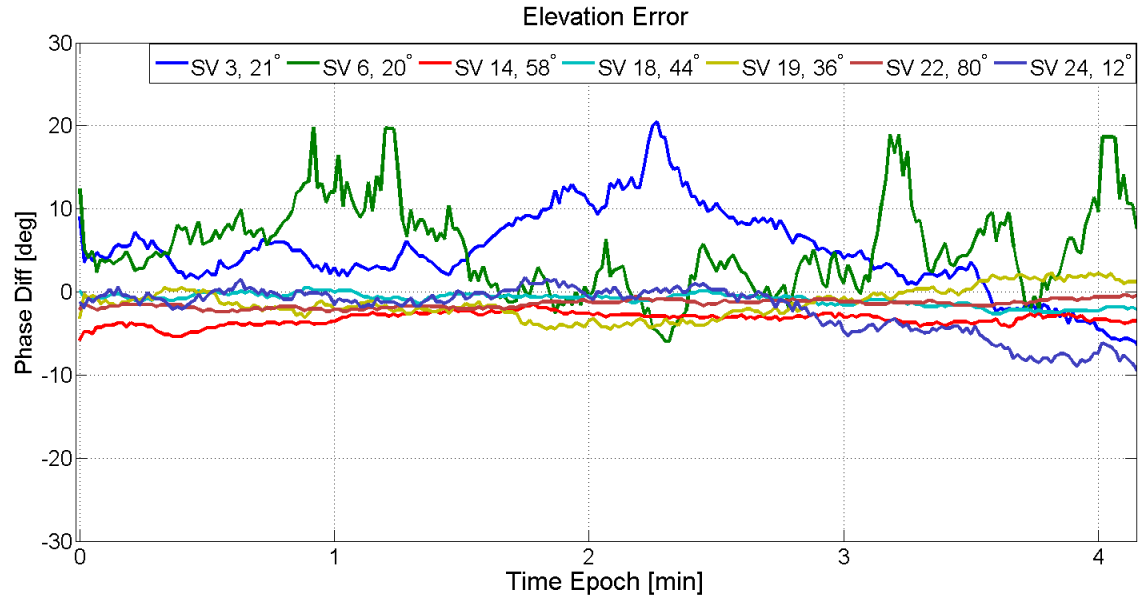


**Figure 4-21 Elevation errors after performing angle of arrival estimation on the calibrated planar array data**

The phase error,  $\epsilon_\theta^i$ , was computed for both elevation and azimuth angles using the formulation

$$\epsilon_{\theta}^i = \theta_{TDOA}^i - \theta_{BDOA}^i \quad (4.22)$$

where  $\theta_{TDOA}^i$  is the true direction of arrival of the incoming signal computed using the ephemeris collected from the reference antenna and  $\theta_{BDOA}^i$  is the direction of arrival that maximizes the energy of the correlator outputs combined through beamforming at the  $i^{th}$  instant in time.

This kind of analysis provides a mean to analyze the effect of residual calibration errors on array processing algorithms. From Figure 4-20, the azimuth error along time is observed to be within  $\pm 10$  degrees for most of the satellites considered.

It is noted that, since only 4 antennas are used, the beam of the array is quite wide leading to a poor resolution in the azimuth domain. This effect is clearly observable for the case of SV-ID 22 (the only satellite available in the first quadrant of the azimuth range) that has a larger error as compared to the other satellites. It can be observed from Figure 4-21 that the elevation error along time is within  $\pm 5$  degrees for high elevation satellite signals (SV-ID 14, 18, 19 and 22) and around  $\pm 10$  degrees for medium-to-low elevation angles (SV-ID 3, 6, 24). Sample results on beamforming for triangular array data after applying the projection based calibration methodology are provided in Figure 4-22 for two different satellites. It should be noted that since only three antennas are considered, the main lobe of the array pattern is wider as compared to the array pattern obtained in Figure 4-19 where four antennas were considered.

From Figure 4-22, it can be observed that calibration maximizes the array pattern around the true direction of arrival (denoted by ‘x’) for the considered satellites. Thus, in both planar and triangular array structures, the proposed calibration algorithm is able to

provide calibrated correlator outputs that maximize the incoming signal power around the true direction of arrival.

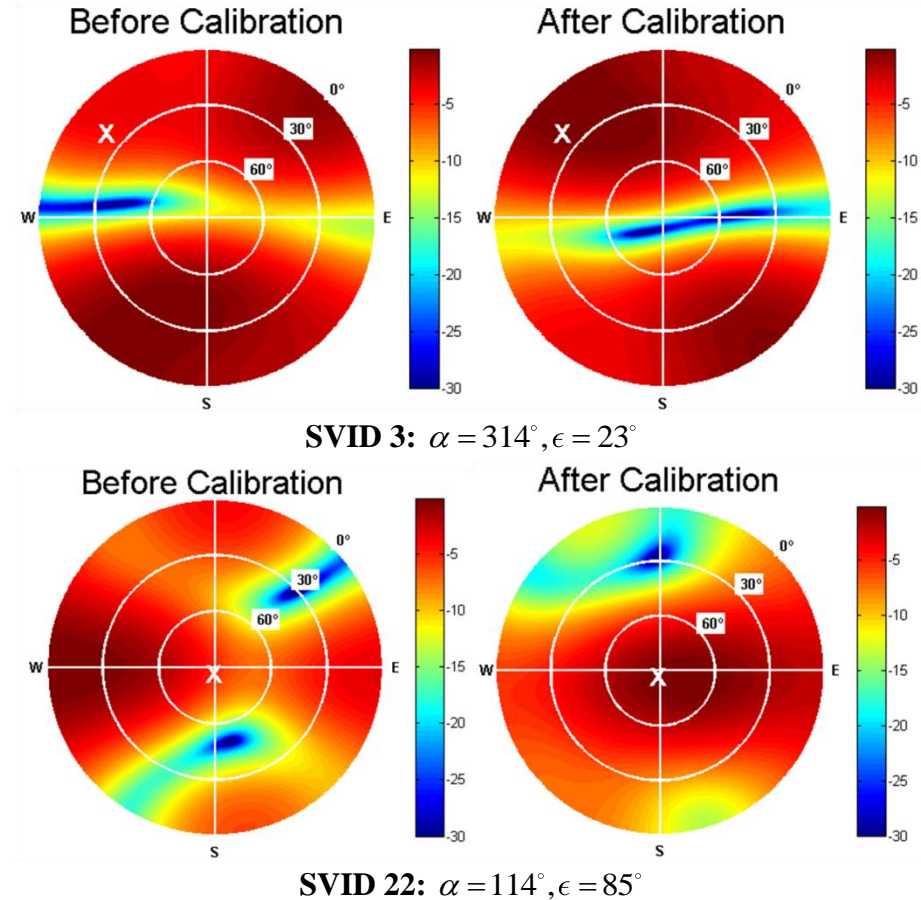


**Figure 4-22 Real data beamforming results before and after applying the projection based calibration methodology on triangular array data**

Calibration results have been analyzed in terms of the C/N<sub>0</sub> gain achieved by combining antenna array correlator outputs. The optimum C/N<sub>0</sub> gain that can be achieved using an antenna array is given by (Mogensen et al. 1999)

$$Gain_{dB} = 10 \log_{10} M \quad (4.23)$$

with  $M$  being the number of antenna elements. The gain values for different number of antenna elements are provided in Table 4-1.

**Table 4-1 Optimum C/N<sub>0</sub> gain achievable using M-antenna array**

No of antennas, M	C/N <sub>0</sub> Gain (dB)
1	0
2	3
3	4.7712
4	6.0206

The C/N<sub>0</sub> values have been estimated using the methodology described in (Dierendonck 1996) as

$$C/N_0 = 10 \log_{10} \left( \frac{\mu - 1}{T_i(N - \mu)} \right) \quad (4.24)$$

where  $\mu$  represents the ratio of narrow band power (NBP) to wide band power (WBP) of the Prompt correlator output obtained over  $K$  samples as

$$\mu = \frac{1}{K} \sum_{k=1}^K \left( \frac{(NBP)_k}{(WBP)_k} \right). \quad (4.25)$$

The NBP and WBP values are computed across  $N$  samples as

$$NBP = \sum_{i=1}^N (I_i^2) + \sum_{i=1}^N (Q_i^2) \quad (4.26)$$

$$WBP = \sum_{i=1}^N (I_i^2 + Q_i^2).$$

The C/N<sub>0</sub> gain obtained after performing calibration and beamforming on a two-antenna linear array is provided in Figure 4-23 that is characterized by three regions:

- *Single Antenna* that provides C/N<sub>0</sub> estimates obtained using  $q_0(t)$  alone,

- *Before Calibration* that provides C/N<sub>0</sub> estimates obtained by compensating only the effects of steering vector,  $\mathbf{s}$ , before combining correlator outputs  $q_{0,1,\dots,M-1}(t)$  from all antennas according to (4.3) and
- *After Calibration* that provides C/N<sub>0</sub> estimates obtained by compensating the effects of both steering vector,  $\mathbf{s}$ , and calibration matrix,  $\mathbf{C}$ , before combining correlator outputs  $q_{0,1,\dots,M-1}(t)$  from all antennas according to (4.3).

For the three cases considered in Figure 4-23, the values of  $N$  and  $K$  were set to 50 and 20 respectively with  $T_i = 1\text{ ms}$  and the inputs to the C/N<sub>0</sub> estimation algorithm are as defined in Table 4-2. I

**Table 4-2 Correlator inputs to the C/N<sub>0</sub> estimation algorithm for the single antenna, before and after calibration case.**

Case type	In-phase Component ( $I$ )	Quadrature component ( $Q$ )
Single Antenna	$I = \Re\{q_0\}$	$Q = \Im\{q_0\}$
Before Calibration	$I = \Re\left\{\sum_{i=1}^{M-1} s_i^H q_i\right\}$	$Q = \Im\left\{\sum_{i=1}^{M-1} s_i^H q_i\right\}$
After Calibration	$I = \Re\left\{\sum_{i=1}^{M-1} q_i \sum_{j=1}^{M-1} (v_{i,j} s_i)^H\right\}$	$Q = \Im\left\{\sum_{i=1}^{M-1} q_i \sum_{j=1}^{M-1} (v_{i,j} s_i)^H\right\}$

It can be observed that after calibration, the beamforming provides approximately a C/N<sub>0</sub> gain equal to the theoretical gain of 3 dB on most of the satellites whereas before calibration, the gain is minimal and, in some cases, negative with respect to the single antenna case. Similar results have been obtained for 3 and 4 antennas planar arrays as shown in Figure 4-24 and Figure 4-25. In both cases, calibration provides gains close to

that achievable theoretically. These results support the effectiveness of the proposed calibration algorithm that enables efficient beamforming.

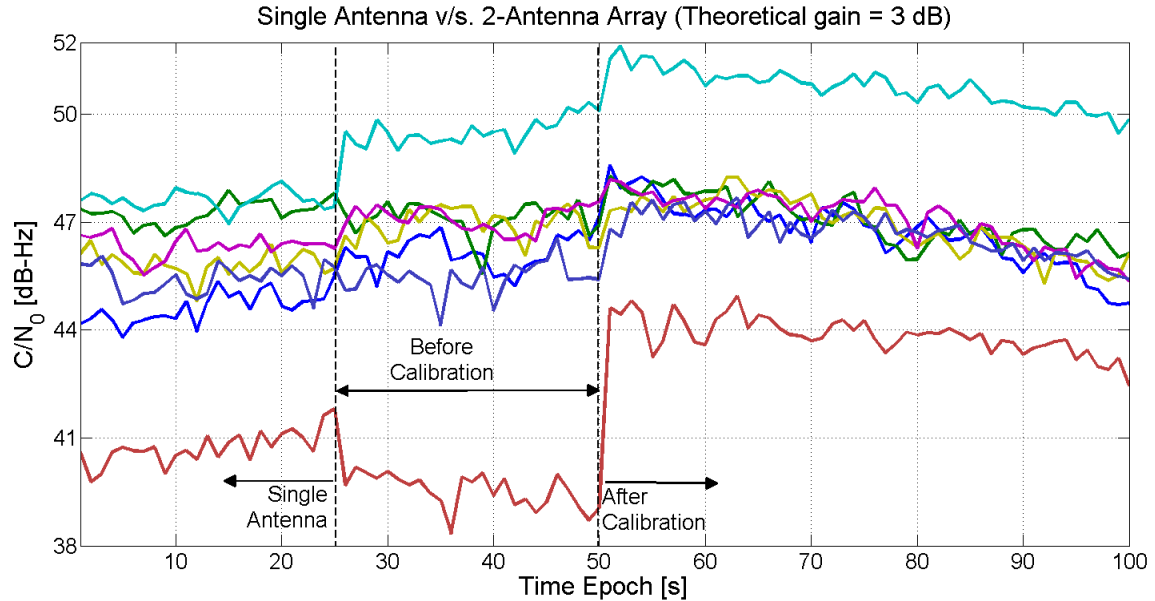


**Figure 4-23**  $C/N_0$  estimates obtained after performing calibration and beamforming on the linear array data for several satellites (represented by different colored lines)

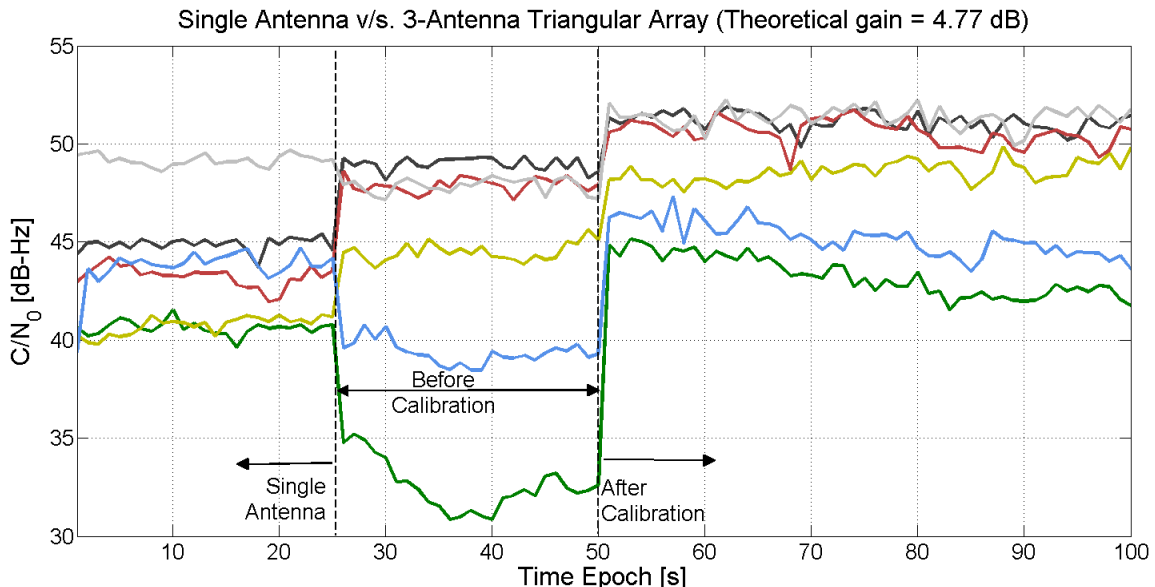


**Figure 4-24**  $C/N_0$  estimates obtained after performing calibration and beamforming on the triangular array data for several satellites (represented by different colored lines)

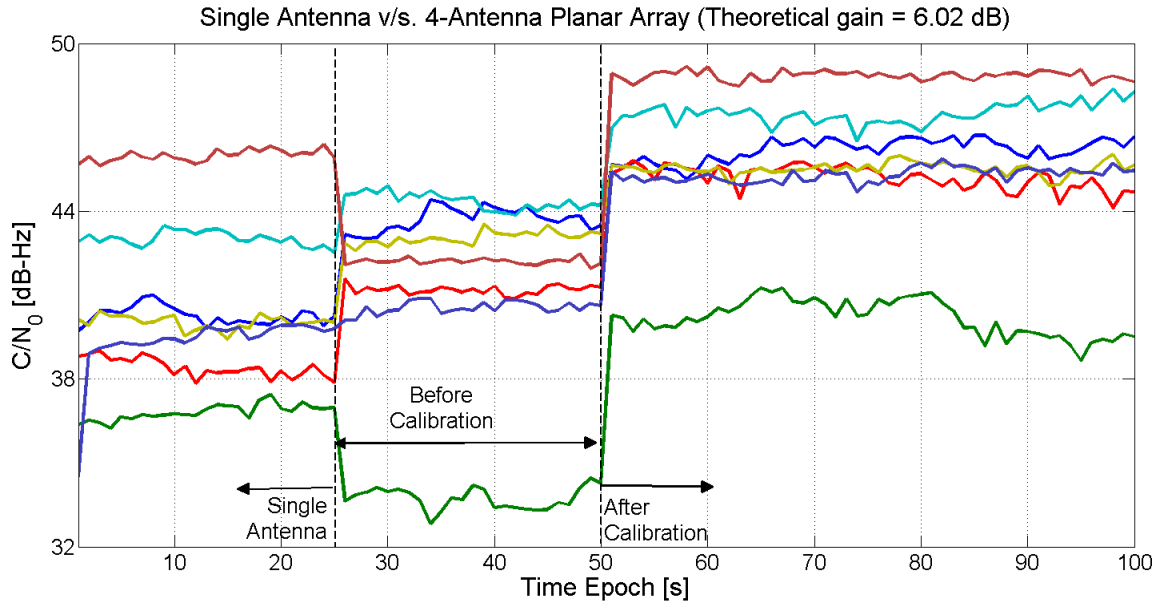


**Figure 4-25** C/N<sub>0</sub> estimates obtained after performing calibration and beamforming on the planar array data for several satellites (represented by different colored lines)

#### 4.7 Conclusions

In this chapter, a self-contained antenna array calibration procedure using GNSS signals has been proposed and analyzed. The proposed technique has been tested using simulation and real data. It was observed that the proposed methodology is able to accurately estimate the calibration parameters for various antenna structures and satellite signal power levels. The proposed algorithm is able to effectively calibrate the antenna array without requiring any additional equipment for the generation of signal from sources at known positions, enabling for in-line calibration of GNSS receivers adopting multiple antennas. Experiments using live GNSS data have demonstrated the feasibility of the proposed algorithm and support its effectiveness in enabling multi-antenna processing.

## Chapter Five: Combined Space-Time Adaptive Processing

The advantages of temporal and spatial processing as applied to new GNSS signals were presented in Chapters 3 and 4. It was observed that temporal processing allows unambiguous tracking of BOC signals while spatial processing provides enhanced signal quality. In this chapter, combined space-time processing is explored to exploit the advantages provided by the two techniques. A detailed introduction to space-time processing techniques is first provided with focus on the existing techniques. A detailed literature review on the applications of space-time techniques to GNSS signal processing is then provided. A combined space-time processing approach is finally proposed in the last section of the chapter along with results and analysis obtained from real data.

### 5.1 Introduction to space-time processing

The combination of spatial and temporal filtering is referred to as space-time processing (Kohno 1998). Space-time processing can yield improved performance in terms of interference rejection, increased signal-to-interference-plus-noise ratio and multipath mitigation. The spatial filter is realized by the usage of antenna arrays while temporal processing is realized by a finite impulse response filter at each antenna output. A simplified representation of a typical space-time processing structure is provided in Figure 5-1. Each antenna element is followed by K taps with  $\delta$  denoting the time delay between successive taps forming the temporal filter. The combination of several antennas forms the spatial filter.  $w_k^m$  are the space-time weights with  $0 \leq k < K$  and  $0 \leq m < M$ .  $k$  is the temporal index and  $m$  is the antenna index.

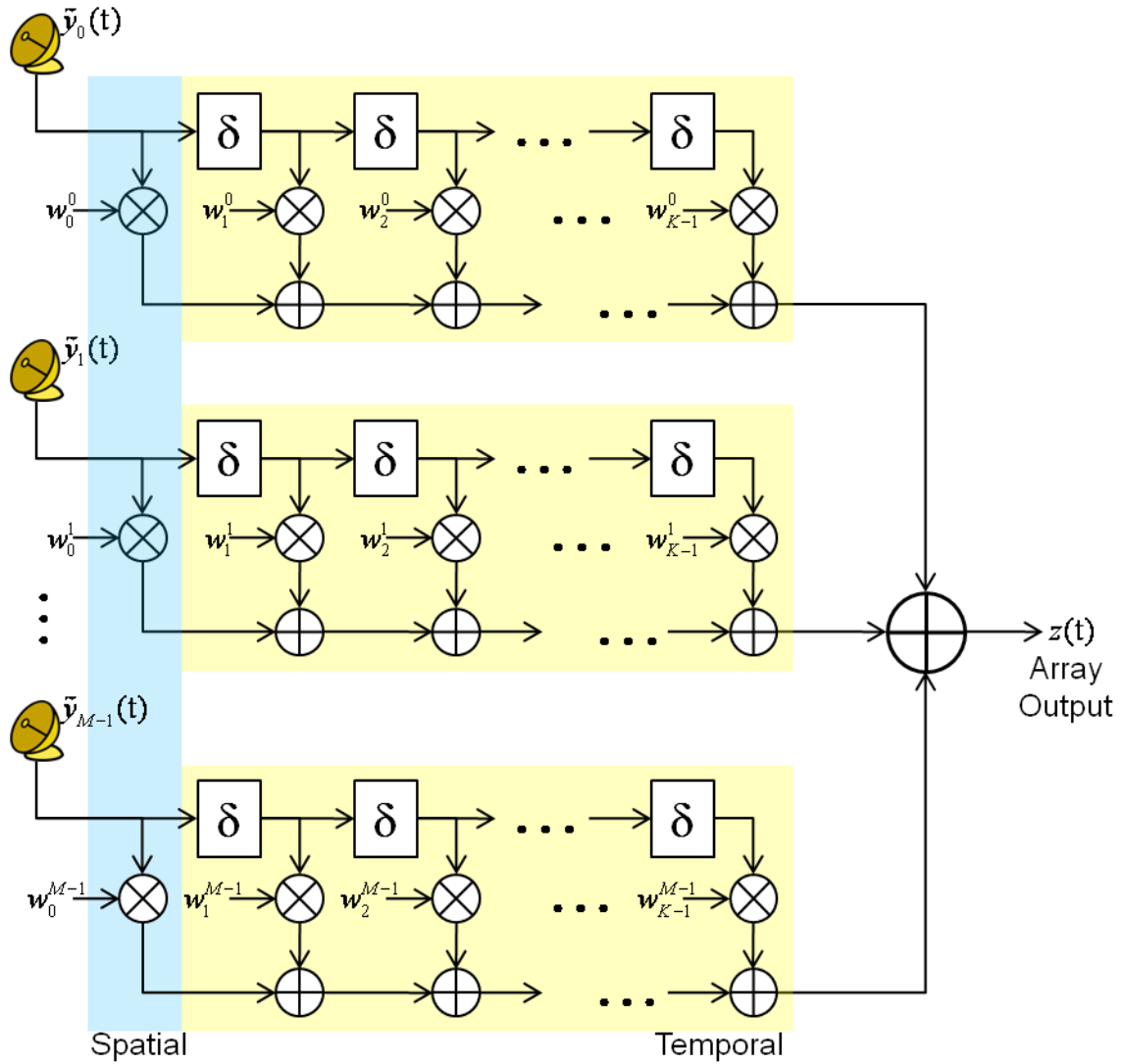


**Figure 5-1 Block diagram of space-time processing**

The array output after applying the space-time filter can be expressed as

$$z(t) = \sum_{m=0}^{M-1} \sum_{k=0}^{K-1} \tilde{y}_m(t - k\delta) w_k^m. \quad (5.1)$$

Spatial-only filtering can be realized by setting  $K=1$  and a temporal-only filtering is obtained when  $M=1$ . The weights are estimated using the different criteria described in detail in Section 5.2 and can be updated depending on signal/noise characteristics subject to user-defined constraints using different adaptive techniques (Haykin 2001). This kind

of processing is often referred to as space-time adaptive processing (STAP). A brief description of different STAP techniques and the adaptive realization of STAP algorithms are provided in the following section.

## 5.2 STAP techniques

Space-time processing algorithms can be broadly classified into two categories: decoupled and joint space-time processing (Paulraj & Lindsborg 1998). The joint space-time approach exploits both spatial and temporal characteristics of the incoming signal in a single space-time filter whereas the decoupled approach involves several temporal equalizers and a spatial beamformer such that interference and multipath effects can be realized in two separate stages as shown in Figure 5-2.

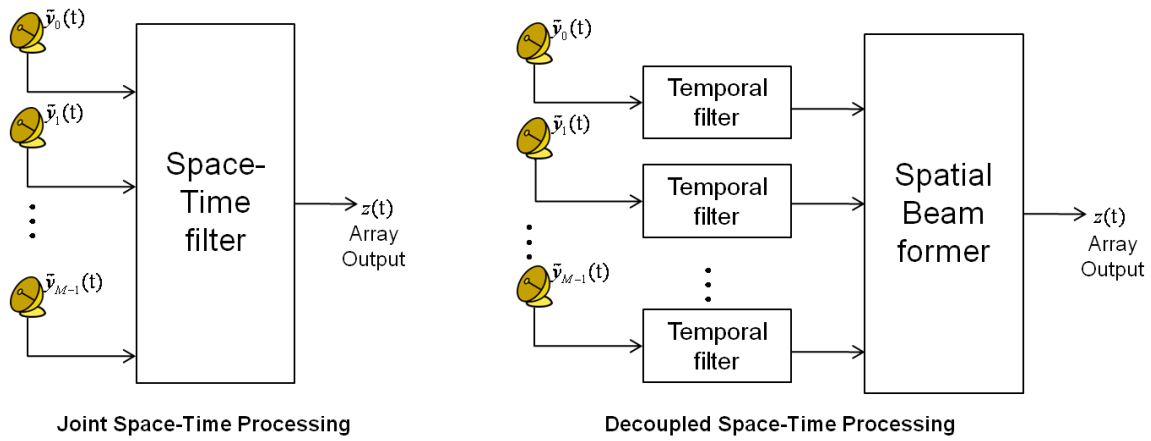


**Figure 5-2 Representation of two different space-time processing techniques.**

While the joint space-time approach provides additional processing gain, the decoupled approach results in a system with reduced computational complexity and minimal performance loss compared to the former approach. When the decoupled approach is considered, the spatial beamformer can implement several approaches such as the *MSE*, *maximum SNR*, *maximum likelihood (ML)* and *minimum variance (MV)* criteria

(Monzingo & Miller 2004, Haykin 2001). A brief description of the application of these criteria for spatial beamforming is provided below.

### 5.2.1 MSE

In this criterion, the MSE between the desired array output (or reference signal) and the actual array output is minimized. This technique was developed by (Widrow et al. 1967)

to adaptively reduce the MSE. The optimum weight vector,  $\mathbf{w} = [w_0^0 \quad w_0^1 \quad \dots \quad w_0^{M-1}]^T$ ,

satisfying the MSE criteria, is provided by

$$\begin{aligned} \min_{\mathbf{w}} E\{e^2(t)\} &= \min_{\mathbf{w}} E\left\{\|d(t) - \mathbf{w}^H \tilde{\mathbf{y}}(t)\|^2\right\} \\ &\Rightarrow \mathbf{w}_{MSE} = R_{\tilde{\mathbf{y}}\tilde{\mathbf{y}}}^{-1} r_{\tilde{\mathbf{y}}d} \end{aligned} \quad (5.2)$$

where  $R_{\tilde{\mathbf{y}}\tilde{\mathbf{y}}}$  is the autocorrelation matrix of the input signal and  $r_{\tilde{\mathbf{y}}d}$  is the cross correlation vector between incoming signal,  $\tilde{\mathbf{y}}(t)$ , and reference signal  $d(t)$ . Since the values of  $R_{\tilde{\mathbf{y}}\tilde{\mathbf{y}}}$  and  $r_{\tilde{\mathbf{y}}d}$  are not accurately known, ensemble averages of these quantities are computed using several snapshots of the input vector and the weight vector is adaptively estimated. In this approach, it is assumed that the reference signal is known which seldom holds true especially in the case of GNSS signals.

A sample plot of the array factor obtained using MSE criterion for a 6-element linear array is provided in Figure 5-3. The desired signal DOA was set to 15 degrees while the interference signal DOA was set to 50 degrees. The steps followed by the least mean square (LMS) algorithm (Haykin 2001) to minimize the MSE in an adaptive spatial beamformer are as follows:

*Step 1* : Initialize weight vector  $w(0) = 0$  and step-size parameter  $\mu \ll 1$

*Step 2* : Compute filter output  $z(t) = \mathbf{w}^H(t-1)\tilde{\mathbf{y}}(t)$

*Step 3* : Compute estimation error  $e(t) = d(t) - z(t)$

*Step 4* : Update weight vector  $\mathbf{w}(t) = \mathbf{w}(t-1) + \mu\tilde{\mathbf{y}}(t)e(t)$

*Step 5* : Repeat steps 2 to 4 until  $t = T$ , the observation interval.

It can be observed that the LMS adaptive algorithm provides improved interference rejection as the number of snapshots used for the adaptive processing increases. A narrower and deeper interference null is possible when the number of snapshots is equal to 100.

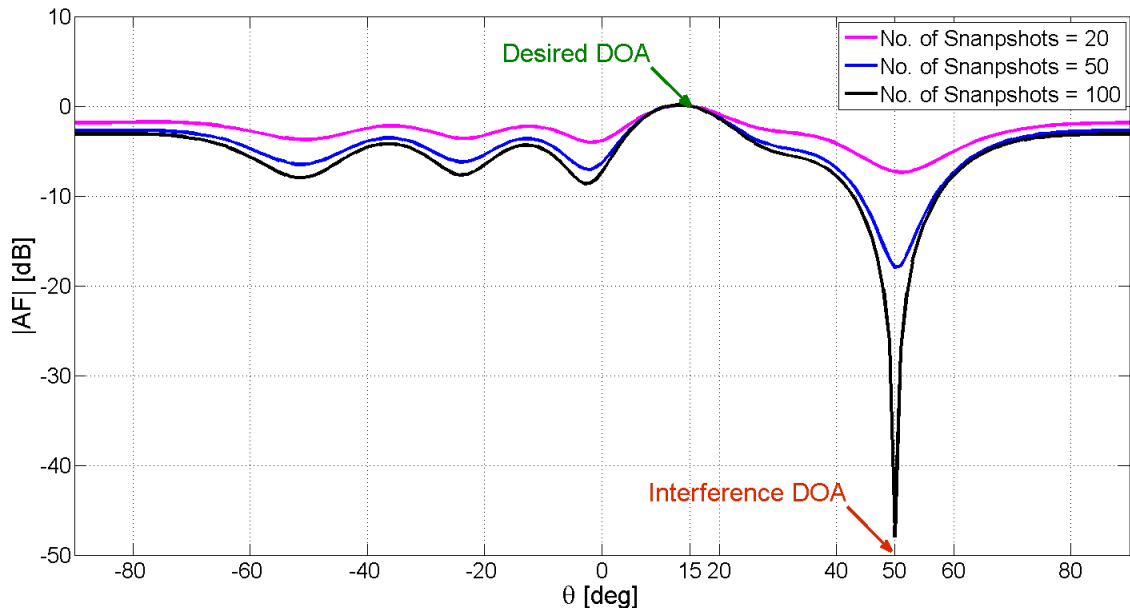


**Figure 5-3 Plot of array factor as a function of the number of snapshots used in adaptive array processing for interference mitigation using a 6-element linear array. Signal DOA = 15 degrees and Interference DOA = 50 degrees**

To analyze the adaptation capabilities of the system, a first interference was placed at 45 degrees and a second interference signal was placed at -30 degrees. It can be observed that the adaptive beamformer efficiently placed nulls in the interference DOA while still

maintaining maximum gain along the desired DOA. A total of 200 epochs were required to obtain the deep nulls in Figure 5-4 at the interference DOA.

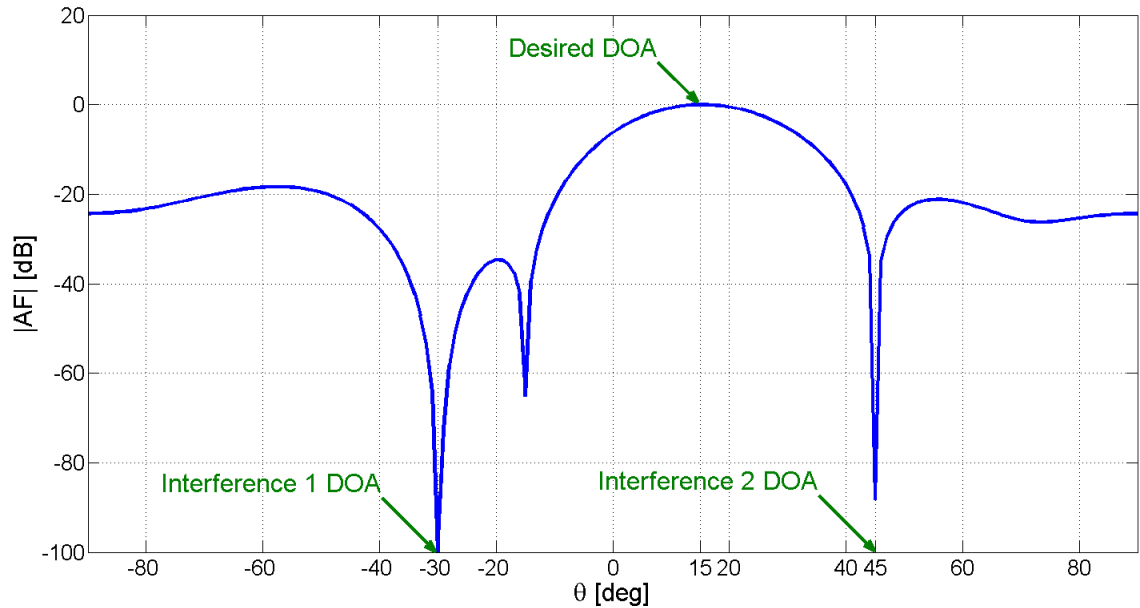


**Figure 5-4 Adaptive array processing mitigating the presence of two interference signals from different directions using LMS algorithm. Signal DOA = 15 degrees, Interference 1 DOA = 45 degrees and Interference 2 DOA = -30 degrees**

### 5.2.2 Maximum SNR

In this criterion, the SNR at the array output is maximized. The beamformer presented in (Applebaum & Chapman 1976) is based on this principle. Consider the system of equations given in (4.3) along with the noise term  $\eta(t)$ :

$$z(t) = \mathbf{w}^H (\bar{\mathbf{y}}(t) + \mathbf{\eta}(t)). \quad (5.3)$$

The mathematical formulation for the SNR and the optimal weight vector maximizing the SNR can be expressed as

$$\begin{aligned}
\max_w \text{SNR} &= \max_w \left( \frac{\text{Signal Power}}{\text{Noise Power}} \right) \\
&= \max_w \left( \frac{\mathbb{E}\{|\bar{y}(t)|^2\}}{\mathbb{E}\{|\eta(t)|^2\}} \right) = \max_w \left( \frac{\mathbf{w}^H R_{\bar{y}\bar{y}} \mathbf{w}}{\mathbf{w}^H R_{\eta\eta} \mathbf{w}} \right) \\
&\Rightarrow \mathbf{w}_{SNR} = \frac{1}{\mu} R_{\eta\eta}^{-1} \mathbf{s}
\end{aligned} \tag{5.4}$$

where  $\mu$  is a complex constant defined as  $(\mathbf{w}^H \mathbf{s}) / (\mathbf{w}^H R_{\eta\eta} \mathbf{w})$ .

### 5.2.3 ML

In this approach, the likelihood function of the signal model with respect to the estimation parameters is maximized. The maximum likelihood estimate (MLE) of a set of unknown parameters,  $E$ , is given by

$$\hat{E} = \arg \max_{\hat{E}} p(\tilde{\mathbf{y}}|E) \tag{5.5}$$

where  $p(\tilde{\mathbf{y}}|E)$  is the likelihood function defined by the probability density function of  $\tilde{\mathbf{y}}$  given a certain  $E$ . In the case of standard GNSS signal processing, the estimation parameters include code delay, Doppler frequency and carrier phase such that  $E = \{\tau, f_D, \phi\}$  and  $\tilde{\mathbf{y}}$  is the correlator outputs defined by (4.12) such that the contribution of estimation parameters on the likelihood function is dominant and realizable. When considering STAP, additional parameters have to be included such as the useful signal and interference DOA.

ML estimates are usually difficult to compute and different iterative techniques can be used for determining  $\hat{E}$ . The space-alternating generalized expectation maximization

(SAGE) algorithm (Fleury et al. 1999) is an example of such techniques for the joint delay, Doppler frequency and DOA estimation.

#### 5.2.4 MV

In this approach, the noise variance (or equivalently output noise power) is minimized subject to a linear constraint to provide unity gain in a desired direction. The Capon beamformer (or Minimum Variance Distortionless Response, MVDR beamformer) is based on this criterion that is formulated as

$$\begin{aligned} \min_{\mathbf{w}} \mathbb{E} \left\{ |\eta(t)|^2 \right\} &= \min_{\mathbf{w}} (\mathbf{w}^H R_{\eta\eta} \mathbf{w}) \text{ subject to } \mathbf{w}^H \mathbf{s} = 1 \\ \Rightarrow \mathbf{w}_{MVDR} &= \frac{R_{\eta\eta}^{-1} \mathbf{s}}{\mathbf{s}^H R_{\eta\eta}^{-1} \mathbf{s}} \end{aligned} \quad (5.6)$$

It can be observed that if  $R_{\eta\eta}^{-1} = \sigma_n^2 \mathbf{I}$ , the MVDR beamformer results in the standard delay and the sum beamformer given in (4.4). A sample plot of the MVDR beamformer output with and without interference for a 9-element linear array is shown in Figure 5-5. The incoming signal is composed of a useful signal with a 20 deg elevation and an interference signal with an 80 deg elevation angle. In the absence of interference, it can be observed that the conventional delay and sum beamformer and the MVDR beamformer provide the same result. In the presence of interference, MVDR is able to successfully place a deep null along the interference DOA while maintaining a unity gain along the signal DOA. To further analyze the performance of the MVDR beamforming, two more interference signals at -60 and -40 degrees were added along with the existing interference and desired signal. The plot of the array factor after applying the MVDR is shown in Figure 5-6. It can be clearly noted that, using MVDR, the spatial beamformer is

capable of placing nulls at the interference DOA without compromising the gain at the desired signal DOA.

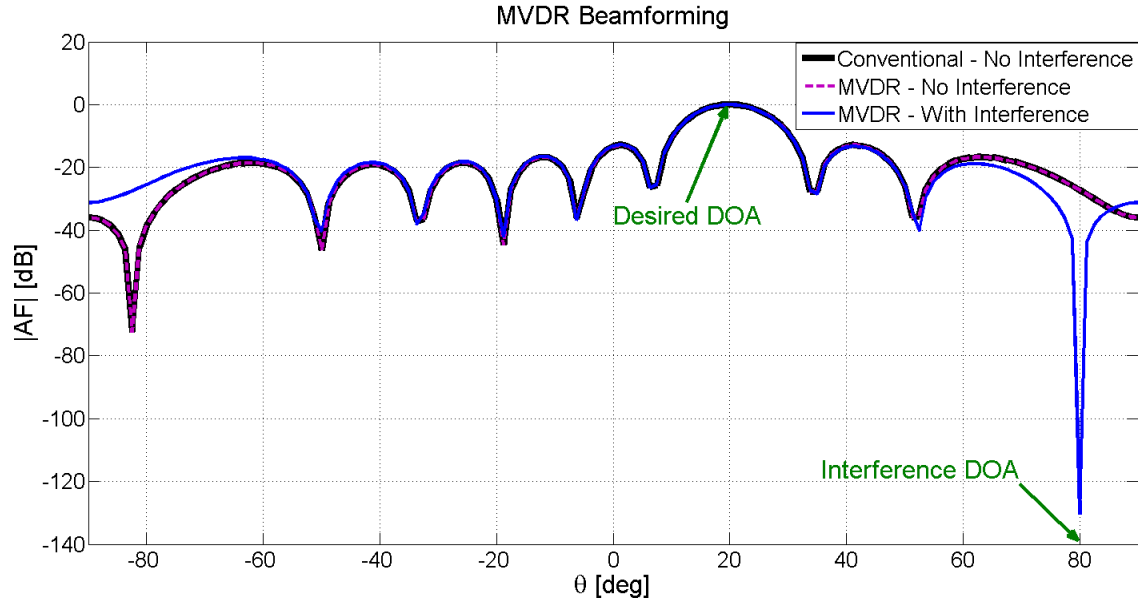


**Figure 5-5 Performance of MVDR beamforming with and without interference (9-element array)**

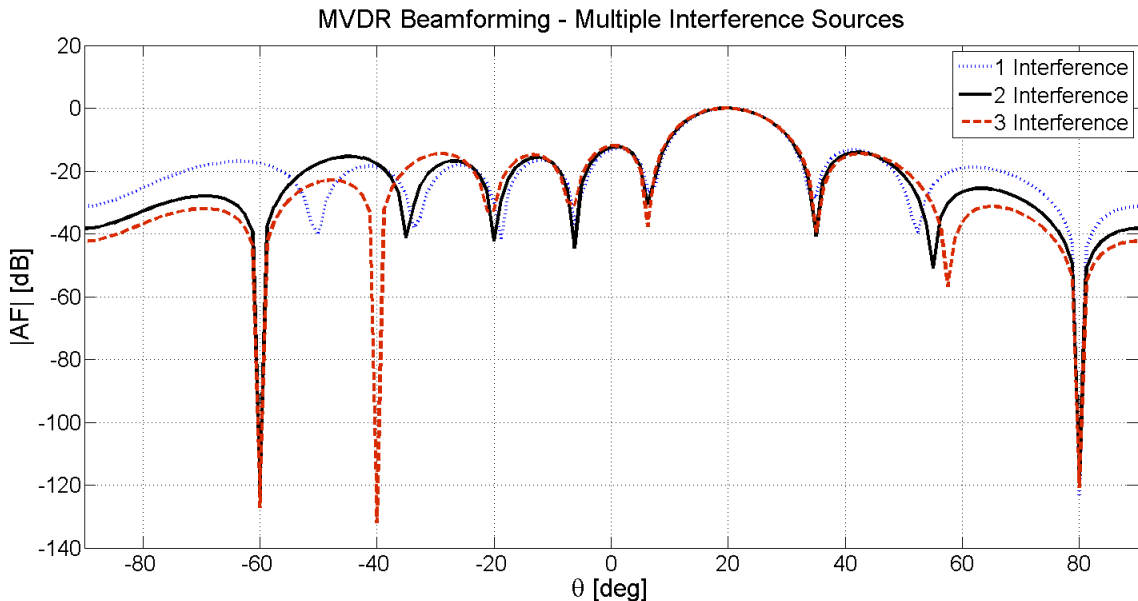


**Figure 5-6 Array factor after applying MVDR beamforming in the presence of multiple interference sources at DOA 80, -60 and -40 degrees with the desired DOA at 20 degrees (9-element array)**

### 5.3 STAP for GNSS signals

The success of STAP techniques has been well demonstrated in radar, sonar, airborne and mobile communication systems (Klemm 2006, Ward 1998). This has led to the application of STAP techniques in the field of GNSS signal processing. Several STAP techniques (O'Brien & Gupta 2008, Vicario et al. 2010, Seco-Granados et al. 2005, Rougerie et al. 2011) have been developed for improving the performance of GNSS signal processing. These techniques exploit the advantages of STAP for minimizing the effect of multipath and interference along with improved signal quality.

In the case of GNSS signals both joint space-time and decoupled approaches have been explored. While considering the decoupling approach, a temporal filter can be applied on each antenna and the spatial filter can be applied at two different stages, namely pre-correlation or post-correlation as shown in Figure 5-7. In the pre-correlation stage, spatial weights are applied on the incoming signal after carrier wipe-off while in the post-correlation stage, spatial weights are applied after the I&D block on the correlator outputs defined by (4.12). In the pre-correlation processing, the update rate of the weight vector is in the order of MHz (same as sampling frequency) whereas the post-correlation processing has the advantage of lower update rate in the order of kHz (I&D frequency). In the pre-correlation processing case, the interference and noise components prevail significantly in the spatial correlation matrix and would result in efficient interference mitigation and noise reduction. But the information of the direct and reflected signals are unavailable as the GNSS signals are well below the noise level (Kaplan & Hegarty 2006). This information can be extracted from the post-correlation processing.

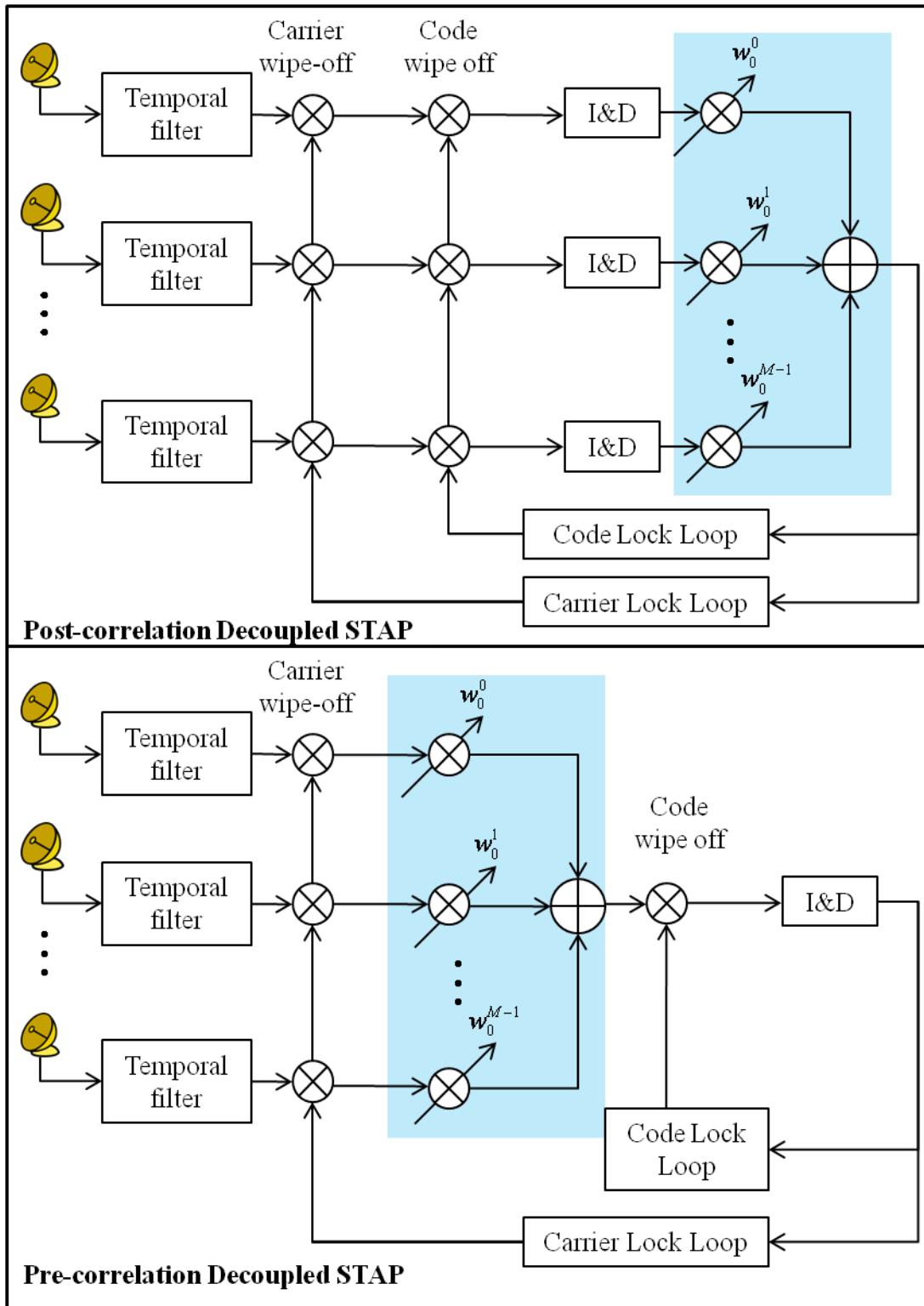


Figure 5-7 Pre and post-correlation decoupled STAP as applied to GNSS signals

In (O'Brien & Gupta 2008), a joint STAP has been considered for GNSS antenna arrays. The weights are adapted according to a linearly constrained minimum power optimum filter to minimize MSE between the incident signal and the reference signal. The linear constraints include the zero carrier phase bias and zero code delay bias on the beamformed signal such that the antenna array induced biases are close to zero. In this kind of processing, the knowledge of the input signal power spectrum, the response of the front-ends and the antenna response of each element in the array are required. A hybrid beamformer comprising of a weighted linear combination of the minimum MSE beamformer calculated with only the temporal reference and the minimum-variance beamformer calculated with only the spatial reference was provided in (Seco-Granados et al. 2005). The main objective of the hybrid beamformer was to cancel multipath components as well as interference to take complete advantage of the spatial domain and hence a post-correlation processing was adopted. In (Vicario et al. 2010) and (Rougerie et al. 2011), adaptive spatial processing was considered based on constrained MVDR beamformer and SAGE algorithms, respectively. In both of the proposed techniques, post correlation processing was employed.

Space-time algorithms applicable to Galileo signals have been applied in (Cuntz et al. 2008, Iubatti et al. 2006). Live Galileo data were used in (Cuntz et al. 2008) to demonstrate the operation of a Galileo navigation receiver using antenna arrays. A linearly constraint minimum variance beamformer was used to steer the array beam to the incoming Galileo signal DOA and the improvements of the antenna array with respect to the single antenna processing was provided using  $C/N_0$  estimates. An interference mitigation technique for Galileo E1 frequencies was proposed in (Iubatti et al. 2006) that

jointly exploits the advantages of space-time-frequency domains. In order to achieve interference mitigation, a projection based algorithm to remove undesired interference signals from the received signals was proposed. Here the incoming signal was projected on to the interference orthogonal subspace and later a joint space-time filter was applied. In this research work, the decoupled space-time processing structure is considered. Temporal processing is applied at each antenna output and spatial processing is applied at the post-correlation stage. Temporal processing based on MMSE equalization and spatial processing based on an adaptive beamformer is described in the following section.

#### **5.4 Proposed STAP for BOC signals**

The proposed STAP architecture for BOC signal tracking is provided in Figure 5-8. In this approach, the incoming BOC signals are at first processed using the temporal equalizer discussed in Chapter 3 that produces a signal with a BPSK-like spectrum. The filtered spectra from several antennas are then combined using a spatial beamformer that produces maximum gain at the desired signal direction of arrival. The beamformed signal is then fed to the code and carrier lock loops for further processing.

The temporal filter is designed according to the MMSE equalization principle described in Chapter 3, Equation 3.5.

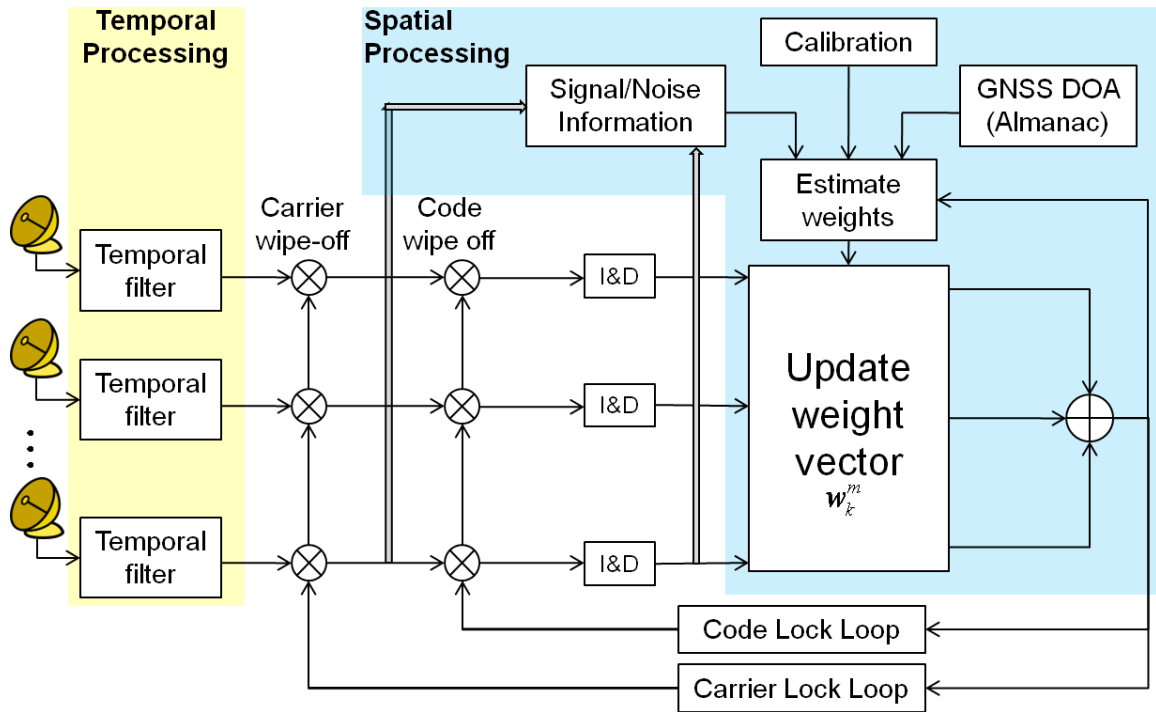


**Figure 5-8 Space-time adaptive processing structure proposed for BOC signal tracking; the temporal filter provides signal with unambiguous ACF and the spatial filter provides enhanced performance to multipath, interference and noise**

Further, the spatial weights are computed and updated based on the following information:

- The signal and noise covariance matrix obtained from the correlator outputs;
- Calibration parameters estimated according to the algorithm described in Chapter 4 to minimize the effect of mutual coupling and antenna gain/phase mismatch;
- Satellite data decoded from the ephemeris/almanac containing information of GNSS signal direction of arrival.

The weights are updated using the iterative approach (Du et al. 2009) for the MVDR beamformer to maximize the signal quality as

while (weight not converged)

Update SV using Calibration parameters

*for i = 1:M*

$$\hat{q}_i(t) = q_i(t) \sum_{j=1}^{M-1} (v_{i,j} s_i)^H$$

$$\hat{s}_i(t) = s_i(t) \hat{q}_i(t)$$

*end*

Update weight vector with new estimates

(5.7)

from covariance matrix and SV

$$\hat{R}_{nn} = \frac{1}{T} \int_0^T (\tilde{\mathbf{y}}^{CaWO}(t)) (\tilde{\mathbf{y}}^{CaWO}(t))^H$$

$$w(t) = \frac{\hat{R}_{nn}^{-1} \hat{\mathbf{s}}(t)}{\hat{\mathbf{s}}(t) \hat{R}_{nn}^{-1} \hat{\mathbf{s}}(t)}$$

end

where  $q(\cdot), v$  and  $\mathbf{s}$  are defined in Section 4.4.

Here  $\tilde{\mathbf{y}}^{CaWO}(t)$  represents the input signal  $\tilde{\mathbf{y}}(t)$  after carrier wipe-off as

$$\tilde{\mathbf{y}}^{CaWO}(t) = \tilde{y}_m(t) \exp\{-j\theta_h\} \quad (5.8)$$

Since the GNSS signals are buried in noise, the carrier wipe-off process brings the incoming signal to baseband and the covariance matrix of the noise plus interference can be obtained using  $\tilde{\mathbf{y}}^{CaWO}(t)$  as shown in (5.7). A sample plot of the antenna array pattern for IF simulated BOCs(1,1) signals for a 4-element planar array using the spatial beamformer obtained in (5.7) is shown in Figure 5-9. Later, two interference signals were introduced at 60 and 45 degree elevation angles and the corresponding antenna array pattern obtained using the MVDR beamformer is shown in Figure 5-10. It can be clearly observed that, in the presence of interference, the MVDR beamformer successfully adapted the array beam pattern to place nulls in the interference DOA. Thus, the proposed

combined processing is an effective space-time beamformer for BOC signals able to take advantages of the spatial and temporal techniques described in previous chapters of this thesis.

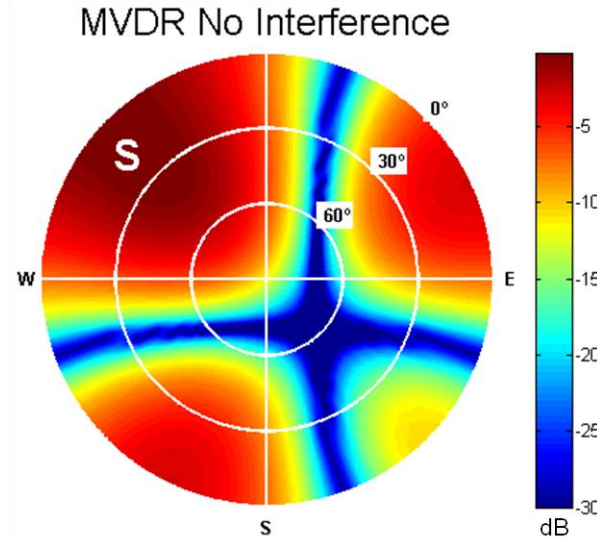


**Figure 5-9** Antenna array pattern for a 4-element planar array computed using a MVDR beamformer in the absence of interference

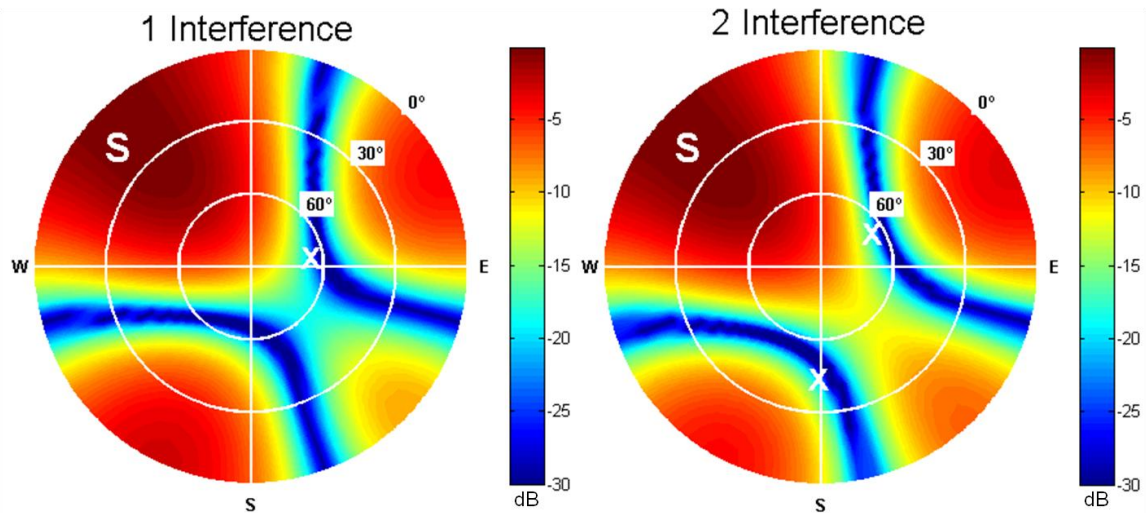


**Figure 5-10** Antenna array pattern for a 4-element planar array computed using a MVDR beamformer in the presence of single and dual interference sources

## 5.5 Results and Analysis

In this section, the proposed combined space-time processing technique for BOC signal tracking has been analyzed for different antenna array structures and satellite signal strengths. Simulated data and live GPS signals have been used to validate the proposed space-time technique.

### 5.5.1 Simulation analysis

In this section, the semi-analytic approach described in Chapter 2 has been considered for the analysis of the tracking loops involving multi-antenna system as shown in Figure 5-11. The semi-analytic model described in Figure 2.15 has been modified to include the effects of multi-antenna system as shown in Figure 5-11. The simulation scheme consists of  $M$  antenna elements with each antenna input defined by either a code delay ( $\tau_m$ ), for DLL analysis, or carrier phase for PLL analysis ( $\phi_m$ ).  $\phi_m$  captures the effect of mutual coupling, antenna phase mismatch and phase effects due to different antenna hardware paths. To analyze the post-correlation processing structure described in Section 5.3, each antenna input is processed independently to obtain the error signal,  $\Delta\tau_m/\Delta\phi_m$  as  $\Delta\tau_m/\Delta\phi_m = \tau_m/\phi_m - \hat{\tau}/\hat{\phi}$ , where  $\hat{\tau}/\hat{\phi}$  are current joint delay/phase estimates. Each error signal is then used to obtain the signal components that are added along with the independent noise components,  $E_n^m, P_n^m, L_n^m$ . The combined signal and noise components from all antenna elements are fed to the spatial beamformer to produce a single output according to the algorithm described in Section 5.4. Further, the beamformer output is passed through the loop discriminator, filter and the NCO to provide a single estimate

$\hat{\tau}/\hat{\phi}$ . The Error to Signal mapping block and the noise generation process accounts for the impact of the temporal filtering.

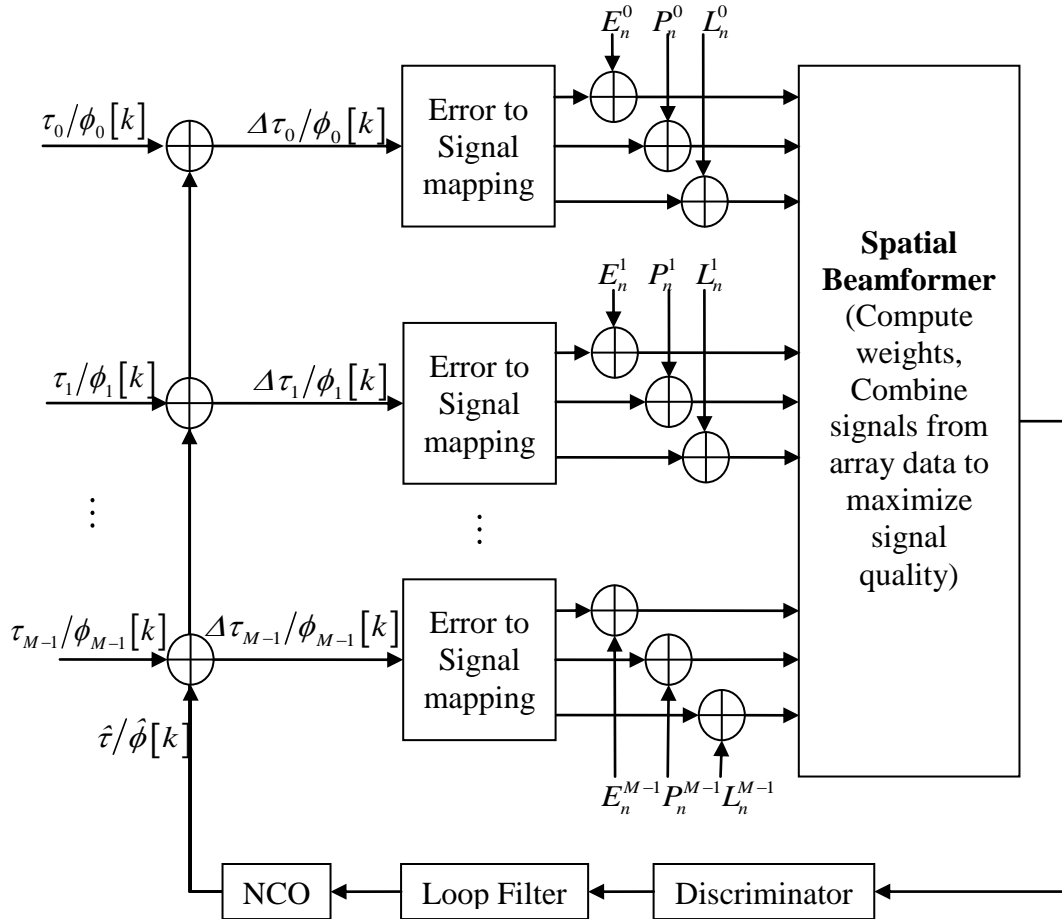


**Figure 5-11 Semi-analytic simulation model for multi-antenna system comprising of M-antenna with a spatial beamformer**

Sample tracking jitter plots for a PLL with a single, dual and three-antenna array system obtained using the structure described above are provided in Figure 5-12. The number of simulation runs considered was 50000 with a coherent integration time of 20 ms and a PLL bandwidth equal to 5 Hz. It can be observed that tracking jitter improves when the number of antenna elements is increased along with improved tracking sensitivity. As

expected, the  $C/N_0$  values at which loss of lock occurs for a three antenna system is reduced with respect to the single antenna system, showing its superiority with respect to single and dual antenna processing.

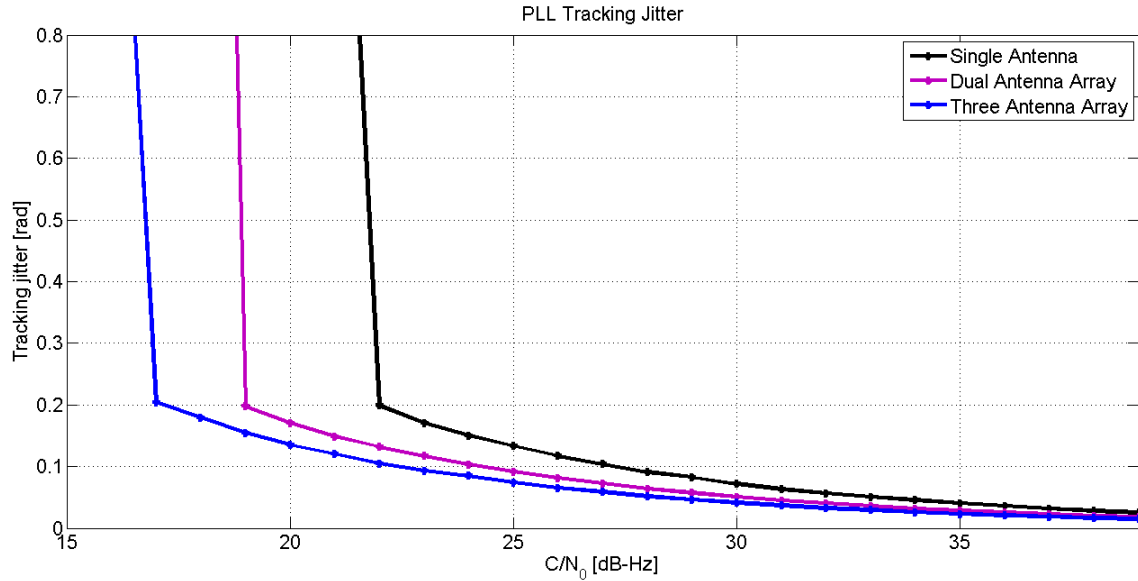


**Figure 5-12 Phase tracking jitter obtained for single, dual and three antenna linear array as a function of input  $C/N_0$  for a Costas discriminator (20 ms coherent integration and 5 Hz bandwidth)**

### 5.5.2 Real data analysis

The experimental setup considered for the analysis of the proposed combined space-time algorithm is shown in Figure 5-13. Two antennas spaced 8.48 cm apart were used to form a 2-element linear antenna array structure. The NI front-end detailed in Section 3.8 was employed for the data collection process to synchronously collect data from a two-antenna system. Data on both channels were progressively attenuated by 1 dB every 10 s to simulate a weak signal environment until an attenuation of 20 dB was reached. When this level of attenuation was reached, the data was attenuated by 1 dB every 20 s to allow for longer processing for weak signal conditions. In this way, data on

both antennas were attenuated simultaneously. Also, data from Antenna 1 was passed through a splitter as shown in Figure 5-13 before attenuation in order to collect unattenuated signal to obtain reference code delay and carrier Doppler frequencies.

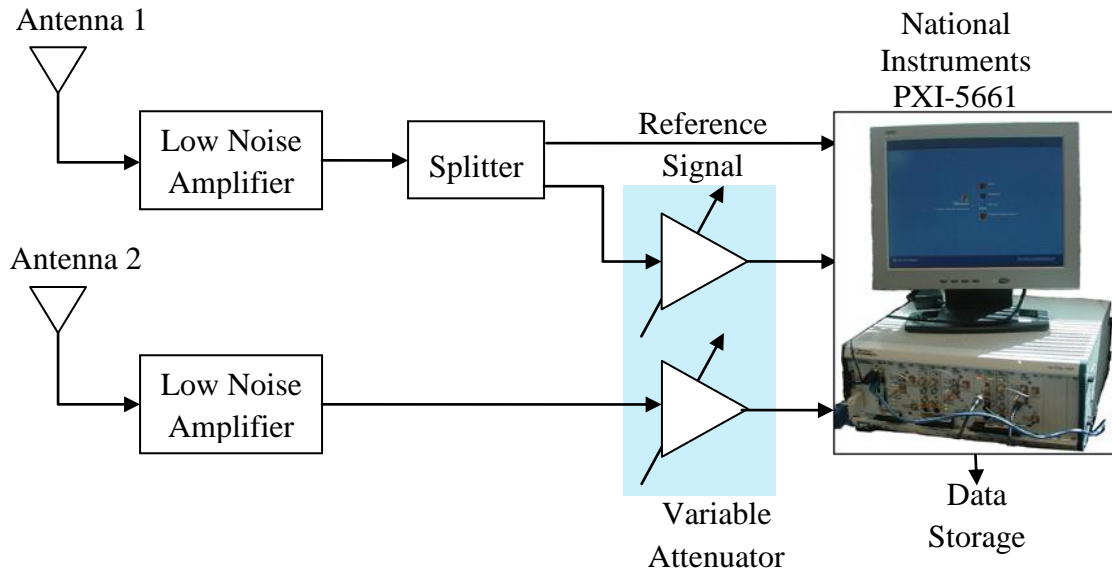


**Figure 5-13 Experimental setup with signals collected using two antennas spaced 8.48 cm apart**

BOCs(1,1) signals collected using Figure 5-13 were tracked using the temporal and spatial processing technique described in Figure 5-8. The  $C/N_0$  results obtained using single and two antennas are provided in Figure 5-14. In the single antenna case, only temporal processing was used. In this case, the loop was able to track signals for an approximate  $C/N_0$  of 19 dB-Hz. During the space-time processing that included MMSES and MVDR beamformer, the dual antenna system was able to track for nearly 40 s longer than the single antenna case, thus providing around 2 dB improvement in tracking sensitivity.

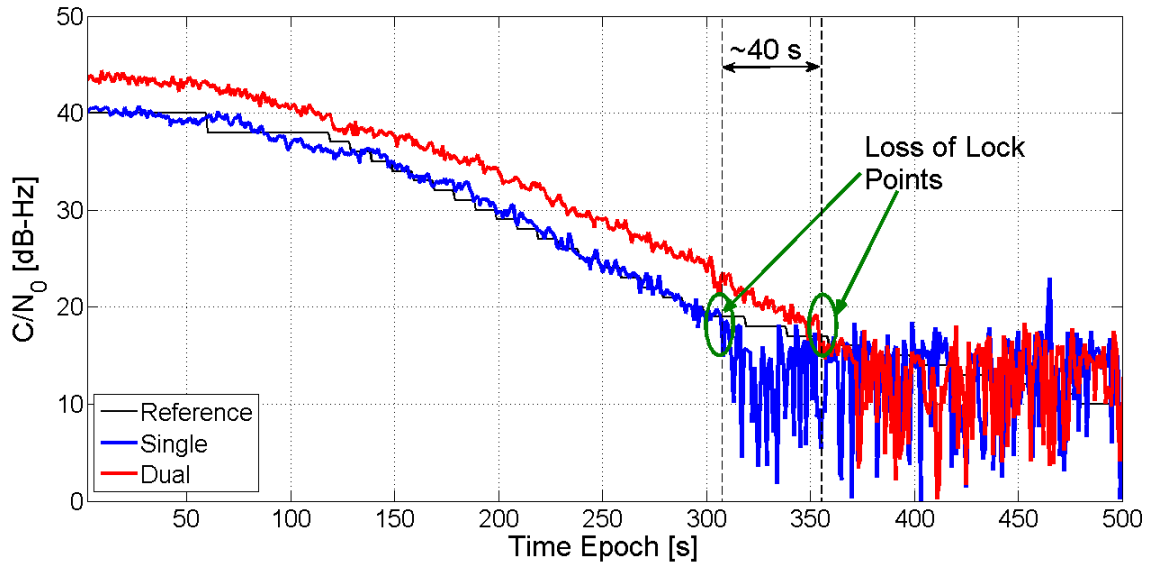


**Figure 5-14**  $C/N_0$  estimates obtained using a single antenna, temporal only processing and a dual antenna array system using space-time processing

## 5.6 Summary

In this chapter, space-time processing techniques and their advantages were introduced. A detailed literature review of the different kinds of space-time processing techniques as applied to GNSS signal processing was provided. A combined space-time processing technique for BOC signal processing was proposed that involved three different components: a temporal filter at the output of each antenna, a calibration algorithm and finally a spatial beamformer to maximize the signal quality in the desired direction of arrival. Simulation analysis showed the effectiveness of combined STAP for interference mitigation and real data analysis showed the advantage of using antenna array over single antenna for attenuated signal conditions.

## Chapter Six: Conclusions and Recommendations

This chapter provides the conclusions of the research work presented in this thesis to efficiently take advantage of space-time techniques for improved GNSS signal processing. Possible future directions that would enhance the proposed methodologies are also suggested.

### 6.1 Conclusions

The main goal of this research work was the development of space-time processing techniques for BOC signal tracking to mitigate the effects of multi-peaked ACF and enhance the signal quality. Towards this, the thesis research work was conducted in three different stages with predefined objectives according to Section 1.3. The following sections provide the related research activities and their outcome with respect to BOC signal tracking.

#### 6.1.1 Temporal Processing

- a. The literature review and analysis of existing pre-filtering techniques highlighted their ineffectiveness in mitigating the noise amplification and secondary peak false locks in a medium to low  $C/N_0$  conditions. For this purpose, the MMSES and ZFS techniques were proposed for unambiguous BOC signal tracking. Through semi-analytic simulations, it was observed that the MMSES technique is able to provide superior performance in terms of tracking jitter, tracking threshold and MTLL with respect to ZFS providing unambiguous BOC tracking and performance comparable to that of the DE.

- b. One of the main concerns during BOC signal tracking is the secondary peak lock condition due to the presence of multiple peaks in its ACF. Analysis on the tracking error convergence shows that the ZFS and MMSES are able to provide unambiguous code tracking. Also, the tracking error always converges to zero when the initial error is within  $\pm 1$  chip.
- c. Simulation analysis of the multipath error envelopes showed that the proposed MMSES technique provides superior good multipath mitigation with its flexibility to shape the ACF.
- d. The proposed techniques were initially developed in the frequency domain and subsequently a time domain equivalent approach was considered. The time domain approach was found to be less computationally demanding compared to the frequency domain approach and the DE technique. The reduced computational requirements of the proposed technique enable its implementation in real time receivers.
- e. Initial analysis of the proposed methodology using live BOC signals showed degradation in the PLL performance due to the filtering process adopted for unambiguous tracking. A modified tracking structure was suggested for separate DLL and PLL processing. As a result of the independent delay and phase tracking structure, it was observed that the PLL is unaffected by the filtering process, thereby providing an improved tracking sensitivity.
- f. Analysis using live data collected from GIOVE-A/B satellites showed that the MMSES technique not only provides unambiguous tracking but is able to shape the BOC ACF base-width providing enhanced multipath mitigation capabilities.

Further, it was observed that MMSES loses lock for a  $C/N_0$  approximately 2 dB-Hz lower as compared to the BJ with performance similar to that of the DE in weak signal environments.

### ***6.1.2 Spatial Processing***

- a. A self-contained antenna array calibration procedure using only the existing GNSS signals and not requiring any other additional reference data was proposed and analyzed. The proposed methodology is able to accurately estimate the calibration parameters for various antenna structures and satellite signal power levels for both simulations and real data.
- b. Through Monte Carlo simulations, it was observed that the integration time of the correlator outputs used for the calibration process significantly affects the accuracy of the proposed methodology. A coherent integration time greater than 100 ms is required to reduce the noise impact.
- c. The proposed algorithm is able to provide in-line calibration of GNSS receivers adopting multiple antennas. Experiments using live GNSS data with a maximum of four antennas demonstrated the feasibility of the proposed algorithm supporting its effectiveness in enabling multi-antenna processing. The phase error on the calibrated planar array output for live GNSS data in both elevation and azimuth domain was observed to be within  $\pm 10$  degrees on all available satellites
- d. Beamforming results for the calibrated array system are analyzed in terms of estimated  $C/N_0$  values. A good agreement between the theoretical and estimated

$C/N_0$  values was observed in most of the satellites for different antenna array structures and varying number of antennas.

### ***6.1.3 Space-Time Processing***

- a. A decoupled space-time approach that includes a temporal filter at the output of each antenna and a spatial post-correlation beamformer was adopted to perform space-time processing on GNSS signals. The temporal filter is based on the MMSE criteria and the spatial beamformer is designed based on the MV criteria. Simulation results show the effectiveness of the proposed methodology in the presence of interference signals. Tracking jitter results using a semi-analytic approach provided for a single, dual and three antenna system demonstrated the effectiveness of the proposed approach.
- b.  $C/N_0$  analysis for real data collected using a dual antenna array showed the effectiveness of combined space-time processing in attenuated signal environments providing around a 2 dB improvement in tracking sensitivity.

In summary, using spatial and temporal processing enables unambiguous BOC tracking along with the maximization of the signal quality in the desired direction of arrival.

## **6.2 Recommendations for future work**

Based on the analysis and experimental results obtained in this research work, the following recommendations can be made:

- a. The proposed ZFS and MMSES tracking techniques were analyzed in detail for BOCs(1,1) modulated signals and a limited insight into their behavior were provided for higher order BOC signals. Thus an extended analysis for higher

order BOC modulated signals such as BOCc(10,5), BOCc(15,2.5), that are transmitted by the Galileo satellites on E6-A and E1-A channels, would provide further insight on the performance of the proposed technique.

- b. The performance of the proposed ZFS and MMSES techniques was analyzed in the tracking domain. A detailed analysis in the pseudorange/position domain would provide a better insight into the effects of filtering on the receiver performance.
- c. The semi-analytic techniques designed in this research considered DLL and PLL independently while the combined analysis could provide a better understanding in terms of the real GNSS receiver performance.
- d. The semi-analytic technique considered in this research work was based only on the standard tracking loop structures defined in (Kaplan & Hegarty 2006). Several other tracking schemes such as vector tracking and Kalman filtering can be developed on a similar basis for performance comparison.
- e. The analysis of the proposed techniques has been considered mainly in signal attenuated conditions. Similar analysis indoors would provide an insight on the behavior of the proposed techniques in fading and multipath rich environments.
- f. During antenna array calibration, it was assumed that the array manifold is constant and analysis was performed based on this assumption. But in real conditions, the array manifold varies due to antenna phase center variations and antenna phase center offsets. These effects could be modeled to provide more accurate calibration results.

- g. Interference mitigation using calibrated antenna array was mainly shown using simulations in Chapter 5. Live interference signals can be transmitted from desired directions to analyze the effectiveness of the antenna array under more realistic conditions.
- h. The effectiveness of the combined space-time processing technique for BOC signal tracking was demonstrated using attenuated signals from a dual antenna array. A similar performance analysis using several other array structures, such as planar and circular arrays, could be analyzed to determine the effective improvement provided by the proposed approach and its application to GNSS receivers.

## References

- Alexiou, A. and M. Haardt (2004) "Smart antenna technologies for future wireless systems: trends and challenges," in *IEEE Communications Magazine*, Vol. 42, Issue 9, September, pp. 90 - 97
- Anantharamu, P. B., D. Borio, and G. Lachapelle (2011) "Self-contained GNSS-based Antenna Array Calibration," in *Proceedings of the 2011 International Technical Meeting of The Institute of Navigation*, 24 - 26 January, San Diego, pp. 1232 - 1239
- Anantharamu, P. B., D. Borio, and G. Lachapelle (2011) "Sub-carrier Shaping for BOC Modulated GNSS Signals," in *EURASIP Journal on Advances in Signal Processing* (*accepted for publication on May 2011*)
- Applebaum, S. P. and D. J. Chapman (1976) "Adaptive arrays with main beam constraints," in *IEEE Transactions on Antenna and Propagation*, Vol. 24, Issue 5, pp. 650-662
- Backen, S., D. M. Akos, and M. L. Nordenvaad (2008) "Post-Processing Dynamic GNSS Antenna Array Calibration and Deterministic Beamforming," in *Proceedings of the 21st International Technical Meeting of the Satellite Division*, 16-19 September, Savannah, GA, The Institute of Navigation, pp. 2806-2814
- Balanis, C. A. and P. Ioannides (2007) *Introduction to Smart Antennas*, Synthesis Lectures on Antennas #5, Morgan & Claypool Publishers' Series, pp. 33-67, ISBN 1598291769
- Balanis, C. A. (1992) "Antenna Theory: A Review," in *Proceedings of the IEEE*, Vol. 80, Issue 1, pp. 7-21
- Balanis, C. A. (2005) *Antenna Theory - Analysis and Design*, A John Wiley & Sons Inc. Publication
- Betz, J. W. and K. R. Kolodziej斯基 (2009a) "Generalized theory of code tracking with an early-late discriminator Part I: Lower bound and coherent processing," in *IEEE Transactions on Aerospace and Electronic Systems*, Vol. 45, Issue 4, Oct, pp. 1538-1550
- Betz, J. W. and K. R. Kolodziej斯基 (2009b) "Generalized theory of code tracking with an early-late discriminator Part II: Noncoherent processing and numerical results," in *IEEE Transactions on Aerospace and Electronic Systems*, Vol. 45, Issue 4, pp. 1551-1564
- Betz, J. W. (1999) "The Offset Carrier Modulation for GPS Modernization," in *Proceedings of the 1999 National Technical Meeting*, 25-27 January, San Diego, CA, The Institute of Navigation, pp. 639-648

- Blunt, P. D., R. Weiler, S. Hodgart, and M. Unwin (2007) "Demonstration of BOC(15,2.5) acquisition and tracking with a prototype hardware receiver," in *Proceedings of the European Navigation Conference*, September
- Borio, D. and C. O'Driscoll (2009) *GNSS Receiver Design*, ENGO 638 Course Notes, Department of Geomatics Engineering, University of Calgary, Canada
- Borio, D., P. B. Anantharamu, and G. Lachapelle (2011) "SATLSim: A Semi-Analytic Framework for Fast GNSS Tracking Loop Simulations," in *GPS Toolbox, GPS Solutions, Springer*, Published Online 06 May 2011
- Borio, D., P. B. Anantharamu, and G. Lachapelle (2010) "Semi-Analytic Simulations: An Extension to Unambiguous BOC Tracking," in *Proceedings of the 2010 International Technical Meeting*, 25-27 January, San Diego, CA, The Institute of Navigation, pp. 1023-1036
- Borio, D., S. Fazio, and G. Lachapelle (2009) "Multirate Signal Processing: a Solution for Wide-band GNSS Signal Recovery," in *Proceedings of the European Navigation Conference 2009 (ENC09)*, 3-6 May, Naples, Italy
- Borio, D. (2008) *A statistical theory for GNSS signal acquisition*, Ph.D. dissertation, Politecnico di Torino, Italy
- Borio, D. (2010) *GNSS Receiver Design*, ENGO 638 Course Notes, Department of Geomatics Engineering, University of Calgary, Canada
- Braasch, M. S. (1996) "GPS Multipath Model Validation," in *Proceedings of the IEEE PLANS-96*, 22-26 April, Atlanta, pp. 672-678
- Broumandan, A., T. Lin, A. Moghaddam, A. Lu, J. Nielsen, and G. Lachapelle (2007) "Direction of Arrival Estimation of GNSS Signals Based on Synthetic Antenna Array," in *Proceedings of the 20th International Technical Meeting of the Satellite Division*, 25-28 September, Fort Worth, TX, The Institute of Navigation, pp. 728-738
- Church, C. M. and I. J. Gupta (2009) "Calibration of GNSS Adaptive Antennas," in *Proceedings of the 22nd International Meeting of the Satellite Division of The Institute of Navigation*, 22-25 September, Savannah, GA
- Cuntz, M., H. Denks, A. Konovaltsev, A. Hornbostel, A. Dreher, and M. Meurer (2008) "GALANT - Architecture Design and First Results of A Novel Galileo Navigation Receiver Demonstrator With Array Antennas," in *Proceedings of the 21st International Technical Meeting of the Satellite DIvision*, 16-19 September, Savannag, GA, The Institute of Navigation, pp. 1470-1477

Dierendonck, A. J.V., P. Fenton, and T. Ford (1992) "Theory and performance of narrow correlator spacing in a GPS Receiver," in *Journal of Institute of Navigation*, Vol. 39, Issue 3, pp. 265-283

Dierendonck, A. J.V. (1996) *GPS Receivers, Chapter 8 in Global Positioning System: Theory and Applications*, American Institute of Aeronautics and Astronautics

Dovis, F., P. Mulassano, and L. L. Presti (2005) "A Novel Algorithm for the Code Tracking of BOC(n,n) Modulated Signals," in *Proceedings of the 18th International Technical Meeting of the Satellite Division*, 13-16 September, Long Beach, CA, The Institute of Navigation, pp. 152-155

Du, L., T. Yardibi, J. Li, and P. Stoica (2009) "Review of user parameter-free robust adaptive beamforming algorithms," in *Digital Signal Processing*, Vol. 19, Issue 4, pp. 567-582

Fante, R. L. (2003) "Unambiguous Tracker for GPS Binary-Offset-Carrier Signals," in *Proceedings of the 59th Annual Meeting of The Institute of Navigation and CIGTF 22nd Guidance Test Symposium*, 23-25 June, Albuquerque, NM, The Institute of Navigation, pp. 141-145

Fine, P. and W. Wilson (1999) "Tracking Algorithm for GPS Offset Carrier Signals," in *Proceedings of the 1999 National Technical Meeting*, 25-27 January, San Diego, CA, The Institute of Navigation, pp. 671-676

Fleury, B. H., M. Tschudin, R. Heddergott, D. Dahlhaus, and K. I. Pedersen (1999) "Channel Parameter Estimation in Mobile Radio Environments Using the SAGE Algorithm," in *IEEE Journal on Selected Areas in Communications*, Vol. 15, Issue 3, pp. 434-450

Fu, Z., A. Hornbostel, J. Hammesfahr, and A. Konovaltsev (2003) "Suppression of multipath and jamming signals by digital beamforming for GPS/Galileo applications," *GPS Solutions*, vol. 6, no. 4, March, Springer Berlin, Heidelberg, pp. 1521-1886

Galileo (2008) *Galileo Open Service Signal In Space Interface Control Document, OS SIS ICD*, Draft 1, Feb 2008 European Space Agency/European GNSS Supervisory , <http://www.gsa.europa.eu/go/galileo/os-sis-icd>

Geist, J. (1979) "Computer generation of correlated gaussian random variable," in *Proceedings of the IEEE*, May, pp. 862-863

GIOVE (2010), <http://www.giove.esa.int/index.php?menu=1>

GIOVEICD (2008) *GIOVE-A+B Navigation Signal-In-Space Interface Control Document*, European Space Agency

Golshan, A. R., S. N. Lu, and T. H. Dang (2005) "Analysis of mean-time to lose lock in a first-order digital DLL for NRZ and BOC signals in the presence of a single-tone interferer," in *Proceedings of the ION/AM (Annual Meeting)*, 27-29 June, Cambridge, pp. 1163-1170

Golshan, A. R. (2005) "Loss of Lock Analysis of a first-order digital code tracking loop and comparison of results to analog loop theory for BOC and NRZ signals," in *Proceedings of the ION/NTM (National Technical Meeting)*, 24-26 Jan, San Diego, California, pp. 299-305

Golshan, A. R. (2006) "Post-Correlator Modeling for Fast Simulation and Joint Performance Analysis of GNSS Code and Carrier Tracking Loops," in *Proceedings of the 2006 National Technical Meeting*, 18-20 January, Monterey, CA, The Institute of Navigation, pp. 312-318

Gupta, I. J. and A. A. Ksieinski (1983) "Effect of Mutual Coupling on the Performance of Adaptive Arrays," in *IEEE Transactions on Antennas and Propagation*, Vol. AP-31, Issue 5, pp. 785-792

Gupta, I. J., J. R. Baxter, S. W. Ellingson, H. G. Park, H. S. Oh, and M. G. Kyeong (2003) "An experimental study of antenna array calibration," in *IEEE Transactions on Antennas and Propagation*, Vol. 51, Issue 3, March, pp. 664-667

Hassab, J. C. and R. E. Boucher (1979) "Optimum estimation of time delay by a generalized correlator," in *IEEE Transactions on Acoustics, Speech and Signal Processing*, Vol. 27, Issue 4, pp. 373-380

Haykin, S. (2001) *Adaptive Filter Theory*, Prentice Hall, ISBN 0130901261

Hein, G. W., M. Irsigler, J. A. Avila-Rodriguez, and T. Pany (2004) "Performance of Galileo L1 Signal Candidates," in *Proceedings of the European Navigation Conference GNSS 2004*, 16-19 May, Rotterdam, The Netherlands

Hodgart, M. S., P. D. Blunt, and M. Unwin (2008) "Double Estimator—A New Receiver Principle for Tracking BOC signals," *Inside GNSS*, vol. 3, no. 3, Spring, pp. 26-36

Hogbom, J. A. (1974) "Aperture synthesis with a non-regular distribution of interferometer baselines," in *Astronomy and Astrophysics Supplement*, Vol. 15, pp. 417-426

Huang, Y. and H. Leib (2000) "SINR maximizing space-time filtering for asynchronous DS-CDMA," *IEEE Journal on Selected Areas in Communications*, vol. 18, no. 7, July, pp. 1191-1202

Iubatti, M., M. Casadei, R. Pedone, A. Vanelli-Coralli, G. E. Corazza, and R. Crescimbeni (2006) "Subspace Array Processing for Interference Mitigation in L1-Band

Galileo Receivers," in *Proceedings of the 2006 International Workshop on Satellite and Space Communications*, 14-15 September, Madrid, pp. 153-157

Johnson, R. C. (1993) *Antenna Engineering Handbook (3rd Edition)*, McGraw-Hill, ISBN 9781601190116

Julien, O., C. Macabiau, M. E. Cannon, and G. Lachapelle (2007) "ASPeCT: Unambiguous sine-BOC(n,n) acquisition/tracking technique for navigation applications," in *IEEE Transactions on Aerospace and Electronic Systems*, Vol. 43, Issue 1, January, pp. 150-162

Kalyanaraman, S. K. and M. S. Braasch (2006) "Phase Compensation in GPS Array Processing using a Software Radio," in *Proceedings of the 2006 IEEE/ION Position, Location, And Navigation Symposium*, 25-27 April, pp. 324-334

Kaplan, E. D. and C. J. Hegarty (2006) *Understanding GPS Principles and Applications*, Artech House, pp. 155-200, ISBN-13:978-1-58053-894-7

Kay, S. M. (2008) *Fundamentals of Statistical Signal Processing, Volume 2: Detection Theory*, Prentice Hall, ISBN 0-13-504135-X

Khalaj, B. H., A. Paulraj, and T. Kailath (1995) "Spatio-temporal channel estimation techniques for multiple access spread spectrum systems with antenna arrays," in *Proceedings of the 1995 IEEE International Conference on Communications 'Gateway to Globalization'*, 18-22 June, Seattle, pp. 1520-1524

Klemm, R. (2006) *Principles of Space-Time Adaptive Processing*, Institution of Engineering and Technology, London, UK, ISBN 0863415660

Kohno, R. (1997) "Software antenna and its communication theory for mobile radio communications," in *Proceedings of the 1997 IEEE International Conference on Personal Wireless Communications*, 17-19 December, Mumbai, pp. 227-233

Kohno, R. (1998) "Spatial and temporal communication theory using adaptive antenna array," in *IEEE Personal Communications*, Vol. 5, Issue 1, February, pp. 28-35

Kunysz, W. (2000) "A Novel GPS Survey Antenna," in *Proceedings of the Institute of Navigation NTM 2000*, 26-28 January, Anaheim, CA, pp. 698-705

Lin, T., A. Broumandan, J. Nielsen, C. O'Driscoll, and G. Lachapelle (2009) "Robust Beamforming for GNSS Synthetic Antenna Arrays," in *Proceedings of the 22nd International Technical Meeting of The Satellite Division*, 22-25 September, Savannah, GA, The Institute of Navigation, pp. 387-401

Lindskog, E. (1999) *Space-Time Processing and Equalization for Wireless Communications*, PhD Thesis Dissertation, Uppsala University

McGraw, G. A. and M. S. Braasch (1999) "GNSS Multipath Mitigation Using Gated and High Resolution Correlator Concepts," in *Proceedings of the 1999 National Technical Meeting of The Institute of Navigation*, 25-27 January, San Diego, CA, pp. 333-342

Mikhail, E. M. (1976) *Observations and least squares* , Intext Educational Publishers, New York, pp. 497, ISBN 0700224815

Mogensen, P. E., L. P. Espensen, I. K. Pedersen, and P. Zetterberg (1999) "Antenna Arrays and Space Division Multiple Access," [Chapter 4] in *GSM Evolution Towards 3rd Generation Systems*, Kluwer Academic Publishers, Netherlands, 117-149

Monzingo, R. A. and T. W. Miller (2004) *Introduction to Adaptive Arrays*, SciTech Publishing, Inc., Raleigh, ISBN 1891121243

Morion (2010) *Double Oven Ultra Precision OCXO MV89*, [http://morion.com.ru/catalog\\_pdf/MV89-OCXO.pdf](http://morion.com.ru/catalog_pdf/MV89-OCXO.pdf), last accessed April 12, 2011

Morrison, A. (2010) *GNSS Signal Tracking Methods Under Ionospheric Scintillation*, PhD Thesis, published as Report No. 20312, The University of Calgary

Morrison, A. (2010) *Leapfrog 2 Channel Wideband Front-End - Usage Guide*, Internal Report, Department of Geomatics Engineering, University of Calgary

Ng, B. C. and C. M.C. See (1996) "Sensor-array calibration using a maximum-likelihood approach," in *IEEE Transactions on Antennas and Propagation*, Vol. 44, Issue 6, June, pp. 827-835

NI (2006) *2.7 GHz RF Vector Signal Analyzer with Digital Downconversion*, National Instruments, [http://www.ni.com/pdf/products/us/cat\\_vectorsignalanalyzer.pdf](http://www.ni.com/pdf/products/us/cat_vectorsignalanalyzer.pdf)

Novatel (2006) "GPS-702L" Datasheet, NovAtel's GPS-700 antenna series, <http://www.novatel.com/Documents/Papers/GPS-702L.pdf>

Nuthalapati, R. M. (2008) "Design of mismatched filters for long binary codes," in *Proceedings of the IEEE Radar Conference*, May, pp. 1-6

O'Brien, A. J. and I. J. Gupta (2008) "Optimum Adaptive Filtering for GNSS Antenna Arrays," in *Proceedings of the 21st International Technical Meeting of the Satellite Division*, 16-19 September, Savannah, GA, The Institute of Navigation, pp. 2796-2805

Oppenheim, V. (1981) "The importance of phase in signals," in *Proceedings of the IEEE*, , pp. 529-541

Pany, T. and B. Eissfeller (2008) "Demonstration of a Synthetic Phased Array Antenna for Carrier/Code Multipath Mitigation," in *Proceedings of the 1st International Technical Meeting of the Satellite Division*, 16-19 September, Savannah, GA, The Institute of Navigation, pp. 663-668

- Pany, T., M. Irsigler, B. Eissfeller, and J. Winkel (2002) "Code and Carrier Phase Tracking Performance of a Future Galileo RTK Receiver," in *Proceedings of the ENC GNSS 2002*, 27-30 May, Copenhagen
- Park, H. G. and S. C. Bang (2003) "Model based antenna array calibration for digital beamforming systems," in *Proceedings of the 57th IEEE Semiannual Vehicular Technology Conference*, Spring, pp. 867
- Paulraj, A. J. and E. Lindskog (1998) "Taxonomy of space-time processing for wireless networks," in *IEE Proceedings Radar, Sonar and Navigation*, Vol. 145, Issue 1, pp. 25
- Petovello, M. G., C. O'Driscoll, G. Lachapelle, D. Borio, and H. Murtaza (2009) "Architecture and Benefits of an Advanced GNSS Software Receiver," *Positioning*, vol. 1, no. 1, August, pp. 66-78
- Prades, C. F. and J. A.F. Rubio (2004) "Multi-frequency GPS/Galileo receiver design using direct RF sampling and antenna arrays," in *Proceedings of the Sensor Array and Multichannel Signal Processing Workshop*, 18-21 July, pp. 475-479
- Pratt, A. R. and J. I.R. Owen (2003) "BOC Modulation Waveforms," in *Proceedings of the 16th International Technical Meeting of the Satellite Division of The Institute of Navigation (ION GPS/GNSS 2003)*, 9-12 September, Portland, pp. 1044-1057
- Qureshi, S. U.H. (1985) "Adaptive equalization," in *Proceedings of the IEEE*, September, pp. 1349-1387
- Rougerie, S., G. Carrie, L. Ries, F. Vincent, R. Pascaud, E. Corbel, and M. Monnerat (2011) "Multipath Mitigation Methods Based on Antenna Array," in *Proceedings of the 2011 International Technical Meeting of The Institute of Navigation*, 24-26 Jan, San Diego, CA, pp. 596 - 605
- Satyanaarayana, S., D. Borio, and G. Lachapelle (2010) "Power Levels and Seconds Order Statistics for Indoor fading Using a Calibrated A-GPS Software Receiver," in *Proceedings of the ION GNSS10*, 21-24 September, Portland
- Schmidt, R. O. (1986) "Multiple Emitter Location and Signal Parameter Estimation," in *IEEE Transactions on Antennas and Propagation*, Vol. 34, Issue 3, March 1986, pp. 276-280
- Seco-Granados, G., J. A. Fernandez-Rubio, and C. Fernandez-Prades (2005) "ML estimator and hybrid beamformer for multipath and interference mitigation in GNSS receivers," in *IEEE Transactions on Signal Processing*, Vol. 53, Issue 3, March, pp. 1194-1208

- Tranter, W. H., K. S. Shanmugan, T. S. Rappaport, and K. L. Kosbar (2004) *Principles of Communication Systems Simulation with Wireless Applications*, Prentice Hall, Communications Engineering and Emerging Technologies Series
- Trefethen, L. N. and D. Bau (1997) *Numerical linear algebra*, Society for Industrial and Applied Mathematics, Philadelphia, pp. 56-61, ISBN 0-89871-361-7
- Tsui, J. B. (2004) *Fundamentals of Global Positioning System Receivers: A Software Approach*, John Wiley & Sons, Inc., ISBN-978-0-471-70647-2
- Van Trees, H. L. (2002) *Optimum Array Processing, Part IV of Detection, Estimation, and Modulation Theory*, John Wiley & Sons, Inc, New York, ISBN 0471221104
- Van Veen, B. D. and K. M. Buckley (1988) "Beamforming: a versatile approach to spatial filtering," *IEEE ASSP Magazine*, vol. 5, no. 2, April, pp. 4-24
- Vicario, J. L. et al. (2010) "ADIBEAM: Adaptive Digital Beamforming for Galileo Reference Ground Stations," in *Proceedings of the ION GNSS 2010*, 22-24 September, Portland, OR
- Ward, J. (1998) "Space-time adaptive processing for airborne radar," in *IEE Colloquium on Space-Time Adaptive Processing (Ref. No. 1998/241)*, pp. 2/1-2/6
- Ward, P. W. (2003) "A Design Technique to Remove the Correlation Ambiguity in Binary Offset Carrier (BOC) Spread Spectrum Signals," in *Proceedings of the 59th Annual Meeting of The Institute of Navigation and CIGTF 22nd Guidance Test Symposium*, 23-25 June, Albuquerque, NM, pp. 146-155
- Widrow, B., P. E. Mantey, L. J. Griffiths, and B. B. Goode (1967) "Adaptive Antenna Systems," in *Proceedings of the IEEE*, Vol. 55, Issue 12, pp. 2143-2159
- Yang, C., M. Miller, T. Nguyen, and D. Akos (2006) "Generalized Frequency-Domain Correlator for Software GPS Receiver: Preliminary Test Results and Analysis," in *Proceedings of the 19th International Technical Meeting of the Satellite Division*, 26-29 September, Fort Worth, TX, The Institute of Navigation, pp. 2346-2630
- Yao, Z. (2008) "A New Unambiguous Tracking Technique for Sine-BOC(2n,n) Signals," in *Proceedings of the 21st International Technical Meeting of the Satellite Division*, 16-19 September, Savannah, GA, The Institute of Navigation, pp. 1490-1496

## APPENDIX A: CODE DISCRIMINATORS AND TRACKING JITTER

In this appendix, the different code discriminators considered in this research work are briefly analyzed and theoretical expressions for the tracking jitter are provided.

### A.1. Code discriminators

The non-coherent, quasi-coherent and coherent discriminators considered in this research work are summarized in Table A-1.

**Table A-1 Description of various code discriminators used in GNSS tracking loops**

Discriminator	Processing	Description
Non-coherent	$ E ^2 -  L ^2$ , $ E  = \sqrt{E_I^2 + E_Q^2}$ $ L  = \sqrt{L_I^2 + L_Q^2}$	Introduces noise due to squaring Can be normalized by $ E ^2 +  L ^2$ to remove any amplitude dependency Requires only Early and Late correlators
Quasi-coherent	$\Re\{(E - L)P^*\}$ $= (E_I - L_I)P_I$ $+ (E_Q - L_Q)P_Q$	Requires all three Early, Late and Prompt correlators Independent of the carrier phase Dependent on square of signal amplitude (It can be normalized by the square of the Prompt correlator).
Coherent	$\Re\{E - L\}$ $= E_I - L_I$	Requires phase lock condition from the PLL Accurate code measurements Dependent on signal amplitude (it can be normalized) Performance degrades in the presence of cycle slips and loss of phase lock

#### A.1.1. Discriminator Gain

Any memory-less discriminator can be approximated by a constant gain when the tracking loop is in lock conditions, i.e., when the residual code error is small. This gain is used in the derivation of the tracking jitter. The discriminator gain can be obtained as

$$g_d = \frac{d}{d\tau} D(\tau) \Big|_{\tau=0} \quad (A.1)$$

where  $D(\tau)$  is the discriminator function. The discriminator gain should be computed in the absence of noise since it represents the gain provided to the signal component alone. The discriminator gains for non-coherent, quasi-coherent and coherent discriminators are provided below.

- Non-coherent

The discriminator function for a non-coherent discriminator is given by

$$D(\tau) = |E|^2 - |L|^2. \quad (A.2)$$

Computing the derivative of (A.2) with respect to  $\tau$  yields

$$\begin{aligned} \frac{d}{d\tau} D(\tau) &= \frac{d}{d\tau} (|E|^2 - |L|^2) \\ &= \frac{dD}{d|E|} \cdot \frac{d|E|}{d\tau} - \frac{dD}{d|L|} \cdot \frac{d|L|}{d\tau} \\ &= 2|E|\dot{R}(\tau - d_s/2) - 2|L|\dot{R}(\tau + d_s/2) \end{aligned} \quad (A.3)$$

where  $E = R(\tau - d_s/2)$ ,  $P = R(\tau)$  and  $L = R(\tau + d_s/2)$  are the correlators in the absence of noise.  $R(\cdot)$  is the signal correlation function.

Evaluating Eq. (A.3) at  $\tau = 0$  and using the identities  $R(\tau) = R(-\tau)$  and  $\dot{R}(-\tau) = -\dot{R}(\tau)$  results in the following expression for the non-coherent discriminator gain

$$g_d = 4R(d_s/2)\dot{R}(-d_s/2). \quad (A.4)$$

- Quasi-coherent

The discriminator function for a quasi-coherent discriminator is given by

$$D(\tau) = \Re\{(E - L)P^*\}. \quad (\text{A.5})$$

In the absence of noise and assuming that the three correlators have the same phase, it is possible to omit the real part operator in (A.5). Computing the derivative of (A.5) with respect to  $\tau$  yields

$$\begin{aligned} \frac{d}{d\tau} D(\tau) &= \frac{d}{d\tau} ((E - L)P^*) \\ &= \frac{dD}{dP} \cdot \frac{dP}{d\tau} + \frac{dD}{dL} \cdot \frac{dL}{d\tau} + \frac{dD}{dE} \cdot \frac{dE}{d\tau} \\ &= 0 \cdot 1 \cdot P \cdot \dot{R}(\tau + d_s/2) + P \cdot \dot{R}(\tau - d_s/2) \\ &= P \dot{R}(\tau - d_s/2) - P \dot{R}(\tau + d_s/2). \end{aligned} \quad (\text{A.6})$$

Evaluating at  $\tau = 0$  and assuming  $P^*|_{\tau=0} = R(0) = 1$ , results in the gain

$$g_d = 2\dot{R}(-d_s/2). \quad (\text{A.7})$$

- Coherent

The discriminator function for a coherent discriminator is given by

$$D(\tau) = \Re\{(E - L)\}. \quad (\text{A.8})$$

Computing the derivative of (A.8) with respect to  $\tau$  yields

$$\begin{aligned} \frac{d}{d\tau} D(\tau) &= \frac{d}{d\tau} ((E - L)) \\ &= \frac{dD}{dL} \cdot \frac{dL}{d\tau} + \frac{dD}{dE} \cdot \frac{dE}{d\tau} \\ &= -\dot{R}(\tau + d_s/2) + \dot{R}(\tau - d_s/2). \end{aligned} \quad (\text{A.9})$$

Evaluating at  $\tau = 0$  results in the discriminator gain

$$g_d = 2\dot{R}(-d_s/2). \quad (\text{A.10})$$

Substituting the expressions for BPSK and BOCs (1, 1) ACF yields the discriminator gains provided in Table A-2.

**Table A-2 Discriminator gain for BPSK and BOCs (1, 1) signal**

Description	BPSK	BOCs (1,1)	Sub-carrier for BOCs(1,1)
ACF, $R(\tau)$	$1 -  \tau ,  \tau  \leq 1$ 0, elsewhere	$1 - 3 \tau ,  \tau  \leq 0.5$ $-1 +  \tau , 0.5 \leq  \tau  \leq 1$ 0, elsewhere	$1 - 4 \tau ,  \tau  \leq 0.5$ $-3 + 4 \tau , 0.5 \leq  \tau  \leq 1$ 0, elsewhere
Derivative of ACF, $R'(\tau)$	$-sign(\tau),  \tau  \leq 1$ 0, elsewhere	$-3sign(\tau),  \tau  \leq 0.5$ $sign(\tau), 0.5 \leq  \tau  \leq 1$ 0, elsewhere	$-4sign(\tau),  \tau  \leq 0.5$ $4sign(\tau), 0.5 \leq  \tau  \leq 1$ 0, elsewhere
Non- coherent gain	$2(2 - d_s), d_s \leq 1$ 0, elsewhere	$6(2 - 3d_s), d_s \leq 0.5$ $-2(-2 + d_s), 0.5 \leq d_s \leq 1$ 0, elsewhere	$16(1 - 2d_s), d_s \leq 0.5$ $-16(-3 + 2d_s), 0.5 \leq d_s \leq 1$ 0, elsewhere
Quasi- coherent gain	2, $d_s \leq 1$ 0, elsewhere	6, $d_s \leq 0.5$ -1, $0.5 \leq d_s \leq 1$ 0, elsewhere	8, $d_s \leq 0.5$ -8, $0.5 \leq d_s \leq 1$ 0, elsewhere
Coherent gain	2, $d_s \leq 1$ 0, elsewhere	6, $d_s \leq 0.5$ -1, $0.5 \leq d_s \leq 1$ 0, elsewhere	8, $d_s \leq 0.5$ -8, $0.5 \leq d_s \leq 1$ 0, elsewhere

## A.2. Tracking jitter

The theoretical expression of the tracking jitter is obtained using the equivalent model of the tracking loop shown in Figure A-1. The equivalent model is generally adopted for the linear analysis of tracking loops. In this model the input noise,  $\eta(t)$ , is propagated after the non-linear discriminator and an equivalent output noise is obtained.

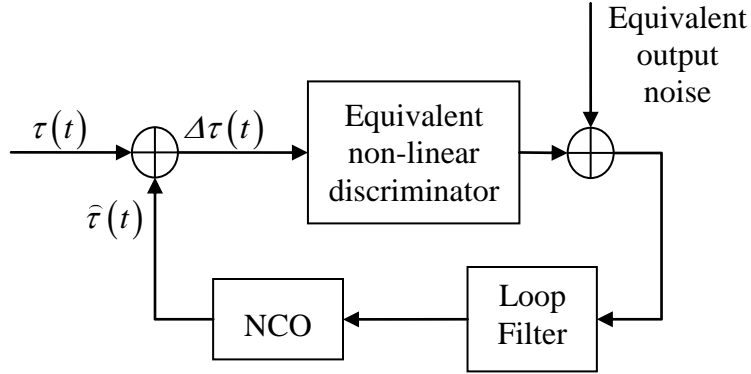


**Figure A-1 Equivalent model of a digital GNSS tracking loop**

An equivalent non-linear discriminator operating on the tracking error is used for describing the discriminator impact on the error driving the loop. By approximating the equivalent non-linear discriminator by a constant gain,  $g_d$ , a linear model is obtained. In this way, it is possible to define the concept of loop bandwidth and derive approximate formulas for quantities such as the tracking jitter (Dierendonck et al. 1992, Dierendonck 1996). The theoretical tracking jitter is defined as

$$\sigma_j = \frac{\sqrt{2B_{eq}T_i}\sigma_d}{g_d} \quad (\text{A.11})$$

where  $B_{eq}$  is the equivalent loop bandwidth in Hz and  $\sigma_d$  is the variance of the discriminator output.

Consider the coherent discriminator,  $D = \Re\{E - L\}$  where  $E = E_I + jE_Q$  and  $L = L_I + jL_Q$ .

The variance of the coherent discriminator is given by

$$\begin{aligned} \sigma_d^2 &= \text{var}\{D\} = \text{var}\{\Re(E - L)\} \\ &= E\left[\Re(E - L)^2\right] - E^2\left[\Re(E - L)\right]. \end{aligned} \quad (\text{A.12})$$

Under perfect lock condition, values of  $E$  and  $L$  are equal and hence

$$E[\Re(E-L)] = E[E_I - L_I] = 0 \text{ and thus (A.12) simplifies to}$$

$$\begin{aligned} \sigma_d^2 &= E[(E_I - L_I)^2] \\ &= E[E_I^2 + L_I^2 - 2E_I L_I]. \end{aligned} \quad (\text{A.13})$$

Under perfect phase lock condition  $E_I \sim \mathcal{N}(R_n(d_s/2), \sigma_i^2)$  and  $L_I \sim \mathcal{N}(R_n(-d_s/2), \sigma_i^2)$

where  $R_n(\cdot)$  is the correlation function between the incoming and locally generated signals. The difference between  $R(\cdot)$  and  $R_n(\cdot)$  is discussed in Appendix B. It is thus possible to evaluate each term in (A.13) independently

$$\begin{aligned} E[E_I^2] &= R_n^2(d_s/2) + \sigma_i^2 \\ E[L_I^2] &= R_n^2(d_s/2) + \sigma_i^2 \\ E[E_I L_I] &= E[(\tilde{E}_I + R_n(d_s/2))(\tilde{L}_I + R_n(-d_s/2))] \\ &= \sigma_i^2 R_n(d_s) + R_n^2(d_s/2) \end{aligned} \quad (\text{A.14})$$

where  $\tilde{E}_I \sim \mathcal{N}(0, \sigma_i^2)$  and  $\tilde{L}_I \sim \mathcal{N}(0, \sigma_i^2)$ . Substituting (A.14) in (A.13) provides the discriminator variance as

$$\begin{aligned} \sigma_d^2 &= R_n^2(d_s/2) + \sigma_i^2 + R_n^2(d_s/2) + \sigma_i^2 - 2\sigma_i^2 R_n(d_s) - 2R_n^2(d_s/2) \\ &= 2\sigma_i^2(1 - R_n(d_s)). \end{aligned} \quad (\text{A.15})$$

Thus the final tracking jitter of a DLL using a coherent discriminator is given by

$$\begin{aligned} \sigma_j^c &= \sqrt{\frac{B_{eq} T_i \sigma_i^2 (1 - R_n(d_s))}{\dot{R}^2(d_s/2)}} \\ &= \sqrt{\frac{B_{eq} (1 - R_n(d_s))}{2 C/N_0 \dot{R}^2(d_s/2)}}. \end{aligned} \quad (\text{A.16})$$

Using a similar approach for non-coherent and quasi-coherent discriminators, the following results are obtained

$$\begin{aligned}
 (\sigma_j^{nc})^2 &= \frac{2B_{eq}T_i 8\sigma_i^2 (1 - R_n(d_s))}{16\dot{R}^2(d_s/2)} \left[ \frac{(\sigma_i^2 (1 + R_n(d_s)))}{R_n^2(d_s/2)} + 1 \right] \\
 &= \frac{B_{eq}(1 - R_n(d_s))}{2C/N_0 \dot{R}^2(d_s/2)} \left[ \frac{(1 + R_n(d_s))}{2C/N_0 T_i R_n^2(d_s/2)} + 1 \right] \\
 (\sigma_j^{qc})^2 &= \frac{2B_{eq}T_i 2\sigma_i^2 (1 - R_n(d_s))}{4\dot{R}^2(d_s/2)} \left[ 1 + 2\sigma_i^2 \right] \\
 &= \frac{B_{eq}T_i(1 - R_n(d_s))}{2C/N_0 \dot{R}^2(d_s/2)} \left[ 1 + \frac{1}{C/N_0 T_i} \right].
 \end{aligned} \tag{A.17}$$

Using (A.16) and (A.17), it is possible to derive the tracking jitter for BPSK and BOCs (1, 1) modulated signals. The theoretical expressions for the tracking jitter under different conditions are given in Table A-3. In the pre-filtering case, an additional term  $\gamma$  is introduced to account for the effect of filtering on the signal and noise components. Detailed expression for  $\gamma$  is provided in Appendix B along with the semi-analytic models for simulating different BOC tracking techniques.

**Table A-3 Tracking jitter for BPSK, BOCs (1, 1) and pre-filtered signals**

Signal → Discriminator ↓	BPSK	BOCs (1, 1)
Non-coherent	$\sqrt{\frac{B_{eq}d_s}{2C/N_0} \left[ \frac{2}{C/N_0 T_i (2 - d_s)} + 1 \right]}$	$\sqrt{\frac{B_{eq}}{6C/N_0} \left[ \frac{2}{C/N_0 T_i (2 - 3d_s)} + 1 \right]}$
Quasi-coherent	$\sqrt{\frac{B_{eq}T_id_s}{2C/N_0} \left[ 1 + \frac{1}{C/N_0 T_i} \right]}$	$\sqrt{\frac{B_{eq}T_id_s}{6C/N_0} \left[ 1 + \frac{1}{C/N_0 T_i} \right]}$
Coherent	$\sqrt{\frac{B_{eq}d_s}{2C/N_0}}$	$\sqrt{\frac{B_{eq}d_s}{6C/N_0}}$
Signal → Discriminator ↓	Sub-carrier for BOCs (1, 1) (SLL tracking jitter)	Pre-filtering
Non-coherent	$\sqrt{\frac{B_{eq}}{8C/N_0} \left[ \frac{2}{C/N_0 T_i (2 - 4d_s)} + \right]}$	$\sqrt{\frac{B_{eq}\gamma(1 - R_n(d_s))}{2C/N_0 \dot{R}^2(d_s/2)} \left[ \frac{\gamma(1 + R_n(d_s))}{2C/N_0 T_i R_n^2(d_s/2)} + 1 \right]}$
Quasi-coherent	$\sqrt{\frac{B_{eq}T_id_s}{8C/N_0} \left[ 1 + \frac{1}{C/N_0 T_i} \right]}$	$\sqrt{\frac{B_{eq}\gamma(1 - R_n(d_s))}{2C/N_0 \dot{R}^2(d_s/2)} \left[ 1 + \frac{\gamma}{C/N_0 T_i} \right]}$
Coherent	$\sqrt{\frac{B_{eq}d_s}{8C/N_0}}$	$\sqrt{\frac{B_{eq}\gamma(1 - R_n(d_s))}{2C/N_0 \dot{R}^2(d_s/2)}}$

## APPENDIX B: SEMI-ANALYTIC TECHNIQUE

In this section, the semi-analytic models developed for the analysis of different BOC tracking techniques are provided. Three different versions of the generalized semi-analytic model developed in (Borio et al. 2011) have been considered for the BJ, DE and pre-filtering techniques.

### B.1. Semi-analytic models

Consider the data sequence  $y(t) = x(t) + \eta(t)$  to be the input to a tracking loop. The signal  $y(t)$  after code and carrier wipe-off is integrated and dumped over  $T_i$  seconds.

The output of the I&D blocks can be expressed as

$$\frac{A}{2} \frac{\sin(\pi \Delta f_D T_i)}{\pi \Delta f_D T_i} R(\Delta \tau) e^{j\Delta \phi} + \tilde{\eta} \quad (\text{B.1})$$

where  $\Delta \tau$ ,  $f_D$ ,  $\Delta \phi$  are the residual code delay, Doppler frequency and carrier phase errors to be minimized by the tracking loops.  $\tilde{\eta}$  is a complex noise term with independent and identically distributed real and imaginary parts obtained by processing  $\eta(t)$ . It is noted that different but correlated noise terms are obtained for the Early, Prompt and Late correlators. The first term in (B.1) represents the signal component while the second term is the noise component at the correlator output. The signal component can be simulated given the  $\Delta \tau$ ,  $f_D$ ,  $\Delta \phi$  values. For simulation purposes, it is possible to normalize the correlator amplitude to 1,  $A = \sqrt{C/2} = 1$ , and scale the noise

component accordingly. In this way, the variance of  $\tilde{\eta}$  assuming ideal front-end filtering, simplifies to (Borio 2008)

$$\sigma_i^2 = \frac{1}{C/N_0 T_i}. \quad (\text{B.2})$$

It is noted that all the parameters in (B.1) are known during the simulation process. The correlation among the noise terms when considering multiple correlators needs to be taken care and it is shown in (Borio 2008) to be a function of the relative delay of the local codes. When considering E, P and L correlators, the noise correlation matrix is given by

$$\begin{aligned} C_\eta &= E \left\{ \begin{bmatrix} \tilde{\eta}_E \\ \tilde{\eta}_P \\ \tilde{\eta}_L \end{bmatrix} \cdot \begin{bmatrix} \tilde{\eta}_E & \tilde{\eta}_P & \tilde{\eta}_L \end{bmatrix} \right\} \\ &= \sigma_i^2 \begin{bmatrix} 1 & R_n(d_s/2) & R_n(d_s) \\ R_n(d_s/2) & 1 & R_n(d_s/2) \\ R_n(d_s) & R_n(d_s/2) & 1 \end{bmatrix}. \end{aligned} \quad (\text{B.3})$$

where  $\tilde{\eta}_E, \tilde{\eta}_P, \tilde{\eta}_L$  are the noise components on E, P and L correlators. To generate the noise components on the correlator outputs accounting for the correlation between the different terms, a procedure based on (Geist 1979) can be used.  $C_\eta$  is decomposed using the Cholesky decomposition as

$$C_\eta = \sigma_i^2 A_c A_c^T \quad (\text{B.4})$$

and the noise component at the correlator output can be generated as

$$\begin{bmatrix} \tilde{\eta}_E \\ \tilde{\eta}_P \\ \tilde{\eta}_L \end{bmatrix} = \sigma_i A_c \begin{bmatrix} \bar{\eta}_E \\ \bar{\eta}_P \\ \bar{\eta}_L \end{bmatrix} \quad (\text{B.5})$$

where  $\bar{\eta}_E$ ,  $\bar{\eta}_P$  and  $\bar{\eta}_L$  are three complex independent Gaussian random variables with independent real and imaginary parts with unit variance.

Using this procedure, a generalized semi-analytic technique has been derived in (Borio et al. 2010). The block diagram of the generalized semi-analytic model for digital tracking loop analysis is shown in Figure B-1.

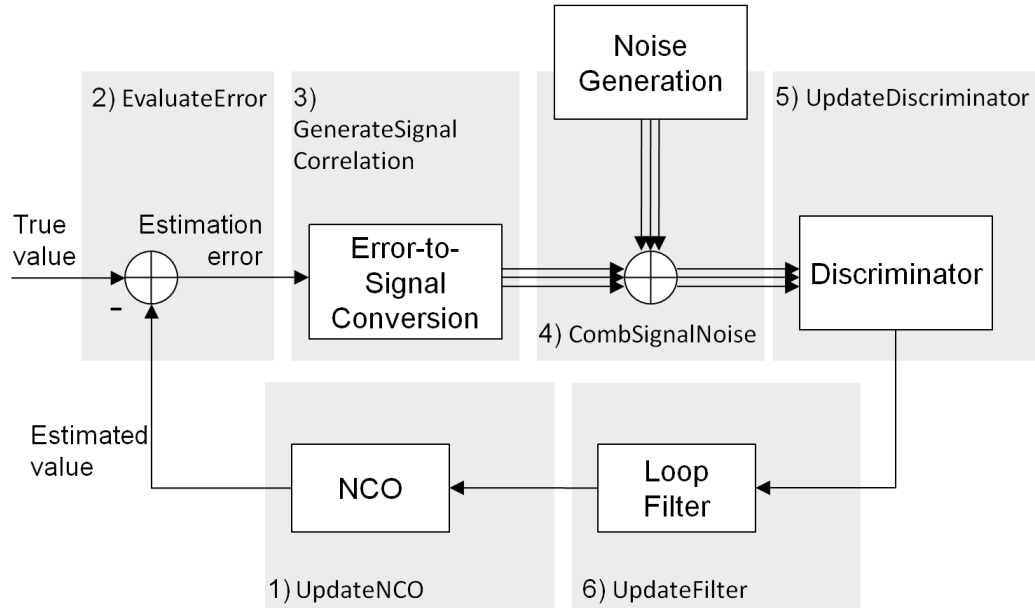


**Figure B-1 Generalized semi-analytic model for digital GNSS tracking loops analysis**

It can be observed that the model includes several blocks, either analytic or simulation blocks. The analytic block includes the error estimation and the generation of signal and noise components at the correlator outputs using the analytic model presented above while the blocks including non-linear discriminator, loop filter and NCO are fully simulated. The parameters analytically propagated can be one among code delay, Doppler frequency and carrier phase depending on the tracking loop analyzed, DLL, FLL or PLL. The error to signal conversion block uses (B.1) to generate the signal

components and the noise generation block generates the noise component according to (B.5). Matlab code for the realization of the generalized model provided in Figure B-1 as applied to DE and PLL is provided in (Borio et al. 2011).

### B.1.1. Bump-Jump

For the BJ technique, the general model in Figure B-1 is used along with a block for the decision logic as shown in Figure B-2. The BOCs (1, 1) ACF is used in the error to signal conversion block to map the code delay error to the signal component of the correlator output. Two additional correlators VE and VL are simulated along with the standard E, P and L correlators to detect secondary peak lock (Fine & Wilson 1999).

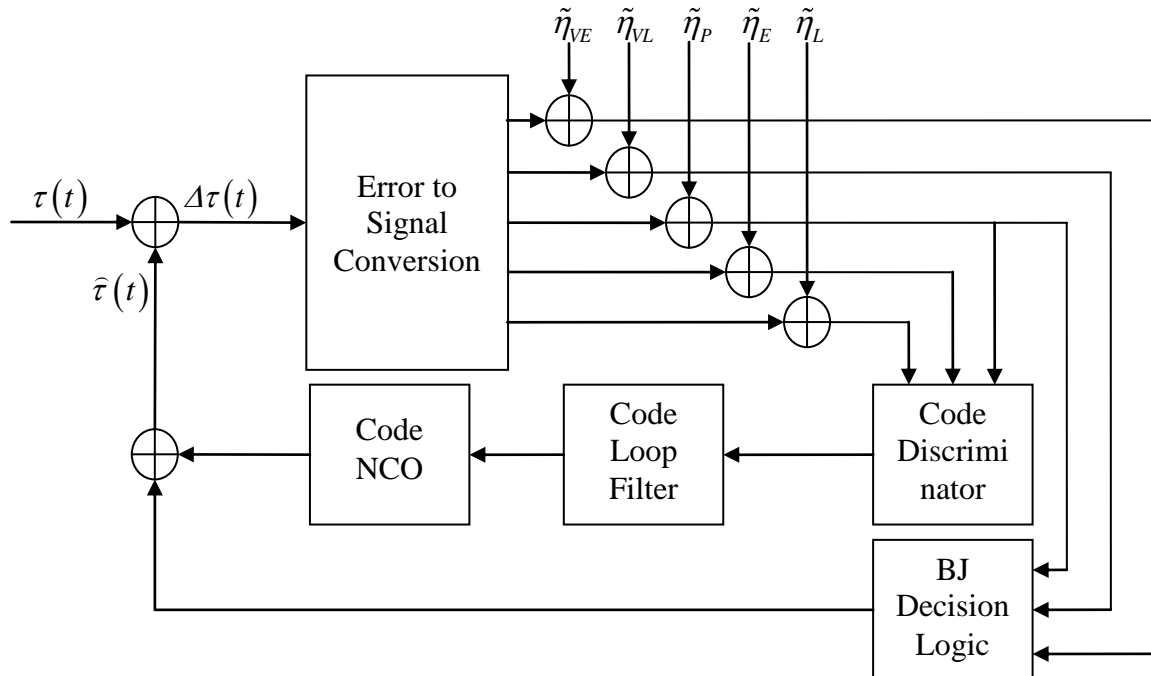


**Figure B-2 Semi-analytic model for the Bump-Jump technique**

The correlation matrix of (B.3) is extended as follows

$$C_\eta = \sigma_i^2 \begin{bmatrix} 1 & R_n\left(\frac{d_v - d_s}{2}\right) & R_n\left(\frac{d_v}{2}\right) & R_n\left(\frac{d_v + d_s}{2}\right) & R_n(d_v) \\ R_n\left(\frac{d_v - d_s}{2}\right) & 1 & R_n\left(\frac{d_s}{2}\right) & R_n(d_s) & R_n\left(\frac{d_v + d_s}{2}\right) \\ R_n\left(\frac{d_v}{2}\right) & R_n\left(\frac{d_s}{2}\right) & 1 & R_n\left(\frac{d_s}{2}\right) & R_n\left(\frac{d_v}{2}\right) \\ R_n\left(\frac{d_v + d_s}{2}\right) & R_n(d_s) & R_n\left(\frac{d_s}{2}\right) & 1 & R_n\left(\frac{d_v - d_s}{2}\right) \\ R_n(d_v) & R_n\left(\frac{d_v + d_s}{2}\right) & R_n\left(\frac{d_v}{2}\right) & R_n\left(\frac{d_v - d_s}{2}\right) & 1 \end{bmatrix} \quad (\text{B.6})$$

where  $d_v$  is the chip spacing between VE and VL correlators. In general, the VE and VL correlators are placed on the secondary peaks.

### B.1.2. Double Estimator

The semi-analytic model for the DE technique is shown in Figure B-3. The generalized model is extended to include an additional tracking loop for the sub-carrier as provided in (Borio et al. 2011). DLL and SLL run in parallel, tracking code and sub-carrier delay independently. The DE technique also requires five correlators (Hodgart et al. 2008) and the noise correlation matrix of (B.3) can be extended as

$$C_\eta = \sigma_i^2 \begin{bmatrix} 1 & R_{DE}\left(\frac{d_{sc}}{2}, \frac{d_s}{2}\right) & R_{DE}\left(\frac{d_{sc}}{2}, 0\right) & R_{DE}\left(\frac{d_{sc}}{2}, \frac{d_s}{2}\right) & R_{DE}(d_{sc}, 0) \\ R_{DE}\left(\frac{d_{sc}}{2}, \frac{d_s}{2}\right) & 1 & R_{DE}\left(0, \frac{d_s}{2}\right) & R_{DE}(0, d_s) & R_{DE}\left(\frac{d_{sc}}{2}, \frac{d_s}{2}\right) \\ R_{DE}\left(\frac{d_{sc}}{2}, 0\right) & R_{DE}\left(0, \frac{d_s}{2}\right) & 1 & R_{DE}\left(0, \frac{d_s}{2}\right) & R_{DE}\left(\frac{d_{sc}}{2}, 0\right) \\ R_{DE}\left(\frac{d_{sc}}{2}, \frac{d_s}{2}\right) & R_{DE}(0, d_s) & R_{DE}\left(0, \frac{d_s}{2}\right) & 1 & R_{DE}\left(\frac{d_{sc}}{2}, \frac{d_s}{2}\right) \\ R_{DE}(d_{sc}, 0) & R_{DE}\left(\frac{d_{sc}}{2}, \frac{d_s}{2}\right) & R_{DE}\left(\frac{d_{sc}}{2}, 0\right) & R_{DE}\left(\frac{d_{sc}}{2}, \frac{d_s}{2}\right) & 1 \end{bmatrix} \quad (\text{B.7})$$

where,  $R_{DE}((\cdot)_{sc}, (\cdot)_c)$  is the two-dimensional autocorrelation (Hodgart et al. 2008) as a function of sub-carrier and code delay.  $d_{sc}$  is the chip spacing between sub-carrier early and late correlators.

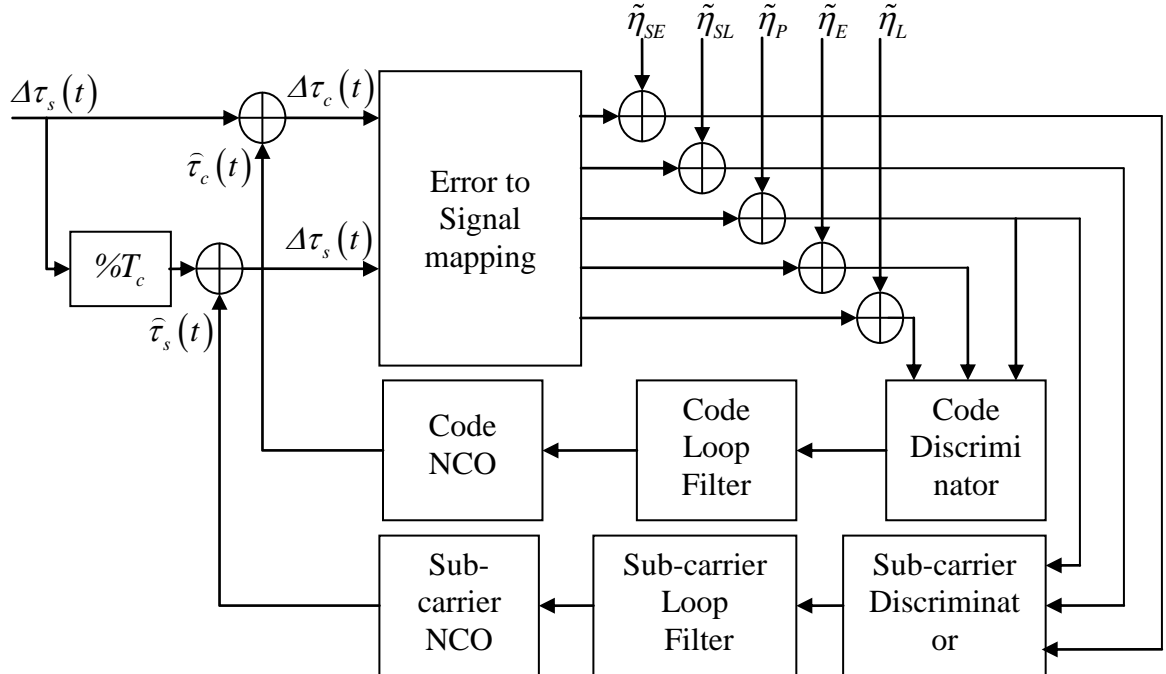


**Figure B-3** Semi-analytic model for the Double Estimator technique

### B.1.3. Pre-filtering

The generalized model for semi-analytic technique is used for the simulation of pre-filtering techniques as shown in Figure B-4. Here, the signal correlation function is modified through filtering (Borio et al. 2010). The effects of filtering are accounted for by modeling the signal and noise ACF accordingly. Pre-filtering introduces noise amplification problem which has to be accounted for in the noise variance simulation.

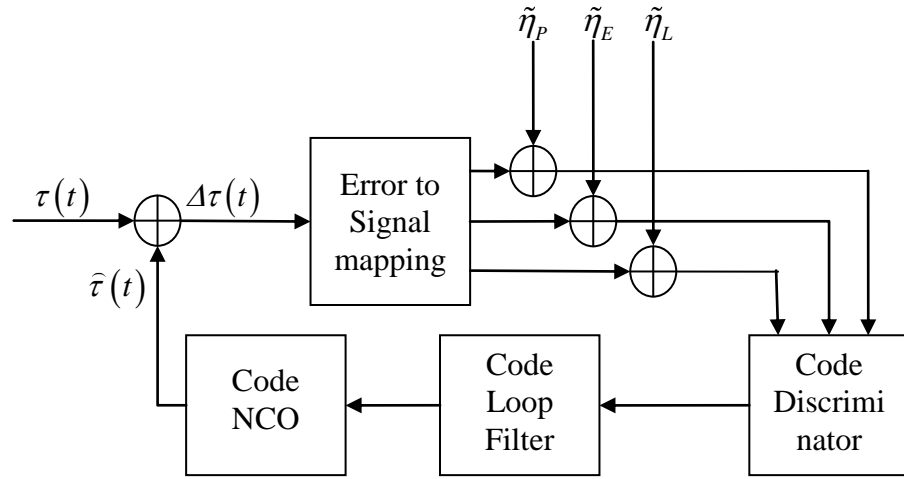


**Figure B-4 Semi-analytic model for pre-filtering technique**

The filter used to shape the signal autocorrelation modifies the signal and noise properties. More specifically, a loss in the SNR at the correlator output is introduced. This effect is the already mentioned noise amplification problem and its impact can be determined using an approach similar to the one adopted by (Borio 2008, Betz & Kolodziejki 2009a, Betz & Kolodziejki 2009b).  $H(f)$ , the transfer function of the pre-filtering stage, generates a colored noise and the post-correlation SNR becomes (Borio 2008):

$$SNR = \frac{C}{N_0} T_i \gamma \quad (B.8)$$

where  $\gamma$  is the filtering loss equal to

$$\gamma = \frac{\left| \int_{-B}^B G_x(f) H(f) df \right|^2}{\int_{-B}^B G_x(f) |H(f)|^2 df}. \quad (\text{B.9})$$

It is noted that the numerator and denominator in (B.9) are the signal and noise terms of the cost function (3.3). The MMSES tries to find a compromise between making  $G_x(f)H(f)$  as close as possible to the desired spectrum,  $G_D(f)$ , reducing the noise term at the denominator of (B.9). If the amplitude of the Prompt correlator output is assumed to be normalized to unity, the inverse of (B.9) determines the variance of the post-correlation noise components:

$$\sigma_i^2 = \frac{1}{C / N_0 T_i \gamma}. \quad (\text{B.10})$$

The signal component after correlation is proportional to the filtered correlation function

$$R(\Delta\tau) = \mathcal{F}^{-1} \left\{ G_x(f) H(f) \right\}_{t=\Delta\tau} \quad (\text{B.11})$$

whereas the noise components of different correlator outputs are characterized by a correlation coefficient equal to

$$R_n(\Delta\tau) = \mathcal{F}^{-1} \left\{ G_x(f) |H(f)|^2 \right\}_{t=\Delta\tau}. \quad (\text{B.12})$$

In (B.12),  $\Delta\tau$  is used to denote the delay difference between two correlators. Early and Late are separated by a delay equal to  $d_s$  whereas the Prompt correlator is characterized by a delay difference equal to  $d_s/2$  with respect to the other correlators.